

University of St Andrews

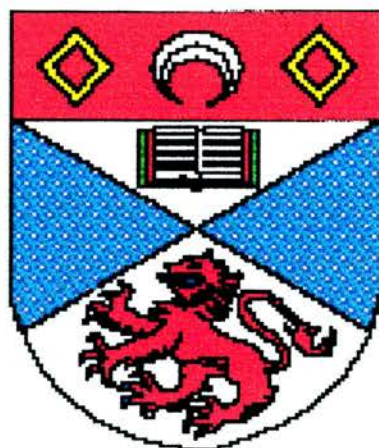


Full metadata for this thesis is available in
St Andrews Research Repository
at:

<http://research-repository.st-andrews.ac.uk/>

This thesis is protected by original copyright

University of St Andrews



School of Chemistry

New studies on reduced lithium
titanates.

Richard Keith Branson Gover



For the degree of Doctor of Philosophy.

I would like to dedicate this work to the 4Ms

For their love, patience and support.

I, Richard K.B. Gover, hereby certify that this thesis, which is approximately 40000 words in length, has been written by me, that it is the record of work carried out by me and that it has not been submitted in any previous application for a higher degree.

date... 5/12/97.....signature of candidate

I was admitted as a research student in October 1994 and as a candidate for the degree of Doctor of Philosophy in October 1995; for higher study for which this is a record was carried out in the University of St Andrews between 1994 and 1997.

date... 5/12/97.....signature of candidate

I hereby certify that the candidate has fulfilled the conditions of the Resolution and Regulations appropriate for the degree of Doctor of Philosophy in the University of St. Andrews and that the candidate is qualified to submit this thesis in application for that degree.

date... 5/12/97.....signature of supervisor

In submitting this thesis to the University of St. Andrews I understand that I am giving permission for it to be made available for use in accordance with the regulations of the University Library for the time being in force, subject to any copyright vested in the work not being affected thereby. I also understand that the title and abstract will be published, and that a copy of the work maybe made and supplied to any bona fide library or research worker.

date... 5/12/97.....signature of candidate.

Acknowledgements.

I would like to acknowledge the following people (in no particular order) for help and assistance during the last three years.

For help with all aspects of diffraction I would like to thank Dr A.R. Armstrong, Dr Raymond R. Thomas (IPNS, USA) and Dr Ron Smith (ISIS, UK).

For help with Magnetic and Muon measurements, I would like to thank sincerely, Ross Stewart, Professor Bob Cynwski and Adrian Hillier. I would also like to thank Dr Nianhua Peng for his help with the low temperature electrical measurements and Dr David Tunstall for collection of the Solid State NMR data.

I would like to thank my supervisor Dr J.T.S. Irvine for his help, encouragement and belief in me. Many thanks are also due to Bob Cathcart, Brian Walker, Colin Smith and Jim Rennie for help with all things technical. I also acknowledge the financial support of the University of St. Andrews and the Russell Trust.

On a more personal level, I would like to thank all of my friends in St Andrews for making life here worthwhile. I would also like to acknowledge the staff of the Cellar Bar and The Yankee clipper for the good food and beer.

I would also like to thank Dr Monica Goff for her encouragement and last but certainly not least my wife, Mhorag for help, love, devotion, support and making me a happy man.

Abstract.

Reduced lithium titanates with spinel and ramsdellite structures have been investigated.

Powder neutron diffraction experiments on LiTi_2O_4 spinel indicate that the lithium **8a** tetrahedral site occupancy varies as a function of temperature with a corresponding Li occupancy on the **16c** octahedral site. It is proposed that this could explain differences seen in the literature for the superconducting transition (T_c) temperature. It was noted in this study that the T_c was linked to the thermal history. Solid State NMR also indicated extra Li sites at higher temperatures.

Penetration depth studies were performed on fresh and aged samples of spinel using $\mu^+\text{SR}$. The penetration depths obtained for the fresh sample was seen to be 320nm, which is different to that seen previously in the literature. Differences were explained in terms of sample preparation and the model used for data analysis. The penetration depth of the aged sample was 561nm and is believed to be due to sample degradation.

Experiments on the spinel to ramsdellite transformation indicate changes in structure occur in the region of 850 to 925°C. A deviation in the unit cell dimensions of spinel supports a second order phase change. The ramsdellite structure at high temperature was found to be stable, with two lithium sites found within the channels.

SQUID and muon studies on LiTi_2O_4 ramsdellite suggest the presence of magnetic order at low temperature in addition to contributions from Curie and Pauli paramagnetism. Electrical measurements were found to be dominated by grain boundaries.

It was found that LiTi_2O_4 and $\text{Li}_2\text{Ti}_3\text{O}_7$ ramsdellite could be related by $\text{Li}_{1+x}\text{Ti}_{2-2x}\text{O}_4$. It was noted that as Li replaced Ti on the framework, vacancies were created in the channel sites. Lithium could only be found on one site within the channels across the solid solution series, although previous studies on the Ti^{4+} end member have shown the presence of two sites. The differences have been explained in terms of thermal history.

Chapter 1. Introduction and Theory.

1.1.1. Introduction to superconductors.....	2
1.1.2. The cuprates.....	3
1.1.3. Theory of superconductivity.....	4
1.1.4. Why study the low Tc Titanate system?.....	6
1.2. Phase diagram studies on lithium titanates.....	6
1.2.1. The spinel structure.....	8
1.2.2. The ramsdellite structure.....	10
1.2.3. Possible applications of ramsdellites.....	12
1.3. Introduction to electronic theory.....	14
1.3.1 Basic theory.....	14
1.3.2. Conductivity.....	14
1.3.3. Concentration of carriers.....	14
1.3.4. Determining the type of conduction mechanism.	16
1.3.5. Semiconductors.....	17
1.3.6. Choosing an electrode material.....	18
1.4.1. Introduction to magnetic theory.....	19
1.4.2. Calculation of magnetic moments.....	26
1.5. References.....	28

1.1.1. Introduction to superconductors.

In order for a material to be classified as a superconductor, it must satisfy two main criteria, that is

1. It has zero resistance to the passage of an electrical current; hence no voltage drop occurs across the material.
2. It completely expels an applied magnetic field and exhibits perfect diamagnetism. This is known as the Meissner effect.

These properties only occur below the critical superconducting temperature, known as the T_c , and give superconducting materials huge potential for energy saving applications¹, such as Maglev trains, power distribution etc.

Superconductivity was first observed by Kammerlingh-Onnes in 1911², when he found that immersing mercury metal in liquid helium, caused an apparent zero resistance state to occur ($T_c \sim 4.2$ K). Further investigations by other workers on metals and alloys pushed the highest T_c to approximately 23 K, with the highest T_c being in an alloy of niobium³

Superconductivity in oxides was unknown until the 1960's when it was found that strontium titanate (SrTiO_{3-x}) exhibited superconductivity at approximately 0.7 K⁴. Subsequently it was discovered that the binary oxides TiO and NbO had superconducting transitions in the region of 1 and 2 K⁵ respectively. A slow increase was seen in the T_c of oxides with the synthesis of various bronzes containing tungsten, molybdenum and rhenium ($4 < T_c < 6\text{K}$)^{6,7}.

In 1973, D.C Johnston⁸ found that LiTi_2O_4 went superconducting at approximately 13 K. This was followed closely by $\text{BaPb}_{1-x}\text{Bi}_x\text{O}_3$, which had a very similar T_c ⁹. These materials represented the highest T_c reported in oxides for the next 13 years, until Bednorz and Mueller discovered superconductivity at 35 Kelvin in 1986, in a sample of $\text{La}_{2-x}\text{Ba}_x\text{CuO}_4$ ¹⁰. Substituting Sr for Ba raised the T_c to approximately 40 Kelvin.

1.1.2. The cuprates.

In 1987, Wu and co-workers¹¹ made perhaps the most significant breakthrough when they discovered that $\text{YBa}_2\text{Cu}_3\text{O}_{7-\delta}$ (YBCO) went superconducting at 91-93 Kelvin. This meant that liquid nitrogen could be used as the coolant instead of the more expensive helium. This discovery led to an explosion in an area known as cuprate superconductors and led to the discovery of other materials with similar or even higher T_c 's. The most important of these being Bi/Sr/Ca/Cu/O¹² ($T_c < 90\text{K}$), Tl/Ba/Ca/Cu/O¹³ ($T_c < 122\text{K}$). At the present moment the highest known T_c is 134 K in mercury containing layered cuprates^a superconductor¹⁴.

All of the cuprates share structural similarities, the most notable of these is that they are derived from the perovskite structure type. They also contain CuO_2 layers, with the copper in approximately square pyramidal coordination. Some layered cuprates have also been found with fluorite/rocksalt intergrowths. The structure of YBCO is presented in figure 1.1.

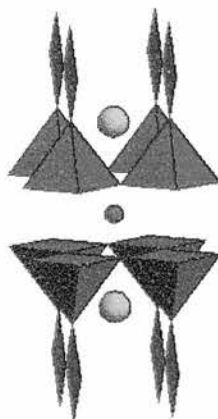


Figure 1.1. The structure of $\text{YBa}_2\text{Cu}_3\text{O}_{7-\delta}$ (YBCO.)

In the above figure, yttrium is shown in blue, with barium shown in yellow, and the copper oxide layers shown in red. However, the existence of superconductivity at these high temperatures could not be explained by the

^a 164 K at 60Gpa pressure.

accepted theory proposed by Bardeen, Cooper and Schrieffer¹⁵(BCS) for superconductivity.

1.1.3. Theory of superconductivity.

The BCS theory was developed to explain the characteristics of the elemental and intermetallic compound superconductor discovered before 1957. It stated that the following must hold,

1. Zero resistance.
2. Perfect diamagnetism known as the Meissner effect.
3. A dramatic increase in the electronic specific heat at T_c , and an exponential $1/T$ contribution to the heat capacity below T_c .
4. An Isotope effect; $T_c \cdot M^\alpha = \text{constant}$; where M is the isotope mass.
5. No change in crystal structure at or below T_c .

The discovery of the isotope effect in 1950^{16,17} gave the first indications to the possible origins of superconductivity, pointing to the involvement of phonons, which indicated a square root dependence on the isotopic mass. This led to Frohlich¹⁸ proposing that interactions by conduction electrons with phonons could explain superconductivity, with the interaction of phonons and electrons leading to an attractive force between them. Cooper¹⁹ demonstrated that this attraction would lead to the condensation of coupled electrons into a single energy state. These paired electrons or Cooper pairs have zero net spin, and are known as bosons.

A conduction electron, on passing an ion core, causes a polarization of the core electrons away from it, leading to a reduction in the screening of the nuclear charge from the passing electron, and results in the attraction of the ion core towards it. This causes a lattice distortions via coupling to a phonon mode, and creates a positively charged furrow within the lattice into which another electron (with opposite spin and momentum) can be attracted, thus forming a spinless Cooper pair.

Bardeen, Cooper and Schrieffer¹⁵ formalized these ideas, showing that the electron-phonon interaction drives a condensation of a small fraction of itinerant electrons, or fermions (those within $k_B T_c$ of the Fermi energy). This creates a small energy gap ($\Delta \sim 2k_B T_c$) between the condensed state of Cooper pairs and the excited fermionic states; a dynamic equilibrium exists between the two states.

The ordering of electrons into a single energy state lowers the entropy of the system, and causes a peak in the heat capacity at T_c . The exponential $1/T$ term in the superconducting state can be explained by the presence of an energy gap. Zero resistance is another consequence of the condensation of superconducting bosons into a single energy state; small changes in the energy of the Cooper pairs through scattering are not possible, and any scattering of the fermions present can be ignored, since they are shorted out by the superconducting pairs.

Two parameters are commonly used to describe superconductors, these are

1. The penetration depth, λ_L which is a measure of the penetration of a magnetic field into a superconductor,
2. The coherence length, ξ . The coherence length describes the range of correlation between the Cooper pairs.

The ratio of λ_L/ξ or κ , is used to distinguish between type 1 ($\kappa \ll 1$) and type 2 ($\kappa \gg 1$) superconductors and describes their behaviour in a magnetic field²⁰.

Type 1 (also known as soft superconductors) are usually pure elemental superconductors and have a single critical magnetic field limit, known as H_c . Above H_c the magnetic field enters the superconductor and destroys the superconducting state.

Type 2 (also known as hard superconductors), which are usually alloys or oxides, exhibit two critical fields, known as H_{c1} and H_{c2} respectively. At H_{c1} the magnetic field penetrates the material but does not destroy the superconductivity (leading to a state known as the mixed state). When the

applied field is larger than H_{c2} , the magnetic field completely enters the material and destroys the superconducting state.

Using the BCS theory, it was predicted that the highest T_c possible was in the region of 30-35K, this was due to the probability of structural transformations for large electron-phonon couplings. Clearly this is not the case in the cuprates. It was also found that the cuprates did not have an isotope effect²¹, which is an important prerequisite of the BCS theory.

1.1.4. Why study the low T_c Titanate system?

The low T_c $Li_{1+x}Ti_{2-x}O_4$ spinel series of superconductors was discovered 13 years before Bednorz and Müller discovered the first of the cuprates. Titanates and cuprates show a number of similarities, the most important being the proximity to the metal-insulator transition (MIT) and the absence of an isotope effect. Therefore, this seems to suggest that titanates and cuprates may share a similar superconducting mechanism and this alone makes the titanates attractive material for further study.

1.2. Phase diagram studies on lithium titanates.

Numerous studies have been performed on lithium titanates, with several studies have been performed on the Li_2O - TiO_2 system, with four main phases known to exist, these phases being Li_4TiO_4 , Li_2TiO_3 , $Li_4Ti_5O_{12}$ and $Li_2Ti_3O_7$.

Li_4TiO_4 was found reported by Dubey et al²² and is an unusual as it contains tetrahedrally coordinated Ti IV. Dubey showed that the material was orthorhombic with the approximate unit cell dimensions of $a = 7.91 \text{ \AA}$, $b = 6.15 \text{ \AA}$, $c = 7.41 \text{ \AA}$ respectively. This phase also exhibits polymorphism, a low temperature polymorph exists below 686°C , which is isostructural with low Li_4GeO_4 ²³, with another form stable above 686°C which has a structure similar to Li_4SiO_4 ²⁴. It was later shown that Li_4TiO_4 melts incongruently to Li_2TiO_3 and liquid²⁵. Li_2TiO_3 is also known to exist as two different

polymorphs²⁶, with the low temperature polymorph known to be monoclinic with the space group C2/c. The unit cell would be $a = 5.069 \text{ \AA}$, $b = 8.799 \text{ \AA}$ and $c = 9.759 \text{ \AA}$ with $\beta = 100.2^\circ$. Izquierdo showed that at approximately 950°C , this phase went to a simple rocksalt structure, however the dimensions of the unit cell were not reported.

Bertaut first reported the occurrence of a lithium titanate spinel and suggested that it had a stoichiometry of $\text{Li}_4\text{Ti}_7\text{O}_{16}$ ²⁷. Jonkers et al²⁸ found that the spinel phase was actually $\text{Li}_4\text{Ti}_5\text{O}_{12}$ and was confirmed by Kim²⁹. The $\text{Li}_{1+x}\text{Ti}_{2-x}\text{O}_4$ spinel system was initially reported by Deschanvres et al³⁰, and was found to form a solid solution over the compositional range $0 \leq x \leq 0.33$. The unit cell range from 8.404 \AA ³¹ in $x=0$ down to 8.357 \AA ³⁰ in $\text{Li}_4\text{Ti}_5\text{O}_{12}$.

A related orthorhombic phase with a stoichiometry of $\text{Li}_2\text{Ti}_3\text{O}_7$ was found to exist by Jonkers and shown to have a ramsdellite structure^{32, 33}. Lundberg also hinted that the stoichiometry was not simply $\text{Li}_2\text{Ti}_3\text{O}_7$ and was later shown by Mikkelsen³⁴ to form a limited solid solution between 74 and 75 % TiO_2 , which was later reported as being 74 to 76% by Izquierdo. Mikkelsen's work did not include some of the findings of Izquierdo most noticeably the transition to rocksalt Li_2TiO_3 at higher temperatures. Even with $\text{Li}_2\text{Ti}_3\text{O}_7$ a number of different polymorphs have been reported, a monoclinic form³⁵ is known, with unit cell dimensions of $a = 7.506 \text{ \AA}$, $b = 3.738 \text{ \AA}$, $c = 9.31 \text{ \AA}$ and $\beta = 98.21^\circ$. Mikkelsen³⁶ also hinted at a tetragonal form of this phase, which $a = 8.78 \text{ \AA}$ and $c = 69.8 \text{ \AA}$, however it was noted that the assignment was suspect.

Examination of the phase diagram reported by Izquierdo highlights the complex polymorphism possible in Ti^{IV} systems.

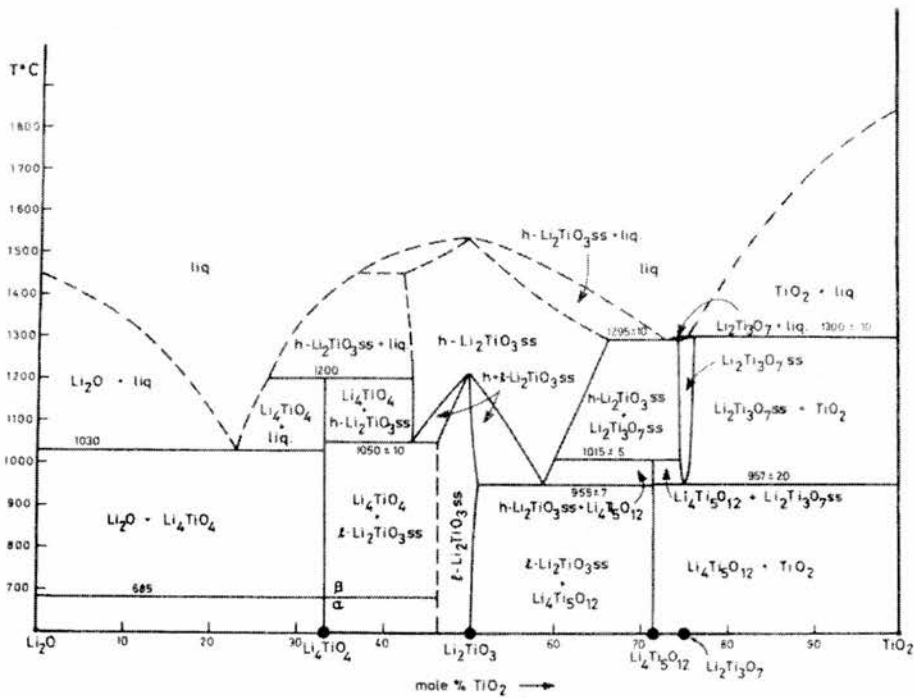


Figure 1.2. The $\text{Li}_2\text{O}-\text{TiO}_2$ phase diagram as reported by Izquierdo et al

1.2.1. The spinel structure.

Many materials crystallize with the spinel structure. The name is derived from the mineral MgAl_2O_4 . The general spinel formula is AB_2X_4 , where **A** and **B** are cations, typically Li, Mg, Fe etc. and X is an anion such as O and S. The vast majority of spinels are oxides, but chalcogenides are also known.

In the cubic spinel structure, the oxide ions occupy a 32e site of the $\text{Fd}3\text{m}$ space group (227) with positional parameter **u**, which allows slight distortion from cubic close packing, and is accommodated by a co-operative expansion of the A-O bonds. **A** cations occupy tetrahedral 8a sites within the structure and the **B** cations occupy octahedral 16d sites.

One of the interesting aspects of spinels³⁷ is the cation distribution between the tetrahedral and octahedral sites within the structure. For example, a spinel of AB_2O_4 can have **A** solely on the tetrahedral sites, or it can have a mixture

of **A** on tetrahedral and octahedral sites. These distributions are usually formulated as follows.

1. $[A]^{Tet} [B_2]^{Oct} O_4$ - normal.
2. $[B]^{Tet} [AB]^{Oct} O_4$ - inverse.
3. $[A_x B_{1-y}]^{Tet} [A_y B_{2-x}]^{Oct} O_4$ - intermediate.

Spinel compounds are known to exhibit a number of different interesting electrical and magnetic properties. Spinel is known to form diamagnetic insulators (Mg_2TiO_4), paramagnetic metals (LiV_2O_4)³⁸, ferro or ferrimagnets (Fe_3O_4)³⁹ as well as superconducting $Li_{1+x}Ti_{2-x}O_4$ spinel.

The structure of the end member $LiTi_2O_4$, is normal⁴⁰, with Li occupying the 8a sites, and as the Li content in the solid solution series $Li_{1+x}Ti_{2-x}O_4$ increases, the spinel becomes less normal with some Li occupying 16d sites within the structure. The increase seen in the Li occupation on the 16d site leads to a decrease in the Ti occupancy. Presented in figure 1.3 is a graphical representation of $LiTi_2O_4$ spinel.

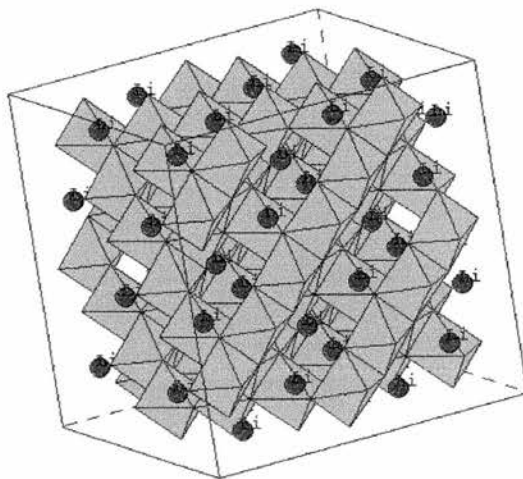


Figure 1.3. A graphical representation of the spinel structure, Li presented in green.

close packed oxygen with the Li being tetrahedrally coordinated with respect to the oxygen (lithium in green). Samples at the $x=0$ end of the solid solution were found to be semiconducting, with the $x=0.33$ end member being electronically insulating ($\text{Li}_{1.33}\text{Ti}_{1.67}\text{O}_4$ can also be written as $\text{Li}_4\text{Ti}_5\text{O}_{12}$).

Examination of the literature concerning the T_c of LiTi_2O_4 show that there is no apparent agreement as to the T_c of this material, with values in the range of 10 to 13.7 Kelvin having been recorded.^{31,41,42,43,44,45}

1.2.2. The ramsdellite structure.

The ramsdellite structure type was first described by Bystrom et al for $\gamma\text{-MnO}_2$. The structure consists of distorted MO_6 octahedra, which link up with adjacent octahedra, by sharing opposite edges, thus forming columns. Adjacent pairs of columns share edges to form double columns, giving rise to an open framework type structure. In between these columns there are tetrahedral channel sites⁴⁶ into which smaller ions such as H and Li can be placed. The ramsdellite structure is orthorhombic and has the Pbnm space group (62). As mentioned above smaller ions such as Li can be placed into the tunnel sites and this had led to a small but significant amount of work being performed on this crystal structure type^{47,48,49} for possible applications in lithium ion batteries^{50,51}. Presented in figure 1.4 is a graphical representation of LiTi_2O_4 ramsdellite.

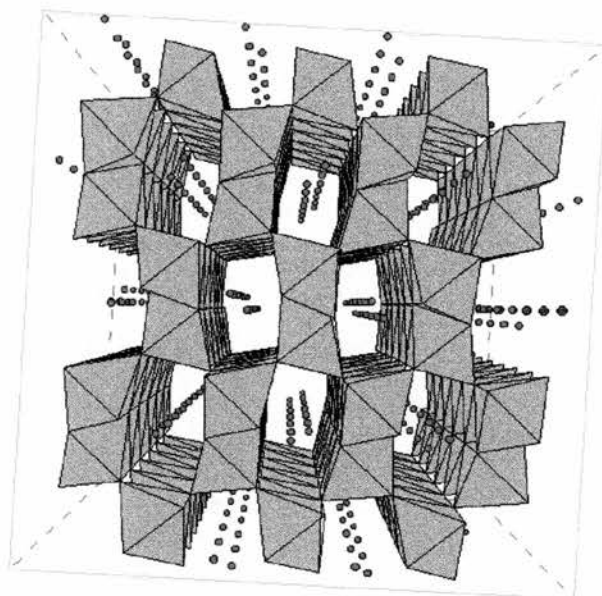


Figure 1.4. A graphical representation of LiTi_2O_4 ramsdellite, Li presented in green.

The TiO_6 octahedra are represented in grey, with Li atoms to be found in the channel sites. In figure 1.4, all the Li atom sites are shown, but due to the short Li-Li bond distance ($\sim 1.76\text{\AA}$) the maximum channel site occupancy is in the region of 50%.

Johnston reported that on heating spinel samples of LiTi_2O_4 to 900–950°C a ramsdellite phase was formed which exhibited a slight difference in the unit cell to that seen for $\text{Li}_2\text{Ti}_3\text{O}_7$ ⁵². Unfortunately he was unable to confirm the stoichiometry of the “ramsdelite” phase. In 1994, Akimoto et al succeeded in preparing single crystals of LiTi_2O_4 ramsdellite and confirmed this phase to have a ramsdellite structure type and a stoichiometry close to LiTi_2O_4 . He found that the occupancy of the 4c-channel site was approximately 45 percent. Akimoto also noted that the structure of LiTi_2O_4 ramsdellite was very similar to that of $\text{Li}_2\text{Ti}_3\text{O}_7$ ^{53, 53}, as described by Morosin et al and later by Abrahams. These studies concluded that Li could be found in both the channel sites and substitute on the Ti framework sites.

The fact that LiTi_2O_4 spinel undergoes a complete conversion to ramsdellite at high temperatures is surprising from symmetry considerations, as there is no apparent intermediate space group that links $\text{Fd}3\text{m}$ and Pbnm .

This single fact makes the study of the structural relationship between spinel and ramsdellite very interesting.

1.2.3. Possible applications of ramsdellites.

With the advent of mobile communications and the explosion in the power of portable computers in recent years⁵⁴, there has been a great demand for improved battery materials. Batteries can be classified as being either a primary or secondary cell. A primary cell is one whose useful life is ended once its reactants have been consumed during the discharge process. Once the battery has been fully discharged it must be discarded and this makes them an expensive and unattractive option. The secondary cell is more attractive as these systems can be discharged and then by application of a current in the opposite direction be recharged.

One of the most important criteria in the design of any battery is the weight. It is this combined with the very high specific capacity of Li that makes it attractive for use in secondary batteries. Combining these factors with the very high standard redox potential of Li makes it a favourable material for use in secondary battery cells.

The development of rechargeable Li based cells has been slow, as a number of major problems have been encountered. Initial work focused on using metallic Li anodes in an organic electrolyte and it was found that this type of system was not completely reversible. Lithium was lost during cycling, causing a degradation in the cell performance⁵⁵. It was also found that Li formed a passivating layer at the electrode-electrolyte interface. This modifies the charge transfer reaction mechanism, decreases the overall ionic diffusion coefficients and causes an overpotential. An increase in overpotential further increases the reactivity of the lithium, which then promotes growth of the passivating layer. A further consequence of the passivating layer⁵⁶ is the growth of dendrites during lithium plating, which has the effect of causing a non-uniform current density distribution at the electrode-electrolyte interface. Accumulation of these dendrites, followed by lithium passivation progressively leads to a gradual decrease in the cell

performance. Eventually the density changes caused by the formation of the dendrites leads to complete battery failure.

Anodes based on transition metal oxides take advantage of the vast experience of composite cathodes and employs materials into which Li can be removed and reinserted. One of the electrodes contains either a lithiated insertion compound or a ternary lithium compound able to deintercalate lithium, providing lithium in the cell. A schematic of this is presented below in figure 1.5:

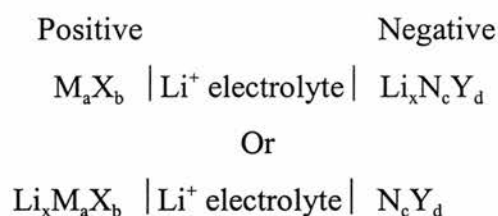


Figure 1.5. - Schematic of a transition metal oxide cell.

Where M, N are transition metals and X and Y is oxygen or sulfur. During discharge, the cathode extracts lithium, while lithium is inserted into the negative electrode and vice-versa during recharging. Such cells have become known as “rocking chair cells”.

Ramsdellites based on lithium titanates may be good materials for anode materials for a number of reasons. The raw materials to be used are abundant⁵⁷ and have low associated toxicity. The ramsdellite structure has channels that run parallel to the **c** axis, and could provide an ideal pathway for the movement of Li during charging and discharging. Electrochemical studies on $\text{Li}_2\text{Ti}_3\text{O}_7$ ramsdellite by Boyce⁵⁸ indicated that the Li was mobile within the channel sites. Akimoto et al⁵⁹ indicated that complete removal of Li using HCl was possible, with the ramsdellite structure being retained at all stages of delithiation. He noted that the unit cell volume slightly decreased as the Li was extracted, with the largest decrease being seen in the **b** direction. In terms of the volume changes on delithiation it was found that on going from LiTi_2O_4 to TiO_2 the total volume change was less than 6 percent.

1.3. Introduction to electronic theory.

1.3.1 Basic theory

Determining the electronic properties of a material can be one of the most informative methods of determining the nature of a material, including the type of bonding and in some case it can be related to the electronic structure of a material. It can also provide information on the type of material that is under examination, i.e. whether it is an insulator, metal or semiconductor, and using certain methods it can be used to determine the type of carriers responsible for the conductivity.

1.3.2. Conductivity.

The conductivity of any material is given by the product of the number of carriers and their mobility, according to the equation.

$$\sigma = n.e_0.\mu \quad (1.1)$$

Where e_0 is the charge on the carrier, n is the number of carriers and μ is the mobility of the carriers. In this work the carrier is assumed to be the electron (unless otherwise stated), with a charge of 1.602×10^{-19} Coulombs.

1.3.3. Concentration of carriers.

The electronic structure of materials are described elsewhere and only a brief description will be given here. Presented in figure 1.6, is a schematic of the band gap.

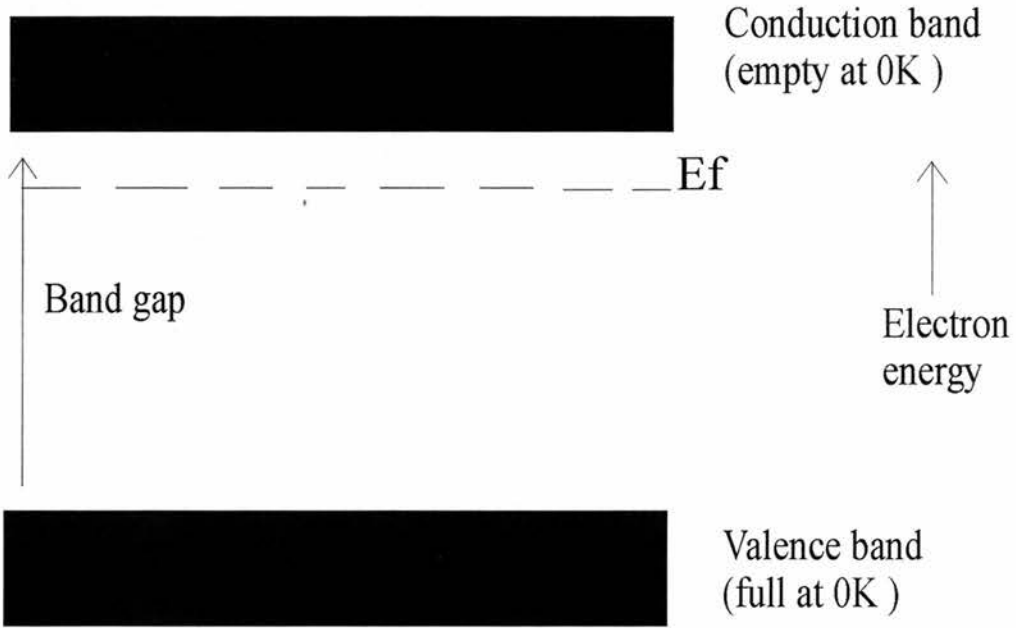


Figure 1.6. Schematic representation of band gaps.

Where E_f is the fermi level. Overlap between orbitals of neighbouring atoms or ions gives rise to a series of narrowly spaced energy levels, termed “bands”. The highest occupied band is known as the valence band, and the lowest unoccupied band is known as the conduction band. In metallic materials the conduction band is partially filled, and electronic conductivity is via the electrons moving around within this conduction band. In semiconductors and insulators the picture is different, conductivity is across the band gap, as shown in figure 1.6. It is the magnitude of this band gap that determines whether a material is a semiconductor or insulator. The band gap tends to be smaller in semi conductors. Semiconductors can also be distinguished further into direct or indirect, p-type or n-type and extrinsic or intrinsic.

Direct and indirect semiconductors are different in terms of valence and conduction band maxima and minima. In a direct band gap semiconductor, the maximum and minimum in the band gap occur at similar k (momentum) vector the electrons can cross the band gap without a change in momentum, whereas this is not the case in indirect semiconductors.

Intrinsic semiconductors are “pure materials”, such as silicon or germanium and have band gaps typically in the region of 1.5 eV. Extrinsic materials are materials that have been deliberately doped with a material that lowers the magnitude of the band gap. An example of this type material is gallium nitride doped with magnesium as used in blue lasers⁶⁰

Extrinsic materials can be further separated into n-type and p-type materials, and this is dependent on the type of dopant. Doping of Si with Al, causes the Al to act as Al⁺, so that it remains isoelectric with Si, and the electron is taken from the valence band causing the formation of *positive hole*. In its ground state the positive hole is located close to the Al and is known as an acceptor state. This is known as a p type semiconductor.

An example of an n type material is Si doped with P, which causes the formation of a net positive charge. This positive charge attracts electrons and the net effect is the formation of a donor state. This donor state is to be found below the conduction band and provides a ready source of electron for populating the conduction band.

1.3.4. Determining the type of conduction mechanism.

The dominant type of conduction present in a material can usually be determined as a function of temperature. The carrier concentration is normally effectively constant at all temperatures, with the mobility dominated by the interactions with the phonons. However the value of n will be slightly different to that seen in semiconductors since the mean free path of l still varies as T^{-1} , the thermal conductivity is effectively constant for a metal, as only the electrons in the Fermi level are available to contribute to the conduction. Presented below in figure 1.7 is a simplified graph showing the changes seen in the conductivity of various type of material as a function of temperature.

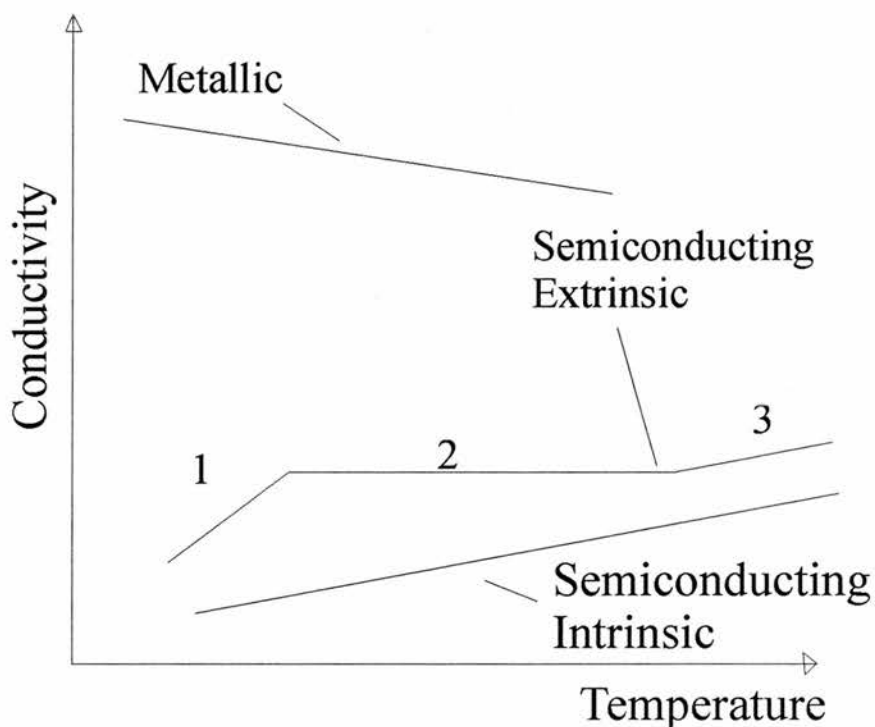


Figure 1.7. Simplified graph showing the changes seen in the conductivity of various type of material as a function of temperature

1.3.5. Semiconductors

The most essential feature of a semiconductor is that over a wide temperature range, the number and type of carriers present in the material determine the conductivity. In an intrinsic semiconductor, the conductivity is seen to rise as a function of temperature. This is simply explained in terms of the mobile carriers having enough energy to be promoted from the valance band into the conduction band.

$$E_g = E_c - E_v \quad (1.2.)$$

In extrinsic semiconductors the conductivity has a slightly more complicated nature and this is due to the different type of carrier present in the material. The conductivity can be seen to have three components, marked 1-3 in figure 7. In region 1, the dominant carriers are those due to doping, i.e. the carriers in the acceptor or donor levels. The number of these carriers is

limited by the concentration of the dopant and hence the number is finite. At certain temperatures, these carriers become exhausted and the conductivity is seen to level out, as shown in region 2. A third region is seen in the conductivity when the intrinsic semiconducting properties of the material come into play. This is simply related to the promotion of carriers from the valence band into the conduction band.

Similarly, in insulators, the conductivity will increase as a function of temperature, when sufficient temperature is applied to the sample, it can become electronically conducting, and is again caused by promotion of carriers from the valence band into the conduction band (region 3).

1.3.6. Choosing an electrode material.

One of the most important factors that need to be considered when performing electrical measurements is the correct choice of electrode material.

Common electrode materials are the precious metals, such as gold, silver and platinum, and the choice of electrode material is dependent on a number of criteria, for example, the curing conditions needed to bond the electrodes, temperature stability, contact potential and temperature related phase changes.

The most important of the criterion mentioned above is that of contact potential. The Fermi level in a semiconductor or metal is a measure of the chemical potential of the electrons, thus if two conductors are placed in electrical contact, charge will flow from one to the other until the Fermi levels are equalized. The charge flux will give rise to a potential difference between the two materials, and is known as the contact potential.

If the sample under investigation is metallic and the electrodes are metallic, then the contact potential is located in a very narrow region at the point of contact, and offers very little barrier to the flow of electrons. In a semiconductor, with metallic electrodes, these contact potentials may be very high and lead to the formation of a Schottky barrier.

1.4.1. Introduction to magnetic theory.

The magnetic moment of a free atom has three principal components: the spin with which electrons are endowed, their orbital angular momentum about the nucleus; and the change in the orbital moment induced by an applied magnetic field.

The magnetization M in SI units is defined as the magnetic moment per unit volume. The magnetic susceptibility per unit volume is defined as

$$\chi = \mu_0 M / B \quad (1.3).$$

Where B is the macroscopic magnetic field intensity and μ_0 is the permeability of free space. The magnetic susceptibility χ is dimensionless, and frequently, susceptibility is expressed in terms of unit mass or a mole of the material. The molar susceptibility is written as χ_m ; with the magnetic moment per gram sometimes written as σ .

Magnetic moments tend to align in the same direction as an applied field, this is due to a parallel configuration having a lower energy. The temperature dependence of susceptibility is a good characterisation parameter.

Diamagnetic materials possess no intrinsic magnetic moments. The negative susceptibility results from Lenz's law: The change produced by an external field induces an e.m.f. which opposes the applied magnetic field. Typical susceptibility values for diamagnetic materials are generally in the range of -1×10^{-7} to -2×10^{-6} range. Diamagnetism is present in all materials to some extent, and is associated with the tendency of electrical charge to partially shield the interior of atoms from an applied magnetic field.

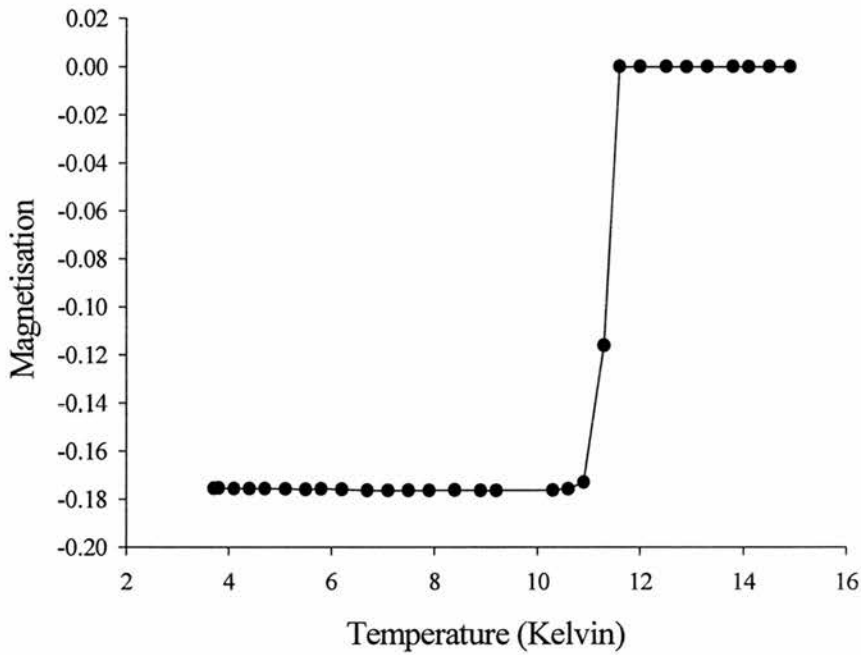


Figure 1.8. Plot of a superconducting diamagnetic transition for Zr_2Rh superconductor⁶¹.

Superconductors are perfect diamagnets, presented in figure 1.8 is the superconducting transition obtained for Zr_2Rh . When a superconductor is cooled through its critical superconducting transition temperature (T_c) in the presence of an applied magnetic field, H , magnetic flux lines are completely expelled from the sample. This is known as the Meissner effect, which is characteristic of a superconductor and/or a perfect diamagnet. In the superconducting state, surface currents are generated, which exactly opposes the applied field and maintains flux lines outside the material. As the applied field is reduced, these flux lines decrease and completely disappears when the field equals zero.

In type 1 materials, there is an upper critical field known as H_c . When the applied field exceeds the value of H_c (which is material specific) then the magnetic field enters the sample, the superconducting state is completely destroyed and the material becomes normal. The situation is slightly more complex in type 2 materials, where a mixed state can exist for certain values of applied field, a partial penetration of the applied field occurs, leading to a mixed or vortex state, which is a mixture of normal and superconducting states. This is characterized by two critical field values known as H_{c1} and H_{c2} respectively. For fields $H < H_{c1}$ the material is superconducting and no field

penetration occurs; normal behaviour exists when $H > H_{c2}$ with total penetration of the material by the applied magnetic field. When $H_{c1} < H < H_{c2}$ there is partial flux penetration. In the mixed state, the flux is said to be pinned and this pinning is usually associated with microstructural defects, such as dislocations, second phases and grain boundaries. When the applied field is increased, the vortices of flux are unpinned and grow through the sample, leading to the normal state.

Paramagnets possess intrinsic magnetic moments, which tend to align in an applied magnetic field, with the sample being slightly attracted to the applied magnetic field, as shown in figure 1.9.

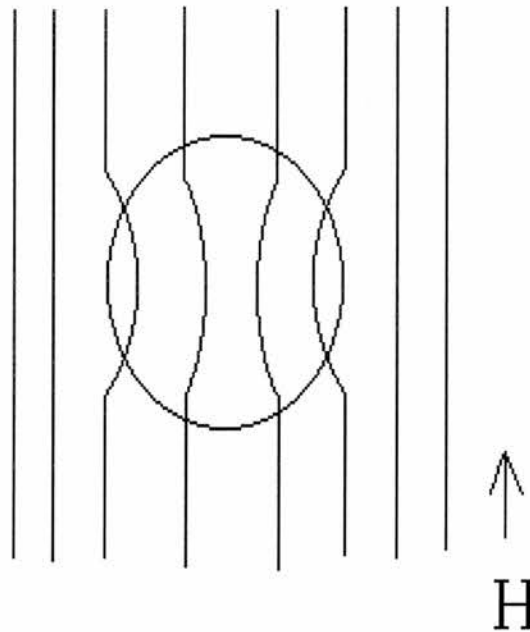


Figure 1.9. Behaviour of a paramagnetic substance in an applied magnetic field.

This aligning of moments tends to be destroyed (or randomised) as the sample temperature is raised which is manifested as a drop in the observed sample magnetisation. A paramagnet manifests itself as shown below in figure 1.10.

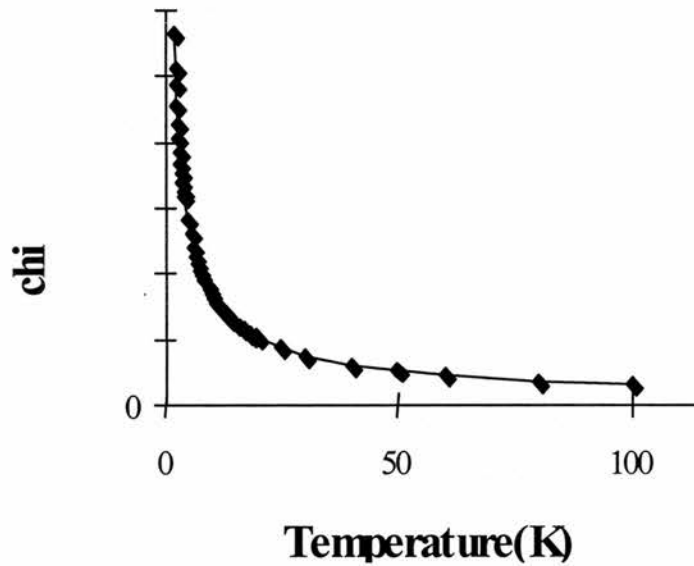


Figure 1.10. Plot of magnetic susceptibility versus temperature for a paramagnetic substance.

A plot of $1/\chi$ versus temperature will give a straight line going through the origin and generally obeys Curie's law.

The susceptibility of paramagnetic materials are distinguished by their different temperature dependencies as well as their absolute magnitudes. Many substances obey the Curie law, which states that magnetic susceptibility is inversely proportional to temperature.

$$\chi = \frac{C}{T} \quad (1.4).$$

Where C is the Curie constant. Often the results are better fitted to the experimental data by the Curie-Weiss law, which is given by

$$\chi = \frac{C}{(T - \theta)} \quad (1.5).$$

Where θ is the Weiss constant and is the x-axis intercept. These two types of behavior are illustrated in figure 1.11.

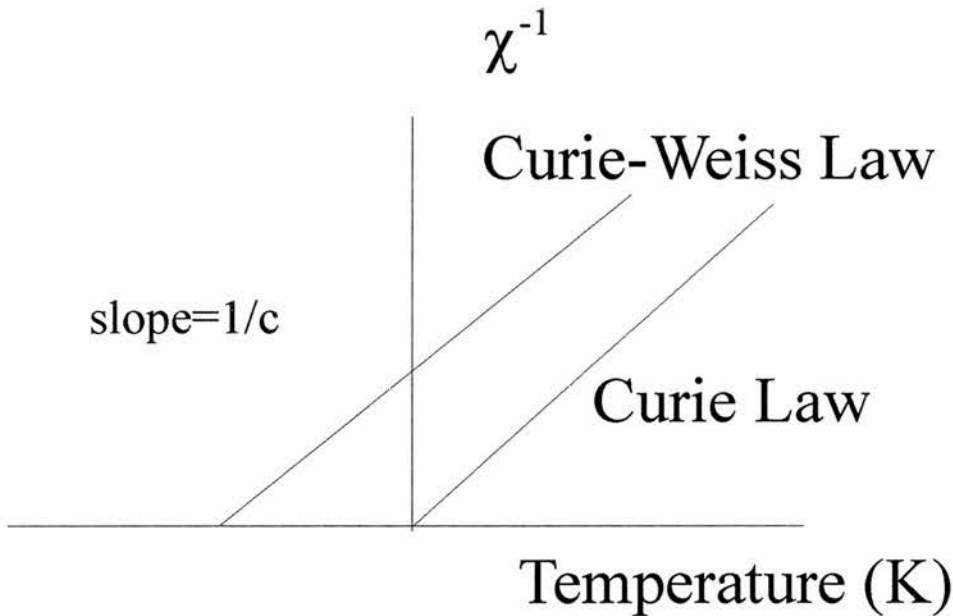


Figure 1.11. Plot of reciprocal susceptibility against temperature showing Curie and Curie-Weiss behaviour

For all materials, the effect of increasing temperature is to increase the thermal energy possessed by ions and electrons. There is, therefore, a natural tendency for structural disorder to increase with increasing temperature. For paramagnetic materials, the thermal energy of ions and electrons acts to cancel the ordering effect of the applied magnetic field. Indeed, as soon as the magnetic field is removed, the orientation of the electron spins becomes disordered. Hence, for Curie paramagnetic materials, χ decreases with increasing temperature.

Another class of paramagnet exists that is known as Pauli paramagnets. Pauli paramagnets have a small positive, constant susceptibility. This is a consequence of the band structure of the energy levels in metals; not all electrons in the band are allowed to invert their spin when an external field is applied. Only electrons near the limit of the band (near the Fermi energy level) are able to occupy states with inverted spin.

In addition to showing large, intrinsic magnetic moments, many materials containing transition elements behave as if they were spontaneously magnetized. Various types of magnetic moment ordering have been observed and are shown schematically in figure 1.12.



Figure 1.12. Ordered arrangement of spins in ferromagnets and antiferromagnets.

If the spins are aligned parallel to each other then the material is said to be ferromagnetic, if the spins are aligned antiparallel to each other and are exactly compensated with respect to each other then the material is said to be antiferromagnetic. The final main type of material is similar in nature to that seen for an antiferromagnetic, but with the antiparallel spins uncompensated, this is known as a ferrimagnet. For a plot of $1/\chi$ versus temperature, if the asymptotic temperature θ is positive then this is an indication that the material maybe ferromagnetic, whereas a negative value indicates the presence of antiferromagnetism. Such materials change from paramagnetic ordering to magnetically order on cooling.

The interactions responsible for these phenomena are extremely strong, since the critical temperature at which magnetic ordering is destroyed by thermal agitation can be very high (1400K in Co). Whether a material is ferro, antiferro or ferrimagnetic is dependent on the something known as the exchange integral, J_{ex} , which is a measure of the degree of interaction between the electrons. Parallel spins lead to positive J_{ex} , whereas negative J_{ex} are a consequence of antiparallel spins.

In ferromagnetic materials the onset of the phenomena is known as the Curie temperature or T_c . Magnetic moments do not disappear at the transition temperature, but become disordered. On increasing temperature, ferromagnetic materials undergo a transition from ordered ferromagnetic to a disordered paramagnetic at $T > T_c$ (shown in figure 1.13). Ferromagnetic magnetisation is always at a maximum at 0K and therefore shows a decrease in magnetisation with increasing temperature.

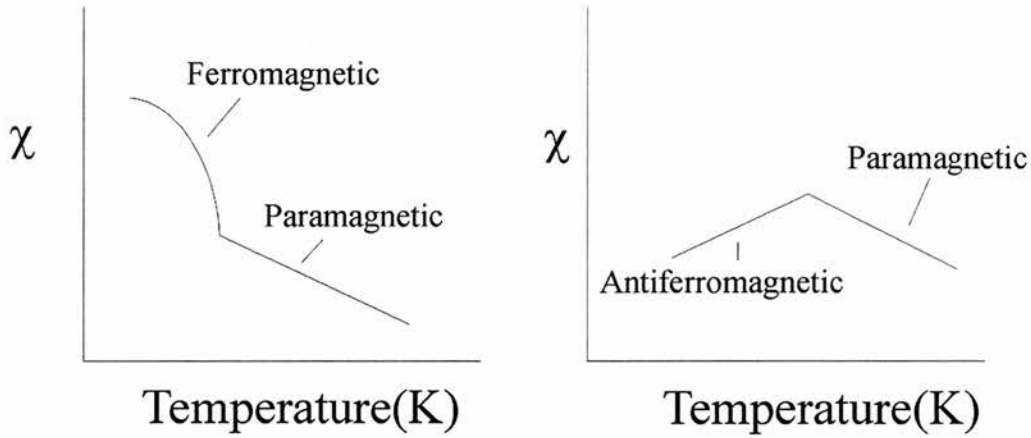


Figure 1.13. Schematic illustrating the differences between ferromagnetic and antiferromagnetic transitions.

The dominant type of ordering mechanism in oxides is antiferromagnetism and is considerably more complex than seen in metals. The transition temperature in oxides is known as the Néel temperature. The problem in oxides is that the exchange has to be assumed to be indirect in nature, and arises from ordering of the cations separated by O^{2-} . In oxides the cations are normally too far apart for direct cation interaction. Direct interactions can occur if the radius of the cation is less than that of the anion. The O^{2-} has no net magnetic moment since it has completely filled shells with the p-type orbitals outermost. Orbital P_x has two electrons: one with spin up and one spin down. When one of the transition-metal orbitals is brought close to the O^{2-} , partial electron overlap can occur only for antiparallel spins, because electrons with the same spin are repelled. Empty 3d states in the cation are available for partial occupation by the O^{2-} electron, with an antiparallel orientation. Electron overlap between the other cation and the O^{2-} then occurs resulting in antiparallel spins and therefore antiparallel order between the cations. Since p orbitals are linear, the strongest interaction is expected to take place for cation- O^{2-} cation angles close to 180° . This phenomenon is also known as superexchange.

In a plot of $1/\chi$ versus temperature, θ is the extrapolation of the linear relation for $T > T_N$ (where θ is the asymptotic temperature- see figure 1.14). The paramagnetic susceptibility of antiferromagnets follows a Curie-Weiss

law with a negative critical temperature. At $T < T_N$, susceptibility depends on the orientation of the applied field relative to the antiparallel axis.

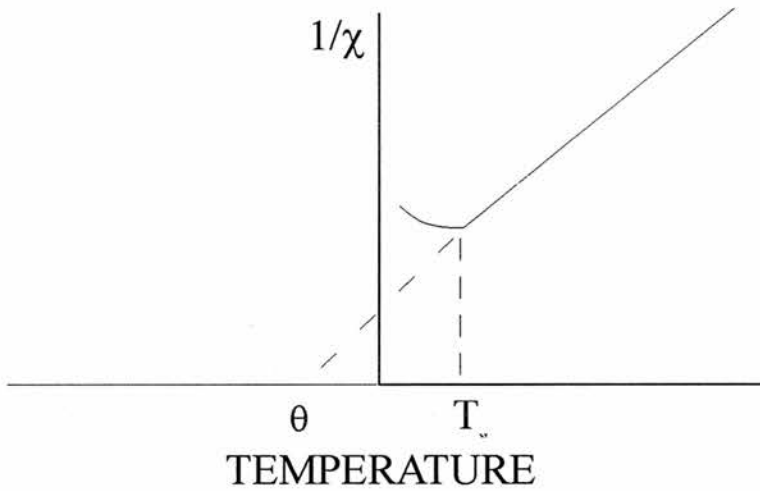


Figure 1.14. Schematic representation of $1/\chi$ versus temperature for an antiferromagnet.^b

As with ferromagnets, the magnetic moments do not disappear at the transition temperature, but become disordered, with increasing temperature, antiferromagnetic materials undergo a transition to a disordered paramagnetic.

1.4.2. Calculation of magnetic moments.

The magnetic properties of materials are often expressed in terms of the magnetic moment, μ , since this is a parameter that may be related to directly to the number of unpaired electrons present in the material. The relationship between χ and μ is

$$\chi = \frac{N\beta^2 \mu^2}{3kT} \quad (1.6).$$

^b The increasing portion may go up or down.

Where N is Avogadro's number ($6.02217 * 10^{23} \text{ mol}^{-1}$), β is the Bohr magneton ($9.27410 * 10^{-24} \text{ JT}^{-1}$) and k is the Boltzmann's constant ($1.38062 * 10^{-23} \text{ JK}^{-1}$). Substituting for N , β and k gives

$$\mu = 1.25\sqrt{\chi T} \quad (1.6).$$

The magnetic properties of unpaired electrons can be regarded as arising from two phenomena; electron spin and orbital electron motion. The most important is the spin component. An electron may be visualized as a bundle of negative charge spinning on its axis. The magnitude of the resulting spin moment, μ_s , is 1.73 Bohr magnetons (BM), where the Bohr magneton is defined as

$$1BM = \frac{e\hbar}{4\pi mc} \quad (1.7).$$

Where e = electron charge, $\hbar = h/2\pi$ ($1.05459 * 10^{-34} \text{ Js}$), m = electron mass ($9.10956 * 10^{-31} \text{ Kg}$) and c = velocity of light ($2.9979 * 10^8 \text{ ms}^{-1}$)^c. The formula used for calculating μ_s for a single electron is

$$\mu_s = g\sqrt{s(s+1)} \quad (1.8).$$

Where s is the spin quantum number, $1/2$, and g is the gyromagnetic ratio, which is approximately 2.00. Substituting for s and g gives $\mu_s = 1.73 \text{ BM}$ for a single electron. For atoms and ions that contain >1 unpaired electrons, the overall spin moment is given by

$$\mu_s = g\sqrt{S(S+1)} \quad (1.9).$$

Where S is the sum of the spin quantum number of the unpaired electrons. The motion of an electron around the nucleus may in some materials, give

^c All units given in SI.

rise to an orbital moment, which contributes to the overall magnetic moment. In cases where the orbital moment makes its full contribution,

$$u_{s+l} = \sqrt{4S(S+1) + L(L+1)} \quad (1.10).$$

Where L is the orbital angular momentum quantum number for the ion. In practice, in solid materials, the above equations do not hold because the orbital angular momentum is either partially or fully quenched.

1.5. References.

-
1. A.M. Campbell, "High temperature superconductivity", Proceeding of the 39th Scottish Universities summer school in physics, Ed. D.P. Tunstall and W. Barford, St. Andrews, (1991) 86.
 2. H. Kammerlingh-Onnes, *Leiden Commum.*, **122b** (1911).
 3. T.H Geballe and J.K. Hulm, *Science.*, **239** (1988) 367.
 4. J.J. Schooley, W.R. Hosler and M.L. Cohen, *Phys Rev Lett.*, **12** (1964) 474.
 5. J.K. Hulm, C.K. Jones, R Mazelsky, R.A. Hein and J.W. Gibson, *Proceedings of the 9th international conference on low temperature physics*, Ed. J.G. Daunt, D.O. Edwards, F.J. Milford and M. Yaqub., (1965) 600.
 6. A. R Sweedler, C Raub and B.T. Matthias, *Phys Lett.*, **15** (1966) 108.
 7. A.W. Sleight, T.A. Bither and P.E. Bierstedt, *Solid State Comm.*, **7** (1969) 299.
 8. D.C. Johnston, H. Prakash, W.H. Zacharisen and R. Viswanthan, *Mater. Res. Bull.*, **8** (1973) 777.
 9. A.W. Sleight, J.L. Gillson and P.E. Bierstedt, *Solid State Comm.*, **17** (1975) 27.
 10. J.G. Bednorz and K.A. Müller, *Z. Phys.*, **B64** (1986) 189.
 11. M.K. Wu, J.R Ashburn, C.J. Torng, C.J Hor, R.L. Meng, L. Gao, Z.J. Huang, Y. Q. Wang and C.W. Chi, *Phys. Rev. Lett.*, **58** (1987) 908.

-
12. M.A. Subramanian, C.C. Torardi, J.C. Calabrese J. Gopalakrishnan, K.J. Morrissey, T.R. Askew, R.B. Flippen, U. Chowdrey and A.W. Sleight, *Science.*, **239** (1988) 1015.
 13. P. Halder, K. Chen, B Maheswaran, A. Roi-Janicki, N.K. Jaggi, S Markiewicz and B.C. Giessen, *Science.*, **241** (1988) 1198.
 14. S.N. Putilin, *Nature.*, **362** (1993) 226.
 15. J. Bardeen, L.N. Cooper and J.R. Schrieffer, *Phys. Rev.*, **108** (1957) 1175.
 16. C.A. Reynolds, B. Serin, W.H. Wright and L.B. Nesbitt, *Phys. Rev.*, **78** (1950) 487.
 17. E. Maxwell, *Phys. Rev.*, **78** (1950) 477.
 18. H. Frohlich, *Phys. Rev.*, **79** (1950) 845.
 19. L.N Cooper, *Phys. Rev.*, **104** (1956) 1189.
 20. C. Kittel, "*Introduction to solid state physics*", Wiley, New York, (1986) 324.
 21. R.B. Schwarz Pascal, J. Yvon and D. Coffey, "*Studies of high temperature superconductors*", **9**, Ed. A. Narlikar, Nova, New York (1991).
 22. B.L. Dubey and A.R. West, *Nature. Phys. Sci.*, **235** (1972) 155.
 23. W. Gratzner, *Z. Kristallogr.*, **133** (1971) 260.
 24. H. McMurdie, *Powder Diffraction.*, **1** (1986) 339.
 25. G. Izquierdo and A.R. West, *Mat. Res. Bull.*, **15** (1980) 1655.
 26. M. Castellanos and A.R. West, *J. Mater Sci.*, **14** (1979) 450.
 27. F. Bertaut and A. Durif, *C.R. Acad. Sc. Paris.*, **C236** (1953) 212.
 28. G.H. Jonkers, Trabajos reunion intern. Reactividad solidos, Madrid., (1957) 413.
 29. K.H. Kim and F.A. Hummel, *J. Amer. Ceram. Soc.*, **43** (1960) 611.
 30. A. Deschanvres, B. Raveau and Z. Sekkal, *Mat. Res. Bull.*, **6** (1969) 699.
 31. P. Lambert, M. Harrison, and P.P. Edwards, *J. Solid State Chem.*, **75** (1988) 332.
 32. A.M. Bystrom, *Acta. Chem. Scand.*, **3** (1949) 163.
 33. M. Lumdberg and S. Anderson, *Acta. Chem. Scand.*, **18** (1964) 817.
 34. J.C. Mikkelsen, Jr, *J. Crystal Growth.*, **47** (1979) 659.
 35. H. Izawa, S. Kikkawa, M.Koizumi, Kyokaishi. Yogyo., *J. Ceram. Assoc Jpn.*, **94** (1986) 621.

-
36. J. Mikkelsen., *J. Am. Ceram. Soc.*, **63** (1980) 331.
 37. T.W.F Barth and E Posnjak, *Z Kristallogr.*, **82** (1932) 325.
 38. E.S.R. Gopal, "Specific heats at low temperatures", Plenum press, New York, (1966) 30.
 39. L. Néel, *Ann. Phys.*, **3** (1948) 137.
 40. R. K. Datta and R. Roy, *J. Am Ceram Soc.*, **50** (1967) 578.
 41. M Dalton, *PhD thesis*, Univ. of Cambridge, 1992.
 42. M.R. Harrison, P.P. Edwards, and J.B. Goodenough, *Philos. Mag.*, **52** (1985) 679.
 43. R.W. McCallum, D.C. Johnston, C.A. Luengo and M.B. Maple, *J Low Temp Phys.*, **25** (1976) 777.
 44. O. Durmeyer, J.P. Kappler, E Beaurepaire, J.M. Heintz and M. Drillon, *J. Phys. Condens. Matter.*, **2** (1990) 6127.
 45. J.M. Heintz, M. Drillon, R. Kuentzler, Y. Dossman, J.P. Kappler, O. Durmeyer and F Gautier, *Z. Phys. B.*, **76** (1989) 303.
 46. A Le Bail and J.L. Fourquet, *Mat.. Res. Bull.* **27** (1992) 75.
 47. J Grins and A.R. West, *J. Solid State Chem.*, **65** (1986) 265.
 48. P.H. Lacorre, M. Hervieu, J Pannetier, J. Choisnet and B. Raveau, *J Solid State Chem.*, **73** (1994) 27
 49. J. Akimoto, Y. Gotoh, M. Sohma, K. Kawaguchi, Y. Oosawa, and H. Takei. *J Solid State Chem.*, **110** (1994) 150.
 50. R.K.B. Gover, J.T. Tolchard, J.T.S. Irvine, H. Murai, H. Tukmato, Submitted to Solid State Ionics.
 51. . M.M. Thackeray, M.H. Rossouw, R.J. Gumnov, D.C. Liles, K. Pearce, A. De Kock, W.I.F. David and S. Hull, *Electrochim. Acta.* **38** (1993) 1259.
 52. B. Morosin and J.C. Mikkelsen, *Acta. Crystallogr., sect B*, **35** (1979) 798.
 53. I Abrahams, P.G. Bruce, W.I.F. David and A.R. West, *J Solid State Chem.*, **78** (1989) 170.
 54. C.A. Vincent, *Chemistry and Industry*, **16 Sep 1996**, 688.
 55. K. Brandt, *Solid State Ionics.*, **69** (1994) 173.
 56. D, Fauteux and R, Kosbang, *J. Applied Electrochem.*, **23** (1993) 1.
 57. N.N. Greenwood and A. Earnshaw, "Chemistry of the elements", Pergammon Press, Oxford, 1984, 1112.

-
58. J.B. Boyce and J.C. Mikkelsen Jr, *Solid State Comms.*, **31** (1979) 741.
59. J. Akimoto, Y. Gotoh, Y. Oosawa, N. Nonose, T. Kumaghi, K. Aoki and H. Takei. *J Solid State Chem.*, **113** (1994) 27.
60. P. Ball, *New Scientist*, 153 (1997) 28.
61. A.D. Hillier, *PhD thesis*, Univ. Of St Andrew, In prep.

Chapter 2. Preparation and characterisation of samples.

2.1 Preparation and characterisation of samples.....	34
2.1.1 Sample preparation.....	34
2.1.2 Thermal analysis.....	36
2.1.3 X-ray diffraction.....	37
2.2 Structural Investigation.	39
2.2.1 Bragg's Law.	39
2.2.2 Unit cells and crystal systems.	41
2.2.3 Miller Indices and d-spacing formula.	41
2.2.4 Systematically absent reflections.....	42
2.2.5 Powder diffraction experiments.....	42
2.2.6 Factors that affect intensities of X-rays.....	43
2.2.7 Form Factors.....	45
2.2.8. Summary of factors that can affect intensities.....	47
2.2.9 Neutron powder diffraction.....	47
2.2.10. Pulsed neutron sources.	48
2.2.11. Structure determination using the Rietveld method.....	50
2.2.11.1 Least squares parameters ¹⁰	51
2.2.12. R factors.	53
2.3. Magnetic characterization of materials.	55
2.3.1. SQUIDS.....	55
2.3.2. Vibrating Sample Magnetometer (VSM).....	56
2.3.3. Muon studies'.	57
2.3.4. Transverse field Muon Spin studies.	57
2.3.5. Measurement of the magnetic penetration depth, λ	59
2.3.6. Methods of data analysis in μ^+ SR studies ¹⁷	60
2.3.7. Maximum entropy method of extracting frequency spectra.....	61
2.3.8. How Maximum Entropy works.....	62
2.3.9. Longitudinal field μ^+ SR.	63
2.3.10. Advantages of the μ^+ SR techniques.	64
2.3.11. Disadvantages of the μ^+ SR techniques.....	64
2.4. Solid state ^6Li magic angle nuclear magnetic resonance.....	65

2.5.1 Electrical property measurements.	66
2.5.2. Impedance spectroscopy.	66
2.5.3 Equivalent circuits.....	69
2.5.4. Capacitance values.	71
2.5.5. Low temperature 4 probe A.C. measurements.....	72
2.5.6 Electrodes.	75
2.6. References.....	75

2.1 Preparation and characterisation of samples.

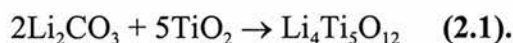
2.1.1 Sample preparation.

One of the most important aspects of this work was the preparation of reduced titanate samples. It is important to be able to accurately control the oxidation state of Ti, with oxidation states between 3.5+ and 4+ being required.

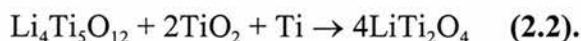
A number of previous studies have been performed in an attempt to prepare single phase samples of the $\text{Li}_{1+x}\text{Ti}_{2-x}\text{O}_4$ solid solution series. Static vacuums were used in the initial studies performed by Deschanvres et al¹ and later Johnston² prepared samples using sealed glass tubes filled with helium. Dalton questioned the nature of the samples prepared using these methods³ during his studies and prepared his samples using flowing inert gas atmospheres. The samples prepared by Dalton had a larger unit cell than had been previously reported in the literature, leading him to suggest that Li_2O was lost from the samples if a vacuum was used during the preparation stage.

Other methods have been utilized in the preparation of these samples. The most interesting of these was that reported by Murphy and co-workers⁴. Murphy found that it was possible to intercalate anatase TiO_2 by chemical methods, which would lead to the formation of LiTi_2O_4 spinel. However this method was found to be rather limited in its uses as only the $x=0$ end member can be prepared. One thing that all of these studies seemed to suggest that samples could be prepared in the temperature range $860\text{-}890^\circ\text{C} \pm 30^\circ\text{C}$. However even the "very good" samples prepared by Dalton showed the presence of a second phase.

It was decided that $\text{Li}_4\text{Ti}_5\text{O}_{12}$ would be used as the precursor for the preparation of LiTi_2O_4 . The $\text{Li}_4\text{Ti}_5\text{O}_{12}$ member of the solid solution series was prepared according to the following equation:



Unless otherwise stated all of the samples were prepared using the following high grade starting materials Li_2CO_3 (Aldrich), Ti metal (Johnson Matthey/Aldrich), and Rutile TiO_2 (Tioxide Specialties materials). For the preparation of $\text{Li}_4\text{Ti}_5\text{O}_{12}$ the Li_2CO_3 and TiO_2 were weighed out accurately in the appropriate ratios described above in equation (I), and ground in an agate mortar and pestle under acetone for 30 minutes. The mixture was then transferred to an alumina crucible and fired in the temperature range 680-705°C overnight to decarbonate the Li_2CO_3 . The resultant powder was then pelleted in a 13mm die at 2 - 3 tonnes and refired for 4 days in a muffle furnace at 915°C to form the $\text{Li}_4\text{Ti}_5\text{O}_{12}$ spinel. LiTi_2O_4 was prepared in the spinel form using $\text{Li}_4\text{Ti}_5\text{O}_{12}$, TiO_2 and Ti metal in the correct ratios as described in (II), the constituents were again mixed under acetone and then pelleted as described for $\text{Li}_4\text{Ti}_5\text{O}_{12}$.



The resultant mixture was then pelleted in a 7mm die at 2 tonnes and wrapped in either copper or gold foil and refired for 14-16 hours in a tube furnace in the temperature range 820 to 860°C under an argon/5% hydrogen atmosphere. A schematic diagram of the tube furnace arrangement is shown in figure 2.1. After cooling to room temperature, the samples were removed from the furnace and found to have a royal blue colour, thus indicating that reduction has been successful.

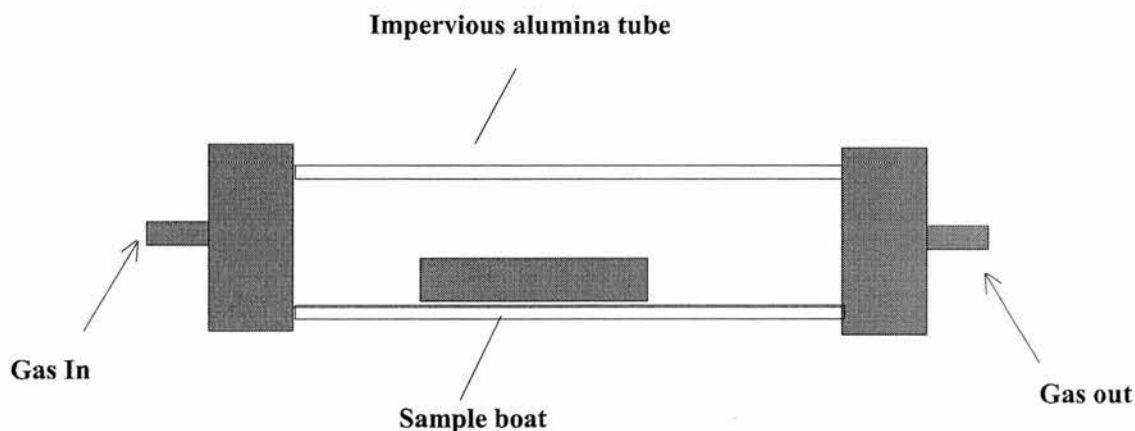


Figure 2.1. Schematic diagram of the sample preparation environment.

The ramsdellite phases were prepared in a similar manner to that indicated above, with the LiTi_2O_4 end member being prepared under an argon/5% hydrogen mixture. As samples with an average titanium oxidation states other than 3^+ may not be stable in 5% H_2 , high purity argon (BOC-Zero Grade) was used to avoid over reduction.

LiTi_2O_4 ramsdellite is a metastable phase and starts to revert back to spinel on cooling from the preparation temperature. To reproduce single-phase materials it was found necessary to quench the samples onto copper turnings under the same flowing gas atmosphere. A vertical furnace was used for these experiments. The samples were suspended in the middle of the furnace hot zone, with the temperature being monitored using a chromel alumel thermocouple. The samples were wrapped in copper foil and suspended by a fine Pt/Rh wire on platinum hang downs. Sample removal was achieved by passing a current across the Pt/Rh wire, this caused the wire to fuse, leading to the sample dropping onto the copper turning. It was found that ramsdellite samples prepared in this manner at 1000°C were usually single phase.

At a later stage of this study, samples were fired in a TORVAC furnace under an argon or static vacuum. Samples prepared in this manner were found to be of good phase purity. The high quality samples prepared using this method are believed to be due to the rapid cooling character of the furnace.

2.1.2 Thermal analysis.

The thermal properties of the materials under investigation were examined using combined thermogravimetric analysis (TGA) and differential thermal analysis (DTA).

Thermal analysis⁵ is defined as the measurement of thermal and chemical properties of a material as a function of temperature. TGA is a technique in which the mass of sample is monitored against time or temperature while the sample is heated in a specified atmosphere DTA is a technique in which the difference in temperature between the sample and a

reference is measured as the temperature is increased. The reference material is usually alumina. Thermal analysis was performed on TA instruments 2960 connected to a personal computer. Both techniques can be examined simultaneously using this type of instrument.

2.1.3 X-ray diffraction.

Powder X-ray diffraction is the workhorse of the materials chemist and is used as the standard tool of analysis to determine the phase purity, structure and composition of inorganic solids. The X-ray powder patterns of inorganic phases can be considered to be their “fingerprint” and are usually unique to a particular phase or family of phases.

X-rays are a type of electromagnetic radiation with a wavelength of approximately 1Å . They occur in the electromagnetic spectrum between γ -rays and ultraviolet radiation. To produce X-rays, a beam of electrons is accelerated to a voltage of the order of 30000 volts, these electrons then strike a metal target, typically copper, and they have sufficient energy to ionize some of the copper 1s electrons (k shell)⁶. An electron in the 2p or 3p orbital then drops down into the vacant 1s level and energy is released as X-rays, with the energy produced by this transition having a characteristic X-ray wavelength. For copper, the wavelengths associated with the 2p \rightarrow 1s and the 3p \rightarrow 1s transitions are 1.5418Å and 1.3922Å respectively. The two different wavelengths are known as K_{α} and K_{β} . The K_{α} is the wavelength is usually used in diffraction experiments and has two slightly different wavelengths at 1.54051 and 1.54433Å , known as $K_{\alpha 1}$ and $K_{\alpha 2}$. The appearance of the $K_{\alpha 1}$ and $K_{\alpha 2}$ is due to the two possible spin states associated with the 2p electron that makes the transition. Presented in figure 2.2. is a typical X-ray powder pattern collected for LiTi_2O_4 ramsdellite.

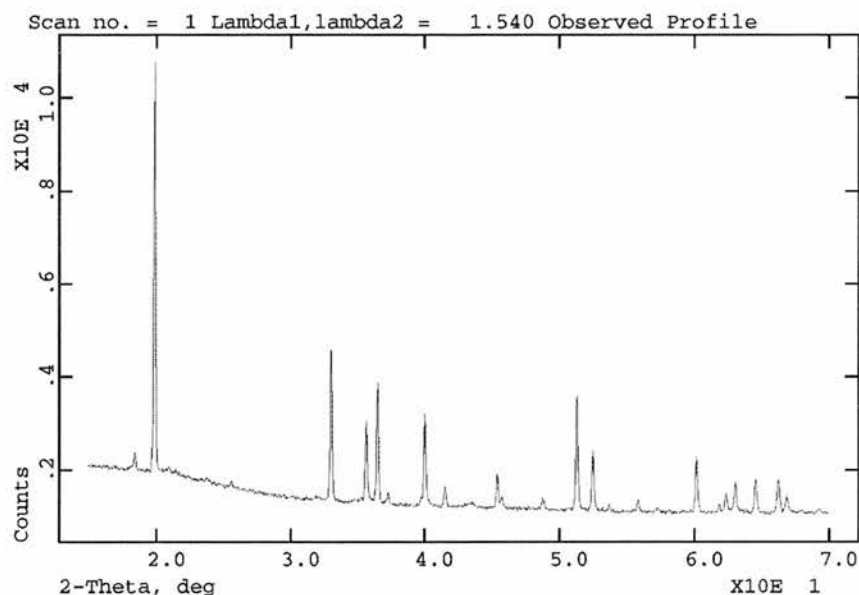


Figure 2.2. Collected powder pattern for LiTi_2O_4 ramsdellite.

The general principles used in the focussing X-rays onto a sample are to be found in most instruments and are described in figure 2.3. The generated X-ray beam is not monochromatic K_α , but contains $K_{\alpha 1}$ and $K_{\alpha 2}$. $K_{\alpha 1}$ and $K_{\alpha 2}$ can be separated out by using a crystal monochromator. A crystal monochromator is usually a large single crystal of quartz or germanium, oriented such that one set of planes diffracts strongly at the Bragg angle to the incident beam. If a flat monochromator were used then the most of the incident X-ray intensity would be lost since X-ray beams emitted from a source are naturally divergent, hence only a small portion of the $K\alpha$ radiation would be at the correct Bragg angle. To overcome this problem, most monochromators are bent. This causes the divergent beam to be refocused, giving an intense monochromatic beam. This principle is known as the Theorem of a Circle. The convergent beam passes through the sample. Radiation that is not diffracted comes to a focus at A, other beams diffracted by the sample focus at B and C, etc. We know from the theorem of a circle that A, B, C and the sample must lie on the circumference of a circle.

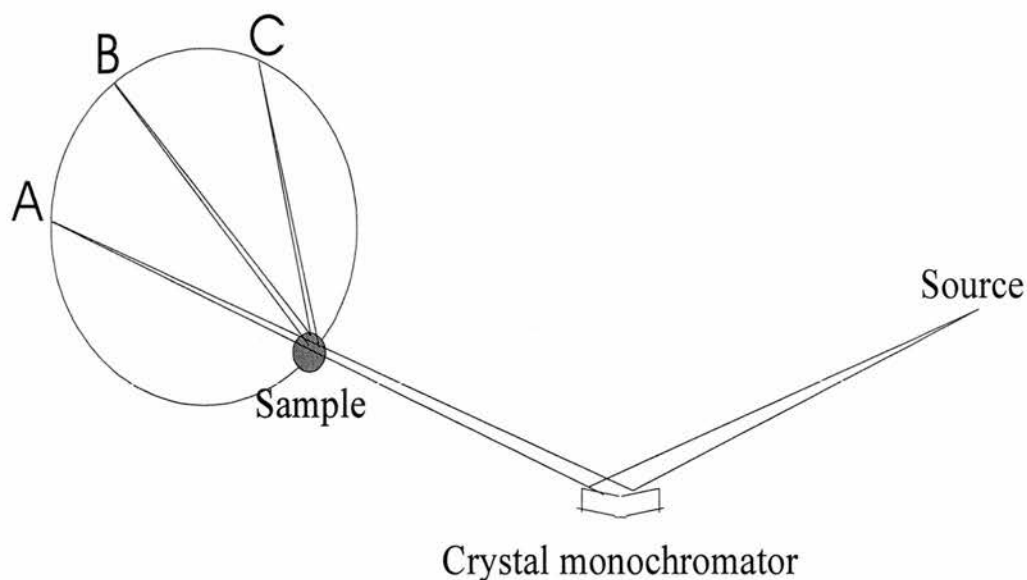


Figure 2.3. Schematic of the principles of an X-ray instrument and theorem of a circle.

X-ray data were collected on a Philips PW1170 or PW3840 reflectance diffractometer using Cu K_{α} radiation, or a Stoe Stadi P transmission diffractometer, using $\text{Cu K}_{\alpha 1}$ radiation.

2.2 Structural Investigation.

2.2.1 Bragg's Law.

In a powder, the small crystals have randomly arranged orientations, which have every crystal plane arranged in random orientations. For each set of planes at least some of the planes must be oriented at the Bragg angle, θ , to the incident beam and therefore diffraction occurs from the planes within the crystal. When crystals diffract X-rays, it is the atoms or ions within the structure that diffract the X-rays, leading to the diffraction pattern.

The Bragg approach to diffraction is to regard the crystals within the material as a semi-transparent mirror. Some of the X-rays are reflected from the planes with the angle of reflection equal to the angle of incidence, the X-rays that are not reflected then proceed to the lattice planes below, etc., until

they eventually meet an atom or ion that fulfills Bragg's equations and are diffracted. The derivation of Bragg's law is shown below in figure 2.4.

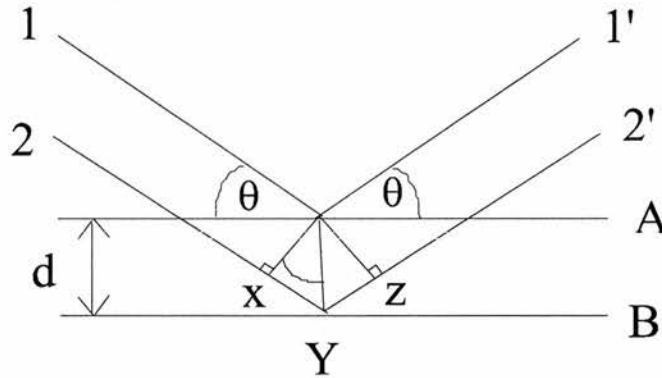


Figure 2.4 - Derivation of Bragg's law for X-ray diffraction.

The X-ray beams 1 and 2 reflect from adjacent planes, A and B, within the crystal and reappear as 1' and 2', they are in phase. Beam 22' has to travel the extra distance xyz compared to beam 11', and for beams 1' and 2' to be in phase, the distance xyz must be equal to an integer number of wavelengths. The perpendicular distance between plane A and plane B is known as the d spacing or d, and the incident angle of the diffracted X-rays is the Bragg angle, θ , and are related to the distance between x and y by the Bragg equations.

$$xy = yz = d \sin \theta$$

$$xyz = 2d \sin \theta$$

$$xyz = n\lambda$$

And therefore

$$2d \sin \theta = n\lambda. \quad (2.3).$$

When Bragg's law is satisfied, the diffracted beams are in phase and therefore constructively interfere, and this manifests itself as lines in the diffraction pattern. If, however the beams are out of phase, they destructively

interfere with each other and no line is seen. The Bragg equations are very stringent and a difference of more than a few degrees cause complete cancellation

2.2.2 Unit cells and crystal systems.

Crystals are built up of a regular arrangement of atoms in three dimensions, this arrangement can be represented by a repeating unit called the unit cell. The unit cell is defined as *the smallest repeating unit that shows the full symmetry of the crystal structure*. It is possible to describe seven different types of structure, and how these values change helps determine the structure type. The arrangement of atoms within the unit cell is also of great importance, and their positions cannot be described in terms of the type of symmetry possessed by the unit cell. To fully describe a crystal structure the space group also needs to be known. This is a set of symbols that summarizes information about the crystal system, lattice type and spatial symmetry. There are 230 different space groups.

2.2.3 Miller Indices and d-spacing formula.

Bragg's law treats X-rays as being diffracted from these various sets of lattice planes and the Bragg angle θ , for each set is related to the d spacing by Bragg's law.

Lattice planes are labeled by assigning three numbers known as the Miller indices. As mentioned previously the distance between adjacent perpendicular planes is known as the d spacing, and it is this d value that appears in Bragg's laws. For a cubic unit cell, the (1 0 0) plane simply have a d spacing of **a**, the value of the unit cell edge. For a (2 0 0) reflection in a cubic cell, $d=a/2$ etc. For an orthogonal crystal (i.e. $\alpha = \beta = \gamma = 90^\circ$), the d spacing for any set of planes is given by the formula

$$1/d_{hkl}^2 = h^2/a^2 + k^2/b^2 + l^2/c^2 \quad (2.4).$$

2.2.4 Systematically absent reflections.

In principle each of the planes within a structure will diffract, but in many cases the resultant intensity is zero. The absent reflection may be the result of two possible phenomena. Reflections may be absent due to some quirk of the structure or the symmetry or type of lattice possessed by the structure. The other type of absence is known as a systematic absence and arise if the lattice type is non-primitive (I, F) or if such phenomena as a screw axes, or glide planes are present.

2.2.5 Powder diffraction experiments.

The basic essentials of an X-ray diffraction experiment are the sample, the X-ray source and the detector(s), as shown below in figure 2.5.

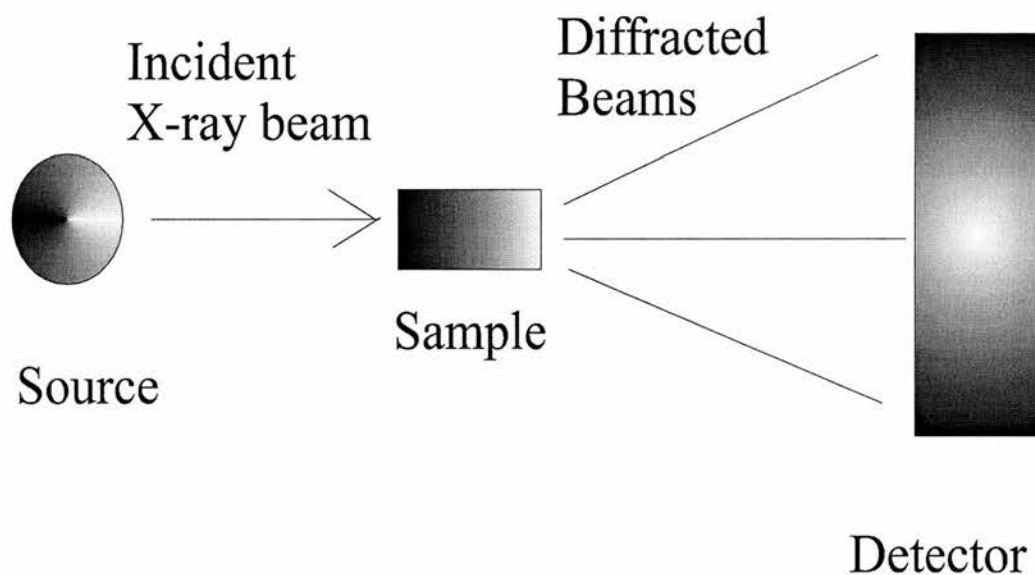


Figure 2.5. An X-ray diffraction experiment.

Two main geometries are used in powder diffraction experiments, these are transmission and reflectance, and each has its own merits. The reflectance type of instrument is the most common type.

Samples are mounted for the experiments in a number of different ways. The STOE samples were mounted on Mylar discs with Vaseline and

placed in a circular sample holder, the sample holder was then placed in the instrument and rotated at a constant rate. The rotation of the sample is necessary to help reduce the effects of preferred orientation.

Samples prepared for the Phillips instrument were prepared in one of two different manners, this being dependent on the amount of sample available for analysis. Smaller sample were placed on a glass slide and held in place using Vaseline. The second method of sample preparation was to place the sample in an aluminum sample holder, with the powder being compacted into position.

The time of exposure was dependent on the type of experiment being performed. In general it was found sufficient to expose the sample for between 20 and 45 minutes in order to determine the phase purity of a sample. If structure determination was the aim of the experiment, then the sample was typically exposed for 12 to 16 hours.

2.2.6 Factors that affect intensities of X-rays.

Intensities of X-rays are important for two reasons. Qualitative or semi-quantitative intensity data is needed for fingerprinting the phases, and also if the powder diffraction file is to be used, then the intensities of unknowns are important. Secondly, quantitative measurements of intensity are very important in determining unknown crystal structures, by least squares methods.

In phase scattering may be likened to an elastic collision between the X-ray and the electron without loss of energy, hence without change of wavelength. The intensity of the radiation scattered is given by the Thomson equation;

$$I_p \propto \frac{1}{2}(1 + \cos^2 2\theta) \quad (2.5).$$

Where I_p is the scattered intensity at any point P, and 2θ , the angle between the incident and the diffracted beam that passes through point P. From this equation it can be seen that the scattered beams are most intense

when parallel or antiparallel to the incident beam and are weakest at 90° to the incident beam. The Thomson equation is also known as the polarization factor and is one of the standard correction factors that is applied during the processing of intensity data (for use in structure determination.)

X-rays scattered by an atom are the result of the wave scattered by each electron in the atom. The electrons may be regarded as particles that occupy different positions in an atom and interference occurs between their scattered waves. For scattering in the direction of the incident beam, beam 1' and beam 2' (figure 2.6), all electrons scatter in phase irrespective of their position. The intensity is then the sum of the individual intensities. The scattering factor or form factor, f , is proportional to the atomic number, Z , or more strictly, to the number of electrons possessed by that atom.

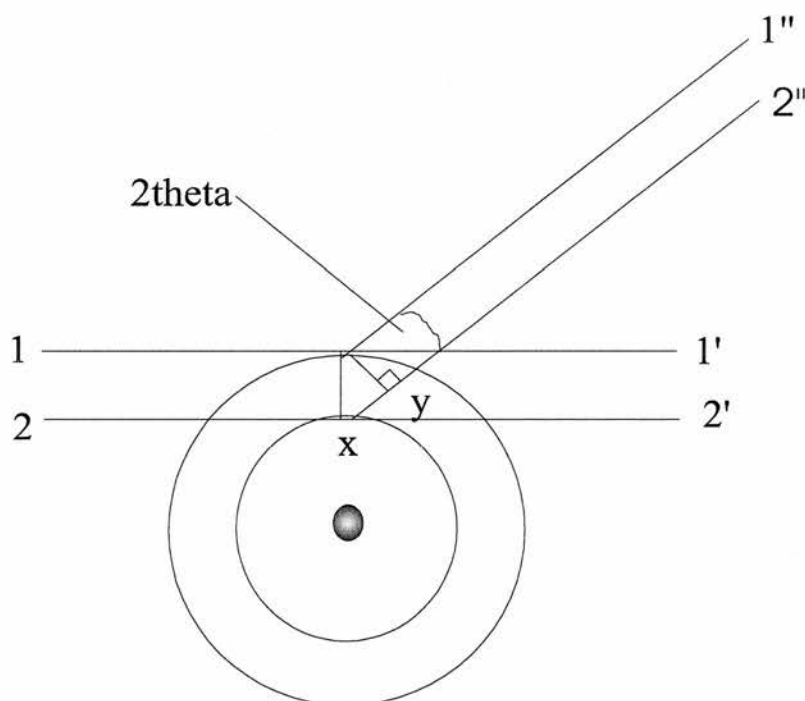


Figure 2.6. Scattering of X-rays by electrons in an atom.

For scattering at some angle 2θ to the direction of the incident beam, a phase difference, corresponding to the distance XY exists between beam 1'' and 2''. The resultant phase difference is usually shorter than 1.5418\AA (i.e. the wavelength of copper $K\alpha$ because interatomic distances are usually short).

This causes partial destructive interference between 1'' and 2''. The result of this interference between beams is that the intensity gradually decreases with increasing 2θ angle.

2.2.7 Form Factors.

X-rays are scattered by their interactions with electrons, and interference takes place between X-rays from different parts of an atom. Consequently, the scattering factor f_x decreases with increased scattering angle, 2θ . At $\sin\theta/\lambda = 0$, f_x is proportional to the atomic number of an element and hence very small for lighter elements such as hydrogen and lithium. To a good approximation, f_x is independent of wavelength, except for resonance effects at certain specific wavelengths.

For an arrangement of several atoms, we have to consider the interference between waves scattered by different atoms. For example, the scattering by a unit cell containing n atoms for a reflection hkl , is given by the structure factor F_{hkl} and takes the form:

$$F_{hkl} = \sum f_n \cos 2\pi(hx_n + ky_n + lz_n) \quad (2.6).$$

Where x_n , y_n and z_n are the fractional coordinates of the n th atom: e.g. for the CsCl structure, figure 2.7.

$$\begin{aligned} F_{100} &= f_{Cl} \cos 2\pi (1*0 + 0*0 + 0*0) + f_{Cs} \cos 2\pi (1*.5 + 0*0.5 + 0*0.5) \\ &= f_{Cl} \cos(0) + f_{Cl} \cos(\pi) \\ &= f_{Cl} - f_{Cs} \end{aligned}$$

Similarly, $F_{110} = f_{Cl} + f_{Cs}$; i.e. chlorine and caesium are scattering in phase for the 110 reflection. For centrosymmetric structures F_{hkl} may be positive or negative, with the structure factor amplitude being $|F_{hkl}|$

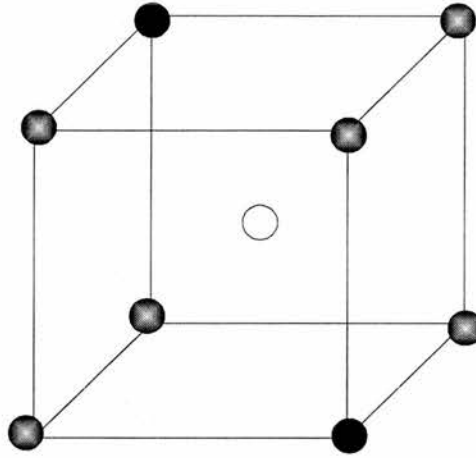


Figure 2.7. CsCl structure, Filled spheres, Cl at 0, 0, 0 and empty sphere, Cs at 0.5, 0.5, 0.5

The intensity of a reflection is something that can be measured and is related to the structure factor using the equation:

$$I_{hkl} = sLpF_{hkl}^2 \quad (2.7).$$

Where s is a scale factor, L = Lorentz correction and p is a polarization correction, $p = (1 + \cos^2 2\theta)/2$, essentially

$$I_{hkl} \propto (f_{Cl} - f_{Cs})^2 \quad (2.8).$$

In CsCl, therefore

$$I_{100} \propto (f_{Cl} - f_{Cs})^2$$

$$I_{110} \propto (f_{Cl} + f_{Cs})^2$$

$$\therefore I_{110} > I_{100}$$

As the scattering factor f_x is related to number of electrons present in an atom, reflections due to lighter elements can be very weak or non-existent. This makes the location of lighter elements and hence full structural determination very difficult.

One possible method to overcome this problem is to use single crystal X-ray diffraction. This method can locate lighter elements by mapping

electron density in three dimensions. However, it may be very difficult to prepare single crystals of sufficient size and quality for this type of experiment.

Another technique, which does not suffer from this problem, is neutron diffraction, and as a consequence a significant amount of structural work is done by neutron diffraction (covered in more depth at a later stage.)

2.2.8. Summary of factors that can affect intensities.

1. Polarization factor- angular dependence of intensity scattered by electrons.
2. Structure factor- dependence on the position of atoms in the unit cell and their scattering power.
3. Multiplicity's- the number of reflections that contribute to an observed powder line.
- 4 Temperature factors- thermal vibrations of atoms can cause a decrease in the scattered intensity of diffracted beams and an increase in background scattering.
- 5 Preferred orientation- occurs in samples, if the arrangement of crystallites is not completely random.

2.2.9 Neutron powder diffraction.

It is certainly possible to solve crystal structures by X-ray techniques, however in many instances neutron techniques provide additional and sometimes more accurate information and thus certain experiments require the use of neutrons. At the present moment, the majority of neutrons used in diffraction experiments are produced by nuclear reactors such as that at the Institute Laue Langevin (ILL) or D3 (RIS ϕ). A recent advance has been the use of spallation sources such as that found at ISIS or IPNS, to produce neutrons.

Unlike X-rays, which are scattered by the atomic electrons, the neutron is scattered by the nucleus. This leads to two noticeable differences between the X-ray and neutron experiments.

1. The interference effects that cause X-ray scattering to diminish with $\sin \theta/\lambda$ are not present with neutrons.
2. As the neutron is scattered from the nucleus, the scattering length (or factors) is not dependent on the atomic number, this often leads to lighter elements such as hydrogen and lithium being easily detectable.

The magnetic moment of the neutron also interacts strongly with the magnetic moment of the electrons⁷. Diffraction of the neutrons by magnetic crystals allows determination of the distribution, direction and order of the magnetic moment.

2.2.10. Pulsed neutron sources.

Recent developments have led to the advent of neutron diffraction by using pulsed neutrons. A pulsed or spallation source produces neutrons using a different method to that used in reactors. Pulses of high-energy protons (typically accelerated to 800 meV in a synchrotron) are fired onto a heavy metal target, this leads to a high flux of neutrons (about 30 per proton), this process is known as the spallation process. The neutrons are not released from the synchrotron continuously but in pulses, the pulsed structure is retained on release and is available for diffraction experiments.

The pulsed structure of the neutrons allows separation of the different wavelengths of neutrons by the Time Of Flight (T.O.F) method. A diffraction pattern is collected from the pulses of white neutrons, where the detector(s) are placed at fixed angles to the sample and the neutron beam. The neutrons diffracted can then be analyzed as a function of time taken to reach the detectors. More energetic neutrons arrive at the detector(s) faster and hence have a shorter time of flight and vice versa. The time of flight of the neutron can be converted to the equivalent d spacing using the de Broglie wave particle duality relationship and the Bragg's diffraction law as follows.

$$\lambda_n = \frac{h}{m_n v_n} = \frac{ht}{m_n l} \quad (2.9).$$

Where λ = the de Broglie wavelength, m_n = the mass of a neutron ($1.6749 * 10^{-27} \text{Kg}$), v_n = the velocity of the neutron, t = the time of flight and l = the distance between the neutron chopper and the detector. Choppers are rotating metal disks with portions removed, these act to remove neutrons with undesirable wavelengths from the beam.

$$\therefore \lambda = \frac{ht}{m_n l} = 2d \sin \theta \quad (2.10)$$

$$\Rightarrow d = \frac{ht}{2m_n l \sin \theta} \quad (2.11)$$

Where θ = the angle between the beam and detectors and d = the lattice plane spacing for the diffraction condition. Presented in figure 2.8, is a schematic of a Time of Flight diffraction instrument.

One advantage of the Time of Flight technique is that in theory a complete diffraction pattern can be collected in one pulse. This rapid collection of data allows time-resolved studies to be performed. One big disadvantage of neutrons is that some elements or particular isotopes such ${}^6\text{Li}$ absorb neutrons and this can be overcome in some cases by using an absorbance correction in the case of ${}^6\text{Li}$.

Source moderator

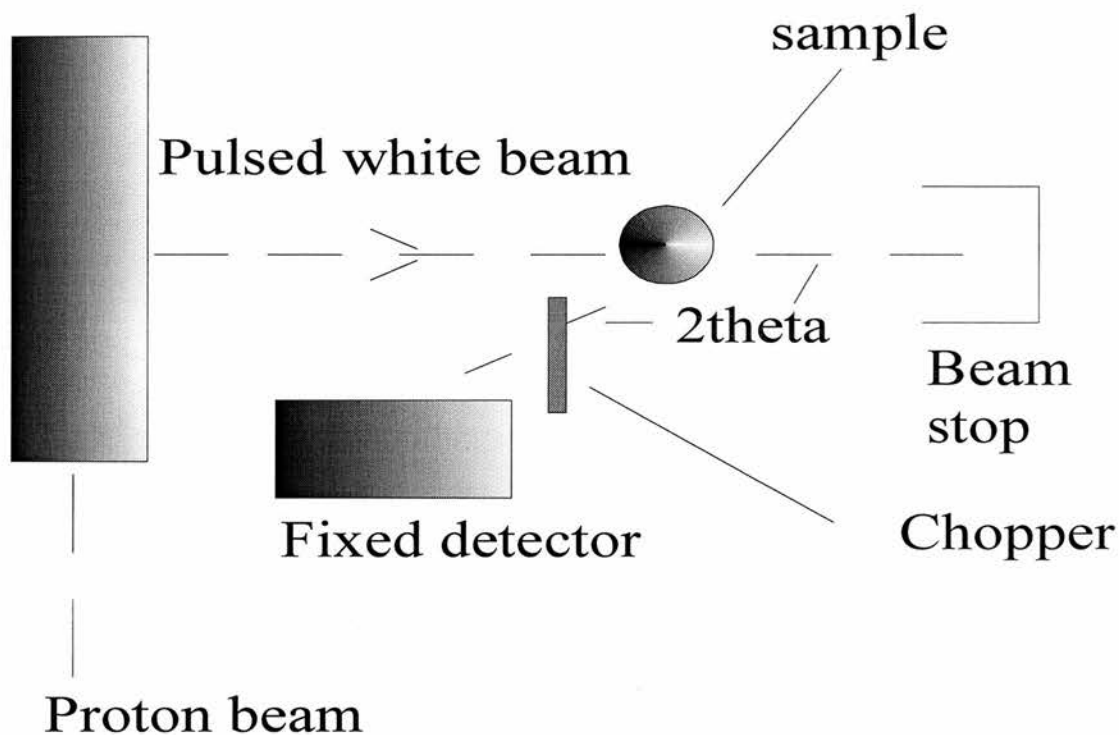


Figure 2.8. A schematic diagram of a Time of Flight diffraction instrument.

The penetrating power of neutrons is high, but the diffracted intensities are quite low, which requires large samples and/or long counting periods to be used. Sample sizes typically range from 1-10 grams with exposure times of about 1 hour or greater necessary. Samples are held in a vanadium sample can, as this material is practically transparent to neutrons, due to its low neutron scattering cross section.

As mentioned previously, the data collected can be used to determine structures, the most important method used is known as the Rietveld method⁸.

2.2.11. Structure determination using the Rietveld method.

The relatively low flux of neutrons when compared to X-rays sources results in the need for large crystals for neutron diffraction experiments, however it is often very difficult or impossible to prepare suitably large single crystals for neutron experiments. This has led to the development of a

technique known as the Rietveld method¹². This technique has been used successfully in the determination of complex low symmetry structures. A conventional refinement using structural factors is feasible for high symmetry structures, but is impossible for low symmetry materials, this is due to the overlap between adjacent Bragg reflections.

Rietveld devised a method that approached the problem from a different perspective. The idea was to fit the entire diffraction pattern by means of curve fitting using least squares methods, rather than fitting intensity maxima. In a Rietveld structure refinement, an attempt is made to fit an experimental model to the observed diffraction pattern, rather than trying to fit the individual reflections of the pattern.

When performing a Rietveld refinement a number of assumptions are made, the most important of these assumptions is that the peak shape of the Bragg peaks can be described as being approximately Gaussian/ Lorentzian.

2.2.11.1 Least squares parameters¹⁰.

The least square parameters used in a refinement can be divided into two groups. The first group, the profile parameters, defines the positions, the half widths, and the possible asymmetry of the diffraction peaks in addition to the properties of the powder sample, i.e. preferred orientation. These parameters are

1. The half width parameters.
2. Zero point.
3. The unit cell parameters.
4. Asymmetry parameter
5. Preferred orientation

The second group, the structure parameters, defines the contents of the asymmetric unit cell:

1. The overall scale factor (c), such that $y(\text{calc}) = c \cdot y(\text{obs})$
2. Overall isotropic temperature parameter.

3. X, Y and Z, the fractional coordinates of the atoms contained in the unit cell.
4. Atomic isotropic temperature parameters.
5. The occupation number of the unit cell.
6. Components of the magnetic vector of atoms in the unit cell.

In order to describe the contents of the complete unit cell, it is important to give not only the content of the unit cell, but also the space group, so that all of the remaining atom positions can be determined.

The principle of the profile refinement is best demonstrated by the function M , which has to be minimized with respect to the parameters. For the normal refinement procedure on separated integrated intensities this function is

$$M = \sum_i W_i \left\{ S_i^2(\text{obs}) - \frac{1}{c} S_i(\text{calc}) \right\}^2 \quad (2.12).$$

And on the integrated intensities of groups of overlapping reflections

$$M = \sum_i W_i \left\{ \sum_k S^2(\text{obs}) - \frac{1}{c} \sum_k S_k(\text{calc}) \right\}^2 \quad (2.13).$$

This function becomes, in the case of a profile refinement,

$$M = \sum_i W_i \left\{ Y_i(\text{obs}) - \frac{1}{c} \sum_k Y_i(\text{calc}) \right\}^2 \quad (2.14).$$

Where Σ_i and Σ_k are the sum over the independent observations and the sum over the overlapping reflections in each group, and S_k^2 is the sum of the nuclear and magnetic contributions.

A computer program based on the above, carries out the least squares refinement. Because the problem is not linear in the parameters, approximate values are required for all of the parameters for the first cycle. These are refined in subsequent cycles until convergence is achieved.

The Rietveld method has recently been modified so that time of flight neutron data can be examined. The procedure is essentially the same as those used in conventional fixed wavelength neutron diffraction refinements except the peak shapes are generally more complex in nature.

Profile refinement using this technique is possible using powder X-ray methods, although it is not nearly as powerful as neutron methods. This is due to the fall off in X-ray intensity with increasing $\sin\theta/\lambda$. Profile analysis is limited by the same drawbacks that affect all powder methods in general: the loss of information arising from the compression of all the data from three dimensions into a single dimension. This leads in turn to problems with using Fourier fitting methods.

With recent advances in computer power, it is possible refine structures on personal computers such as a PC, and involves the use of specialist software such as the Cambridge crystallography library (CCSL) TFLS software (used at ISIS)⁹ and GSAS¹⁰.

2.2.12. R factors.

The quality of refinement, i.e. closeness of fit between experimental and calculated patterns is expressed in terms of R factors or residual factors. These are usually quoted as percentages¹¹. The R factors are

- 1 Profile R factor, R_p
- 2 Weighted R Factor, R_{wp}
- 3 Intensity or Bragg R factor, R_I
- 4 Expected R factor, R_E

R_p profile residual factor.

$$R_p = \frac{\sum_i |Y_i(obs) - Y_i(calc)|}{\sum_i Y_i(obs)} \quad (2.15).$$

R_{wp} -weighted R factor.

$$R_{wp} = \left[\frac{\sum_i |Y_i(obs) - Y_i(calc)|^2}{\sum W_i Y_i^2(obs)} \right]^{1/2} \quad (2.16).$$

Where Y is the intensity of the point on the powder diffraction profile, and w is a weighting factor.

$$R_1 = \frac{\sum_k |I_k(obs) - \frac{1}{c} I_k(calc)|}{\sum_k I_k(obs)} \quad (2.17).$$

I is the peak intensity. The intensity R factor is helpful in determining the quality of structural fit since it relates to the peak area and not the peak shape.

R_E expected residual factor.

$$R_E = \left[\frac{N - P + C}{\sum W_i Y_i(obs)^2} \right]^{1/2} \quad (2.18).$$

N is the number of observations, P is the number of variables and C is the number of constraints. Another guide to the quality of a refinement is the χ^2 . This is calculated using the following relationship.

$$\chi^2 = \left(\frac{R_{wp}}{R_E} \right)^2 \quad (2.19).$$

Therefore, in an ideal refinement, the weighted and expected R factors should be identical and hence a value of 1 obtained. However, a number of things can affect the value of χ^2 , such as the background associated with a vanadium furnace, and hence the value should not be used solely on its own as a guide to the quality of a refinement. It is also of paramount importance to examine the observed and calculated profiles at each stage of refinement in

order to assess the progress and future strategy of the refinement. The R factors obtained during the course of a refinement are the best guide to the quality of the fitted profile. A value of 1 % would be considered a very good fit, however this is rarely seen. As a rule of thumb a value of less than 5 % is considered a very good fit, with value between 5 – 10 % being considered acceptable.

The value of R may be artificially high for a number of reasons, such as short counting times (this will lead to a systematic error in the background, poor peak separation, etc). Experiments performed in specialist environment, such as a furnace, cryostat, etc, can lead to a contribution to the background of the collected profile and hence will lead to a lower than expected R factor. These factors and others must be considered when reporting the R factors obtained from a refinement.

2.3. Magnetic characterization of materials.

2.3.1. SQUIDS

The first type of Superconducting Quantum Interference Device was constructed a few years after the discovery by Josephson¹² in 1962 of the effect of superconductive tunneling. In its simplest form it act as a flux to voltage converter of unsurpassed sensitivity.

The majority of modern SQUIDS contain Josephson junctions. These junctions consist of a thin layer of insulator or semiconductor, sandwiched between two superconducting electrodes. The quantised state of the superconducting ring and the non-linear behaviour of the Josephson junction means that extremely small changes in magnetic field can be measured. The SQUID does not directly measure the magnetic field from the sample. Instead, the sample moves through a system of superconducting detection coils, which are connected, to the SQUID with superconducting wires, allowing the current from the detection coils to inductively couple with the SQUID sensor. The SQUID electronics produce an output voltage that is proportional to the current flowing in the SQUID input coil. Measurements

are made by passing the sample through the superconducting detection coils. As the sample moves through the coils, the magnetic moment of the sample induces an electric current in the detection coils. Any changes in the persistent current in the detection circuit are proportional to the changes in magnetic flux.

The SQUID used during this study was located at the University of Edinburgh, Department of Chemistry and was a Quantum Design MPMS2 SQUID magnetometer.

2.3.2. Vibrating Sample Magnetometer (VSM)

A vibrating sample magnetometer is a device in which the sample is vibrated in a uniform magnetic field, and the magnetization of the sample is detected. The instrument allows precise magnetization measurements to be made as a function of temperature, magnetic field strength, magnetic field ramp rate and crystallographic orientation. However the sensitivity of the method is much lower than that a SQUID.

When a specimen is placed in a uniform magnetic field, a magnetization M is induced in the sample equal to the product of the susceptibility and the applied magnetic field. If the sample is vibrated, say in a sinusoidal motion, then an electrical signal depending on the magnetic moment, the amplitude of the vibration and vibration frequency is produced. The magnetization is converted to molar magnetic susceptibility by the expression.

$$\chi_m = \frac{M_s (MW)_s}{H_a W_s} \quad (2.20).$$

Where M_s is the magnetization of the sample, $(MW)_s$ is the molecular or formula weight, H_a is the applied magnetic field and W_s is the weight of the sample.

The VSM used in this work was located at the School of Physics and Astronomy, University of St. Andrews. The instrument used was an Oxford Instruments 12 Tesla Vibrating Sample Magnetometer.

2.3.3. Muon studies^{13,14}.

Muons are subatomic particles of the Pion class, and can be used as a microscopic spin probe of the magnetics of a system. Work presented in this thesis was performed in two different geometries on two different samples. Experiments were performed on the MuSR beam line at the ISIS pulsed muon facility, Rutherford Appleton Labs, OXON, UK. The production of muons at ISIS is achieved by scavenging approximately $5\mu\text{A}$ of the total proton beam before it strikes the heavy metal target that is used in the production of neutrons. The scavenged beam is then focused onto a graphite filter leading to the production of muons.

2.3.4. Transverse field Muon Spin studies.

The transverse or muon spin rotation technique can provide a sensitive measure of the microscopic field distribution inside a superconductor, which in turn can be related to the penetration depth. By using the μ^+ SR to measure λ as a function of temperature, it might be possible to investigate the pairing mechanism of the superconducting state. It can also provide details on the flux lattice distribution within a sample when in the superconducting state. Presented below in figure 2.9 is a schematic diagram of a transverse μ^+ SR. experiment.

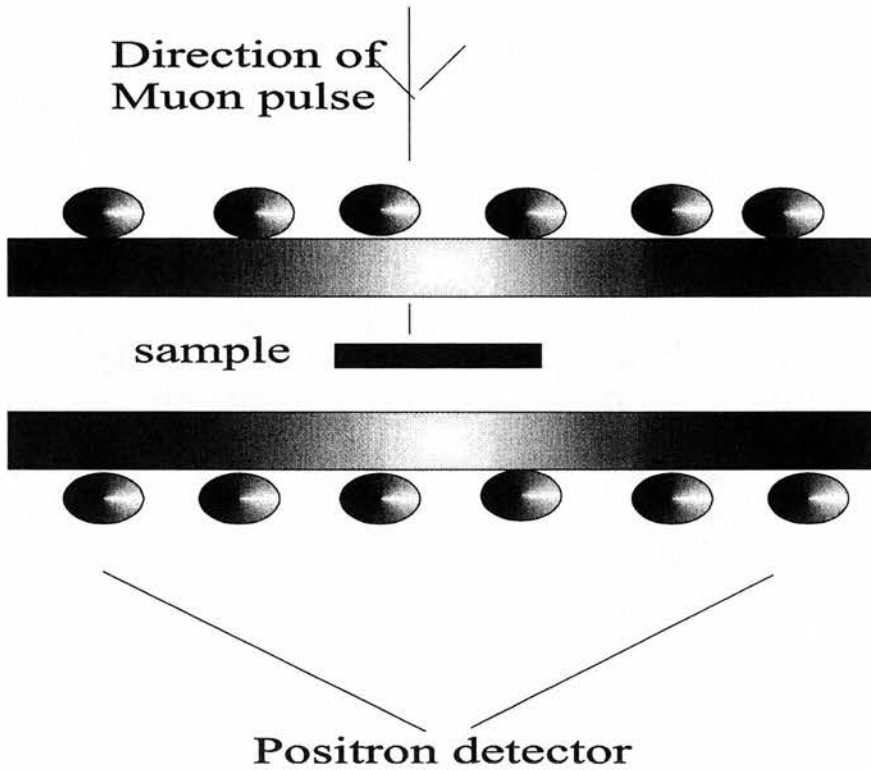


Figure 2.9.- A schematic diagram of a transverse μ^+ SR. experiment.

In the mixed state of a superconductor (when both the normal and superconducting states are present), for an applied field larger than the lower critical field, H_{c1} , flux enters the bulk in the form of quantised lines of flux. Each quanta of flux, $\Phi_0 = h/2e$ consists of a core of normal electrons around which a vortex of supercurrent flows.

1. The temperature dependent superconducting coherence length $\xi(t)$, can be thought of as the distance over which the superconducting wave function $\psi(\mathbf{R})$ can fall to zero, and as such defines the dimensions of the normal core.
2. The magnetic penetration depth, $\lambda(T)$, which is a measure of the distance over which the current screens a magnetic field.

If the applied field is increased, the internal density of the flux lines also increases, and eventually they will begin to overlap. In this case the field no longer drops to zero between the flux cores. Due to mutual repulsion

between the flux lines they form a Abrikosov lattice of plane spacing, d , so that the internal flux density $B \approx \Phi_0 / d^2$. For a very large range of fields, $H_{c1} \leq H \leq H_{c2}$, the flux distribution is determined largely by λ .

In the transverse μ^+ SR technique, highly spin-polarized muons are brought to rest in a sample which sits in a magnetic field H_{ext} perpendicular to the muon spin. The muons then undergo a Larmor precession in the local internal field B_{int} at an angular frequency $\omega = \gamma_{\mu} B_{\text{int}}$, where $\gamma = 2\pi * 1.36 * 10^8 \text{ HzT}^{-1}$. The evolution of the muon with time may be measured by the detection of positrons which are emitted preferentially along the muon spin direction during the muon decay process, the half life of this decay being approximately $2.2\mu\text{s}$ (T_{μ}). The observed spectrum can be described by

$$N(\theta, t) = N_0 \exp\left(\frac{-t}{T_{\mu}}\right) [1 + AR(t)\text{Cos}(\omega t + \theta)] + b. \quad (2.21)$$

Where N_0 is the normalization constant, A is the precession amplitude, θ is the initial phase, b is a constant background, ω and T_{μ} are as above.

2.3.5. Measurement of the magnetic penetration depth, λ

For an isotropic type II superconductor in the “clean limit” the magnetic penetration depth may be derived from

$$\frac{1}{\lambda^2}(0) = \frac{\mu_0 e^2 n_s(0)}{m^*} \quad (2.22).$$

Where $n_s(0)$ is the density of the superfluid pair at 0 Kelvin and m^* is the effective mass of the superconducting pairs.

$$\lambda(T) = \frac{\lambda_0}{(1 - t^n)^{1/2}} \quad (2.23).$$

where $t = T/T_c$ is the reduced temperature.

The penetration depth λ may also be obtained from the second moment (linewidth) $\langle \Delta B^2 \rangle$ of the field distribution $p(B)$, which may be written as the sum over the reciprocal lattice vector G

$$\langle \Delta B^2 \rangle = \sum_{G \neq 0} h(G) \quad (2.24).$$

For simple geometry^a of the applied field, this has been calculated to give

$$\langle \Delta B^2 \rangle = \frac{0.00371 \Phi_0^2}{\lambda^4} \quad (2.25).$$

The linewidth $\langle \Delta B^2 \rangle$ can give an idea of the flux lattice, and field distribution within the sample being examined.

2.3.6. Methods of data analysis in μ^+ SR studies¹⁷.

The methods used to extract useful data from all μ^+ SR experiments can be complicated, therefore this will be a brief overview of the subject. Depending on the physics, there are two perspectives

(1) The muons precess at frequency ω_L but their polarization decays with time:

$$C_j^t = N_0^j e^{-t/\tau_\mu} [1 + A_j P_x(t) \cos(\omega_L t + \phi_j)] \Delta t \quad (2.26).$$

taking $t_0 = 0$. $P_x(t)$ describes the decay of the muon polarization. In certain cases, it is possible to assume particular forms for $P_x(t)$, i.e. rapid fluctuating local fields,

^a In this case, the sample was compressed on to a silver plate, \perp to the direction of the incident beam.

$$Px(t) = \exp.(-\lambda t) \quad (2.27).$$

Or with a Gaussian distribution of fields

$$Px(t) = \exp.\left(-\frac{1}{2}\sigma^2 t^2\right) \quad (2.28).$$

Where ($\sigma = \gamma Brms$) In these cases σ and λ can be extracted from data by least squares fitting packages like Universal Data Analysis (UDA)¹⁵.

Muons see an arbitrary distribution of internal fields

$$C_i^j = N_0^j \Delta t. e^{\frac{-t}{\tau_j}} [1 + A_j F_j(t)] \quad (2.29).$$

where

$$F_i(t) = \int_0^\infty F(\omega) \cos.(\omega t + \phi_j) d\omega \quad (2.30).$$

The distribution of internal fields is derived from $F(\omega)$ since $\omega = \gamma B$. The problem is to extract $F(\omega)$ from the data, this can be done by use of a Fourier transformation. This however has a number of problems associated with it.

As few muons are present at long decay times, this method gives poor statistics thus leading to noisy transforms. Therefore we have to choose the optimum window for data collection, and this in turn causes data points being excluded from the calculations, and this leads to a reduction in frequency resolution. It also means that combination of the separate histograms is difficult and hence it is difficult to obtain a unique $F(\omega)$

2.3.7. Maximum entropy method of extracting frequency spectra.

This method is complicated but has been used successfully in a number of unrelated fields, such as radio astronomy and image reconstruction (i.e. on the Hubble space telescope.). It is superior to the methods deccribed above as its

not affected by spurious features arising from fluctuations in the data. It works by finding the maximum entropy of the data set being analyzed and does not try to fit all of the data obtained using least squares methods. It has a number of advantages over least squares methods, these are listed below.

- (1) Use all available data.
- (2) Allows extraction of unique $F(\omega)$ from multiple histograms.
- (3) $F(\omega)$ is positive.
- (4) Picks most uniform distribution consistent with data.
- (5) No prior assumption about the form of $F(\omega)$.
- (6) Possible to include convolution with muon pulse shape.
- (7) Can achieve ultimate frequency resolution.

2.3.8. How Maximum Entropy works.

The maximum entropy technique determines the field distribution, as the name suggests, by maximising the entropy of the probable field distribution, $p(B)$. The entropy of the system is given by

$$S = \sum_i \frac{p(B_i) \ln(p(B_i))}{d_i} \quad (2.31.)$$

Where d_i are the initial default values. The probable field distribution, as determined by maximising the entropy, is then compared to the data by determining the errors of the fit using the relationship

$$\chi^2 = \sum_i \frac{(R_i - \mathfrak{F}(p(B_i)))^2}{\sigma_i^2} \quad (2.32.)$$

where R_i is the muon spin rotation data after correction for deadtime^b and removal of the muon radioactive decay, $\mathfrak{F}(p(B_i))$ is the Fourier transform of

^b This is when the detectors are swamped by the large number of muon decays and do not have time to recover.

the probable field distribution and σ_i are the experimental errors. The resulting field distribution is then obtained by minimising

$$L=S-\lambda\chi^2 \quad (2.33.)$$

Where λ is the Lagrange multiplier. The maximum entropy algorithm searches for the solution, which minimises $S-\lambda\chi^2$. Initially λ is chosen so that the algorithm puts most effort into minimising χ^2 , with the aim of reducing its value to equal the number of data points. In the later stages the value of λ is altered to concentrate on maximising the entropy.

2.3.9. Longitudinal field μ^+ SR.

In transverse μ^+ SR, we are examining superconducting properties of the material. Longitudinal μ^+ SR is however of more use for examination of magnetic properties. The most fundamental difference between transverse and longitudinal is the geometry used in the experiments. Shown below in figure 2.10 is a schematic of the geometry used.

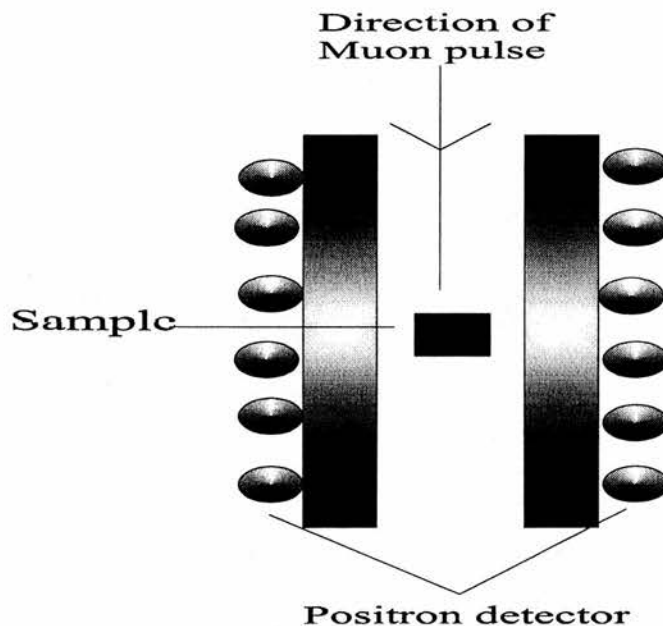


Figure 2.10. Schematic of the geometry used in Longitudinal field μ^+ SR experiments.

In transverse geometry, the muon decay is seen as a function of time, it also seen to have a sinusoidal type component, with the amplitude decreasing as the number of events at longer time's decreases. Only the decay is seen in longitudinal μ^+ SR. The spectra obtained can be used to determine the kinetics of the muon decay. When only one type of relaxation is seen then the data can be fitted with a simple fitting function. If the muon decay is more complicated and require other function to be fitted, this may indicate that more than one type of relaxation process is occurring in the sample

The application of this type of muon study has a number of advantages over more common methods of magnetic characterisation, as well as a few disadvantages.

2.3.10. Advantages of the μ^+ SR techniques.

- (1) This technique will only see an averaging of relaxation times, therefore it is relatively insensitive to small amounts of impurities.
- (2) The muon will only sit on a site that can reasonably stabilise it (before it decays), therefore it will only see a true representation of the local magnetic field and structure.
- (3) The muon on implantation into a magnetically favourable site, will form a weak muon - oxygen bond with a bond length of approximately 1Å, hence an idea of the possible muon site can be guessed if a good prior knowledge of the structure is known.

2.3.11. Disadvantages of the μ^+ SR techniques.

- (1) The decay time of the muon is $T_{\mu} = 2.2\mu\text{s}$, and this can not be changed. This leads to limits in the frequency resolution and therefore it means that long relaxation time phenomena cannot be examined.

- (2) A problem with the pulsed muons produced at ISIS is the average muon pulse width (@ ISIS $\tau\omega = 35$ nanoseconds), this means that the effective asymmetry is reduced on application of a high field, the pulse is given by

$$I_0 e^{-2t/\tau\omega} \quad (2.34).$$

Where I_0 is the incident muon intensity. Therefore the asymmetry is approximately

$$\frac{\varepsilon - \tau\omega^2\omega^2}{8} \quad (2.35).$$

This limited the maximum applied field to 0.1 Tesla. Hence experiments cannot be performed as a function of high magnetic field.

2.4. Solid state ${}^6\text{Li}$ magic angle nuclear magnetic resonance.

NMR spectroscopy is a technique that probes the magnetic spin energy of atomic nuclei. For elements that have a non-zero nuclear spin, such as ${}^1\text{H}$, ${}^2\text{H}$, ${}^6\text{Li}$ and ${}^7\text{Li}$, an applied magnetic field will influence the energy of the nuclei. The energy levels of the nuclei are aligned parallel or antiparallel with the applied magnetic field. The magnitude of the energy difference between parallel and antiparallel spin states is small, typically of the order of magnitude of $\sim 0.001\text{Jmol}^{-1}$ for an applied field of 1 Tesla.

Until recently, solid state NMR has yielded very limited information on the structure of solids, with broad featureless peaks were observed in solids, but recently, considerable success has been achieved. One the most noted successes have been in the field of magic angle spinning (MAS) technique. In this technique the sample is rotated at a high velocity at the critical magic angle of 54.74° to the applied magnetic field. In this technique, the number of distinctly different Li sites within the structure can be determined. Each site within the structure experiences a different local nuclear environment and hence should give a different chemical shift with

respect to the reference material. In the case of Li NMR the reference used was LiCl solution.

Although ${}^7\text{Li}$ is the most abundant isotope, ${}^6\text{Li}$ is the favoured isotope to examine for these kinds of experiments. The main contribution to line width in ${}^7\text{Li}^\circ$ NMR is the direct dipole interaction between adjacent nuclei. This leads to line broadening and hence loss of resolution, there are fewer dipole-dipole interaction in ${}^6\text{Li}$ compounds due to lower abundance. These factors are not a problem with experiments designed to probe the ${}^6\text{Li}$ nuclei. All NMR experiments were performed using a DOTY probe at the frequency of the ${}^6\text{Li}$ nuclei, on a Bruker MSL500 solid state NMR instrument.

2.5.1 Electrical property measurements.

The techniques used in this thesis were designed to probe the electronic properties of the materials. The two techniques used in this work are as follows,

- (1) A.C. Impedance spectroscopy.
- (2) A.C. Low temperature 4 probe conductivity.

2.5.2. Impedance spectroscopy.

A.C. impedance spectroscopy is a well-developed technique that has been used to investigate the electrical properties of a number of types of system, such as ceramics^{16,17} cements^{18,19} and interfacial phenomena^{20,21}.

Electrical properties can be measured using a variety of D.C. techniques, however, this approach has problems associated with it. The D.C. resistance of a material is the total of all of the components and deconvolution is impossible. Ionically mobile species in an applied D.C. field will drift in the direction of current flow and hence the equilibrium state of the sample is destroyed. Impedance spectroscopy has the advantage that it can be used to

[°] The quadrupole moment arises from the interaction of the nuclear spin with a non-spherically symmetric field gradient at the nucleus. This effect only exists for nuclei with spin $>1/2$.

probe such things as ionic conductivity, impurity effects, bulk, grain boundary and surface layer phenomena. MacDonald et al²² has made a more comprehensive study of impedance spectroscopy. The technique involves the application of an A.C. voltage (V) of varying frequency (f) across the sample.

$$V = V_o \sin.\omega t \quad (2.36).$$

By convention, the current (I) leads the voltage by 90°, this is known as the phase shift and has the symbol ϕ , so

$$I = I_o \sin(\omega t + \phi) \quad (2.37).$$

The impedance is given by

$$Z = \frac{V}{I} \quad (2.38).$$

Impedance is a vector quantity and can be defined using complex numbers

$$Z^* = Z' - jZ'' \quad (2.39).$$

The magnitude and direction of the complex impedance can be expressed as real (Z') and imaginary components (Z''). The impedance can be plotted by Cartesian (Z' Vs Z'') or polar coordinates ($|Z|$ Vs ϕ), and is shown in figure 2.11.

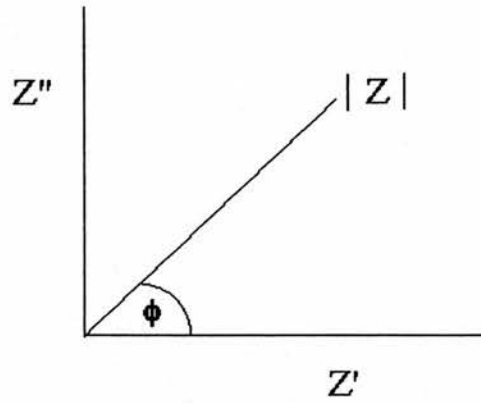


Figure 2.11. Representation of the real impedance versus the imaginary impedance.

Thus,

$$Z' = |Z| \cos \phi \quad (2.40).$$

$$Z'' = |Z| \sin \phi \quad (2.41).$$

By measuring the amplitude and phase shift (ϕ) of the current for any frequency (ω), with a fixed applied voltage (V), the impedance can be calculated. Therefore, with scanning a number of frequencies a complex impedance plot as shown below in figure 2.12 can be obtained.

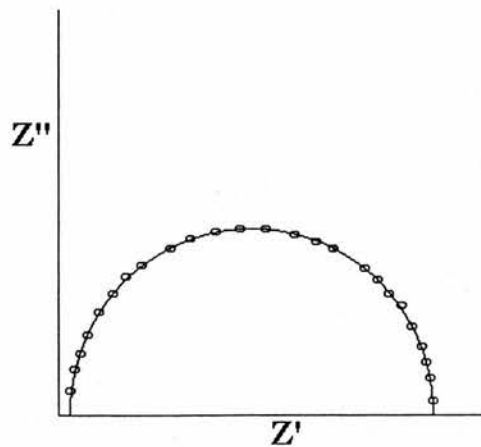


Figure 2.12. Typical impedance plot.

2.5.3 Equivalent circuits.

Ceramic materials may contain many components, such as bulk, grain boundary and surface effects which can be identified by impedance spectroscopy; each component can be considered as consisting of a number of resistors or capacitors. This combination of different elements is known as an equivalent circuit, and depending on the material will have different combinations.

The simplest equivalent circuit is obtained for either an individual ideal resistor or an ideal capacitor. For an ideal resistor, current and voltage are in phase and given by

$$R = \frac{V_0}{I_0} \quad (2.42).$$

Where R is the resistance, and hence

$$Z = R \quad (2.43).$$

Therefore for a phase shift, ϕ , figure 2.13 is obtained

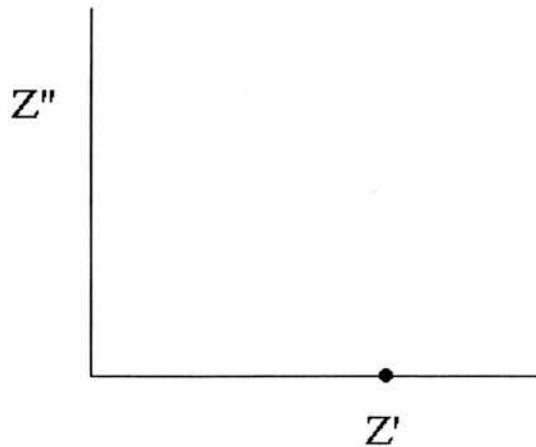


Figure 2.13. Complex impedance plot of an ideal resistor.

For an ideal capacitor, the capacitance(C) is given by

$$C = \frac{q}{V} \quad (2.44).$$

Where q is the stored charge (C) and V is the voltage across the capacitor.

$$I = \frac{dq}{dt} = C \left(\frac{dV}{dt} \right) \quad (2.45).$$

For a capacitor, the current by convention leads the voltage by 90° out of phase, and therefore current I can be determined from

$$I = \omega CV_o \sin \left(\omega t + \frac{\pi}{2} \right), \sin ce \phi = 90^\circ$$

$$\Rightarrow I_o = \omega CV_o \quad (2.46).$$

An ideal capacitor allow the flow of an A.C. current but blocks a D.C. current

$$Z^* = \frac{1}{j\omega C} \quad (2.47).$$

Producing the complex plane plot as shown in figure 2.14

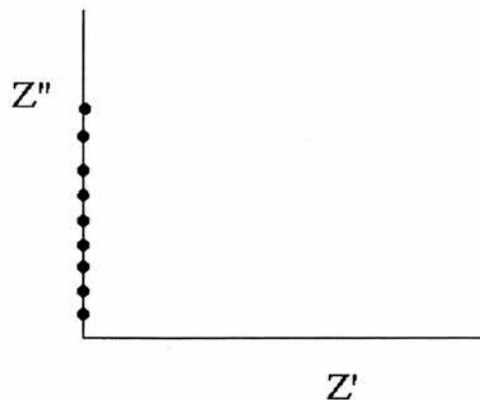


Figure 2.14. Complex impedance plots for an ideal capacitor.

A resistive element and a capacitive element in parallel can model most components, e.g. bulk. The complex impedance of a parallel RC element is defined as

$$\frac{1}{Z_T^*} = \frac{1}{Z_1^*} + \frac{1}{Z_2^*} \quad (2.48).$$

By varying the frequency, a complex impedance plot, such as that shown in figure 11 is obtained. When $\omega RC = 1$, a maximum in Z'' has been reached and at this point

$$Z' = Z'' = \frac{R}{2} \quad (2.49).$$

From this simple treatment, the resistance and capacitance of an unknown component can be determined from real and imaginary impedance over a wide frequency range. The equivalent D.C. resistance is equal to the intercept on the Z' (real) axis. The capacitance can be calculated from the relationship

$$\omega RC = 1 \quad (2.50).$$

Where ω is the frequency at Z'' maximum. In addition to the complex plane analysis described above, a plot of imaginary impedance versus frequency can yield important information that may not have been apparent by complex plane analysis. This method allows for the separation of poorly resolved semicircles by means of their differences in capacitance. Therefore it is possible to determine the degree of sintering in a material.

2.5.4. Capacitance values.

Capacitance value can be obtained from any RC element and gives an indication of the type of component being measured and are presented below in table 2.1.

Capacitance (F)	Phenomenon responsible
10^{-12}	bulk
10^{-11}	second phase
10^{-11} to 10^{-9}	grain boundary
10^{-7} to 10^{-5}	surface layer / sample electrode interface.
10^{-4}	electrochemical reaction

Table 2.1. Capacitance value and possible assignments

The capacitance or rather the magnitude of the capacitance can provide information on the bulk and grain boundary, i.e. the degree of sintering. The conductivity of the bulk or grain boundary component can be determined from the inverse of the resistance and is quoted in Sm^{-1} or $\Omega^{-1}\text{m}^{-1}$.

$$\sigma = \frac{1}{R} \quad (2.51).$$

The activation energy for any component can be obtained by measuring the change in conductivity with temperature. The slope of the Arrhenius plot, $\log\sigma T$ versus $1/T$, allows calculation of activation energies.

$$E_A = \frac{2.303 * slope * (1.38e10^{-23})}{1.6e10^{-19}} \quad (2.52).$$

A disadvantage of impedance technique is that low resistance materials cannot be examined, due to sample inductance. Impedance data was collected using a Solartron 1260 frequency response analyzer. The 1260 was driven by Scribners Associates Zplot and Zview software.

2.5.5. Low temperature 4 probe A.C. measurements.

This method is similar to A.C. impedance spectroscopy, but omits the electrode response, we choose appropriate frequency to avoid interference with mains electricity, e.g. 333 Hz, it is primarily used for samples with low

resistance ($<1000 \Omega$), where no information on the bulk can be obtained from impedance spectroscopy. In the four probe techniques the current is forced through a sample via electrodes I and IV, and the potential difference is measured across electrodes II and III, as shown in figure 2.15.

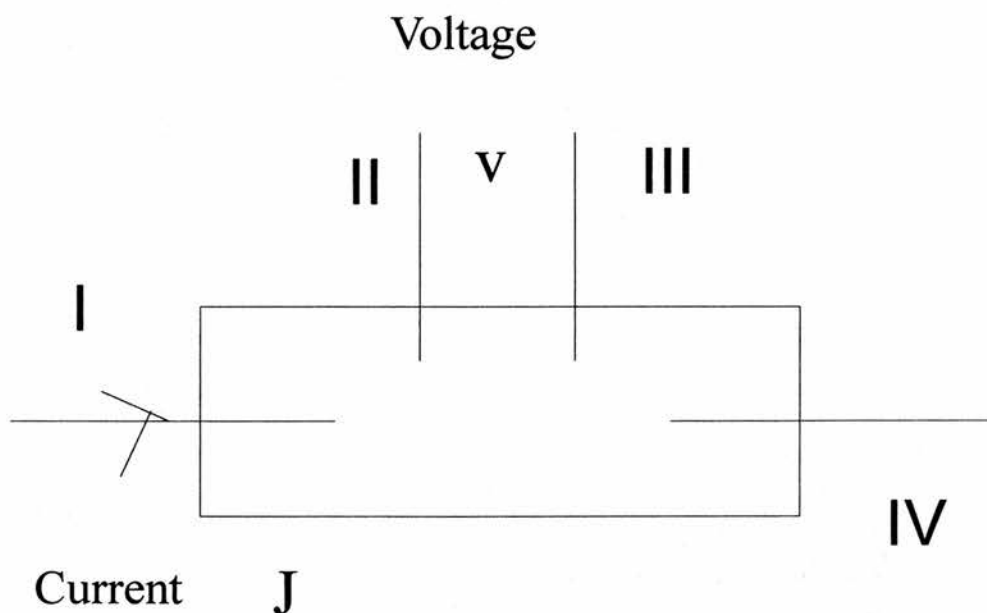


Figure 2.15. Simple electrode arrangement for four probe conductivity measurements.

Measurements are performed using a lock-in amplifier²³. Lock-in amplifiers are used to detect and measure very small A.C. signals and require a frequency reference. Typically a sample is excited at a fixed frequency (from an oscillator or function generator) and the lock-in detects the response from the experiment at the reference frequency.

The lock-in amplifier used during this study was a Stanford Research Systems, SR830 under microcomputer control. Temperature control was achieved by the use of a Oxfords Instruments ITC 503.1 temperature controller, with the experiments themselves being performed in an Oxford Instruments variable temperature insert.

All of the instruments used during this study were controlled using the Oxford Object bench software running on a microcomputer.

2.5.6 Electrodes.

Gold contacts were painted onto the samples and then fired under an inert atmosphere at 500°C for 4 hours. If the sample was being prepared for low temperature experiments, the gold contacts were polished and thin gold wires attached to the sample using silver dag. For high temperature experiments, gold or platinum electrodes were attached to the gold contacts. These wires were then carefully soldered into place. Electrodes were attached, as follows; two voltage electrodes were attached parallel to each other on the top face of the pellets. The current electrodes were placed perpendicular to the voltage electrodes on the sides of the pellet.

2.6. References.

1. A. Deschanvres, B. Raveau and Z. Sekkal, *Mat. Res. Bull.*, **6** (1969) 699.
2. D.C. Johnston, *J Low Temp Phys.*, **25** (1976) 145.
3. M Dalton, *PhD thesis*, Univ. of Cambridge, 1992.
4. D.W. Murphy, M. Greenblatt, S.M. Zahurak, R.J. Cava, J.W. Waszcak, G.W. Hull and R.S. Hutton, *Rev. Chim. Min.*, **19** 441 (1982).
5. A.R. West, *Solid state chemistry and its application.*, John Wiley and son, Chichester, (1984) 102.
6. A.R. West, *Solid state chemistry and its applications*, John Wiley and son, Chichester, (1984) 117.
7. C. Kittel, *Introduction to solid state physics*, John Wiley and son, New York, 1986 436.
8. H.M. Rietveld, *J. Appl. Cryst.* **2** (1969) 65.
9. P.J. Brown and J.C. Mathewmann, Rutherford Appleton Laboratory Report, RAL-87-010 (1987).
10. A.C. Larsen and R.B. Von Dreele, *Los Alamos Laboratory report*, NO-LA-U-86-748 (1987).
11. Profile analysis of neutron powder diffraction data at ISIS. W.I.F David, R.M. Ibberson, J.C. Mathewmann., RAL-92-032, version 2.1, May 1992.
12. B.D. Josephson, *Phys. Lett.*, **1** (1962) 251.

-
13. E. H. Brandt, *Phys Rev B.*, **37** (1988) 2349.
 14. B.D Rainford, *Aspects of transverse MuSR, Lecture notes from the training course in pulsed μ SR techniques*, S.H. Kilcoyne(editor), RAL-TR-96-007.
 15. MuSR User Guide, S.H Kilcoyne, S.R. Brown, S.P. Cottrell, S.D. Johnston and C.A. Scott, RAL-94-109, October 1994.
 16. D.C. Sinclair, *Ph.D. Thesis*, Univ. of Aberdeen, 1989.
 17. J.T.S. Irvine, D.C. Sinclair, A.R. West: *Advanced Materials* 2., **3** (1990) 132.
 18. Ping Gu, Ping Xie, J.J. Beaudoin and R. Brousseau: *Cement and Concrete Research.*, **22** (1992) 833.
 19. W.J. McCarter, S. Garvin and N Bouzid: *Journal of Material Science Letters.*, **7**, (1988) 1056.
 20. R.D. Armstrong and R A. Burnham, *J Electroanal chem.*, **72** (1976) 257.
 21. G.J. Bignold and M Fleishmann, *Electrochem Acta.*, **19** (1974) 363.
 22. J. Ross MacDonald, *Impedance spectroscopy*, Wiley and son, Chichester, UK, 1987.
 23. Stanford Research Systems, SR830 operating manual and programming references, Revision 1.3 (6/93) 1993.

Chapter 3. New studies on LiTi_2O_4 spinel.

3.1. Introduction.....	78
3.2. Effects of preparation temperature on phase purity.....	79
3.2.1. Introduction and experimental	79
3.2.2. Discussion.....	83
3.3. Neutron diffraction on LiTi_2O_4 spinel as a function of temperature.....	84
3.3.1. Experimental.....	84
3.3.2. Results. The spinel structure.....	84
3.3.3. Changes in the structure of spinel on heating.....	87
3.3.4. Discussion.....	91
3.4. Second neutron study performed on spinel at higher temperature.....	92
3.4.1. Experimental.....	92
3.4.2. Effects of high temperature on spinel structure.....	92
3.4.3. Discussion.....	96
3.5. Unknown peaks.....	96
3.6. Effects of thermal history on the T_c of LiTi_2O_4 spinels.....	100
3.6.1. Experimental.....	100
3.6.2. Magnetic Results.....	101
3.6.3. Electrical results.....	103
3.6.4. Discussion.....	104
3.7. ^6Li Magic Angle Spinning studies.....	104
3.7.1. Experimental.....	105
3.7.2. Results.....	106
3.7.3. Discussion.....	108

3.8. Conclusions.....	111
3.9. References.....	112

3.1. Introduction

D.C. Johnston¹ first observed the LiTi_2O_4 spinel superconductors while investigating the superconducting properties of Li_xTiS_2 . He observed that air exposed samples showed behaviour consistent with superconductivity in the region of 13K. Johnston believed that this apparent superconductivity was probably due to the presence of oxides rather than sulfides. On making this observation he immediately commenced studies on a number of Li/Ti/O systems and found that the superconducting phase was due to nearly stoichiometric $\text{Li}_{1+x}\text{Ti}_{2-x}\text{O}_4$ phase (where $x = 0$). He also noted that superconductivity was present in other members of the solid solution series (for compositions in the range $0 \leq x \leq 0.20$).

It was widely believed that the superconducting transition temperature of the $\text{Li}_{1+x}\text{Ti}_{2-x}\text{O}_4$ spinels could be explained using the widely accepted BCS theory². However, with the discovery by Bednorz and Mueller of superconductivity in $\text{La}_{2-x}\text{Ba}_x\text{CuO}_4$ cuprate³, some doubt was cast on this assumption, due to a number of similarities between the titanates and cuprates, these being the apparent lack of an isotope effect and more importantly the proximity to a metal insulator transition. It was felt that a common mechanism may exist that may explain superconductivity in LiTi_2O_4 spinels and cuprates. This led to the system being re-investigated to answer a number of questions concerning the superconducting behavior of this system^{4,5,6}.

Johnston reported that LiTi_2O_4 spinel went superconducting in the region of 13K, however the results presented in references 5-7 and 12 all report slightly different transition temperatures, with no apparent attempt being made to explain the differences. An additional problem encountered when studying this system is the conversion to ramsdellite if the initial firing temperature used is too high. Johnston indicated that on heating spinel samples with the composition LiTi_2O_4 , a conversion to a ramsdellite-like structure was seen with a slight difference in unit cell dimensions from that seen for $\text{Li}_2\text{Ti}_3\text{O}_7$ ⁷.

Amongst the most important experiments to be performed on this material are investigation of the effects of temperature on the LiTi_2O_4 spinel structure and determination of the optimum firing temperature required to produce a single-phase sample with a high T_c .

3.2. Effects of preparation temperature on phase purity.

3.2.1. Introduction and experimental

Samples prepared in this section were prepared in the manner described in chapter 2. In a comparative study, samples were fired for 16 hours at 750 and over the range 800 to 880°C in 10° intervals, with exception of LiTi_2O_4 ramsdellite, which was fired for 20 hours at 1000°C. All samples were fired under a 5% hydrogen atmosphere/argon atmosphere. A selection of the obtained X-ray powder patterns are presented below in figure 3.1 (a) to (g). Patterns were collected on a Philips PW3840 diffractometer, with the exception of the last pattern, which was collected on a Stoe Stadi P diffractometer.

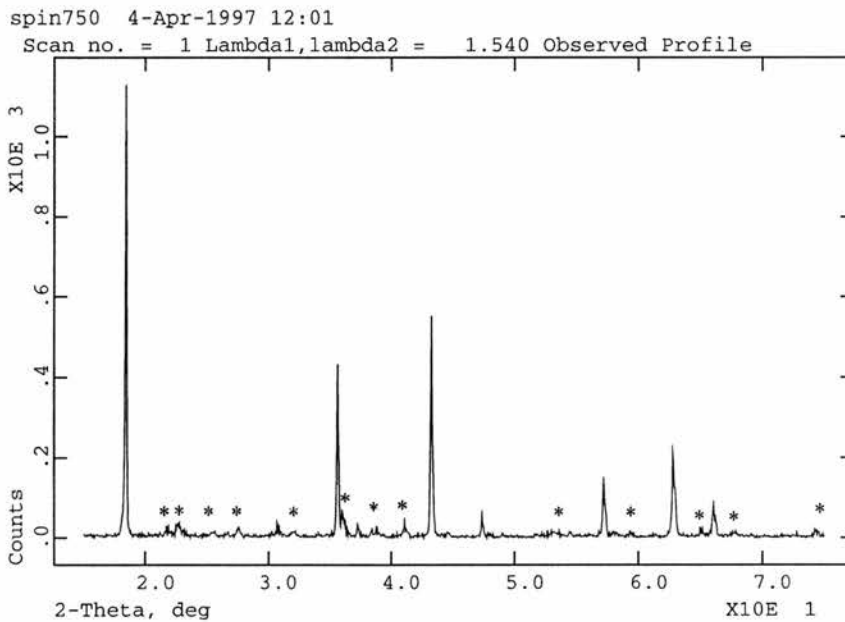


Figure 3.1 (a) Spinel sample prepared at 750°C.

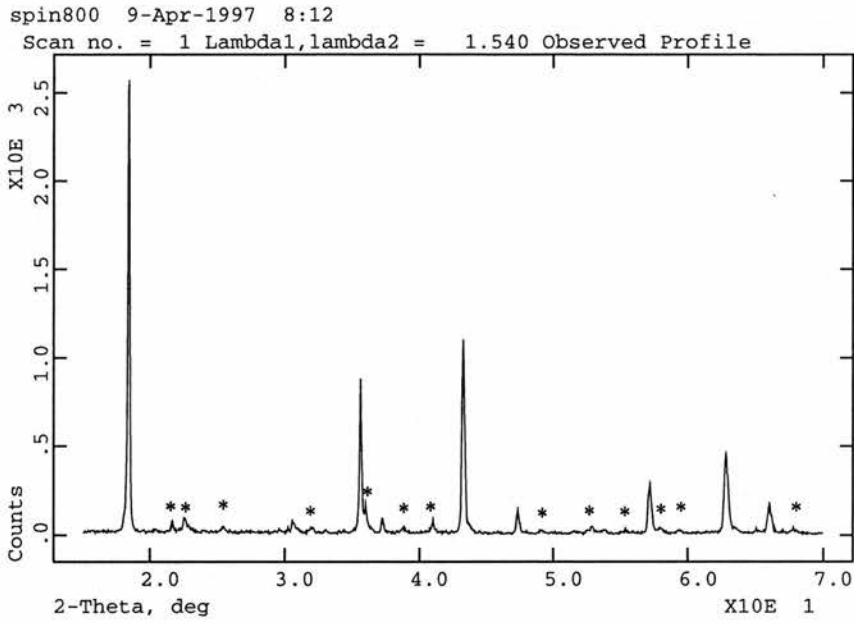


Figure 3.1(b). Spinel prepared at 800°C

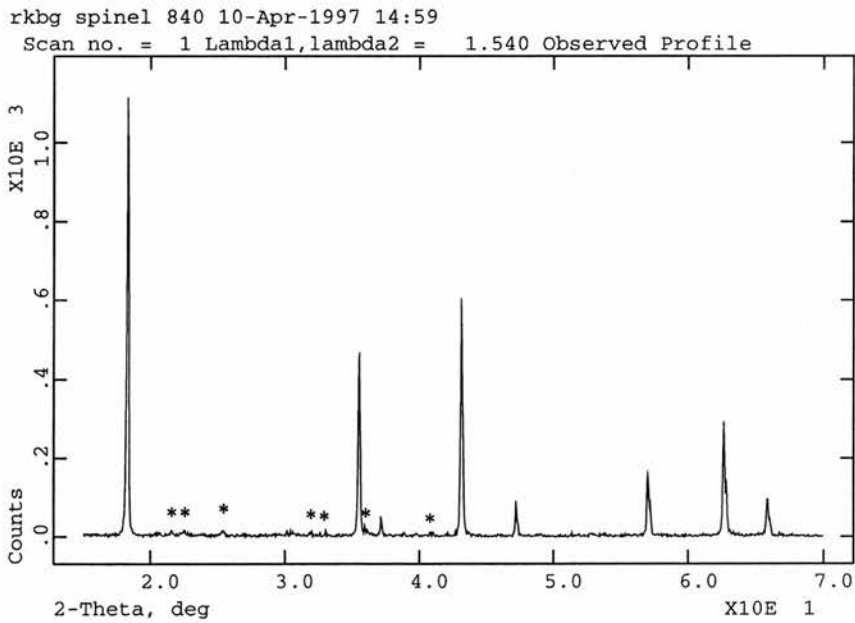


Figure 3.1(c) Spinel prepared at 840°C .

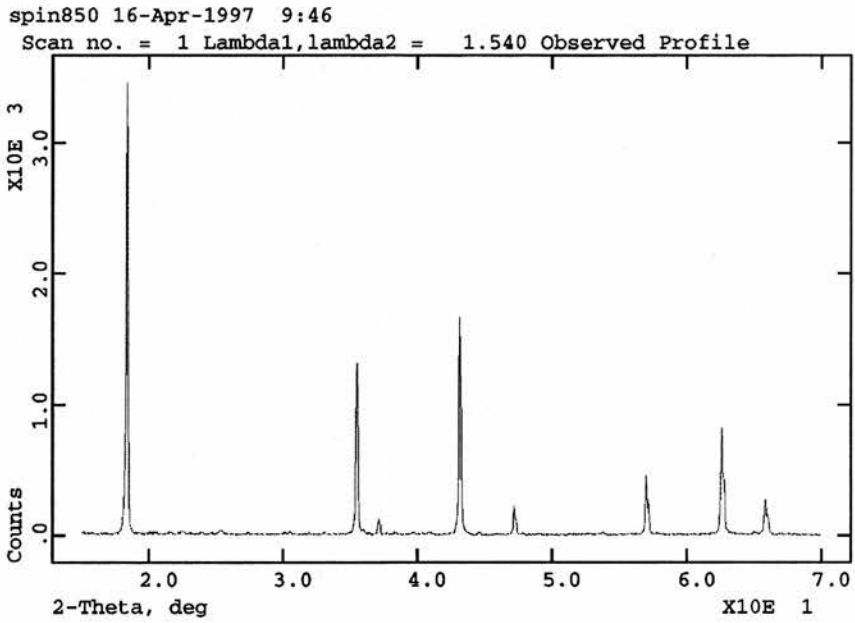


Figure 3.1(d) Spinel prepared at 850°C

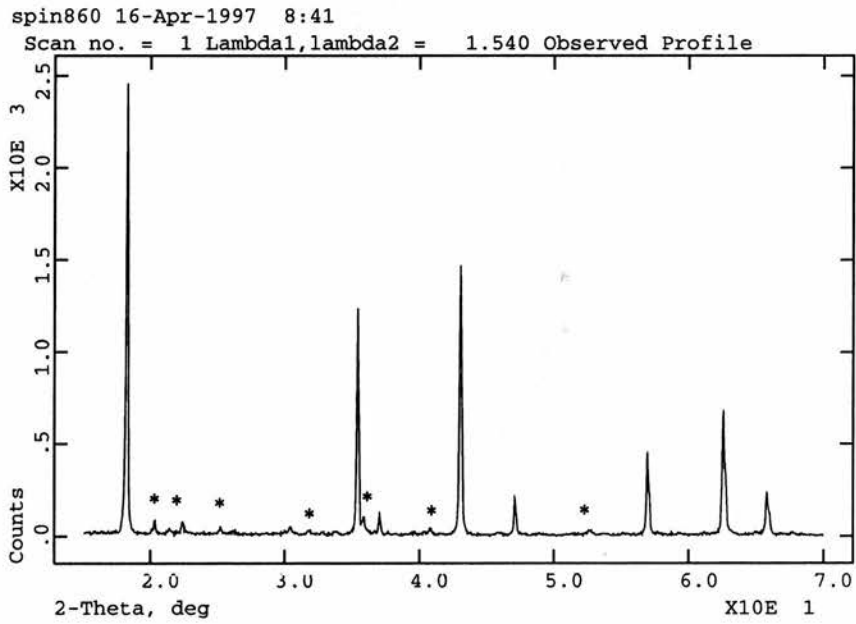


Figure 3.1(e) Spinel prepared at 860°C

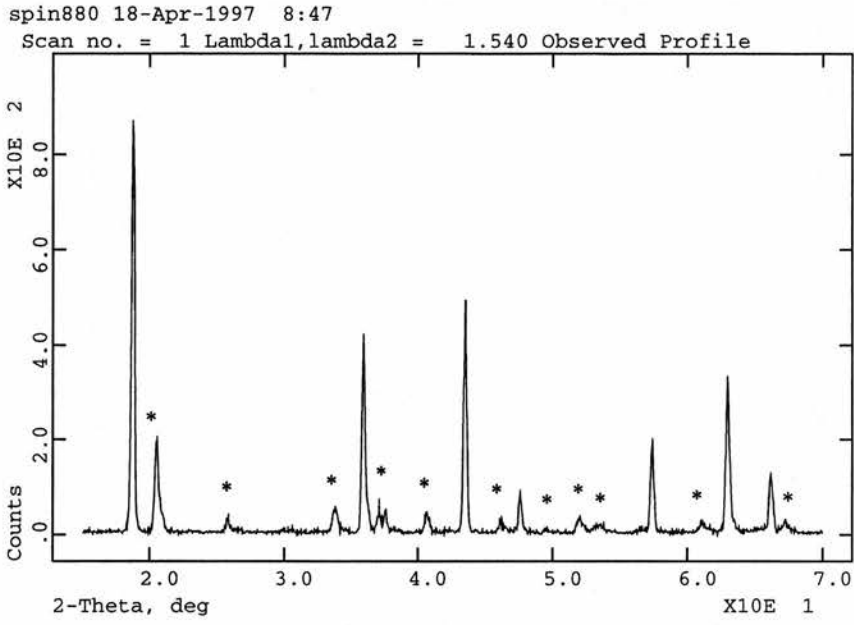


Figure 3.1(f) Spinel prepared at 880°C

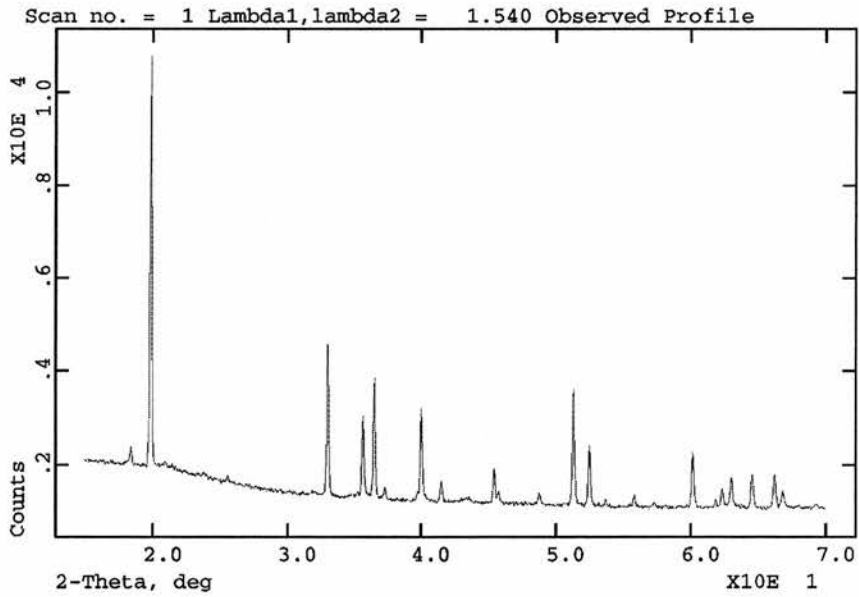


Figure 3.1(g) LiTi_2O_4 ramsdellite at room temperature

The samples prepared at 750°C , and between 800°C and 830°C contained an unknown phase which are similar in nature to that reported by Dalton⁵, several attempts were made to determine the nature of the impurity phase, with little success. The impurity peaks are marked with a *. However, samples prepared at 840 and 850°C , were found to be of good phase purity. It was noted that impurities were present in the sample prepared at 860 , 870 and 880°C . The pattern collected for the sample fired at the 880°C also shows the presence of two phases, the main phase is spinel with the second phase thought to be ramsdellite. The nature of the impurity phase will be examined at a later stage in this chapter.

3.2.2. Discussion.

Examination of the literature concerning the effects of preparation temperature on the LiTi_2O_4 spinel suggests that samples could be prepared in the temperature range^{8,5} 860 to $890 \pm 10^\circ\text{C}$, however this study suggests that this is not the case. The powder patterns collected indicate that LiTi_2O_4 spinel of high phase purity can only be prepared in a narrow temperature range, this temperature range seems to be 840 - 850°C ^a.

Johnston⁹ and Dalton⁵ indicated that the ramsdellite was single phase in the region of 940°C , but did not indicate at what temperature the spinel converts to ramsdellite. The powder patterns collected during the course of this study suggest that spinel starts to convert to ramsdellite in the range of 860 to 880°C .

^a This is subjective as exact furnace temperatures can be difficult to reproduce in different laboratories.

3.3. Neutron diffraction on LiTi_2O_4 spinel as a function of temperature.

3.3.1. Experimental.

The sample was prepared according to the method described in chapter 2 and initially examined using X-ray powder diffraction. X-ray investigations were performed using a Stoe Stadi P diffractometer for data collection and the GSAS Rietveld software¹⁰ for structural refinement. Time Of Flight neutron powder diffraction was performed on the high intensity medium resolution Polaris diffractometer situated at the ISIS neutron facility, Rutherford Appleton Laboratories, Didcot, Oxon, UK.

A pattern of LiTi_2O_4 spinel was collected at room temperature in a standard vanadium sample can. The pattern was collected for 4 hours (700 μAh) and used to provide a starting point for the refinements. The sample was then heated under vacuum in a vanadium furnace, increasing temperature in a stepwise fashion up to 925°C. Data were collected at a number of temperatures in the range 200 - 800°C and then in 25°C steps up to 925°C. At temperatures of 800°C and above the data were collected in three segments at each temperature, so that any changes could be investigated, as it was unknown exactly when spinel converts to ramsdellite. The sample was exposed to the neutron beam at each temperature / time for approximately 45 minutes (300 μAh after equilibrating at that temperature for 15 minutes. Rietveld refinement was performed using the CCSL software packages running on the ISISE HUB computer^{11,12}. Refinement of the neutron powder patterns was performed on data collected from the backscattering detectors ($135^\circ < 2\theta < 160^\circ$).

3.3.2. Results. The spinel structure.

Both neutron and X-ray powder diffraction were used to determine the initial structure of the spinel. From combined X-ray and neutron refinement, the unit cell was found to be 8.4046(2) Å which is in good agreement with the values

of 8.404Å reported by Lambert¹³ and 8.405Å by Johnson for LiTi₂O₄, although a slightly higher value has been reported by Dalton⁵. Initial Ti occupancy used during the Rietveld analysis of the neutron powder patterns was obtained from X-ray refinement. Refinement of the spinel structure confirmed the composition as being close to LiTi₂O₄. The crystallographic data obtained during these refinements are presented below in table 3.1.

Crystal system	Cubic
Space group	Fd3m ^b
a(Å)	8.4046(2)
Rwp (%)	5.83
Rp (%)	4.81
O u parameter	0.26251(4)
Li ITF^c	0.46(6)
Ti ITF	0.37(2)
O ITF	0.34(1)
Li 8a site occupancy	1
Ti 16d site occupancy	0.975(1)

Table 3.1- Crystallographic data obtained for LiTi₂O₄ spinel at room temperature.

Although models with Li on the 16d site were tested, no evidence was obtained to support such cross-substitution. The final R-values obtained from the neutron refinement of the spinel starting material was Rwp = 5.83 % and Rp = 4.81 %, this indicated that the refined pattern was a relatively good fit to the experimental model. The refined X-ray and neutron powder pattern is presented below in figure 3.2.

^b Refinement performed using Fd3m setting 2.

^c B temperature factors used not u, B can be related to U temperature factors using $B_{iso} = 8\pi^2 U_{iso}$.

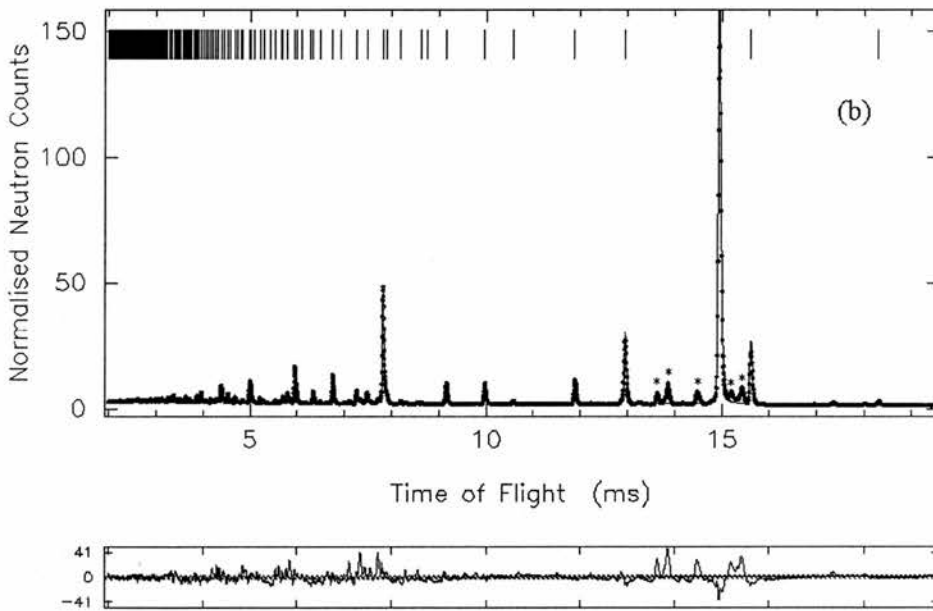
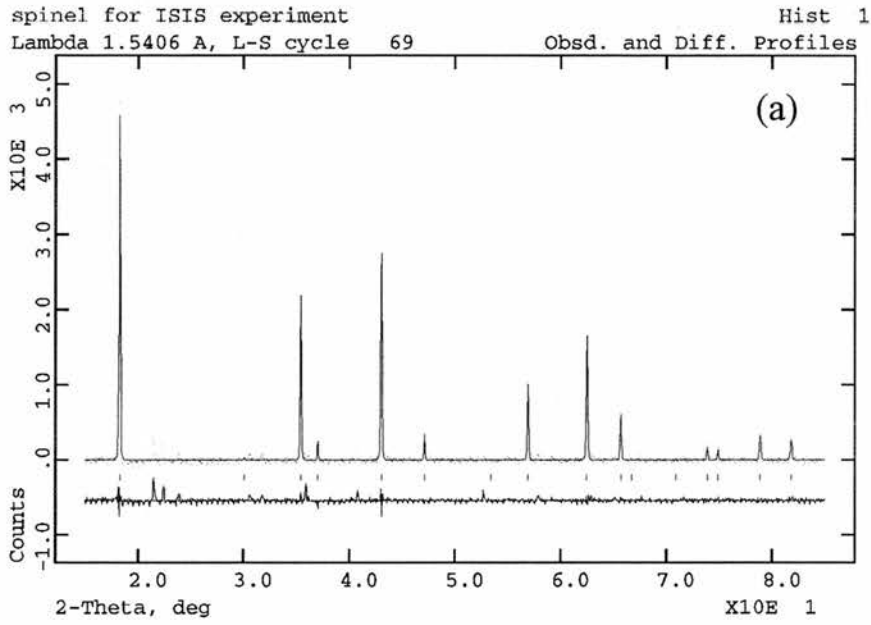


Figure 3.2(a) Refined X-ray powder pattern for LiTi_2O_4 spinel. (b). Refined neutron powder pattern collected for LiTi_2O_4 spinel at room temperature.

As can be seen from the X-ray powder pattern presented above in figure 3.2(a), the sample examined was of a good quality, although a second phase was present. The d-spacings of the unknown peaks will be more fully examined at a later stage. The two peaks present in the X-ray powder pattern at approximately 4.14 and 3.74 Angstroms are due to the Vaseline used during sample mounting. The refined neutron powder pattern shown in figure 3.2(b) indicates that a slight second phase is present in the sample at room temperature. The origins of the second phase are not known, with the d-spacing of the most intense second phase peaks as obtained from neutron experiments being presented in table 3.2. A fuller treatment of the obtained impurity peaks will be made at a later stage in this chapter

Peak number	2 θ	T.O.F (μ S) *10 ³	d-spacing (\AA)
1	43.038	13.583	2.101
2	40.078	13.833	2.248
3	38.303	14.416	2.348
4	36.511	15.166	2.459
5	35.833	15.350	2.504

Table 3.2. d-spacings of the five most intense peaks obtained from neutron powder diffraction as shown in figure 3.2(b).

3.3.3. Changes in the structure of spinel on heating

The most obvious change in the structure of the spinel on heating to 900°C was a linear expansion of the unit cell, as shown in figure 3. The coefficient of thermal expansion was found to be $1.58(1) \times 10^{-5} \text{ K}^{-1}$ up to 900°C. At 925°C, the unit cell edge was observed to deviate from linear behaviour, figure 3.3, perhaps indicating a change in the spinel phase composition. Above 925°C, there was no evidence of spinel in the sample.

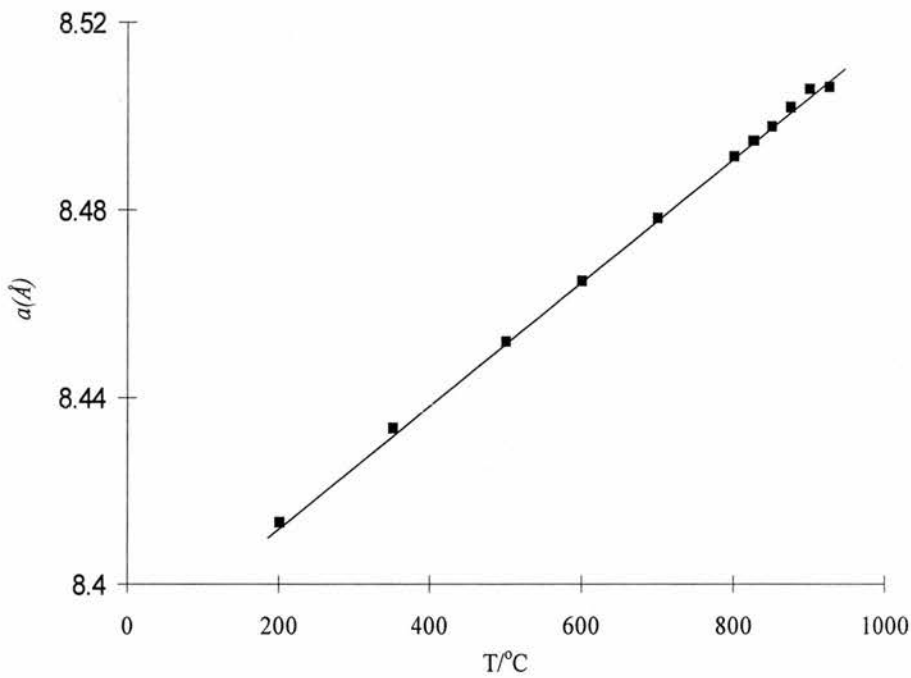


Figure 3.3. Plot of unit cell dimensions of LiTi_2O_4 spinel versus temperature.

The change in unit cell edge was not the only change observed in the spinel structure as a function of temperature. Clear anomalies were observed in both the isotropic temperature factor (ITF) and the site occupancy of the Li 8a site at elevated temperatures. As these two parameters are interdependent, two different models were utilized to examine the anomalies in more detail.

In the first model, the occupancies of all sites were assumed to be constant in the temperature range 25 to 900°C , and the isotropic temperature factors (ITF) were refined for O, Ti and Li respectively. The ITFs obtained for O, Ti and Li are presented below in figures 3.4(a) and 3.4(b). The ITFs for oxygen and titanium were observed to increase linearly with increasing temperature; however, the ITF for lithium deviated sharply from linearity at about 500 and showed a maximum at 700°C . In the second model, the occupancy of Li and Ti on the 8a and 16d sites, respectively, were refined assuming that all the ITFs vary linearly with temperature, as has previously been predicted¹⁴ and observed in other oxides¹⁵. A line of best fit for the temperature factors presented in figure 3.4(a) was used to obtain estimated values of ITF, ignoring the anomalous intermediate temperature range for Li.

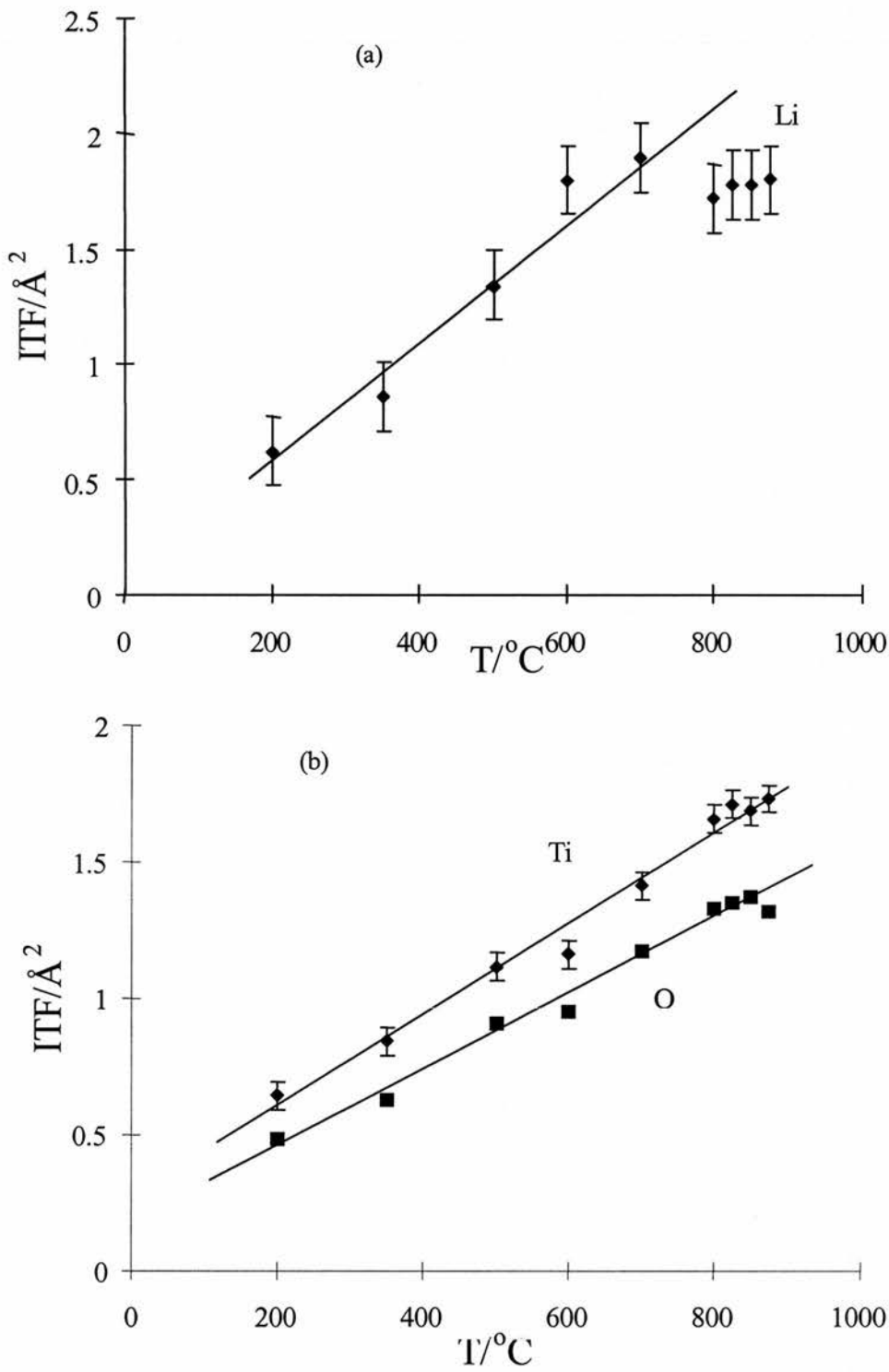


Figure 3.4(a). The obtained isotropic temperature factors for 8a Li assuming constant site occupancy. (b). The obtained isotropic temperature factors for Ti and assuming constant site occupancy.

The resulting variations in Li and Ti site occupancies factor are presented in figure 3.5(a) and (b). Although Ti occupancies remain relatively constant throughout the experiment, the Li occupancy of the 8a site clearly drops by $\sim 8\%$ above 500°C . Fourier difference mapping was performed and indicated that the missing Li had probably moved to the 16c site, however it was found not possible to refine the Li occupancy of this site.

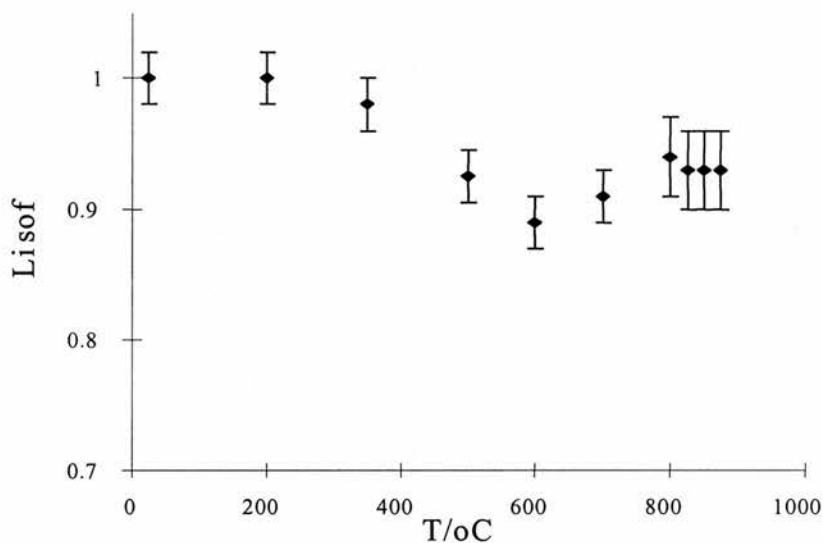


Figure 3.5(a). Obtained Li 8a site occupancies as a function of temperature assuming linear variations in isotropic temperature factors.

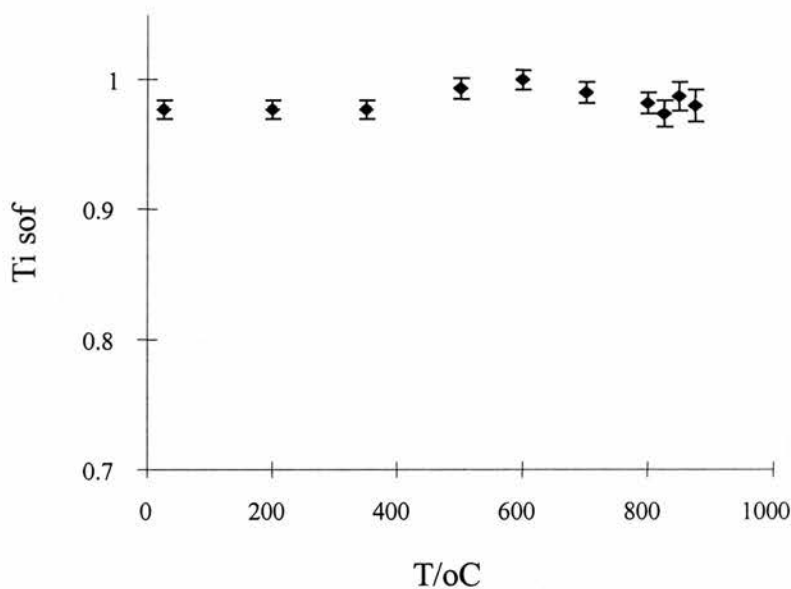


Figure 3.5(b). Obtained Ti site occupancies as a function of temperature assuming linear variation in isotropic temperature factors.

3.3.4. Discussion.

The samples examined during this section of works were prepared according to the preparation conditions described by Dalton in reference 5. It was seen from the refined powder patterns that a second phase of unknown composition was present at room temperature. It is also well known, that high quality single phase samples of $\text{Li}_{1+x}\text{Ti}_{2-x}\text{O}_4$ are difficult to prepare, indeed the main aim of the work presented in references 5 and 16 was to prepare high quality samples of LiTi_2O_4 spinel. Examination of these works also indicates problems associated with obtaining very high phase purity.

The results obtained during this section of work have shown that at temperatures well below the transition temperature some Li is observed to migrate from the tetrahedral 8a site, probably moving to the 16c site. This initially affects the Li ITF values, which became anomalously large as Li start to move from their 8a site. At higher temperatures the ITF values were seen to stabilize and the Li occupation of the 8a site has been seen to drop by 8-10%. This change in lithium distribution within the spinel structure with temperature may have important implications for the superconducting properties. Samples of LiTi_2O_4 prepared by rapid cooling are likely to have significantly different Li distributions in their structures to those prepared by normal furnace cooling and this may affect their properties.

From the results presented above, it was decided that a number of new studies should be performed. These are highlighted below.

1. A second neutron study, with the specific aim of examining the high temperature behaviour of the Li distribution within the spinel structure.
2. The effects of thermal history on LiTi_2O_4 spinel, using magnetic, electrical and NMR magic angle spinning techniques.

3.4. Second neutron study performed on spinel at higher temperature.

3.4.1. Experimental.

A sample of LiTi_2O_4 spinel was prepared in accordance with the method described in chapter 2. Time Of Flight powder neutron diffraction was performed on the General Purpose Powder Diffractometer (GPPD) situated at the Intense Pulse Neutron Source (IPNS), Argonne National Laboratory, Illinois, USA. All of the experiments were performed under vacuum in a vanadium furnace, with the results obtained in the temperature region 840-900°C being presented below. The unit cell dimensions are presented in the range 840 to 900 and presented in figure 5. As the quantity of spinel is diminishes rapidly after the onset of the transformation to ramsdellite, only crystallographic data obtained from the patterns collected at 840 and 850°C is presented.

Refinement of the models was performed using the GSAS¹⁰ software running on a personal computer. The data sets were collected on the backscattering detector banks (148°)¹⁷, with the Time of flight range 3000 to 29000 microseconds being used.

3.4.2. Effects of high temperature on spinel structure.

The unit cell of LiTi_2O_4 spinel was determined in the temperature range 840-900°C, after which it was found that the total amount of the spinel present became too low to refine properly. The unit cell was seen to vary in a linear fashion in the region 840-870°C, after which there is a slight change in the gradient of the line, which may indicate a phase change is occurring in this temperature region. The unit cell edges obtained during this portion of experiments are in good agreement with the results presented in the previous section. These results are presented below in figure 3.6.

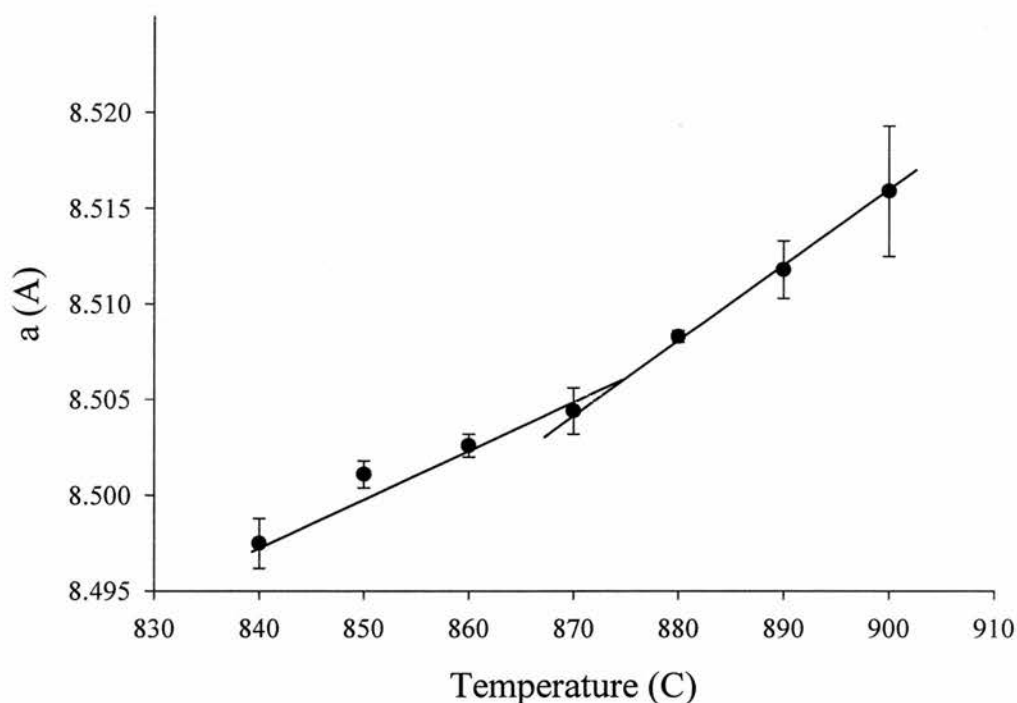


Figure 3.6. Obtained unit cell dimension of the LiTi_2O_4 spinel in the temperature range 840 to 900°C. Lines used as a guide to the eye.

The results presented in the previous neutron experiment performed at ISIS, indicated anomalous trends in the ITF and site occupancy factors for the Li located on the 8a site. In addition to the Li found on the 8a site, lithium was thought to be present on the 16c site, although it could not be refined.

Refinement of the models for the powder patterns collected at IPNS indicated that the 8a had an occupancy lower than one at 840°C. In an attempt to determine the presence of the missing Li, Fourier mapping was attempted and it was found that Li was probably located on the 16c site at (0 0 0). Subsequent refinement of the model indicated that octahedral 16c site was partially occupied. These have been referred to Li1 (8a) and Li2 (16c) respectively. Presented in table 3.3. is the obtained crystallographic data obtained from refinement of spinel at 840 and 850°C.

	840°C	850°C
Space group	Fd3m	Fd3m
a(Å)	8.4975(13)	8.5011(7)
Rwp (%)	7.13	6.87
Rp (%)	4.29	4.03
Li1 ITF	2.7(4)	2.7(5)
Li2 ITF	6.9(3)	5.1(5)
Ti ITF	2.49(12)	2.42(13)
O ITF	2.61(6)	2.07(6)
Li1 8a site occupancy	0.78(3)	0.80(4)
Li2 16c site occupancy	0.12(2)	0.11(3)
Oxygen u parameter	0.26307(14)	0.26302(14)
Spinel fraction	1	0.21
Ramsdellite fraction.	0	0.79

Table 3.3. Results obtained from refinement of spinel structure at 840 and 850°C. Temperature factors multiplied by 100.

Presented below in figure 3.7(a) is the refined neutron patterns for LiTi_2O_4 spinel at 850°C. The results obtained above indicate that at 840 and 850°C, the occupancy of the 8a site is approximately 80%, with the balance of lithium to be found on the 16c site. Presented in figure 3.7(b) is a difference Fourier map showing unfitted intensity.

The value obtained for the **u** parameter is in accordance with the values obtained for other spinels¹⁸, with the values presented above showing little change with increasing temperature. Some impurities were seen to be present in the collected patterns, and will be treated more fully at a later stage in this chapter.

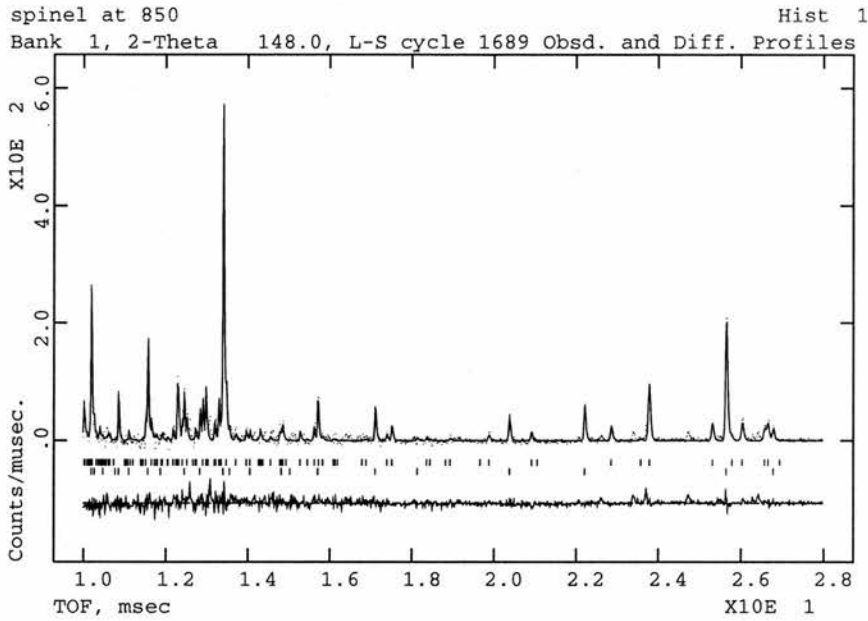


Figure 3.7(a). Refined powder pattern for LiTi_2O_4 ramsdellite collected at 850°C . Top set of tick marked for ramsdellite, lower set for spinel.

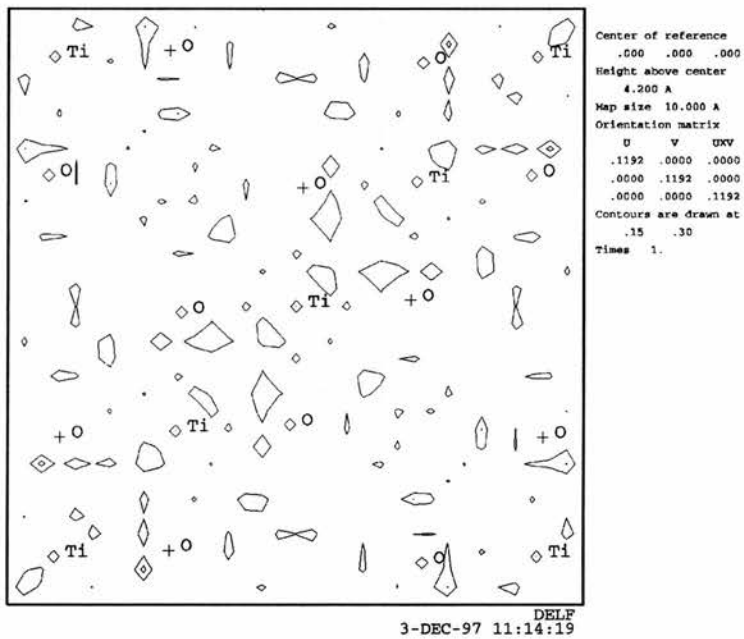


Figure 3.7(b) Difference Fourier map obtained at 840°C .

3.4.3. Discussion.

As mentioned previously, the aim of this section of work was to re-examine the effects of temperature on the LiTi_2O_4 spinel at higher temperatures. A deviation was seen in the unit cell edge of the spinel as function of temperature, with the gradient of the slope seen to change in the region of 870°C . This was not seen in the results presented previously in this chapter. This change in gradient may signal that the spinel structure is undergoing some changes in structure. This would also manifest itself as a change in volume which could indicate a second order phase transformation occurs as the spinel converts to ramsdellite. One of the most important aspects of this study was the location of Li on a second site within the spinel structure, as previous work has shown that the 8a site is not always fully occupied with some lithium apparently “missing”. It was found that the 16c site contained this “missing” lithium. Attempts to refine cross substitution at these temperatures were found to give unstable refinements.

3.5. Unknown peaks.

It was noted during the X-ray experiment presented in section 3.2 and both of the neutron studies (sections 3.3 and 3.4 respectively) that an unknown phase was present in all of the samples of spinel to some extent. A number of common peaks were found to be present in both neutron and X-ray experiments. The position of these peaks in the 2-2.5 Å range is presented below in table 3.4(a), with the intensities of these peaks presented in table 3.4(b).

	1	2	3	4	5	6	7
ISIS@RT*	2.211	2.247	-	2.349	-	2.464	2.501
IPNS@RT*	2.200	2.231	-	2.359	2.399	-	-
IPNS@750*	2.223	2.253	-	2.363	-	-	2.489
IPNS@840*	2.227	2.258	2.331	-	2.420	-	2.492
Spinel 750	2.198	-	2.319	2.344	-	-	2.492
Spinel 800	2.198	-	2.318	-	-	-	2.493
Spinel 810	2.196	-	2.313	-	-	-	2.485
Spinel 820	2.200	-	2.316	-	-	-	2.491
Spinel 830	2.205	-	2.323	-	-	-	2.499
Spinel 840	2.202	-	-	-	-	-	2.497
Spinel 850	-	-	-	-	-	-	-
Spinel 860	2.209	-	-	-	-	-	2.507
Spinel 880	2.216	-	-	-	2.394	-	-

*Table 3.4(a). Unassigned peak positions from X-ray and neutron diffraction in the 2 to 2.5 Angstroms d-spacing range. Experiments performed at 750 and 840 have been corrected for thermal expansion. * denoted results obtained from neutron diffraction, all of the other samples collected using X-ray diffraction.*

Examination of the work performed by Dalton⁵ showed the presence of a similar unknown in the samples he called “Batch 1”. Dalton never determined the composition of this unknown. Whether these peaks are related to an intermediate phase or simply impurities could not be determined without reasonable doubt, and hence the origins are unknown.

	1(%)	2(%)	3(%)	4(%)	5(%)	6(%)	7(%)
ISIS@RT*	4.2	7.2	-	4.8	-	5.4	6.0
IPNS@RT*	1.5	2.9	-	2.3	-	-	3.1
IPNS@750*	5.5	13.8	-	9.1	-	-	11.5
IPNS@840*	6.0	11.7	-	7.5	-	-	12.1
Spinel 750	1.8	-	2.7	4.2	-	-	6.5
Spinel 800	2.7	-	1.5	-	-	-	6.8
Spinel 810	1.8	-	4.0	-	-	-	4.9
Spinel 820	1.1	-	0.5	-	-	-	4.2
Spinel 830	2.4	-	1.8	-	-	-	4.3
Spinel 840	0.19	-	-	-	-	-	2.1
Spinel 850	-	-	-	-	-	-	-
Spinel 860	1.7	-	-	-	-	-	4.2
Spinel 880	4.2	-	-	-	4.5	-	-

*Table 3.4(b). Unassigned peak intensities from X-ray and neutron diffraction in the 2 to 2.5 Angstroms d-spacing range, taken relative to the (1 1 1) in X-ray and (2 2 2) in neutrons. * denoted results obtained from neutron diffraction, all of the other samples collected using X-ray diffraction.*

Examination of intensities obtained during the room temperature experiments performed at ISIS and IPNS show a number of similarities. However the intensity of the peaks seen in the IPNS experiments as a function of temperature show an increase in intensity from room temperature to 750. This suggests that the unknown decrease as a function of increasing sample temperature. It is felt that the results obtained at 750 and 840 are slightly suspect and maybe due to slight sample oxidation on heating, as it was noted that the furnace was relatively unstable as the temperature was increased.

Presented below in table 3.4(c) is a selection of lithium titanates and titanates with peaks in the range of 2 to 2.5 Å, with the relevant JCPDS number shown.

Phase	JCPDS	1	2	3	4	5	6	7
$\text{Li}_2\text{TiO}_3\text{-m}$	33-831	-	2.254	-	-	2.404	-	2.502
$\text{Li}_2\text{Ti}_4\text{O}_9\text{-m}$	33-0832	-	-	-	2.380	2.417	-	2.502
$\text{Li}_2\text{Ti}_3\text{O}_7\text{-o}^*$	34-393	2.222	2.243	-	2.388	-	2.457	2.507
$\text{Li}_2\text{Ti}_3\text{O}_7\text{-h}$	35-52	2.23	-	2.33	-	-	-	-
$\text{Li}_2\text{Ti}_6\text{O}_{13}\text{m}$	37-952	-	2.276	2.359	2.386	-	-	-
$\text{Li}_2\text{Ti}_3\text{O}_7\text{-m}$	40-303	-	-	2.312	2.371	2.386	2.478	-
$\text{LiTiO}_2\text{-h}$	40-1053	-	-	-	-	2.390	2.453	-
$\text{Ti}_3\text{O}_5\text{-o}$	9-309	-	-	-	2.37	2.42	-	-
TiO-h	12-754	-	-	-	-	2.396	-	2.495
$\text{Ti}_6\text{O}_{11}\text{tri}$	18-1401	2.226	2.254	2.33	2.386	-	2.488	-
$\text{Ti}_4\text{O}_7\text{tri}$	18-1402	2.225	-	2.306	2.349	2.423	2.477	2.508
$\text{Ti}_7\text{O}_{13}\text{tri}$	18-1403	2.218	2.287	2.327	-	2.404	-	-
$\text{Ti}_8\text{O}_{15}\text{tri}$	18-1404	2.216	-	2.312	2.363	2.418	2.487	2.505
$\text{TiO}_2\text{-o}$	21-1236	-	2.262	-	2.396	2.450	-	-
$\text{TiO}_2\text{-t}‡$	21-1272	-	-	2.32	2.378	2.431	-	-
$\text{Ti}_3\text{O}_5\text{-m}$	23-606	2.203	-	-	-	2.410	2.472	-

Table 3.4(c). Selection of possible phases to be found in X-ray and neutron studies. *Similarly LiTi_2O_4 ramsdellite. ‡ anatase reverts to the rutile form of TiO_2 above 700°C , so can be discounted. Codes are m=monoclinic, tri=triclinic, o=orthorhombic, h=hexagonal and t=tetragonal. Intensities over 10% presented in bold type.

The peaks obtained from the X-ray and neutron experiments were compared to the peaks of the phases presented above. It was found that none of the above was a good match, with the files 18-1401 to 18-1404 or more probably a combination of these providing the best match. These phases belong to a family of phases known as the Magneli phases¹⁹. They form a series of closely related phases with very similar formulae and structure instead of the more usual continuous solid solution series. Further studies will have to be performed in order that the unknowns can be examined more fully.

3.6. Effects of thermal history on the T_c of LiTi_2O_4 spinels.

It was shown in sections 3.3 and 3.4 that the lithium distribution on the 8a tetrahedral sites varies as a function of temperature. Therefore the differences in T_c reported in the literature could in some way be related to the cooling and annealing regime used during the synthesis. To determine whether this was the case, a number of samples were examined, with the T_c being determined as a function of annealing temperature.

3.6.1. Experimental.

Three samples were prepared from one batch for the magnetic studies and another three sample were prepared for the electrical measurements according to the method described in chapter 2. In order to examine the effects of annealing on the superconducting properties it was found necessary to quench some of the samples. The samples examined using magnetic measurements were annealed and then quenched from 300 and 500°C with a third sample prepared using a normal furnace cooling regime^d. Approximately 100mg of sample were used for all experiments.

The superconducting transition temperatures were then determined using Vibrating Sample Magnetometry (VSM). All samples were cooled in zero applied field and examined using an applied field of 100 gauss. Electrical measurements were performed using 4 probe D.C. methods, with samples being annealed and quenched from 500 and 700°C, and another prepared using standard furnace cooling. The 4 terminal electrical experiments were performed using a Stanford Research Instrument SR830 DSP lock-in amplifier. The conductivity jig was an Oxford Instruments variable temperature insert, with the temperature of the insert being controlled using an Oxford Instruments ITC504 temperature controller.

^d Samples cooled by cutting power to the furnace and allowing to cool as quickly as thermal mass will allow.

3.6.2. Magnetic Results.

The superconducting transition for normal furnace cooling sample of LiTi_2O_4 spinel is presented below in figure 3.8. Closer examination indicates that the sample went superconducting in the region of 13.2 to 13.4 Kelvin. This is considered to be near the optimum transition temperature for this material.

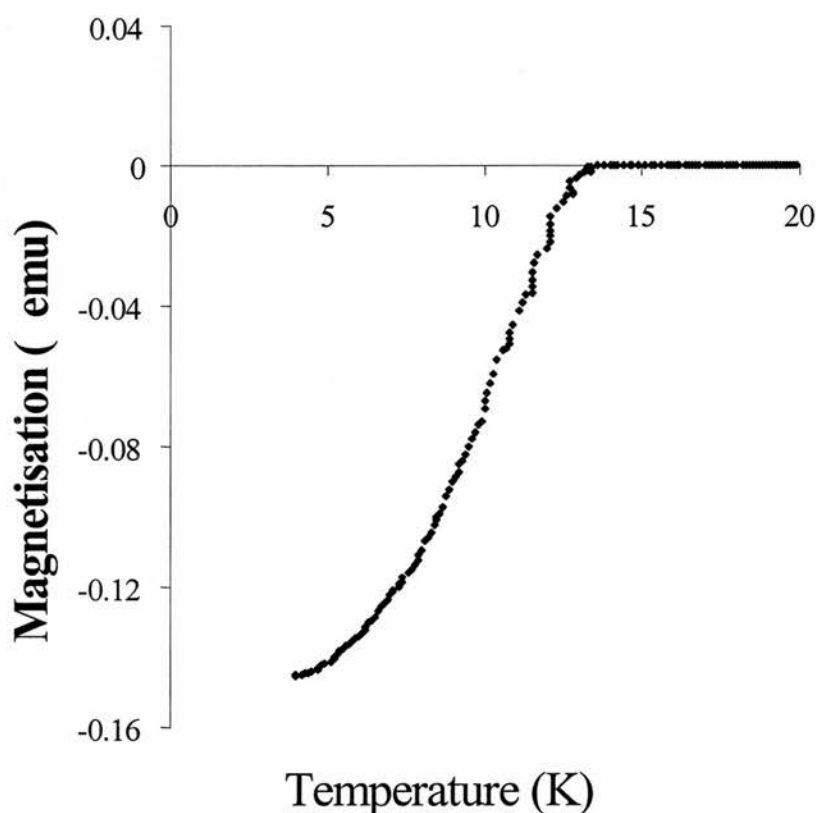


Figure 3.8. Superconducting transition obtained for the normal furnace cooling for sample of LiTi_2O_4 spinel.

The second sample was heated to 300°C and held at this temperature for approximately twelve hours and then quenched. The T_c of this sample was found to be in the region of 11.6 Kelvin, with a slight decrease in the magnitude of the magnetization also being seen (See figure 3.9). The third sample was heated to 500°C and held at this temperature for approximately twelve hours. The T_c obtained for this sample was found to slightly higher in the sample with a value of 11.7 Kelvin, but again the magnitude of the magnetization was seen to have

decreased slightly. The results obtained for this sample are presented in figure 3.10.

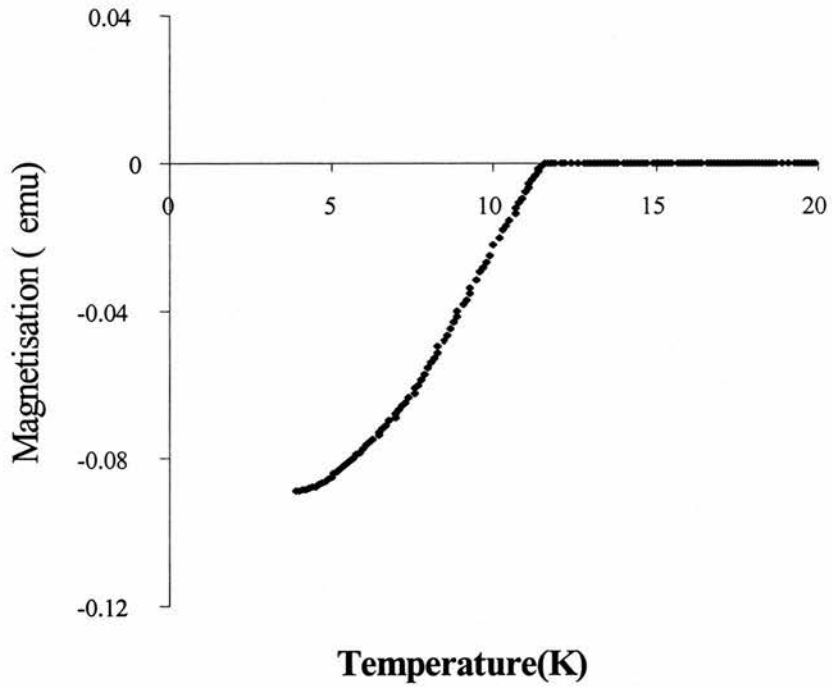


Figure 3.9. Superconducting transition of 300°C annealed and quenched LiTi_2O_4 spinel.

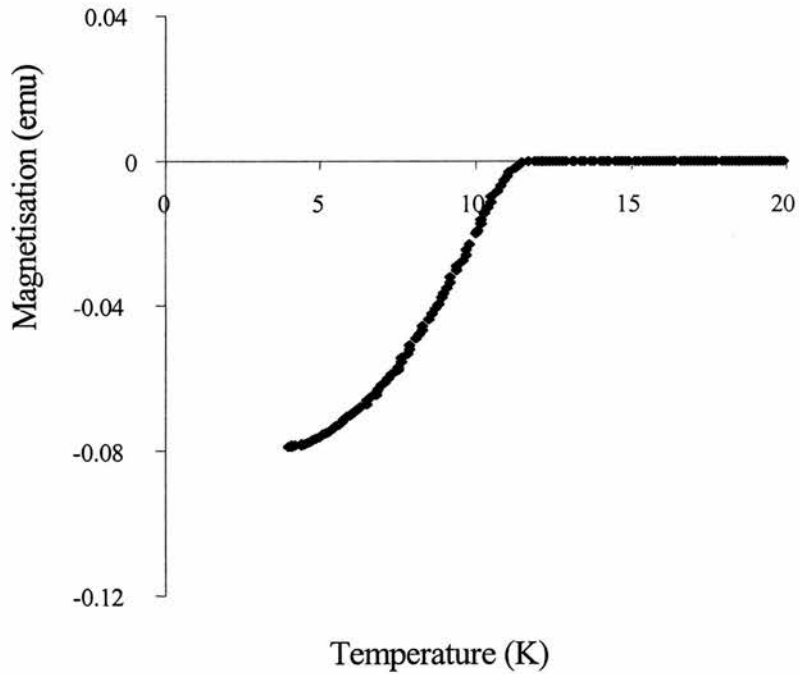


Figure 3.10. Superconducting transition of 500°C annealed and quenched LiTi_2O_4 spinel.

3.6.3. Electrical results.

The samples used in this portion of work were prepared according to the methods described in chapter 2. Three samples were examined during this section of work. These were a sample prepared using normal furnace cooling (known as nfc), a sample annealed at $\sim 400^\circ\text{C}$ overnight and then quenched (known as 400aq), with a final sample annealed at $\sim 700^\circ\text{C}$ overnight and then quenched (known as 700aq). It must be noted that the samples prepared during this section of work were somewhat larger than those used in previous sections, with 13mm pellets being prepared instead of 8mm pellets. This would mean there are differences in thermal mass, and hence differences in the cooling rates.

The results presented in this section have T_c defined as the first point at which the resistance is seen to deviate from linear behaviour. Presented in table 3.5 are the values of obtained for T_c (onset).

Sample name	$T_c(\text{onset})$
nfc	12.4
400aq	12.4
700aq	12.6

Table 3.5. Obtained superconducting transition data for the three samples examined during this study.

As can be seen from the results presented above in table 3.5, there are two noticeable differences between the magnetic and electrical data. It was noted that the T_c obtained using electrical methods are different in all of the samples examined compared to that obtained from the magnetic data. The quenched samples show a similar trend to that seen from the magnetic data, however the T_c of normal cooled sample was found to be lower than seen previously.

3.6.4. Discussion.

This portion of work indicates that the sample annealing and quenching can influence the superconducting properties of LiTi_2O_4 spinel. This could be attributed to the proposed Li migration highlighted earlier in this chapter. It must be noted from the three different magnetic measurements performed in this section of work, that the magnitude of obtained magnetisation decreases, in order from normal cooling regime $\Rightarrow 300 \Rightarrow 500^\circ\text{C}$. This decrease in the magnitude of magnetisation could be interpreted as a decrease in the volume of the superconducting fraction. The electrical results obtained show similar trends for T_c .

The apparent differences seen in these results and those obtained from magnetization cannot be fully explained, but may in some ways be due to a number of different things. Possible reasons for the difference could include the location of sample with respect to the thermocouple in the insert, grain boundaries in the samples or possible contact problems between the polycrystalline samples and the electrodes.

Samples that have lower temperature annealing are seen to have lower T_c . This is likely to be due to the proposed migration of Li as presented previously in this chapter, with the lower T_c related to the fuller occupancy of the 8a site within the spinel structure.

3.7. ^6Li Magic Angle Spinning studies.

The results presented so far in this chapter have centered on the effects of temperature and thermal history on the lithium distribution within the spinel structure. The results obtained from in-situ neutron diffraction studies have shown both 8a and 16c can be occupied by Li. Therefore these experiments were performed to determine if these changes could be examined using solid state NMR.

3.7.1. Experimental.

Samples examined during this portion of work were initially prepared according to the methods described in chapter 2, and then quenched or furnace cooled from different temperatures. The NMR experiments were performed using a DOTY probe on a Bruker MSL500 Solid State Nuclear Magnetic Resonance spectrometer. The spinning frequency used in this series of experiments was 4 kHz.

Although ⁷Li is the most abundant isotope, ⁶Li is the favoured isotope to examine for these kinds of experiments. The main contribution to line width in ⁷Li is the direct dipole interactions between adjacent lithium nuclei. This leads to line broadening, and hence a loss of resolution. This is not a problem with experiments to probing the ⁶Li nuclei, as the natural abundance of ⁶Li is approximately 7.5%, and hence these interactions are far lower. The physical properties of ⁶Li and ⁷Li are presented below in table 3.6.

Property	⁶ Li	⁷ Li
Spin	1	3/2
Magnetic moment μ (μN) ^e	1.163	4.204
Magnetogyric ratio $\gamma/10^7$ ($\text{radT}^{-1}\text{s}^{-1}$)	3.937	10.398
Quadrupole moment 10^{28}Q (m^2)	-8×10^{-4}	-4×10^{-2}
Resonant frequency (MHz)	73.3	194.0
Abundance (5)	7.42	92.58

Table 3.6. Physical properties of ⁶Li and ⁷Li isotopes.

The main aims of this series of experiments were to try and determine the effects of different cooling regimes on the ⁶Li MAS NMR signal. Four different heating and cooling regimes were used and are presented below in table 3.7.

^e μN is the nuclear magneton: $1\mu\text{N}=5.05 \times 10^{-2} \text{JT}^{-1}$.

Sample name and code	Curing conditions
Normal cooled 1 (NC1)	Standard cooling conditions ^f
Slow cooled 2 (SC2)	As NC1, but then slow cooled from 500°C at 30°C/hr
Quenched 1 (Q620)	As NC1, then annealed and quenched from ~620°C
Quenched 2 (Q700)	As NC1, then annealed and quenched from ~700°C

Table 3.7. Sample preparation conditions used during NMR experiments.

3.7.2. Results.

The results obtained during this section of work show a number of different phenomena. Examination of the observed spectra presented in figure 13, show the presence of at least two distinct peaks, with a third peak being seen in the spectrum for samples NC1 and Q700. Presented below in figure 3.11 are the observed spectra for the four different heat treatments.

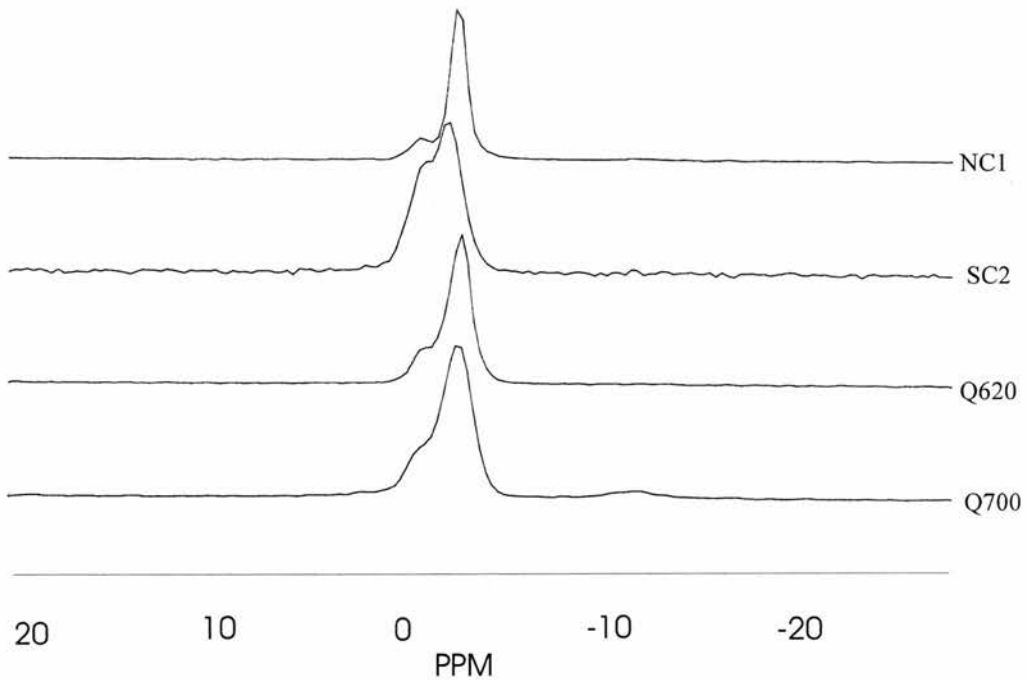


Figure 3.11. Obtained MAS NMR spectra for LiTi_2O_4 under different thermal histories.

^f Furnace cooled by removing power, and then cooled as fast as furnace thermal mass will allow.

Examination of the most intense peaks located at ~ -2 PPM (the chemical shift) has been shown by Dalton et al²⁰ to be due to tetrahedral 8a lithium. Although these experiments were performed using a ⁷Li probe rather the ⁶Li used in this experiment, similar chemical shifts would be expected. Presented below in table 3.8 are the shifts obtained for the different samples.

Sample name	8a δ (PPM) .	n δ (PPM).	16c δ (PPM)
NC1	-1.93	0.09	-11.63
SC2	-1.53	-0.14	-
Q620	-2.08	0.05	-
Q700	-1.99	0.17	-11.76

Table 3.8. Obtained chemical shifts as a function of thermal history. Relative to a LiCl standard solution. PPM=Parts Per Million.

The chemical shift for NC1 was found to be approximately -1.93 PPM with a slight increase seen for SC2 and a decrease seen for Q620 and Q700. The significance of this result will be discussed in section 3.6.3.

The doublet associated with these results suggests that two tetrahedral sites are present, the most intense of these has already been assigned to the 8a site. These results are presented below in table 8. The obtained spectra were fitted using a gaussian function for each peak, with the peak widths constrained to be equal. The fitted intensities presented below in table 3.9.

Sample name	8a peak height	n peak height	(8n/(8a))
NC1	3.79×10^6	6.50×10^5	0.1715
SC2	3.78×10^6	2.30×10^6	0.6085
Q620	2.19×10^6	5.80×10^5	0.2648
Q700	2.54×10^6	7.90×10^5	0.3110

Table 3.9. Ratio of 2nd peak intensity against total peak intensity.

Therefore from examination of the results presented above in table 3.9, it can be seen that the total intensity of the 2nd peak is lowest in the normal furnace

cooled sample, with an increase as a function of quenching temperature in Q620 and Q700. The sample that was slow cooled from 500°C (SC2) shows the highest intensity for the second peak.

The full width half maximum of the larger right-hand peak shows some variations with thermal history as shown in figure 3.11, with the full width at half maximum being presented below in table 3.10.

Sample name	FWHM (ppm)
NC1	0.0577
SC2	0.0895
Q620	0.0753
Q700	0.0930

Table 3.10. FWHM obtained for the different thermal histories.

The normal cooled sample and the samples quenched from 700°C shows an additional broad peaks at -11.76 and -11.63 -PPM. This peak may be attributable to Li on an octahedral site within the structure. Justification for this will be provided in the next section.

3.7.3. Discussion.

The chemical shift of a nucleus observed by NMR is a measure of the effective magnetic field around the nucleus due to the influence of the electron cloud surrounding it. For a filled electron shell, such as Li^+ , Ti^{4+} , all electrons are paired and hence the cores are diamagnetic. This causes a decrease in the effective magnetic field experienced by the nucleus, and therefore the corresponding frequency. In order to be able to compare this effect for different environments of a given nucleus, a reference material must be chosen, which in this case was a LiCl solution. Therefore the chemical shift (δ) of a particular site can be assigned as below.

$$\delta = \left(\frac{\nu_{\text{experimental}} * 10^6}{\nu_{\text{nuclei}}} \right) - \nu_{\text{reference}} \quad (3.1)$$

Where $\nu_{\text{experimental}}$ is the resonant frequency obtained experimentally, ν_{nuclei} the resonant frequency of the nuclei being examined and $\nu_{\text{reference}}$ the resonant frequency of the reference sample. The resonant frequency of ⁶Li is known to be approximately 73.3 MHz.

A sample whose nuclei are more shielded than those of the reference will have a negative chemical shift. For a nucleus within an atom with an incomplete electron shell (paramagnetic), the applied field is reinforced, leading to a negative shielding constant and hence a higher resonant frequency. This type of effect is usually found in metals, where the conduction electron density causes a localised paramagnetic susceptibility.

From the results presented in table 6, it was seen that the chemical shift for the sample prepared under normal furnace cooling gave a value that was slightly smaller than that seen by Dalton in reference 20. The sample prepared by slow cooling (SC2) showed an increase in the chemical shift to -1.53 PPM, with a slight decrease being seen for the two quenched samples (Q620 and Q700 respectively). It is felt that the sample prepared by slow cooling may have undergone some degree of oxidation. Examination of the results obtained by Dalton et al for Li₄Ti₅O₁₂ indicates that the chemical shift is positive, which is consistent with the lithium not interacting with the conduction band of the Ti-O octahedra, which results in a positive shift. Although the sample known as SC2 has a negative chemical shift, the value in comparison to seen for the other samples suggests oxidation may have occurred. Therefore any further results will not deal with this sample.

The appearance of the second peak in the doublet was not expected and could be due to occupancy of a possible second Li site within the structure. Whatever the origins of this second peak its total intensity is lowest in the normal furnace cooled sample. It may possibly be related to impurities in the samples.

The broad peak seen at -11.63 and -11.76 PPM is likely to be related to lithium on an octahedral site. The structure of LiTi_2O_4 spinel is described as normal²¹ and therefore no vacancies should exist on the Ti-O framework. Work performed by Soubeyroux²², Kanno²³, Tarascon²⁴ and work presented in this chapter indicated that Li could be found on the 16c site of the spinel. As the position of the peak is far removed (relatively) from the tetrahedral peaks, this shows a large shift, indicating that the Li is in a different environment. Octahedral Li ought to display very different broadening effects. The octahedral site should have an associated trigonal distortion due to imperfect packing of oxygen. This means that the local site symmetry is axial, so that both chemical shift anisotropy and quadrupole^g interactions are expected, this will manifest itself as a broad featureless peak. Therefore it can be concluded that sample history leads to expected 16c occupancy in the sample quenched from 700°C and the sample prepared by normal cooling.

The FWHM of the peaks is also an important indication as to the state of the Li within the sample. The tetrahedral sites in the spinel structure has local cubic symmetry, therefore the dominant source of any line broadening should be through dipole interaction between the ^6Li on the 8a tetrahedral sites (and also Ti dipoles from the framework). The dipole interaction is defined as the direct “through-space” interaction between the nuclear moment of two nuclei.

It was seen that the FWHM is lowest in the normal cooled sample. This again suggests that the disorder on the tetrahedral site is lowest in the normal cooled sample.

These results in association with those presented in sections 3.3 to 3.5 suggest a definite link between the thermal history and Li distribution.

^g The quadrupole moment arises from the interaction of the nuclear spin with a non-spherically symmetric field gradient at the nucleus. This effect only exists for nuclei with spin $>1/2$.

3.8. Conclusions.

The studies on the optimum temperature at which to prepare the spinel are interesting as this could explain the difficulties in preparing samples, with only a very narrow temperature range giving high quality samples. The neutron diffraction studies described at the start of this chapter have provided a number of interesting observations for the LiTi_2O_4 spinel superconductor. The most interesting of these is the distribution of Li within the structure may be an important factor in the superconducting properties of the system. The changes in the lithium distribution within the structure were also seen in the second neutron study, with the missing Li being seen on the 16c site within the structure.

The theory that the thermal history of LiTi_2O_4 is important with respect to T_c was found to be valid, as the T_c of the LiTi_2O_4 spinel was seen to decrease when the sample was quenched from various temperatures. As indicated above the lithium distribution was also seen to change as a function of thermal history.

This distribution of Li within the spinel structure has been mooted as an important factor in the ionic conductivity of the analogous non-superconducting LiMn_2O_4 spinel system²⁵. Various other studies^{23,24} have shown that the distribution of Li on the 8a site in the spinel structure changed as a function of increasing temperature. However, they did not report that the 8a site later refilled at higher temperature, although it must be noted that no transformation occurs in those systems.

The experiments performed using ^6Li Magic angle spinning (MAS) also suggest that LiTi_2O_4 spinel is sensitive to thermal history. The FWHM was found to be lowest in a normal slow cooled sample indicating the lowest disorder. It was also noted that more than one tetrahedral Li site may be present, with the one being 8a and the other possibly related to 8b. Refinement of the neutron powder patterns could only locate 2 possible sites within the structure and therefore the theory that Li goes onto the 8b site cannot be definitely proved. It maybe possible that the NMR is actually detecting rapid movement of Li within the channel like structure of the spinel. Work by Hayashi et al²⁵ on

$\text{Li}_4\text{Ti}_5\text{O}_{12}$ suggested that $8a \Rightarrow 16c \Rightarrow 8a$ was the most likely conduction pathway in this material. The proposed conduction mechanism of Li through the structure was based on the ratio of bottleneck radius to Li^+ ion radius.

In general, the results presented in this chapter suggest that further study is definitely necessary on this system, before it can be conclusively stated whether the $\text{Li}_{1+x}\text{Ti}_{2-x}\text{O}_4$ spinel solid solution is more closely related to BCS^2 or High T_c cuprate superconductors. It might be fair to say that more new questions have been asked than older questions answered.

3.9. References.

-
1. D.C. Johnston, *J Low Temp Phys.*, **25** (1976) 145.
 2. J. Bardeen, L.N. Cooper and J.R. Schrieffer, *Phys. Rev.*, **108** (1957) 1175.
 3. J.G. Bednorz and K.A. Müller, *Z. Phys.*, **B64** (1986) 189.
 4. Y. Ueda, T. Tanaka, K. Kosuge, M. Ishikawa and H. Yasuoka, *J. Solid State Chem.*, **77** (1988) 401.
 5. M Dalton, *PhD thesis.*, Univ. of Cambridge., 1992.
 6. M.R. Harrison, P.P. Edwards, and J.B. Goodenough, *Philos. Mag.*, **52** (1985) 679.
 7. B. Morosin and J.C. Mikkelsen, *Acta. Crystallogr., sect B*, **35** (1979) 798.
 8. A.H. Mousa and N.W. Grimes, *J. Mat. Sci. Lett.*, **15** (1980) 793.
 9. D.C. Johnston, H. Prakash, W.H. Zacharisen and R. Viswanthan, *Mater. Res. Bull.*, **8** (1973) 777
 10. A.C. Larsen and R.B. Von Dreele, *Los Alamos Laboratory report*, NO-LA-U-86-748 (1987).
 11. J.C. Mathewmann, P. Thompson and P.J. Brown, *J. Appl. Crystallogr.*, **15** (1982) 167.
 12. P.J. Brown and J.C. Mathewmann, Rutherford Appleton Laboratory Report, RAL-87-010 (1987).
 13. P. Lambert, M. Harrison, and P.P. Edwards, *J. Solid State Chem.*, **75** (1988) 332.

-
14. D.N. Argyriou, *J. Appl. Crystallogr.*, **27** (1994) 155.
 15. I.R. Gibson and J.T.S. Irvine. *J. Mater. Chem.*, **6**(5) (1996) 895.
 16. J.M. Heintz, M. Drillon, R. Kuentzler, Y. Dossman, J.P. Kappler, O. Durmeyer and F. Gautier, *Z. Phys B*, **76** (1989) 303.
 17. J.W. Richardson Jr, *IPNS progress report*, 1 (1991-1996) 16.
 18. A.R. West, *Solid state chemistry and its application.*, John Wiley and Son, Chichester, (1984) 571.
 19. A.R. West, *Solid state chemistry and its applications.* John Wiley and Son, Chichester (1984) 333.
 20. M. Dalton, D.P. Tunstall, J. Todd, S. Arumugan, P.P. Edwards, *J. Physics-Cond. Matt.*, **6** (1994) 8859.
 21. R. K. Datta and R. Roy, *J. Am Ceram Soc.*, **50** (1967) 578.
 22. J.L. Soubeyroux, C. Cros, Wang. Gang, R. Kanno and M. Pouchard, *Solid State Ionics*, **15** (1985) .293.
 23. R. Kanno, Y. Takeda, O. Yamamoto, C. Cros, Wang Gang, P Hagenmueller, *Solid State Ionics*, **20** (1986) .99
 24. J.M. Tarascon, W.R. McKinnon, F. Coowar, T.N Bowmer, G. Amatucci and D. Guyomard, *J. Electrochem. Soc.*, 141 (1994) 1421.
 25. S. Hayashi and H Hatano, *J. Ceram Soc Japan*, **102** (1994) 378

Chapter 4. μ^+ SR studies on the LiTi_2O_4 spinel superconductor.

4.1. Introduction.....	115
4.2. Experimental.....	117
4.2.1. Results.....	119
4.2.2. Phase characterization.....	119
4.2.3. D.C. magnetic studies.....	120
4.2.4. Transverse μ^+SR experiments.....	122
4.2.6. Discussion.....	127
4.3. Longitudinal field μ^+SR.....	129
4.3.1. Experimental.....	129
4.3.2. Results.....	129
4.3.3. Discussion.....	131
4.4. Conclusions.....	131
4.5. Acknowledgements.....	132
4.6. References.....	132

4.1. Introduction.

One of the fundamental parameters of a superconductor is its magnetic penetration depth, λ , which is a measure of the distance over which the current screens a magnetic field and hence the flux lattice and flux lattice pinning. The penetration depth of LiTi_2O_4 has been previously examined by Harrison¹ using conduction electron density and by Wu² using transverse field μ^+ SR. However, the method of sample preparation utilized by Harrison is thought to be susceptible to Lithia loss, and no mention was made about how the sample used by Wu was prepared. Therefore it would seem appropriate to reexamine LiTi_2O_4 of known purity and high T_c using the μ^+ SR technique.

The muon³ can be implanted into virtually any material and its spin polarisation monitored to enable its site in crystal lattices or molecules to be determined. This gives information about the local atomic structure and dynamics. The muon is essentially a sensitive microscopic magnetometer with spin $\frac{1}{2}$ and a magnetic moment three times that of the proton. The frequencies of its magnetic resonance or precession signals give a direct measurement of local magnetic fields. Measurements of the relaxation of the muon polarisation characterise the distribution of these fields.

Muons are produced by the collision between an energetic proton and the atomic nucleus of a light element, usually graphite. Their behaviour within a material is determined via one of the decay products: each muon produces a positron, which is emitted preferentially along the instantaneous direction of the muon's spin. Detection of these positrons indicates how the muon interacts with the sample. This is shown schematically below in figure 4.1.

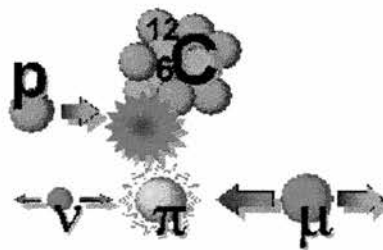


Figure 4.1. Schematic of muon production. Blue arrows show the direction of momentum, green arrows that of spin

Muon spin experiments are usually performed in one of three modes, these being rotation, relaxation and resonance. The resonance mode was not used during the following experiments and will not be discussed any further. The rotation mode (also known as transverse field μ^+ SR) is used in this chapter to determine the superconducting penetration depth of LiTi_2O_4 , whereas the relaxation method (also known as longitudinal field μ^+ SR) was used to probe any magnetic properties of the material. Presented below in figure 4.2 is a schematic of the muon instrument used during these studies.

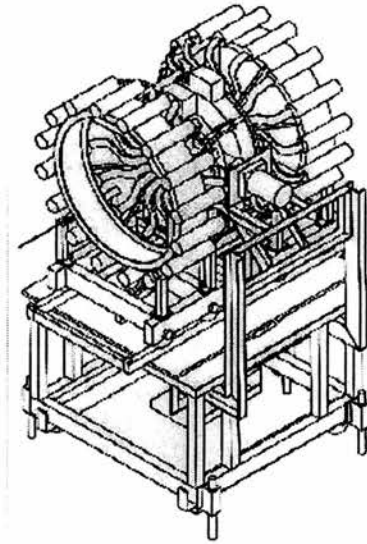


Figure 4.2. Schematic of the MuSR spectrometer in longitudinal geometry.

To change the mode of operation, the instrument is moved through 90° relative to the muon beam and aligned using a laser.

Transverse field μ^+ SR has been extensively used in the determination of superconducting properties^{4,5} of High Tc superconductors⁶ and other type 2^A superconductors such as the $\text{YNi}_2\text{B}_2\text{C}$ ^{7,8} and in the heavy fermion systems such as UPt_3 ⁹.

The relaxation method is used to determine the nature of any magnetic environments within a sample. It has been utilised in a number of different types of sample, such as the spin ladders, SrCu_2O_3 ¹⁰, the zigzag spin ladder, SrCuO_2 ¹¹, and the spin glass phases of $\text{Cr}_{1-x}\text{Fe}_x$ ¹²

^A Experiments performed in the mixed state.

In both the transverse and longitudinal experiments the sample was characterised using a number of other techniques prior to the actual muon experiments.

The aim of these experiments was to examine the penetration depth of LiTi_2O_4 and compare it to that seen previously by Wu² and Harrison¹. The sample was then re-examined at a later date to determine if any changes had occurred on ageing. The fresh sample was also examined to determine if any magnetism could be detected.

4.2. Experimental.

These experiments were conducted in two stages. The first stage of the experiments was performed within 36 hours of the sample preparation (referred to as the fresh sample) and the second stage was performed after a further 3 months (referred to as the aged sample). The aged sample was stored in an evacuated desiccator in the intervals between the measurements. The samples were characterised using X-ray powder diffraction, DC magnetisation and muon spin techniques.

The X-ray powder patterns were collected overnight on a STOE Stadi P X-ray powder diffractometer in the range $15-90^\circ$ 2theta, with the structural models being refined using the GSAS^{13,14} refinement program.

The magnetisation measurements were performed using Vibrating Sample Magnetometry. A sample of known weight was mixed with epoxy resin and allowed to set. On setting it was placed in a DELRIN sample holder. The samples were initially cooled in zero applied field below the reported superconducting transition¹⁵ and a 60 gauss field applied. The magnetisation of the sample was measured as a function of temperature. Using the same field, the sample was field cooled and again the magnetisation was measured as a function of temperature. H_{C1} of the sample was also determined (found to be in the region of 60-100 gauss). An idea of H_{C1} must be known, as the sample has to be examined in the mixed state.

The transverse field muon spin rotation experiments were undertaken at the pulsed muon facility at ISIS, RAL, U.K. using the MuSR spectrometer in transverse geometry. A field of 400 gauss was applied perpendicular to the

incident muon beam and initial muon spin. The μ^+ SR spectra were collected, on warming, after field cooling the samples below their respective superconducting transition temperatures¹⁷. The samples were mounted onto an Aluminium sample holder and held in position with a Mylar cover. The incident muons have sufficient energy to penetrate the Mylar cover. Any exposed Aluminium perpendicular to the muon beam was covered using dried $\alpha\text{-Fe}_2\text{O}_3$ mixed with an epoxy resin. The $\alpha\text{-Fe}_2\text{O}_3$ gives an incoherent background and therefore is not seen in the analysis. Full data analysis was performed using the Maximum entropy¹⁶ algorithms running on a DEC ALPHA workstation. Presented in figure 4.3 is a picture of the instrument used during these measurements.

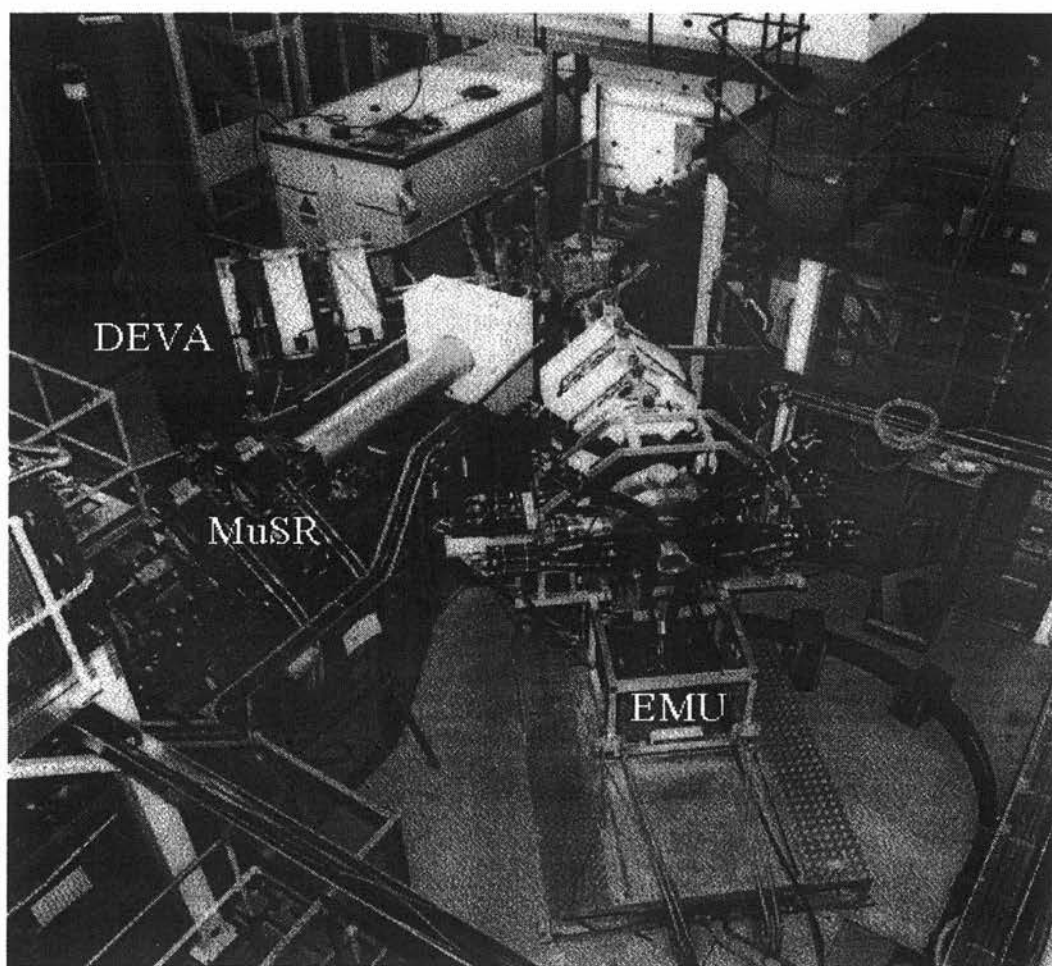


Figure 4.3. A picture of the Muon spectrometers at ISIS.

4.2.1. Results.

4.2.2. Phase characterization.

Fresh and aged samples were both examined by Rietveld analysis of the X-ray powder patterns using the $\text{Fd}3\text{m}$ space group (227). The unit cell of the fresh sample was determined to be $8.4062(2) \text{ \AA}$, which is in good agreement with that reported by Lambert¹⁷ and work presented in chapter 3. The collected powder pattern is presented below in figure 4.4(a). It was noted from the X-ray powder pattern that the peaks are narrow, indicating that the sample was of a high crystallinity.

The aged sample was found to have a smaller unit cell than the fresh sample, with the unit cell dimension being found to be $8.3699(7) \text{ \AA}$. Examination of the X-ray powder pattern collected for the aged sample shows significant broadening of the peaks, indicating that sample may have undergone some form of degradation. Presented in figure 4.4(b) is the collected X-ray powder pattern of the aged sample.

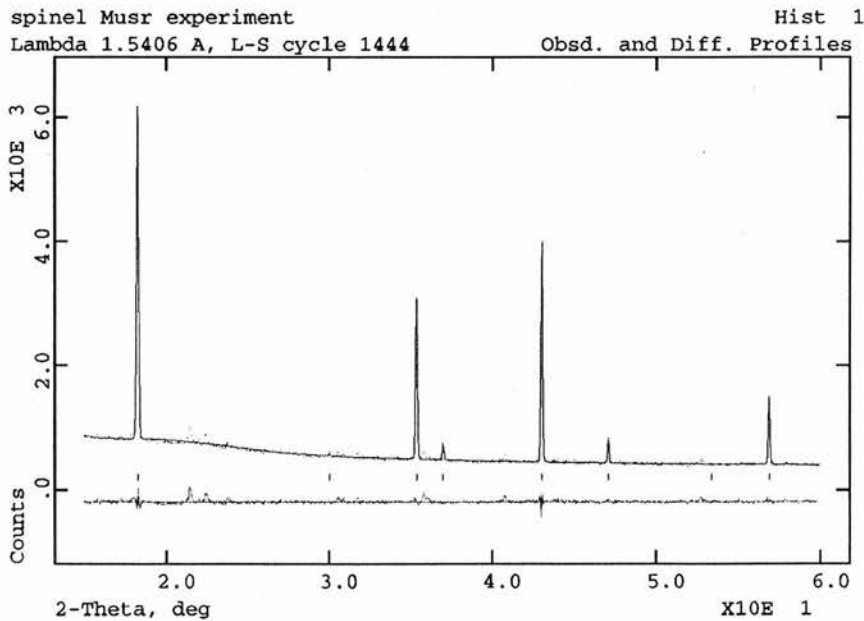


Figure 4.4(a). Collected X-ray powder pattern of the freshly prepared LiTi_2O_4 spinel sample.

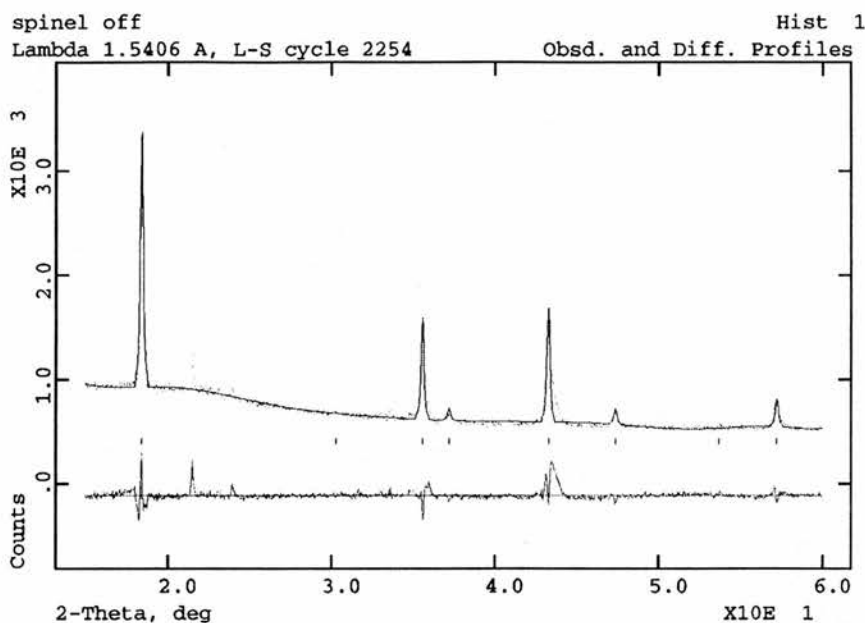


Figure 4.4(b). Collected X-ray powder pattern of the aged LiTi_2O_4 spinel sample.

Peaks were found to be present in both of the collected powder patterns at approximately 21 and 24° 2θ , these peaks have been attributed to the Vaseline used in the sample mounting.

4.2.3. D.C. magnetic studies.

Presented below in figure 4.5(a) and (b) are the magnetic results relating to the fresh and aged samples of LiTi_2O_4 spinel. The fresh sample was found to have a transition of $13.2(2)$ K, with the aged sample having a significantly lower transition of $11.2(2)$ K. The superconducting transition for the fresh sample is significantly sharper than that of the aged sample, indicating better sample homogeneity, as could be expected from the X-ray powder patterns. It is also interesting to note that the superconducting fraction is considerably lower in the aged sample.

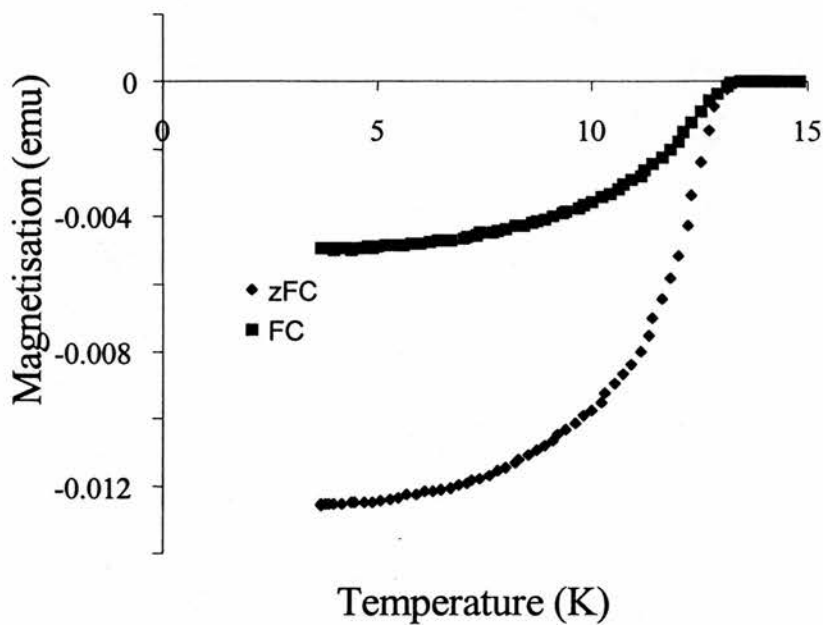


Figure 4.5(a). Magnetic data collected for fresh sample of LiTi_2O_4 .

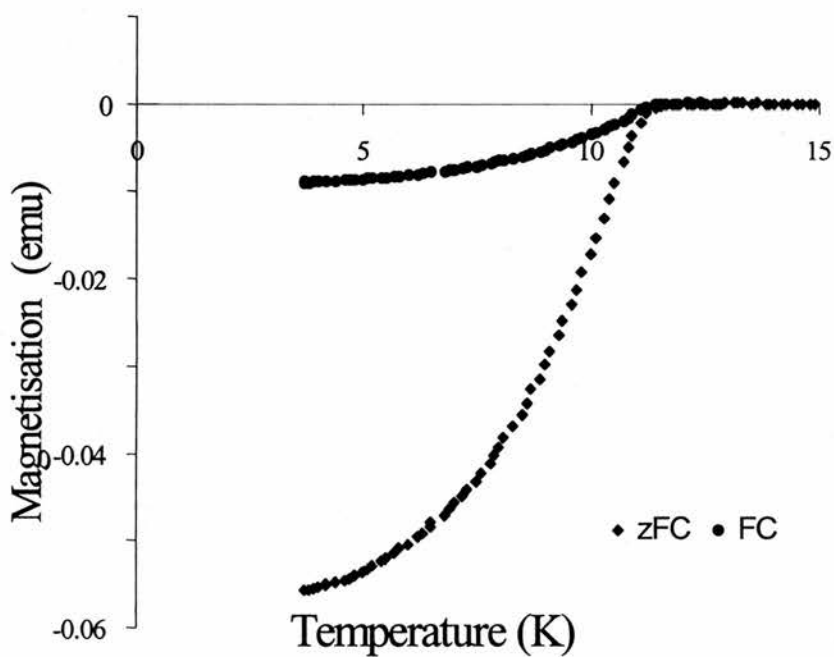


Figure 4.5(b). Magnetic data collected for aged LiTi_2O_4 sample.

4.2.4. Transverse μ^+ SR experiments.

Presented in figure 4.6(a) and (b) are the raw spectra collected for the fresh sample, below and above the superconducting transition temperature.

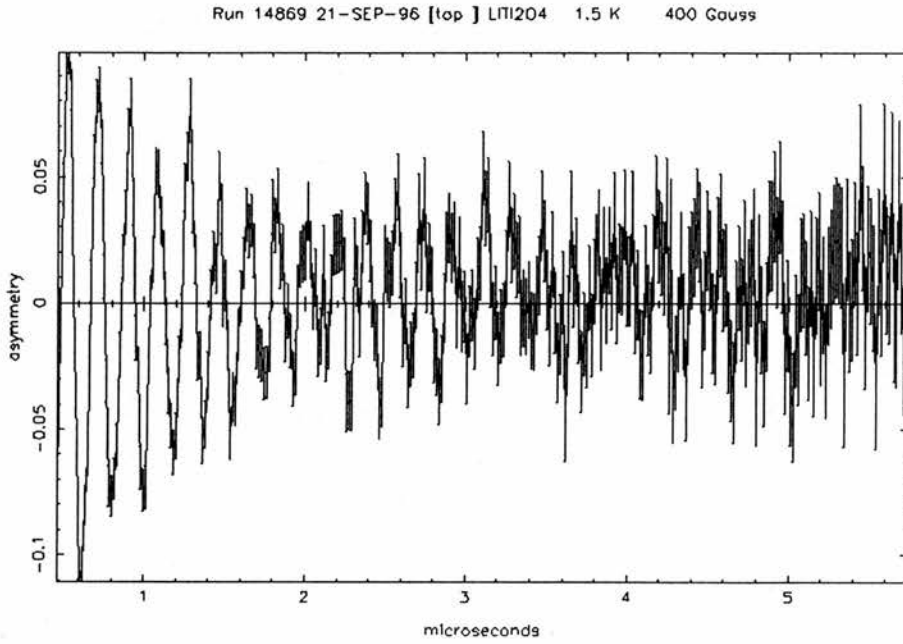


Figure 4.6(a). Raw spectra obtained for LiTi_2O_4 spinel from μ^+ SR spectra collected at 1.5 K

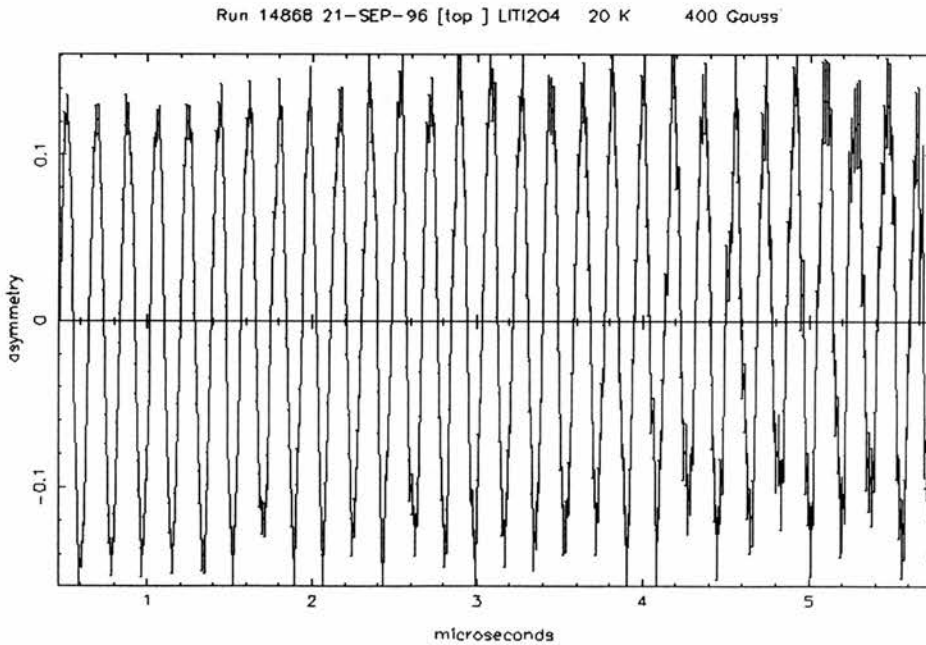


Figure 4.6(b). Raw spectra obtained for LiTi_2O_4 spinel from μ^+ SR spectra collected at 20 K.

The asymmetry term is defined as angular distribution of the decay positron intensity and describes the depolarisation of the muon as a function of time. It can be seen from the spectra presented in figures 4.6(a) and (b) that the nature of the spectra changes completely above and below the transition temperature. Below the superconducting transition temperature the obtained spectra shows a sinusoidal decay within a gaussian envelope. The spectrum collected at 20 K shows a simple sinusoidal response with increasing muon decay time. Both of the spectra are noisier with increasing muon decay time, this is related to the finite muon decay lifetime, which is approximately 2.2 microseconds. At longer decay times very few muons are still present in the sample and hence very few data points are collected. As a consequence the spectra become noisier at longer decay times.

The spectra were examined using Maximum Entropy analysis and are presented below in figure 4.7(a), (b) and (c). The Maximum entropy method of analysis is presented previously in chapter 2 (section 2.3.8). The results give the field distribution inside the fresh sample, with $p(B)$ being the probable distribution of the internal field.

As can be seen in the results presented in figure 4.7 a \rightarrow c, the field distribution changes dramatically as the sample temperature is raised above the superconducting transition temperature.

The results obtained from the aged sample are presented in figure 4.8 (a) \rightarrow (c). Examination of the probable field distribution for the aged sample shows a marked difference as a function of temperature. The first noticeable difference between the field distributions for the fresh and aged sample is the field width at temperatures below the superconducting transition temperature. It was found that the field width is larger in the fresh sample compared to that of the aged sample

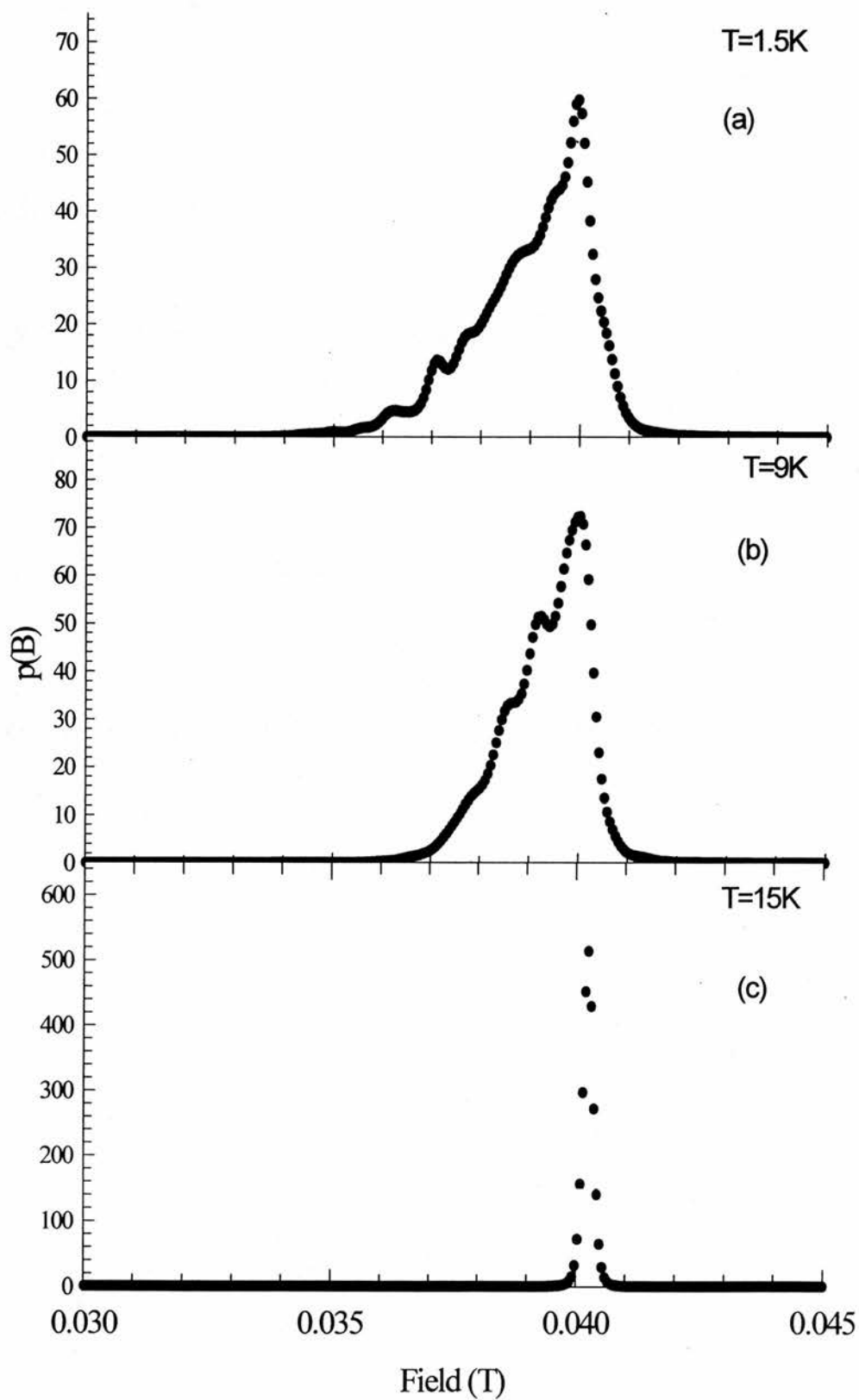


Figure 4.7. Field distribution in fresh sample at (a) 1.5K (b) 9 K and (c) 15K.

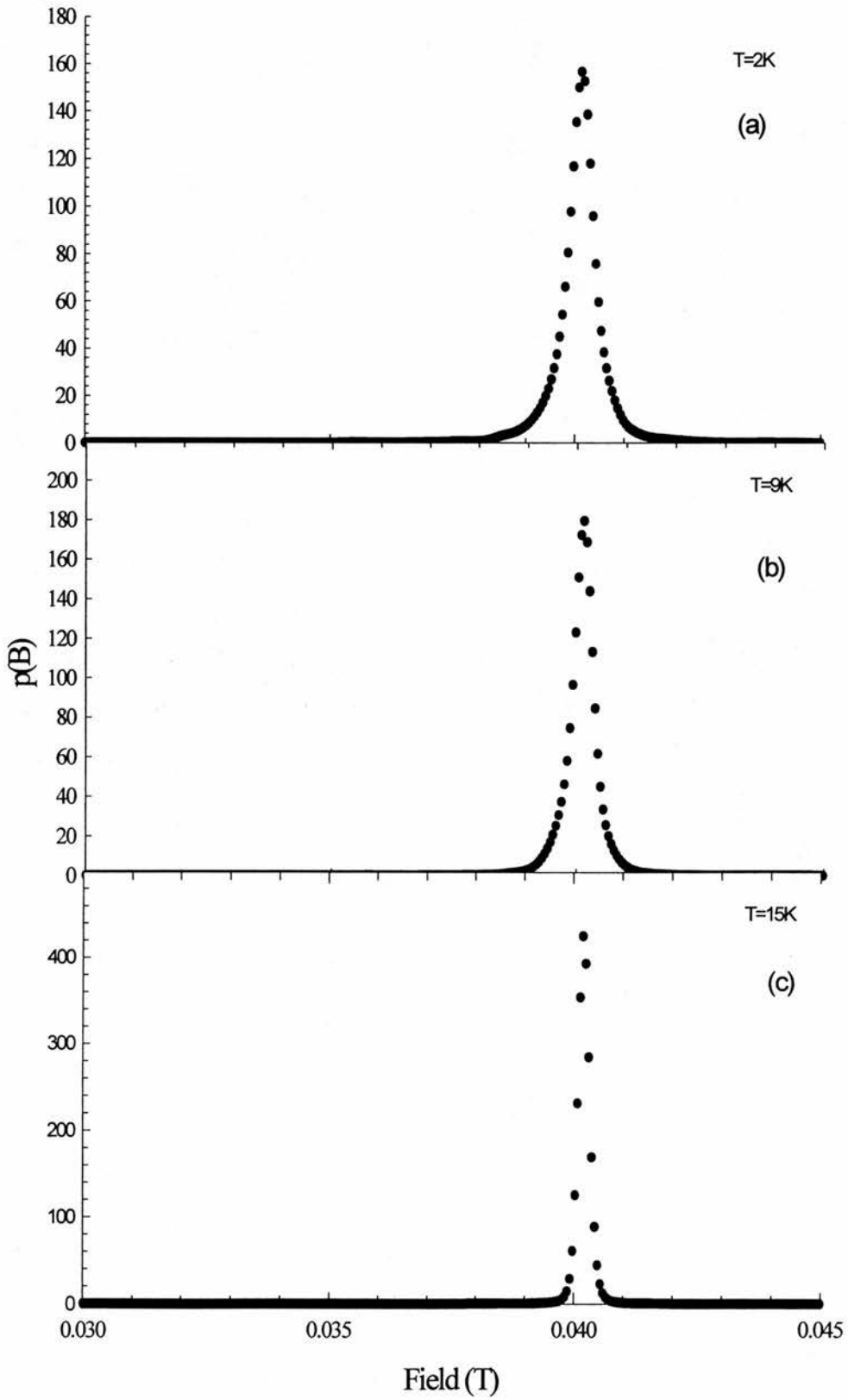


Figure 4.8. Field distribution in aged sample at (a) 2K (b) 9 K and (c) 15K.

Examination of the second moment of the field width is presented in figure 4.9 for the fresh sample of LiTi_2O_4 spinel.

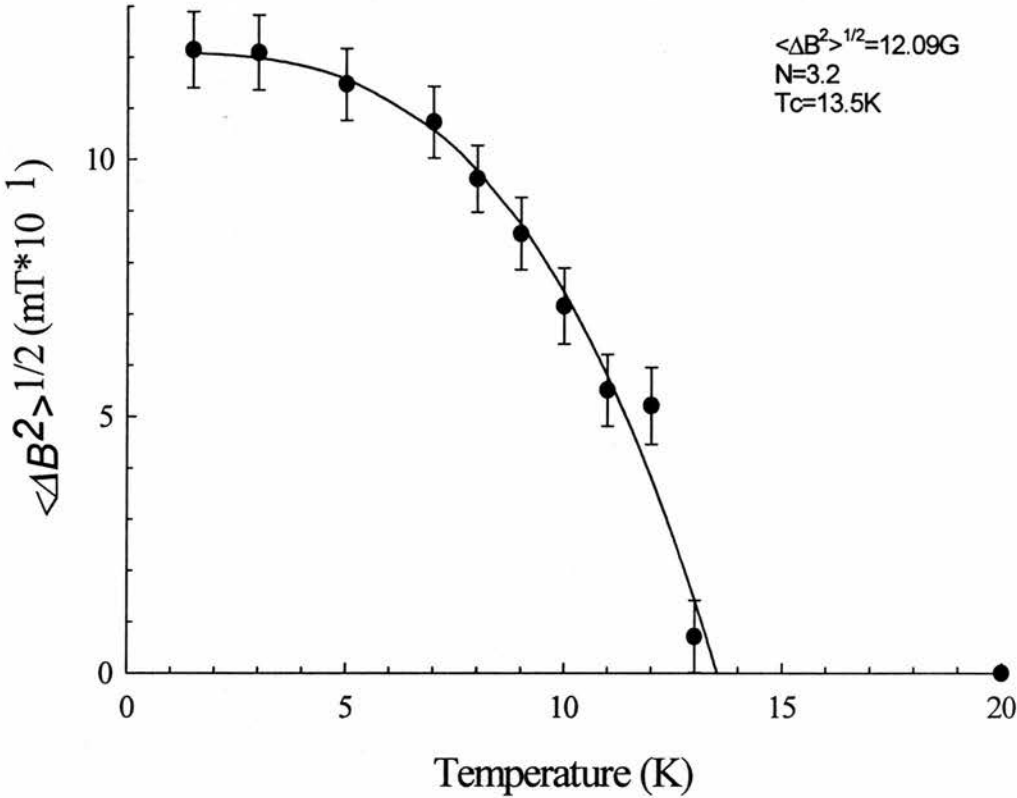


Figure 4.9. Plot of $\langle \Delta B^2 \rangle^{1/2}$ versus temperature for fresh LiTi_2O_4 spinel.

It shows a decrease in the second moment of field width as a function of increasing temperature. For the fresh sample, the temperature dependence of the field width, $(\Delta B^2)^{1/2}$, was fitted using the N-fluid model,

$$\sqrt{(\Delta B)^2}(T) = \sqrt{(\Delta B)^2}(0) \left(1 - \left(\frac{T}{T_c} \right)^N \right) \quad (4.1)$$

The extrapolated value of $(\Delta B^2)^{1/2}$ at $T=0$ was found to be 1.2 mT. The superconducting transition temperature and N were found to be 13.5(2) K and 3.2(1) respectively. The superconducting transition temperature is in close agreement with the magnetization results presented previously in this chapter. The value of N being close to 4 indicates a strong pair binding strength of the Cooper pairs¹⁸. The second moment of the field distribution is directly related to magnetic penetration depth by the relationship¹⁹,

$$\sqrt{(\Delta B)^2} = \frac{\sqrt{0.00371}\Phi_0}{\lambda^2}. \quad (4.2).$$

Where Φ_0 is the flux quantum ($2.07 * 10^{-15}$ Wb)

The magnetic penetration depth has been found to be 322nm. The aged sample low temperature value of $(\Delta B^2)^{1/2}$ was found to be 0.4 mT, and gives a magnetic penetration depth of 561nm using equation 4.2. A summary of these results is presented in table 4.1.

Sample	lattice constant (Å)	T_c (K)	λ (nm)
Fresh	8.4062(2)Å	13.2(2)	320
Aged	8.3699(7) Å	11.5(2)	561

Table 4.1. Summary of the results obtained from transverse μ^+ SR for fresh and aged LiTi_2O_4 spinel.

4.2.6. Discussion.

It is not immediately apparent from visual examination of the aged LiTi_2O_4 sample that any changes had occurred. The colour was seen to be a dark blue-black in both fresh and aged samples. Dalton²⁰ observed that on aging, his samples took on a greyish/white hue. However his samples were aged in air, whereas the sample prepared during this study were stored under a vacuum, when not being examined. It can be seen from examination of the X-ray patterns presented in figures 4.2(a) and 4.2(b), that the sample has undergone some kind of physical change. Dalton²⁰ noted substantial X-ray line broadening during his experiments, with a decrease in the intensity of the lines. He also noted that the unit cell edge decreased. The same effects were noted during these studies, however there was no evidence from the X-ray powder patterns to suggest the formation of an “impurity” phase on aging.

Dalton²⁰ indicated that the T_c actually increased on aging during his study, with the T_c in his “fresh” and “aged” samples being 12.4(1) and 13.0(1) K respectively. This was not seen in our experiments, where the T_c of the aged sample lower than in the fresh sample, with a decrease also seen in the

superconducting volume. This observation seems to suggest that the aged samples may have undergone some kind of sample segregation to a lithium rich and a lithium deficient phase, it could also be explained in terms of an oxidised rim on the grains, which does not superconduct, with the centre of the grain still found to be superconducting.

This model could explain the decrease in the superconducting fraction seen in the aged sample. From the μ^+ SR experiments it was seen that the penetration depth, λ , for the fresh sample was 322nm, which increased to 561nm on aging.

Harrison¹ used conduction electron measurements to determine λ , and found it be in the region of 270nm, which is not significantly different to that obtained during this study. In the study performed by Wu², the penetration depth was determined to be 210nm, which is different to that obtained in this chapter. It is important to note that the values obtained by Wu may be different for a number of reasons;

- No mention of the preparation method and temperature of synthesis were made. It is believed that the method of sample preparation is very important.
- Wu also assumed a Gaussian distribution of the fields in the mixed state. The plots presented in figure 4.5(b) and 4.5(c) clearly shows this is not the case^B.

Overall, it can be seen that the LiTi_2O_4 spinel may not be stable on storing under vacuum. This has not been reported previously in the literature for this method of sample preparation. Thermal analysis experiments performed on the aged sample did indicate that the total oxygen content was higher than predicted from stoichiometry, so the sample may have picked up some oxygen when not being stored under vacuum.

The pair binding strength was determined to be 3.2, with the theoretical maximum being 4, this suggests that the pair binding is relatively high in LiTi_2O_4 spinel.

4.3. Longitudinal field μ^+ SR.

In addition to the experiments performed in transverse mode (rotation), the fresh sample was also examined in longitudinal mode (relaxation), to determine if the sample had any magnetic ordering.

4.3.1. Experimental.

Longitudinal field muon spin relaxation experiments were undertaken at the pulsed muon facility located at ISIS, RAL, UK using the MuSR spectrometer in longitudinal geometry. A field of 20 gauss was applied parallel to the incident muon beam and the data normalised using T20FIT. T20FIT is used to calibrate the forward and backward detectors, such that they appear to be identical for the data analysis. The sample was cooled to 1.5 Kelvin in zero field and spectra collected on warming. Data analysis was performed using a number of different functions. It was found that the spectra could be best fitted using a Kubo-Toyabe function²¹, this is presented below in equation 4.3.

$$G_z = \frac{1}{3} + \frac{2}{3} \left(1 - \sigma^2 t^2\right) e^{-\frac{\sigma^2 t^2}{2}} \quad 4.3.$$

The Kubo-Toyabe provides information on the distribution and dynamics of internal fields at the muon site.

The data analysis is performed using Fortran code, and is done by least squares fitting. It was found that the contribution from the background was very low and hence this component was fixed and took no part in the fitting. All of the spectra were fitted in the temperature range 1.5 to 150 Kelvin.

4.3.2. Results.

The spectra collected at 1.5 and 150 Kelvin are presented below in figure 4.10.

^B It should be noted that the field distribution in the mixed state is more Gaussian in nature in the aged sample.

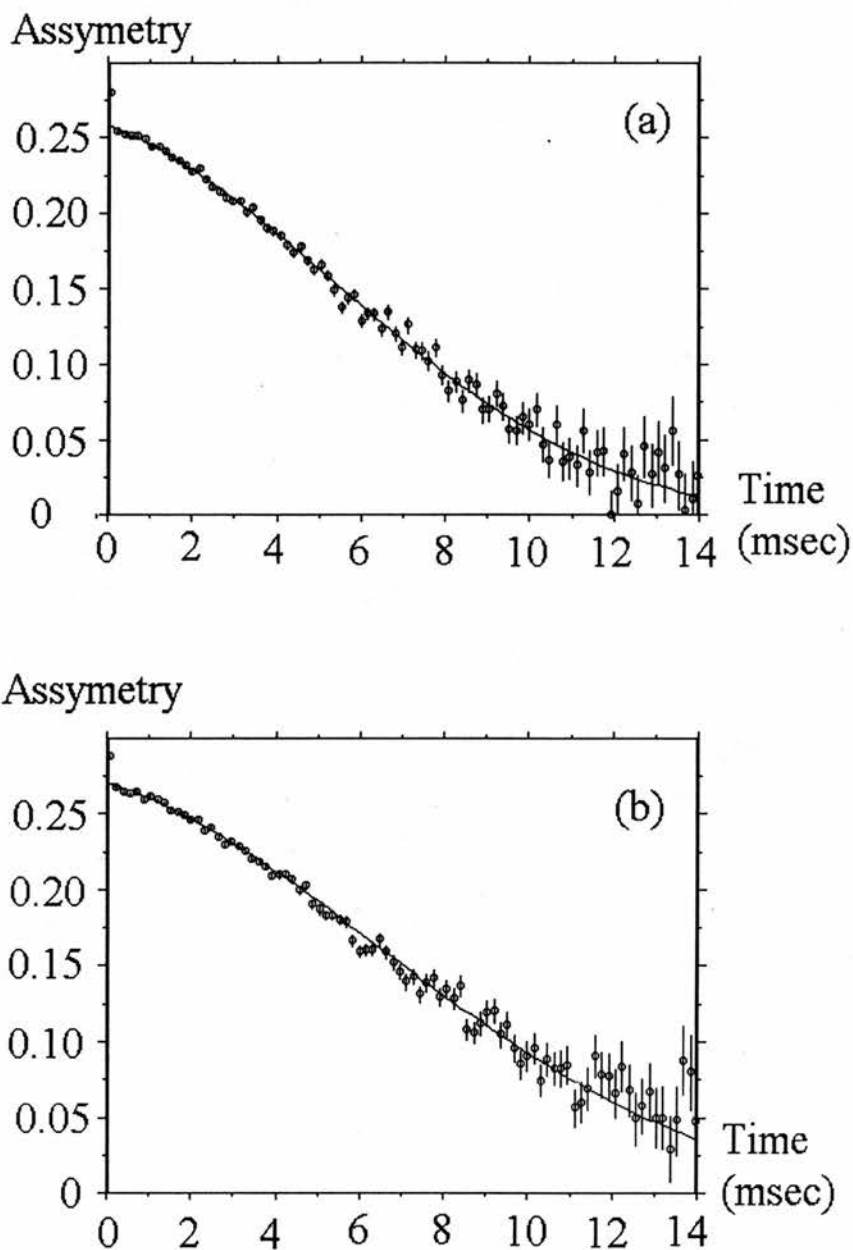


Figure 4.10. The fitted longitudinal μ^+ SR patterns at 1.5K (a) and 150 K (b).

Again the spectra is seen to be good at short muon lifetime and much noisier at longer decay times (reasons indicated previously). The asymmetry was seen to be essentially constant over the temperature range studied. Presented in figure 4.11 is a plot of the initial asymmetry as a function of temperature. The initial asymmetry is essentially independent of sample temperature.

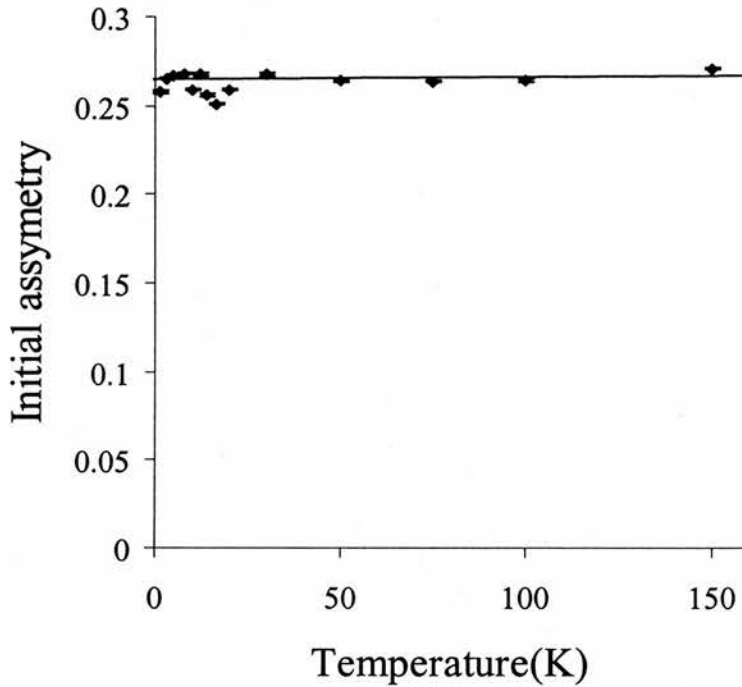


Figure 4.11. Initial asymmetry as a function of temperature for LiTi_2O_4 spinel

As no changes were seen in the different components in the fitted spectra it was concluded that no changes occur in the sample and hence no magnetic phase change occurred.

4.3.3. Discussion.

The results presented above seem to indicate that nothing magnetically interesting occurs in this material as a function of temperature. Due to time constraints no measurements could be made on the aged sample. The Kubo-Toyabe describes the nuclear magnetic moment. This would be expected in a sample of this nature.

4.4. Conclusions.

The muon experiments presented in this chapter have shown a number of different results. The penetration depth found for the fresh sample were seen to be larger than that found by Wu et al² during their studies. It is felt that the method used by Wu during the data analysis was also partially responsible for the lower penetration depth. They assumed that the field distribution in the

mixed state was gaussian in nature, whereas the treatment provided by Brandt¹⁹ at al is probably more accurate. It is also important to note that no mention of the sample preparation methods used was made. During the experimental portion of Wu's work a field of 2000 gauss was used instead of the 400 gauss used in these experiments. This could explain the differences seen in the penetration depth, as a higher field would be expected to have caused more of the applied field to have encroached on the flux lattice in the mixed state and hence cause a lower penetration depth.

The pronounced differences in penetration depths between the aged and fresh samples, could also indicate that the properties of the spinel are probably related to the age of the sample, however further studies would have to be performed before this can be known for sure.

The longitudinal μ^+ SR experiments indicated that no magnetic impurities were present in the sample and that this sample does not exhibit any magnetic properties, other than that associated with superconductivity, i.e. diamagnetism. Results presented in chapter 6, indicate this is not the case in the high temperature ramsdellite polymorph.

4.5. Acknowledgements.

Adrian Hillier is acknowledged for his help in performing the muon and magnetisation experiments and his help and expertise in the analysis of the transverse and longitudinal field experiments.

4.6. References

-
1. M.R. Harrison, P.P. Edwards, and J.B. Goodenough, *Philos. Mag.*, **52** (1985) 679.
 2. W. D. Wu, A. Keren, L.P. Le, G.M. Luke, B.J. Sternlieb, Y.J. Uemera, D.C. Johnston, B.K. Cho, and P. Gehring. *Hyperfine Interact.*, **86** (1994) 615.
 3. S.F.J. Cox, *J. Phys. Solid State Physics.*, **20** (1987) 3187.

4. B. Nachumi, A. Keren, K. Kojima, M. Larkin, G.M. Luke, J. Merrin, W.D. Wu, Y.J. Uemura, Y. Xue, F. Chen, Q. Xiong, Z. Huang, Z. He, Q. Lin, J. Clayhold, C. W. Chu., *Hyperfine Interactions.*, **105**, (1997) 119.
5. B. Nachumi, A. Keren, K. Kojima, M. Larkin, G.M. Luke, J. Merrin, O. Tchernyshov, Y.J. Uemura, N. Ichikawa, M. Goto, S. Uchida, *Phys Rev Lett.*, **77** (1996) 5421.
6. J.G. Bednorz and K.A. Müller, *Z. Phys.*, **B64** (1986) 189.
7. S. Lee, M. Brunner, H. Keller, M. Warden, D. Zech, R. Bewley, R. Cywinski, Z.P. Han, R. Cubitt, E.M. Forgan, M.T. Wylie and S.H. Kilcoyne, *Physica C.*, **235** (1994) 2535.
8. R. Cywinski, Z.P. Han, R. Bewley, R. Cubitt, M.T. Wylie, E.M. Forgan, S. Lee, M. Warden, S.H. Kilcoyne: *Physica C.*, **233** (1994) 273.
9. G.M. Luke, J.D. Garrett, K. Kojima, M. Larkin, J. Merrin, B. Nachumi, Y.J. Uemura., *Czech J. Phys.*, **46** (1996) 781.
10. M. Azuma, Z. Hiroi, M. Takano, K. Ishida and Y. Kitaoka, *Phys. Rev Let.*, **73** (1994) 3463.
11. M. Matsuda, K. Katsumata, K.M. Kojima, M, Larkin, G.M. Luke, J. Merrin, B. Nachumi, Y.J. Uemura, H. Eisaki, N. Motoyama, S. Uchida and G. Shirane, *Phys. Rev. B.*, **55** (1997) 11953.
12. M. T. F Telling and R. Cywinski, *J. Mag and Mag Mat.*, **144** (1995), 45.
13. A.C. Larsen and R.B. Von Dreele, *Los Alamos Laboratory report*, NO-LA-U-86-748 (1987).
14. H.M. Rietveld, *J. Appl. Cryst.*, **2** (1969) 65.
15. D.C. Johnston, *J Low Temp Phys.*, **25** (1976) 145.
16. B.D. Rainford. *Aspects of data treatment of transverse μ SR*. *MuSR, Lecture notes from the training course in pulsed μ SR techniques*, S.H. Kilcoyne (editor), RAL-TR-96-007.
17. P. Lambert, M. Harrison, and P.P. Edwards, *J. Solid State Chem.*, **75** (1988) 332.
18. L.N Cooper, *Phys. Rev.*, **104** (1956) 1189.
19. E.H. Brandht, *Phys Rev Let.*, **66** (1991) 3213.
20. M Dalton, *PhD thesis.*, Univ. of Cambridge., 1992.
21. S. Hayano, *Phys. Rev. B.*, **20** (1979) 850.

Chapter 5. The spinel to ramsdellite transformation.

5. Introduction.....	135
5.1. Neutron studies performed as a function of temperature and time.....	137
5.1.1. Experimental.	137
5.1.2. Results from high temperature neutron diffraction studies.	138
5.1.3. Discussion.	140
5.2. A detailed study by powder neutron diffraction.....	140
5.2.1. Experimental.	141
5.2.2. Results.	141
5.2.3. Method 1.	142
5.2.4. Method 2. Refinement of two phase powder patterns.....	145
5.3. The ramsdellite structure at high temperatures.....	146
5.4. Spinel to ramsdellite transformation temperature.....	160
5.5. Determination of the possible intermediate(s).....	162
5.6. Discussion.....	163
5.7. Conclusions.....	165
5.8. Acknowledgements.....	166
5.9. References.....	166

5. Introduction.

In 1973, Johnston¹ reported that on heating a sample of lithium titanate spinel with the composition LiTi_2O_4 , a conversion to a ramsdellite-like structure occurred. The resultant phase was found to have a slightly different unit cell from that seen for $\text{Li}_2\text{Ti}_3\text{O}_7$ ². Unfortunately, Johnston was unable to prepare single crystals of this material and hence unable to confirm the stoichiometry of this "ramsdellite" phase. Akimoto et al³ recently succeeded in preparing single crystals of this material and confirmed by single crystal X-ray diffraction that the stoichiometry of this phase was LiTi_2O_4 and that it had a ramsdellite structure.

A spinel to ramsdellite transformation would be unusual, as on conversion from spinel to ramsdellite, the symmetry of the unit cell decreases, instead of the usual increase in symmetry⁴ associated with phase changes that occur on increasing temperature. Very little is known about the spinel to ramsdellite phase transformation, except that the stoichiometry is the same before and after the transformation. Examination of the two space groups shows that the transformation from the cubic $\text{Fd}3\text{m}$ (227) to the orthorhombic Pbnm (62) space group cannot be direct and that some intermediate space group could be present. Work by Izquierdo⁵ on $\text{Li}_4\text{Ti}_5\text{O}_{12}$ spinel and $\text{Li}_2\text{Ti}_3\text{O}_7$ ramsdellite showed that it was possible for these two polymorphs to coexist over a wide temperature range. Therefore, the same may occur in the LiTi_2O_4 analogue. Examination of the literature does not provide any evidence as to the type of transformation, the temperature at which the transformation starts, if the transformation occurred over a range of temperatures or whether it goes via an intermediate phase.

According to the Buerger classification^{6,7}, phase transformations can be roughly divided into two groups: reconstructive and displacive transformations. Reconstructive transformations involve a major reorganization of the crystal structure, in which bonds are broken and new bonds formed. Displacive phase transformations involve the distortion rather than the breaking of bonds, with the structural changes usually small. For this reason, displacive phase transition have

very small activation energies, and therefore cannot be prevented from occurring, i.e. they are spontaneous.

It seems likely that the spinel to ramsdellite transformation is reconstructive in nature. It is possible, that there is no simple structural relationship between the polymorphs. This is the case in spinel and ramsdellite which have completely different structure types.

Thackeray and co-workers⁸ proposed a mechanism for the ramsdellite-spinel transformation in the analogous ramsdellite MnO_2 and its various lithiated forms. It was suggested that the R- MnO_2 structure initially shears in the (1 0 0) direction, this is followed by a co-operative displacement of the manganese, and then by a second shear in the (1 1 1) direction to give the spinel framework. They also indicated that the transformation was reversible. It should be noted that this transformation was composition dependent and not temperature dependent.

As mentioned previously the two structures are completely different. The LiTi_2O_4 spinel known to be cubic with the space group $\text{Fd}\bar{3}\text{m}$. The ramsdellite structure however is known to be orthorhombic with the space group Pbnm .

Diffraction methods are an appropriate option for the determination of the transformation temperature, range of transformation temperatures and whether any intermediates link the two phases. However, X-ray diffraction on lithium titanates is limited in a number of respects, as the position of the oxygen in the structure cannot be accurately determined due to its relatively low scattering factor with respect to X-rays. The case is worse with the Li, which is virtually transparent to X-rays. Therefore, only the location of the Ti can be determined with any reasonable accuracy from X-rays. This would make it virtually impossible to determine whether the Li moved prior to the transformation or whether the cubic close packed oxygen undergoes any radical changes prior to the transformation.

X-ray diffraction is also limited^a by the fact that 2θ is scanned sequentially. This means that if the sample transformation occurred as a function of time and temperature that the sample may have a different phase composition at the

^a Not so, if the instrument is fitted with detector banks over a wide 2θ range, rather than a fixed detector that is moved through different values of 2θ .

end of the measurement compared to that seen at the start of the experiment. Thus the patterns collected would be hard if not impossible to accurately model using the Rietveld method.

It was felt that the phase transformation would be best studied using Time Of Flight neutron diffraction. This method is ideally suited for high temperature experiments on phase transformations, due to the pulsed structure of the neutron beam, which allows patterns to be collected over very short time intervals. Experiments performed using powder X-ray diffraction are presented in chapter 3, and these suggest that the LiTi_2O_4 spinel to ramsdellite transformation may start in the region of 860 - 870°C.

5.1. Neutron studies performed as a function of temperature and time.

5.1.1. Experimental.

A sample was prepared from ^7Li enriched Li_2CO_3 (ISIS isotope bank), Ti metal (Johnson Matthey), and anatase/rutile TiO_2 (Tioxide Specialities). Powder neutron diffraction was performed on the high intensity medium resolution Polaris diffractometer situated at the ISIS neutron facility, Rutherford Appleton Laboratories, Didcot, Oxon, UK.

A pattern of LiTi_2O_4 was collected at room temperature in a standard vanadium sample can for 4 hours (700 μAh). These data were used to provide a starting point for the refinements. The sample of spinel was then heated *in-situ* under vacuum in a vanadium furnace, increasing temperature in a stepwise fashion up to 1000°C. From 800°C, patterns were collected in three segments at each temperature, so that the transformation could be investigated as a function of time as well as of temperature. The sample was exposed to the neutron beam at each temperature/time for approximately 45 minutes (300 μAh after equilibrating at that temperature for 15 minutes). Rietveld refinement was performed using the CCSL software packages running on the ISISE HUB computer^{9,10}. Refinement of the

models was performed on data collected from the backscattering detectors only ($135^\circ < \theta < 160^\circ$).

5.1.2. Results from high temperature neutron diffraction studies.

As mentioned previously in chapter 3, a slight impurity phase of unknown composition was present in the sample at room temperature and hence made it difficult to determine the exact onset temperature of the transformation. However, examination of the intensities of the spinel and the impurity peaks, as a function of temperature seemed to indicate that the conversion from cubic spinel to orthorhombic ramsdellite did not start to occur until 875°C .

The transformation was noted to have started between 875 and 900°C , with some peaks from the ramsdellite phase becoming apparent in the diffraction patterns at 900°C . The powder patterns collected between 875 and 925°C are presented in figure 5.1.

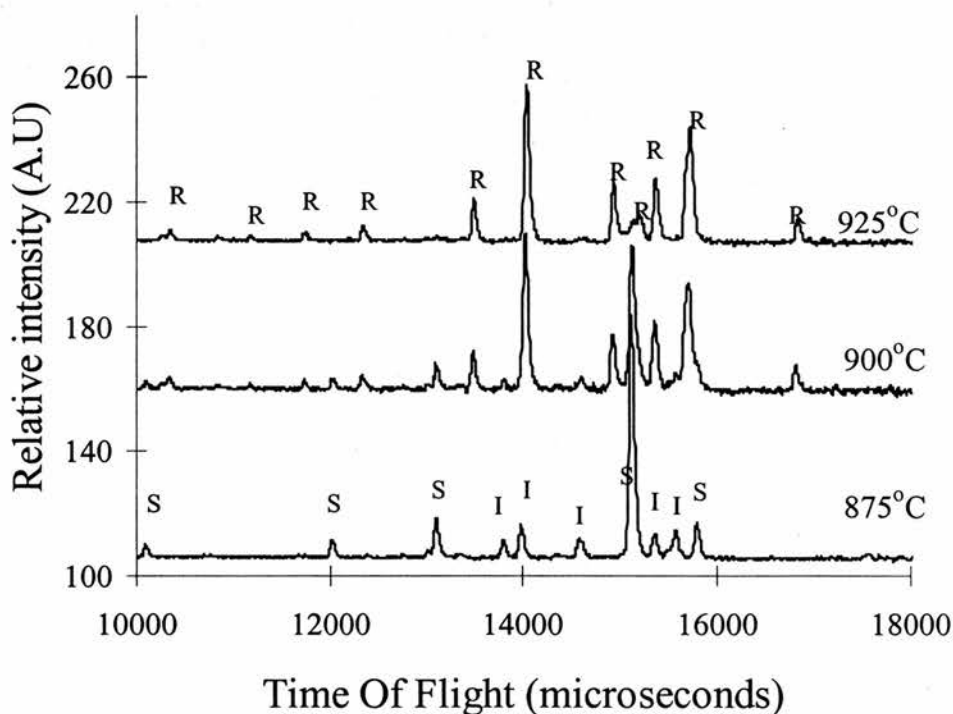


Figure 5.1. Combined raw plot collected in the region of 875 - 925°C . S=spinel, R=ramsdellite and I=unknown.

Examination of the raw patterns collected at 900°C indicates that the composition of the two-phase mixture is changing very little at constant temperature. This observation suggests that the rate of conversion of the spinel to ramsdellite is slowing down, indicating that the system is approaching an equilibrium state, without going to completion. When the temperature was increased from 900 to 925°C, the rate of conversion was seen to increase drastically, but again the two-phase mixture was seen to come to equilibrium without attaining completion. On raising the sample temperature to 950°C no evidence for any remaining spinel could be found. To obtain a quantifiable guide to the extent of conversion at each temperature it was decided the relative intensities of peaks attributable to spinel and ramsdellite should be examined.

It was found that the (4 0 0) peak in spinel and the (1 4 0) peak in ramsdellite were the best, as no peak overlap was seen for either of these peaks from the other polymorph. The changes in the ratio of the ramsdellite (1 4 0) peak to the spinel (4 0 0) peak with temperature and time are presented in figure 5.2.

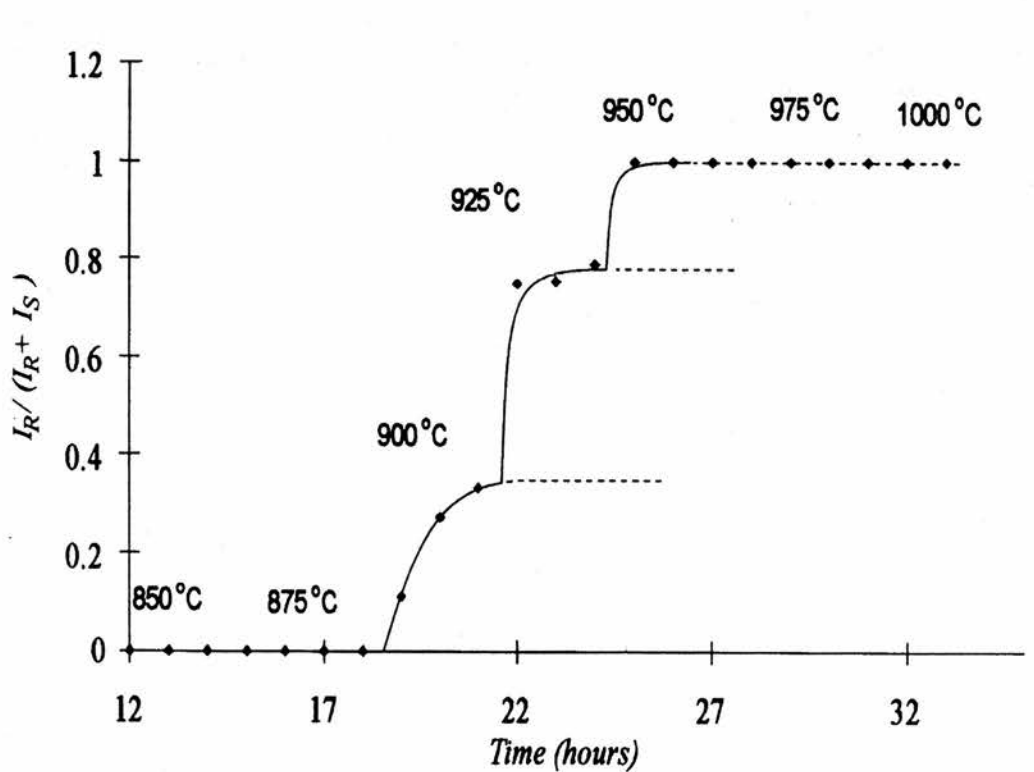


Figure 5.2. Changes in ratio of ramsdellite (1 4 0) peak (I_R) to the spinel (4 0 0) peak (I_S) as a function of temperature.

The results present in figure 5.1 and 5.2, indicate that the transformation starts in the region of 875 to 900°C, and has gone to completion in the region 925-950°C.

5.1.3. Discussion.

These experiments suggest that the spinel to ramsdellite transition starts to occur in the region of 875- 900°C, however the presence of a slight impurity phase did make the onset difficult to judge with certainty. No apparent intermediate phase was found in the patterns, but again the presence of the unknown phase made this difficult to determine. The results obtained indicate that spinel and ramsdellite can co-exist over a temperature range as has been seen previously in the literature for the $\text{Li}_4\text{Ti}_5\text{O}_{12}$ spinel and $\text{Li}_2\text{Ti}_3\text{O}_7$ ramsdellite⁵. One important thing that must be noted from this experiment is that the sample preparation temperature of 860°C, indicated by Dalton¹¹ may be slightly high for preparation of single phase spinel samples. This observation is in agreement with the X-ray results presented in chapter 3, which indicated that 850°C was a better firing temperature, with a second phase becoming apparent at 860°C. It was decided that a second neutron diffraction experiment should be performed in more detail on the spinel to ramsdellite transformation.

5.2. A detailed study by powder neutron diffraction.

The method of sample preparation is as described in chapter 2. However, to minimize the amount of impurity the sample was prepared at $840^\circ\text{C} \pm 10^\circ\text{C}$. This second study into the nature of the spinel to ramsdellite transformation was attempted in order to determine the exact nature of the phase transition. In the previous experiment it was decided that study of the transformation should be performed as a function of time and temperature. This experiment was performed purely as a function of temperature, with powder being collected at smaller temperature intervals in the range 840-940°C.

5.2.1. Experimental.

Time Of Flight powder neutron diffraction was performed on the General Purpose Powder Diffractometer (GPPD) situated at the Intense Pulse Neutron Source (IPNS), Argonne National Laboratory, Illinois, USA. All of the experiments were performed in a vanadium furnace, with the powder patterns being collected for approximately 5 hours at each temperature ($\sim 75\mu\text{Ah}$). A pattern of LiTi_2O_4 spinel was collected at room temperature in order that a good starting model was available for the refinements of the subsequent data. The pattern was collected for 4 hours as this was felt to be sufficient for determination of the structure at room temperature. The sample was then heated to 840°C and held to allow the sample to come to thermal equilibrium. A pattern was collected at 840°C , with subsequent patterns being collected at 10°C intervals in the temperature range $850\text{-}940^\circ\text{C}$. Refinement of the structural models was performed using the GSAS¹² data analysis software running on a personal computer. The powder patterns were refined from the data collected on the backscattering detectors¹³ (148°), with the models being refined in the range 3000 to 29000 microseconds

5.2.2. Results.

The collected powder patterns were then refined at the various temperatures, using three different methods. These methods are presented below,

1. Refinement of the dominant phase present in the powder patterns (method 1).
2. Two phase refinement of the spinel and ramsdellite together if appropriate (method 2).
3. Determination of possible intermediates.

5.2.3. Method 1.

As with all Rietveld refinements, it is necessary to adopt a strategy for the refinement that once found to be stable should be applied to all of the refinements. This ensures that the information collected is comparable in nature. The initial models used were those of Akimoto et al^{3,14}. The refinements in this case were performed as follows,

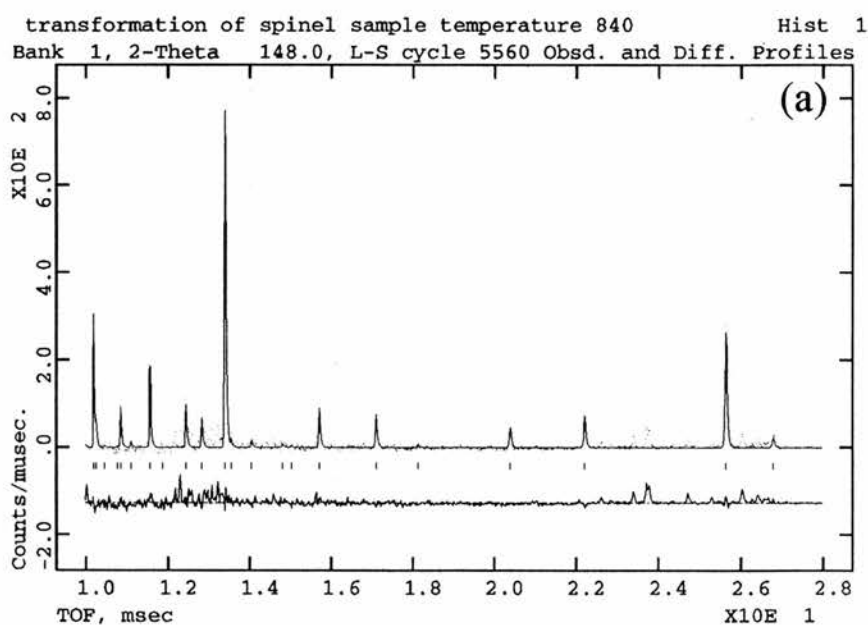
1. The minimum time of flight range was set to 3 microseconds.
2. Background using the Power series in $Q^{2n/n!}$ function (GSAS option 4)
3. Histogram scaling, zero point and lattice parameters.
4. Peak shapes using the profile coefficients described by Von Dreele, Jorgensen & Windsor¹⁵.
5. Atomic position of the atoms for O1, O2 and Ti.
6. Isotropic temperature factors, refinement of the above parameters
7. Anisotropic temperature factors were refined for O1 and O2 and Ti.
8. Li atomic positions and the isotropic temperature factors. Anisotropic refinement of the Li temperature factors was found to be unstable.

The refinements were performed on the powder patterns collected in 10°C intervals in the range 840-940°C with the results obtained presented in table 5.1. Examination of the refined patterns shows that the sample undergoes the transformation at lower temperatures than was found in the previous experiment, with the transformation underway at a similar temperature to that seen by X-ray experiments (chapter 3).

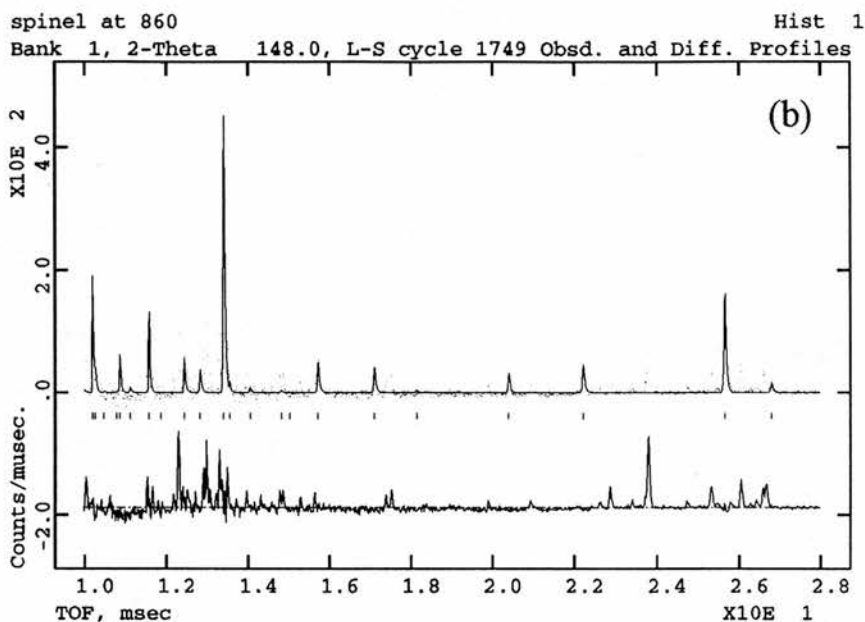
Temperature(°C)	Dominant structure	Rwp (%)	Rp (%)	Chi ²
840	Spinel	9.66	5.12	3.974
850	Spinel	11.77	5.99	5.836
860	Spinel	13.06	6.57	7.07
870	Ramsdellite	15.12	7.98	7.695
880	Ramsdellite	7.54	4.18	2.35
890	Ramsdellite	6.31	3.88	1.637
900	Ramsdellite	5.74	3.59	1.393
910	Ramsdellite	5.79	3.67	1.345
920	Ramsdellite	6.83	4.41	1.225
930	Ramsdellite	6.82	4.54	1.214
940	Ramsdellite	6.85	4.44	1.217

Table 5.1. Table showing dominant pattern at each temperature with errors obtained from single phase refinements.

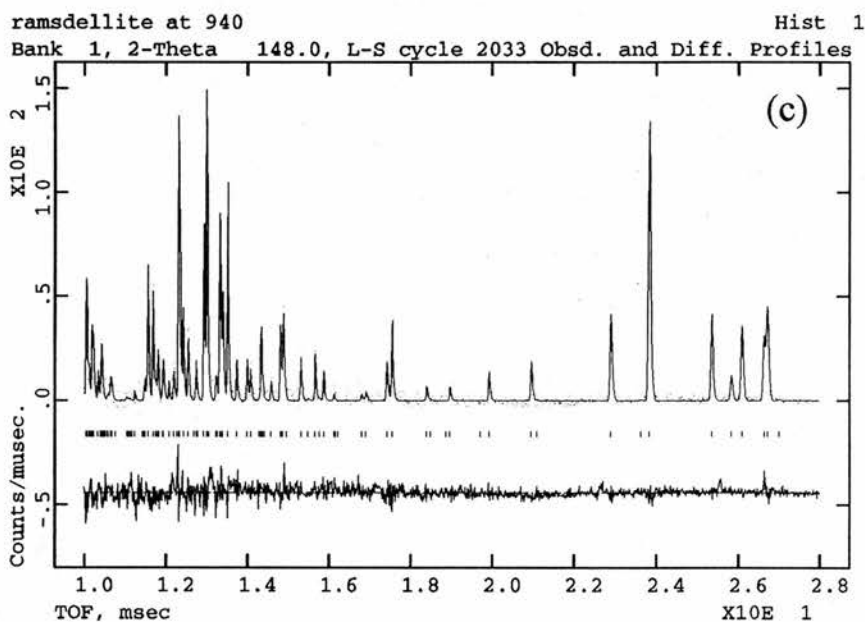
Presented in figure 5.3 are the refined profiles of the sample at 840, 860 and 940°C. Examination of the powder patterns clearly indicates that the sample is in a two-phase region at 860°C.



Pattern collected at 840°C.



Pattern collected at 860°C



Pattern collected at 940°C

Figure 5.3. The refined profiles of the sample at 840 (a), 860 (b) and 940°C (c), patterns shown from 10 to 28 ms only.

5.2.4. Method 2. Refinement of two phase powder patterns.

In order to improve the quality of the fit it was then necessary to perform two phase refinements of the patterns. When performing a two phase refinement it is necessary to first switch off all of the variables mentioned previously and add a scaling factor for each of the phases. This is so that the software can assign the correct peak intensities for each phase. The refinement was then performed according to points 2-7 mentioned previously, both phases being refined simultaneously. The errors associated with these refinements were seen to fall indicating that the quality of the fit had improved. The R factors obtained during these refinements are presented in table 5.2. These values assume the model is similar in nature to that described by Akimoto.

temp(°C)	spinel	ramsdellite	Rwp (%)	Rp (%)	Chi ²	fraction spinel	fraction ramsdellite
840	Yes	No	9.66	5.12	3.974	1.00	0.00
850	Yes	Yes	6.93	4.07	2.031	0.211	0.789
860	Yes	Yes	6.36	3.77	1.684	0.152	0.848
870	Yes	Yes	6.62	4.07	1.482	0.085	0.915
880	Yes	Yes	6.15	3.74	1.567	0.03	0.97
890	Yes	Yes	6.18	3.81	1.575	0.01	0.99
900	Yes	Yes	5.73	3.58	1.387	0.01	0.99
910	trace	Yes	5.78	3.66	1.344	0.00	1.00
920	No	Yes	6.85	4.42	1.23	0.00	1.00
930	No	Yes	6.83	4.55	1.218	0.00	1.00
940	No	Yes	6.85	4.44	1.217	0.00	1.00

Table 5.2. Errors and refined structures obtained from two phase refinements.

The spinel was found to be completely refineable up to at least 860°C, with the unit cell being obtained up to and including 900°C, after which it became impossible to obtain a stable two-phase refinement.

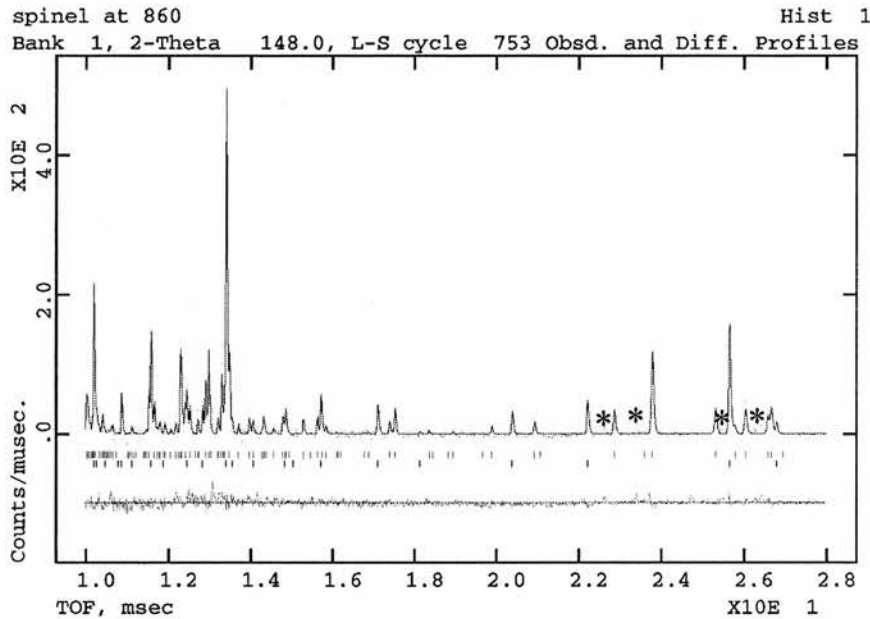


Figure 5.4. Refined pattern obtained at 860°C after two phase refinement. Ramsdellite (upper tick marks). Spinel (lower tick marks).

The pattern presented above in figure 5.4 shows the improvements obtained by using a two phase refinement, although there are still peaks that have not been fitted with the use of two phases. These peaks are marked in the pattern presented above as *.

5.3. The ramsdellite structure at high temperatures.

It was possible to refine peaks related to ramsdellite in the temperature region 850 to 940°C, as was indicated previously in figure 5.4. A small amount of an additional phase was also present in the material at 840 to 850°C, as has been discussed in chapter 3.

In the first instance, attempts were made to refine only Ti, O1 and O2 atomic positions and temperature factors. It was found possible to refine this for the full

temperature range from 850 to 940°C, although at 850°C the low concentration of the ramsdellite phase mean there will be fairly significant errors.

The first refinements of Li distribution was attempted only on the (-0.057, 0.47 .25) channel site described by Akimoto et al, but this model was found to give significantly lower than expected site occupancies. Therefore, three different models were refined in order to ascertain the most likely distribution of Li, these models are presented below,

1. Li located and split over (-0.057, 0.47, 25) and (0.5, 0.05 and 0.25) as described by Morosin et al for $\text{Li}_2\text{Ti}_3\text{O}_7$.
2. Li located and split over (-0.057, 0.47, 151) and (0.5, 0.05 and 0.25) as described by Abrahams et al for $\text{Li}_2\text{Ti}_3\text{O}_7$.
3. Li located at (-0.057, 0.47, 0.151), which is an 8-fold site and hence Li occupancy set to 0.25.

The errors obtained during these refinements are presented below in table 5.3.

Temp	Rwp(%)	Rp(%)	Rwp(%)	Rp(%)	Rwp(%)	Rp(%)
	Model 1		Model 2		Model 3	
850	6.88	4.04	6.87	4.03	6.89	4.03
860	6.32	3.75	<i>NOT</i>	<i>STABLE</i>	6.32	3.74
870	6.55	4.03	6.55	4.03	6.57	4.04
880	6.12	3.72	6.12	3.72	6.13	3.74
890	5.74	3.66	5.74	3.66	5.76	3.70
900	5.42	3.49	5.42	3.48	5.45	3.52
910	5.75	3.63	5.74	3.63	5.73	3.63
920	6.81	4.39	6.80	4.38	6.83	4.41
930	6.73	4.43	6.72	4.43	6.74	4.45
940	6.81	4.43	6.80	4.42	6.82	4.44

Table 5.3. Errors obtained from refinement of the 3 Li distributions presented above

As can be seen from the errors obtained from the refinements the value are not significantly different whichever model is used during the refinements. In an attempt to ascertain which model was most physically meaningful, the bond angles and lengths were examined. It was stated by Akimoto that the Li-O₄ tetrahedra were distorted with one Li-O bond distance in the region of 2.22(2)Å angstroms and the other 1.80(2)Å. On this basis, the bond distances of the Li-O(1) and Li-O(2) were examined at 940°C and used as the basis of which model was likely to be correct. These results are presented below in table 5.4.

Distance/model	1 (4c, 4c)	2 (8a, 4c)	3 (8a)
Li1 -O(1)	2.09(5)	2.10(4)	2.10(4)
Li1-O(1)	-	2.67(4)	2.63(4)
Li1-O(2)	1.88(5)	1.70(5)	1.66(5)
Li1-O(2')*2	2.08(4)	-	-
Li1-O(2)	-	2.02(4)	2.05(4)
Li1-O(2)	-	2.46(4)	2.55(4)
Li2-O(1)	2.16(5)	2.14(6)	-
Li2-O(1)	2.54(4)	2.56(5)	-
Li2-O(2)	1.76(5)	1.78(6)	-
Li2-O(2)	2.28(4)	2.26(4)	-

Table 5.4. Li-O bond distances obtained for three model proposed for Li distribution.

As model 3, does not contain any Li2 sites, only half of the bond lengths are present in the above table. Models 1 and 2, have one short bond distance, being that for Li2-O(2), they are not significantly different to the value of 1.80 Å indicated by Akimoto. From ionic radius considerations, it would be expected that an average Li-O bond distance would be 1.95Å, thus interatomic distances of 1.70 Å or less must be viewed with some caution, therefore the most reasonable model would be that described in model 1. Looking at the Li1-O(1) and Li1-O(2) bond distance we see that they have changed significantly from the 2.22 and 1.80Å indicated by Akimoto, suggesting that the Li-O₄ units becomes less distorted at higher temperatures. In

order to make a distinction between the model 1 and 2, the Li-Li intersite distances were examined. These are presented below in table 5.5,

	Model 1	Model 2
Li1-Li1	2.9948(2)	2.9949(2)
Li1-Li1	1.98(7)	2.06(5)
Li1-Li1	-	1.48(8)
Li1-Li1	-	2.92(9)
Li1-Li1	-	1.93(10)
Li1-Li1	-	1.06(10)
Li1-Li2	3.31(3)	2.86(5)
Li1-Li2	1.41(7)	1.04(5)
Li1-Li2	1.53(2)	2.06(5)
Li2-Li2	2.9948(2)	2.9949(2)
Li2-Li2	2.14(8)	2.18(9)

Table 5.5. Selection of Li-Li Intersite distances obtained for model 1 and 2.

It was noted that some of the intersite distances between Li1 and Li2 at high temperature are relatively short in both model 1 and 2. It is conceivable that with low occupancies these bond distances may be accommodated. However two of the bond distances for model 2 were found to be approximately 1 Angstrom. This is anomalously short for a Li-Li Intersite distance, therefore on this basis, model 1 was thought to be the most likely. In all of the discussions to follow, model 1 was used.

In the all of the graphs to follow, lines have been drawn on the plot to indicate the extent of the transition or 2 phase region. These points have been deduced from visual inspection of the powder patterns, as well as the stability of the refinement at the relevant temperatures. The onset and end of the transformation are marked as T_{onset} and T_{end} respectively. Presented below in 5.5(a) to (c) are the unit cell edges obtained from the refinements.

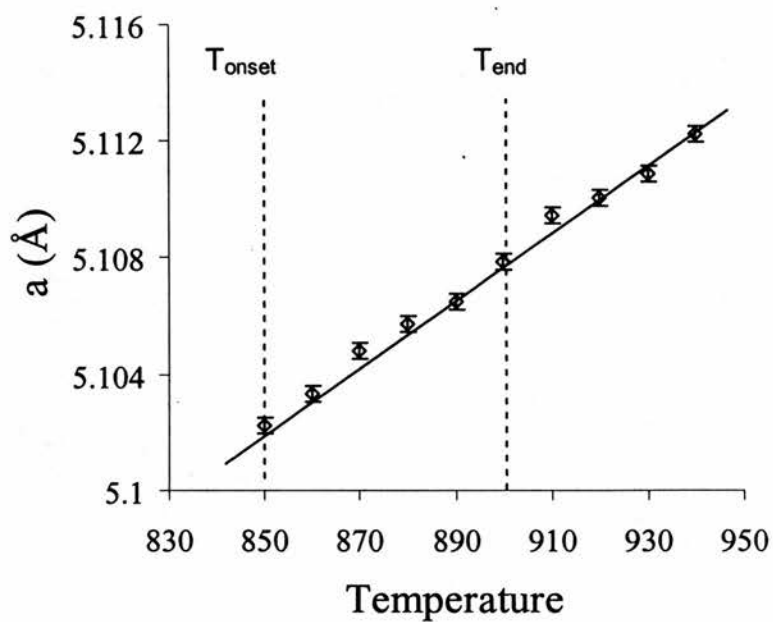


Figure 5.5(a). Unit cell edge **a** versus temperature.

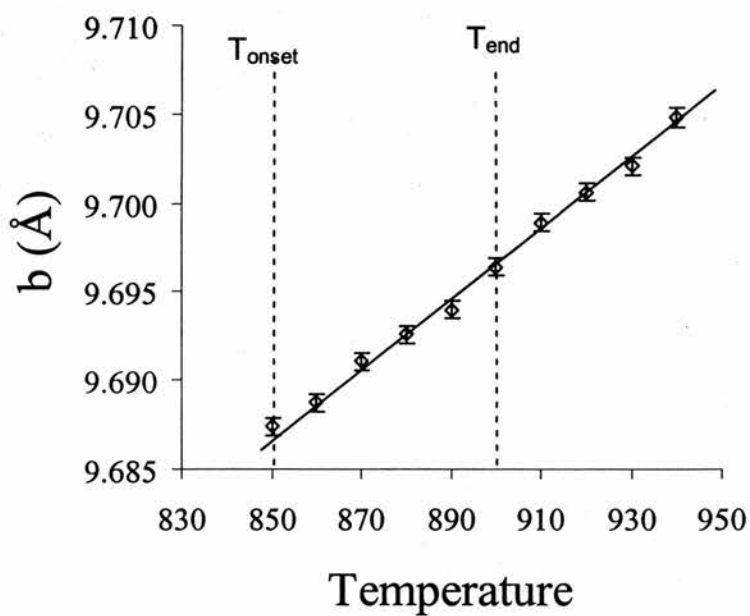


Figure 5.5(b). Unit cell edge **b** versus temperature.

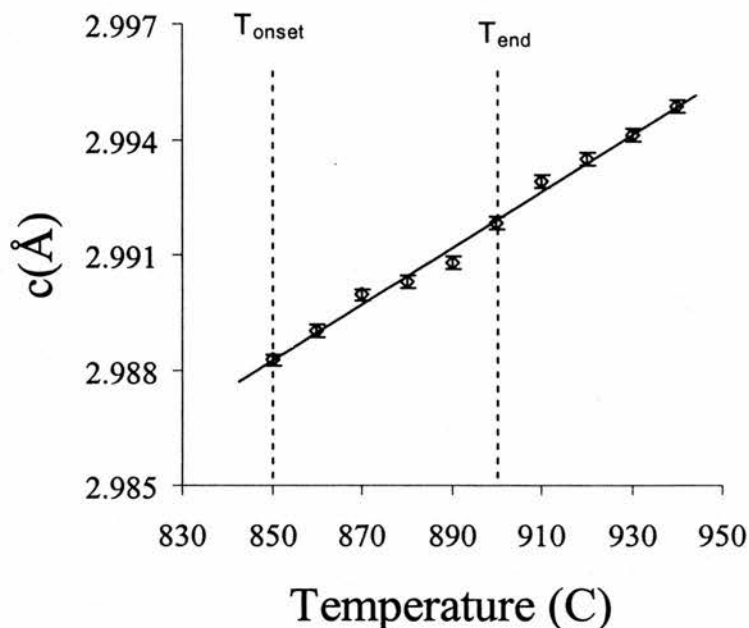


Figure 5.5(c). Unit cell edge c versus temperature.

Presented in table 5.6 are the obtained atomic positions of Li1 and Li2. The Li position is seen to move very slightly as a function of temperature, with Li1 moving more towards the Li position described by Akimoto of $(-0.057 \ 0.47 \ 0.25)$ at approximately 890°C,

Temp	Li1 X	Li1 Y	Li2 X	Li2 Y
850	-0.060(10)	0.411(7)	0.498(13)	0.033(10)
860	-0.066(11)	0.413(7)	0.492(16)	0.041(11)
870	-0.056(9)	0.426(7)	0.481(11)	0.052(7)
880	-0.062(8)	0.423(6)	0.489(12)	0.057(7)
890	-0.064(7)	0.448(4)	0.489(9)	0.058(5)
900	-0.058(6)	0.443(4)	0.494(8)	0.055(5)
910	-0.078(10)	0.449(6)	0.494(9)	0.068(6)
920	-0.057(9)	0.452(6)	0.482(9)	0.062(5)
930	-0.058(21)	0.448(15)	0.508(12)	0.052(9)
940	-0.070(11)	0.444(1)	0.473(10)	0.081(6)

Table 5.6. Obtained atomic position of Li1 and Li2 versus temperature.

Presented in table 5.7 are the obtained Ti, O1 and O2 atomic positions as a function of temperature.

Temp	Ti X	Ti Y	O1 X	O1 Y	O2 X	O2 Y
850	-0.027(3)	0.142(2)	0.674(2)	0.2739(9)	0.2030(1)	-0.0348(8)
860	-0.022(2)	0.140(1)	0.674(1)	0.2746(7)	0.2032(9)	-0.0331(5)
870	-0.022(1)	0.143(1)	0.678(1)	0.2744(5)	0.2038(8)	-0.0336(4)
880	-0.023(1)	0.142(1)	0.681(1)	0.2746(4)	0.2027(6)	-0.0338(3)
890	-0.019(1)	0.1409(6)	0.681(1)	0.2748(3)	0.2034(5)	-0.0335(3)
900	-0.022(8)	0.1406(6)	0.6807(6)	0.2745(3)	0.2028(5)	-0.0338(3)
910	-0.022(8)	0.1406(6)	0.6807(6)	0.2745(3)	0.2028(5)	-0.0338(3)
920	-0.022(1)	0.1415(7)	0.6798(8)	0.2752(4)	0.2034(6)	-0.0332(3)
930	-0.022(1)	0.1425(6)	0.6816(7)	0.2751(4)	0.2037(6)	-0.0334(3)
940	-0.022(1)	0.1424(7)	0.6786(8)	0.2739(4)	0.2046(6)	-0.0336(3)

Table 5.7. Obtained atomic position of Ti1, O1 and O2 versus temperature.

Examination of the results presented above suggests that the Ti, O1 and O2 positions vary little with temperature in the range 850-940°C, indicating that the octahedra are fairly stable.

The isotropic temperature factors obtained for Li1 and Li2 are presented below in figure 5.6(a). The temperature factors for Li1 show an increase across the temperature range examined, with a plateau seen in the range 910 to 940°C. The isotropic temperature factors for Li2 were seen to decrease as the temperature increased. As the temperature factors are intimately related to the occupancy of a site, this could indicate that the occupancy of the second lithium site at high temperature is decreasing as the temperature is increased.

Presented in figure 5.6(b) are the temperature factors obtained for Ti, O1 and O2 respectively. They show a basically linear behaviour in the temperature range examined. Presented below in figures 5.7, 5.8 and 5.9 are the obtained anisotropic temperature factors obtained for Ti, O1 and O2

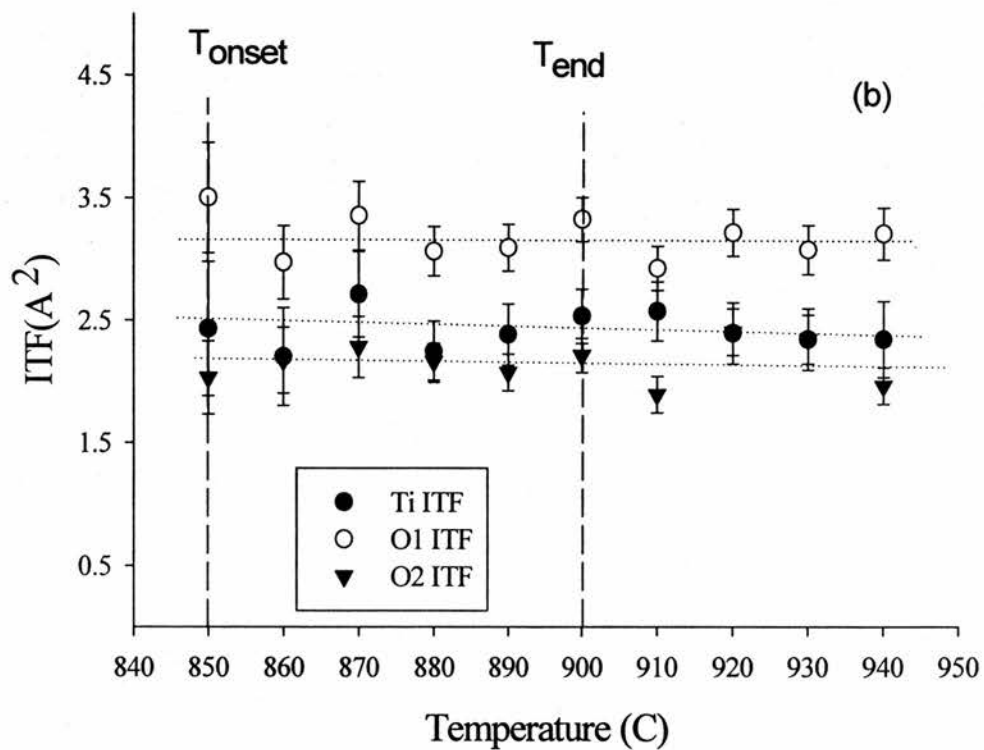
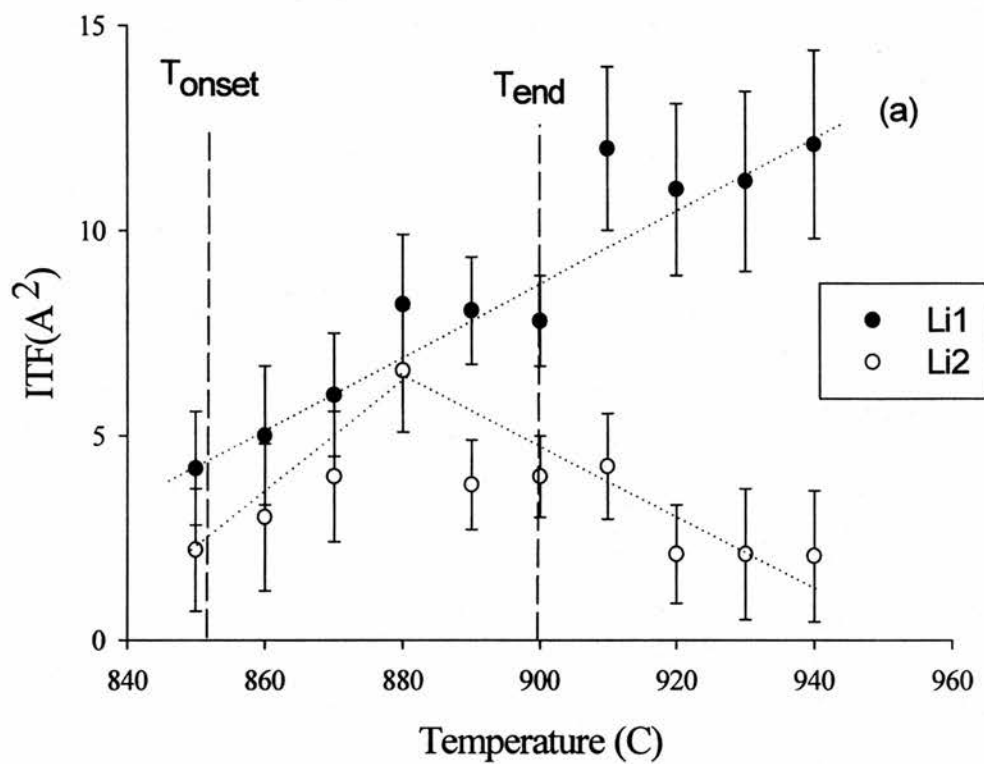


Figure 5.6(a). Obtained Li1 and Li2 ITFs versus temperature for LiTi_2O_4 ramsdellite (b) Ti, O1 and O2 ITFs versus temperature for LiTi_2O_4 ramsdellite. Lines used as a guide to the eye.

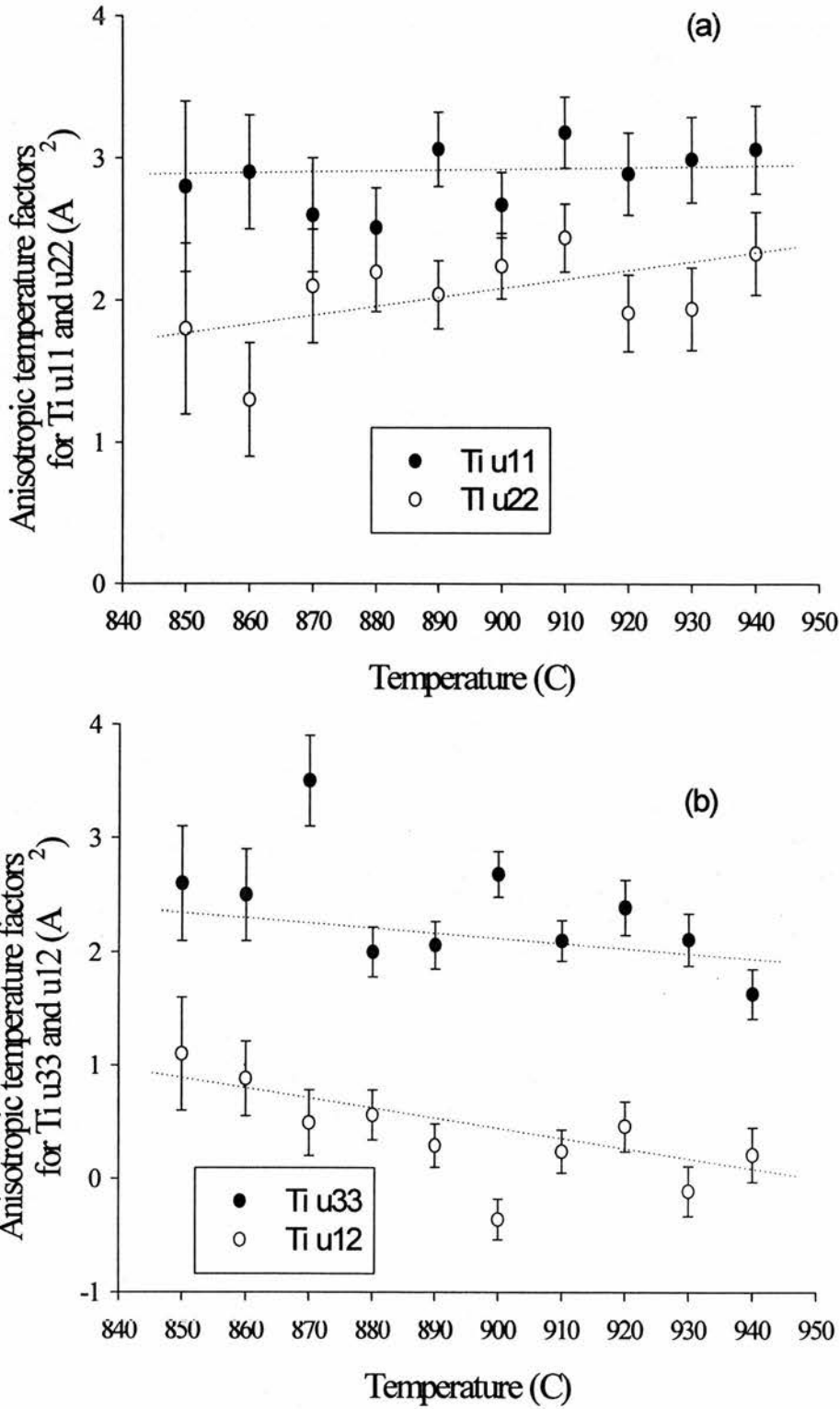


Figure 5.7(a). The Anisotropic temperature factors obtained for u11 and u22 for Ti as a function of temperature (b) The Anisotropic temperature factors obtained for u33 and u12 for Ti as a function of temperature. Lines used as a guide to the eye

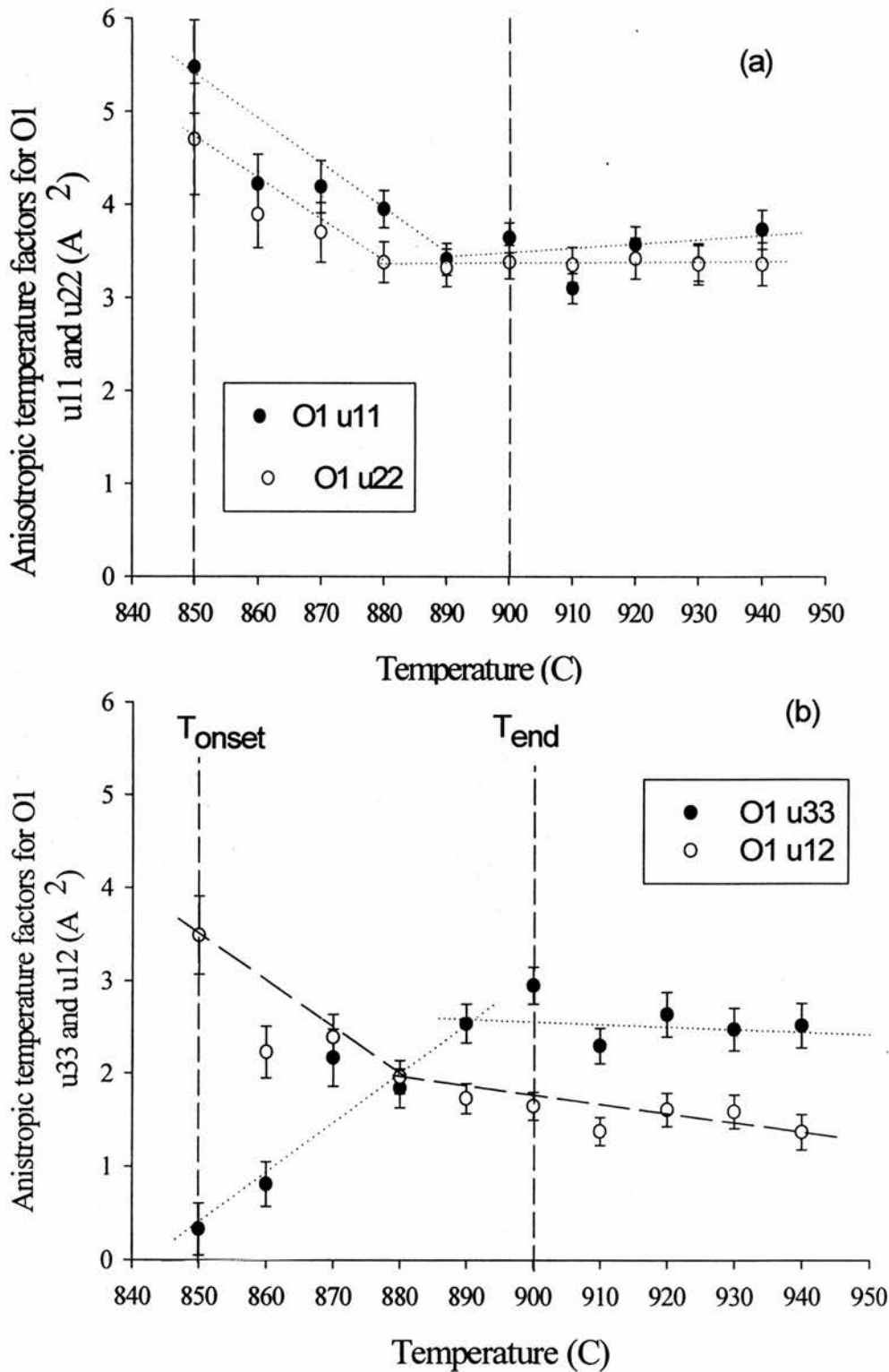


Figure 5.8(a). The Anisotropic temperature factors obtained for u_{11} and u_{22} for O1 as a function of temperature. (b) Anisotropic temperature factors obtained for u_{33} and u_{12} for O1 as a function of temperature. Line used as a guide to the eye.

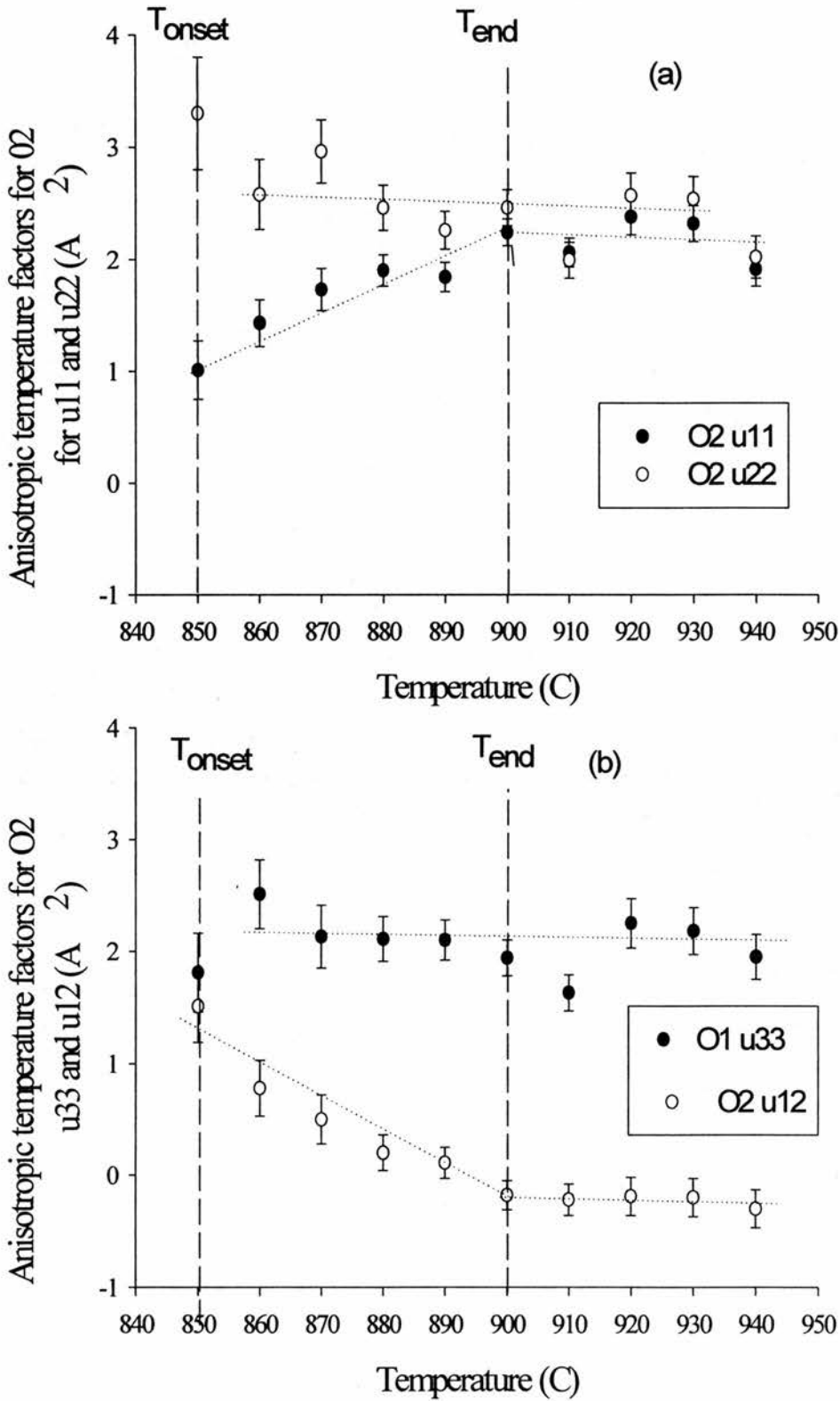


Figure 5.9(a). The Anisotropic temperature factors obtained for u11 and u22 for O2 as a function of temperature. (b) Anisotropic temperature factors obtained for u33 and u12 for O2 as a function of temperature. Line used as a guide to the eye.

The results presented above in figures 5.7 to 5.9 show the variation in the anisotropic temperature factors as a function of increasing temperature. It is noted that the greatest changes occur in the region indicated as the transition region, with the values obtained after the transition seen to be basically constant.

It was indicated above it was found possible to refine the Li site occupancy in the range 850-940°C assuming the model described as model 1 being used. It would be incorrect to hold the total occupancy of the Li1 (site at $\sim -0.06, 0.45, 0.25$) and Li2 (site at $\sim 0.5, 0.05, 0.25$) to equal 0.5, as it could be possible that the phases become Li rich or deficient as a function of temperature.

Presented in figure 5.10 are the obtained Li1, Li2 and total lithium occupancy as a function of increasing temperature. Over the temperature range examined the occupancy of the Li1 site was seen to increase as the sample temperature was raised, with an approximately equal and opposite effect seen for total occupancy of the occupancy of the Li2 site. This suggests that the site splitting is related to the development of longer range order in the ramsdellite.

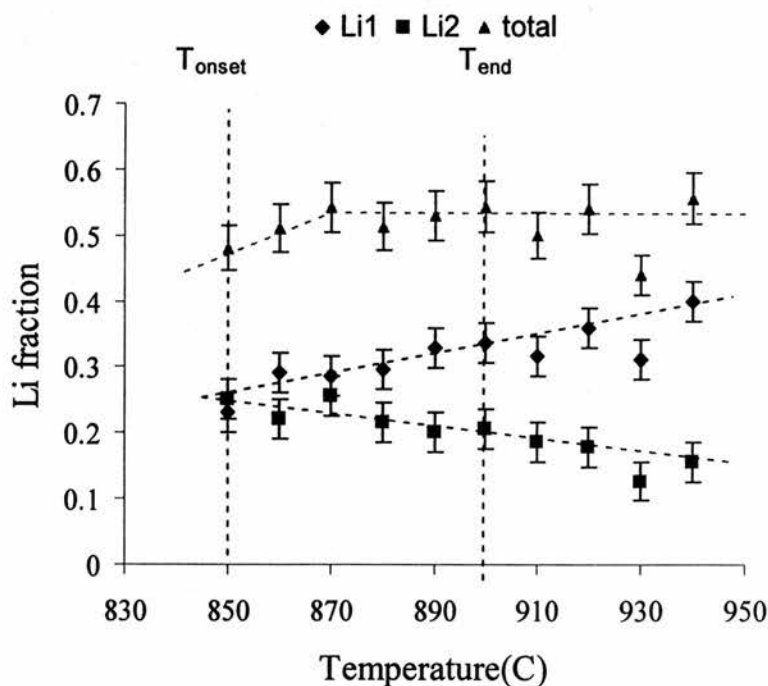


Figure 5.10. Li site occupancy for Li1, Li2 and total as a function of temperature, dashed lines used as a guide to the eye.

Presented in figure 5.10 is the proposed distribution of Li in LiTi_2O_4 at high temperatures. Note that the model proposed in figure 5.11 shows all sites with 100% occupancy, where the actual occupancies of Li1 and Li2 are dependent on sample temperature and in this sample not going to be higher than approximately 50%.

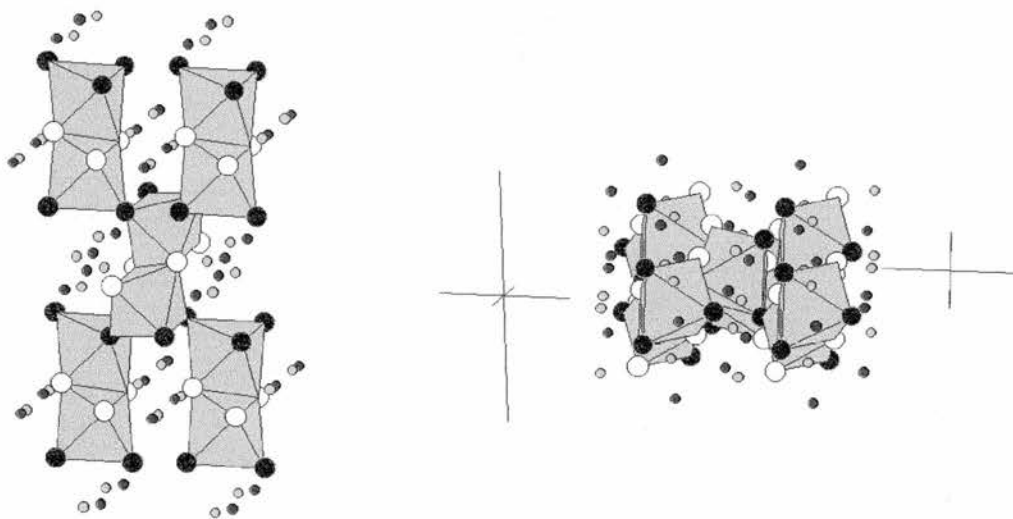


Figure 5.11(a). Proposed Li distribution within the ramsdellite structure at high temperatures looking down the *c* axis (Li1 in green, Li2 in yellow). (b) Looking down the *b* axis.

Refinement of the powder patterns collected at ISIS at 1000°C also produced stable refinements, which are in approximate agreement with the results present above in figure 5.10. Presented in figure 5.11(c) is a DELF Fourier map of the ramsdellite structure taken. Presented in figure 5.11(d) is a section of the ramsdellite structure projected onto the *a/c* cell plane.

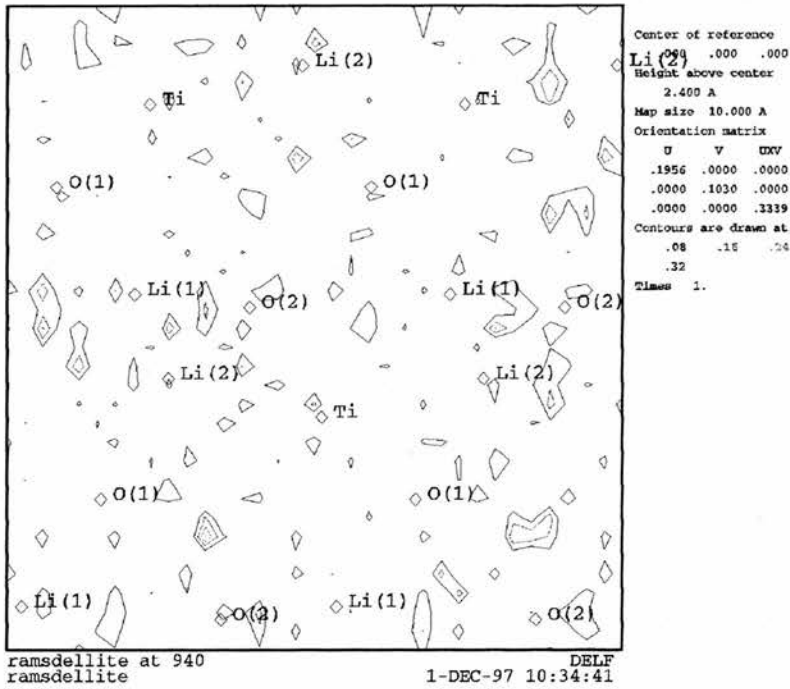


Figure 5.11(c). DELF Fourier map of a section of the ramsdellite structure at 940°C.

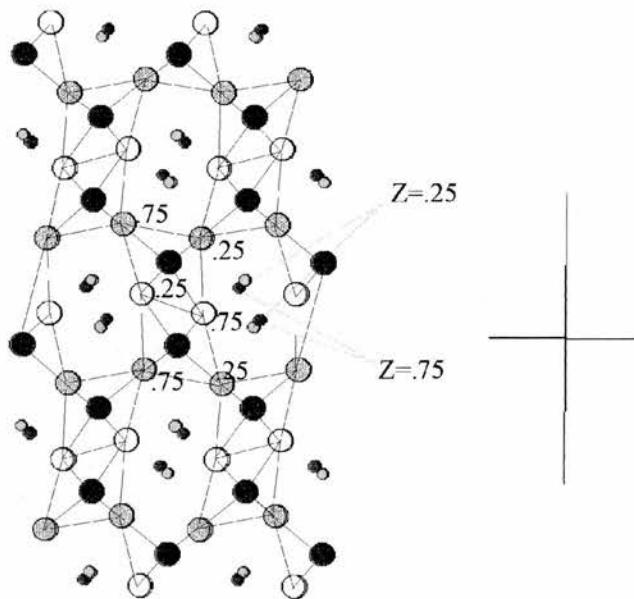


Figure 5.11(d). LiTi_2O_4 ramsdellite at 940°C projected onto the a/c plane. Li1 in green, Li2 in yellow, O1 in white, O2 in light grey. Height up the Z axis given. These show the distribution of Li sites with Li S.O.F $\neq 1$.

The Ti occupancy was refined in order to see if any changes could be seen in the occupancy as the sample temperature was increased. However, it was found that the occupancy of the Ti was very close to one at all temperatures. Attempts were also made to refine lithium on the framework sites in place of the titanium. This was found to lead to no significant improvement in the quality of the fits.

5.4. Spinel to ramsdellite transformation temperature.

The experiments presented in section 5.1 suggest that the transformation onset temperature was in the region of 875°C. This was not found to be the case in this experiment. Presented in figure 5.12 is the powder pattern collected at 850°C.

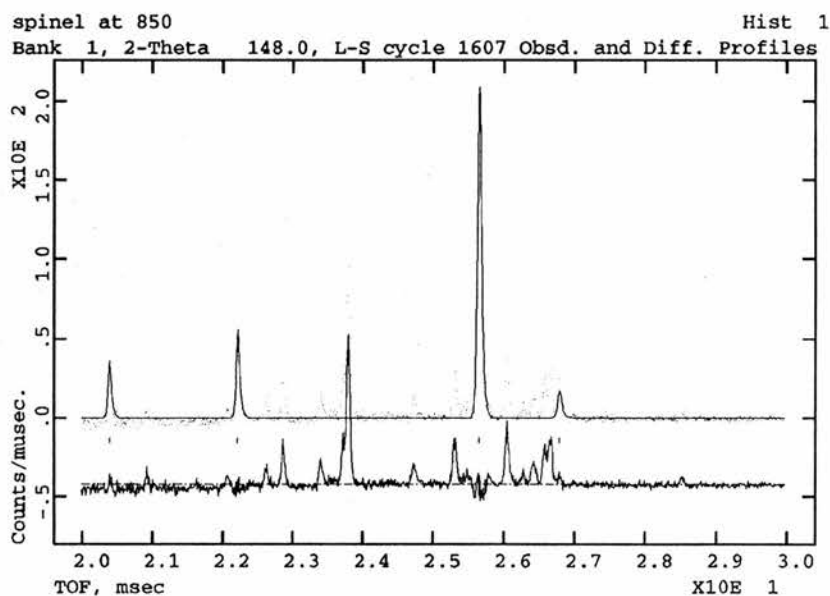


Figure 5.12. Refined powder pattern for pattern collected at 850°C

The pattern presented above clearly shows the presence of a ramsdellite phase, examination of the pattern collected at 910°C (see figure 5.13), indicates that the sample is predominantly ramsdellite.

Examination of the phase fraction of spinel and ramsdellite was used to provide a guide to the extent of conversion from spinel to ramsdellite as a function of sample temperature. This is presented in figure 5.14.

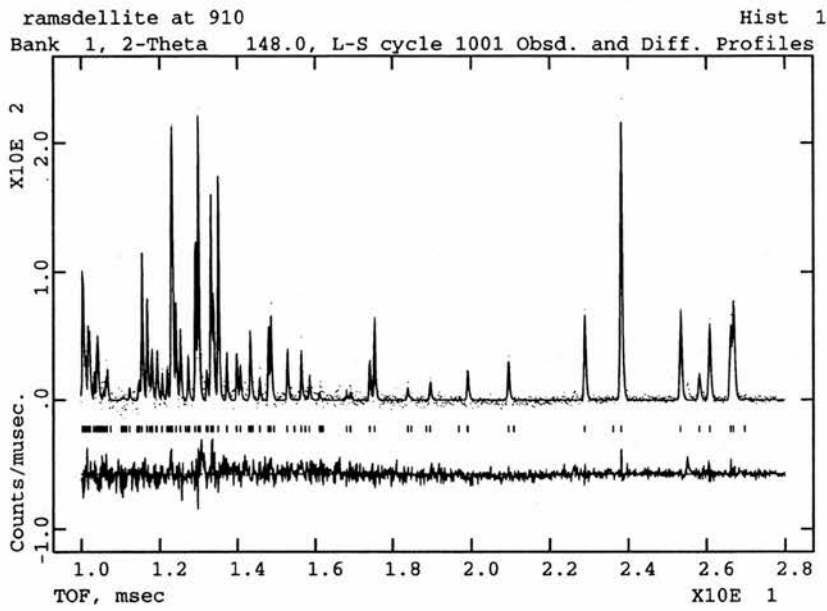


Figure 5.13. Refined powder pattern for pattern collected at 910°C

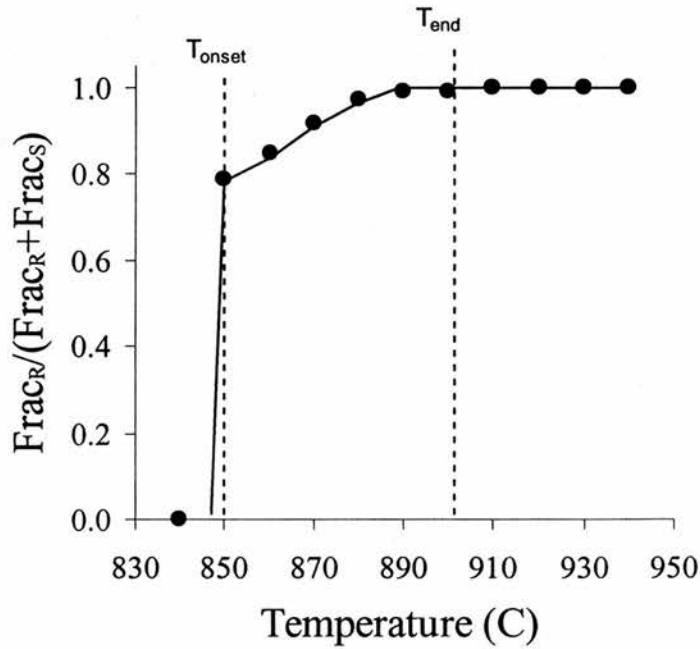


Figure 5.14. Ratios of the phase fractions for spinel and ramsdellite as obtained from refinement of the neutron powder patterns in the region of 840-940°C.

Presented below in table 5.8 is a summary of the results obtained of X-ray experiments (presented in chapter 3), the results obtained from the ISIS experiments and the results obtained during the IPNS experiments.

	X-ray	Neutrons (ISIS)	Neutron (IPNS)
Onset (°C)	850-860	875	850
Completion(°C)	N/A	925	900

Table 5.8. Table of temperatures of transformation obtained from spinel to ramsdellite transformation experiments.

It is seen from the results presented in table 5.8, the transformation probably occurs at just over 850°C, although nearly single phase samples of LiTi_2O_4 spinel can be produced on firing at 850°C. The ISIS experiments show the highest transformation onset temperature, this may well reflect a difference between the sample temperature and the temperature measured by the thermocouple as the completion temperature is also 25°C higher. A good correlation is seen between the results obtained from powder X-ray experiments and the neutron experiments performed at IPNS. From these results it can be concluded that the transformation starts at approximately 850°C, with it having gone to completion at 900°C. The neutron results presented in chapter 3 (section 3.4.3) for spinel shows a deviation in the spinel unit cell edge in the region of 860 to 870°C.

5.5. Determination of the possible intermediate(s).

Examinations of the powder patterns collected in the region of 910 to 940°C indicate a small amount of a second phase. Presented in figure 5.15 is the refined powder pattern collected at 930°C, with the unknown peak marked with a *.

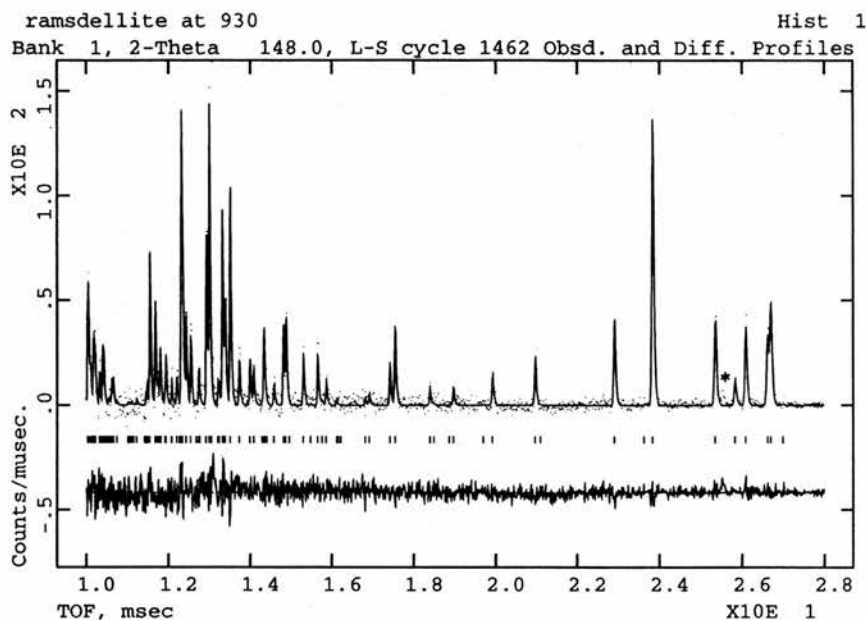


Figure 5.15. Refined powder pattern for pattern collected at 930°C

The unassigned peak present shown above (marked as *) was found to have a d spacing of approximately 2.447 angstroms. The origins of this peak could not be determined, but may be related to the (2 2 2) reflection of a spinel cell of unknown composition and may be a residual of the transformation. However assignment as spinel cannot be made on the basis of one peak. In the intermediate temperature range 840-850°C it was noted that unfitted peaks were present in the powder patterns, however these have been covered more fully in chapter 3, section 3.5.

5.6. Discussion.

The spinel unit cell (see chapter 3) does show a deviation from linear behaviour in the region of 870°C, which could be a possible indication of a change in the spinel composition preceding the transformation. The unit cell of ramsdellite shows a linear expansion along all three axes as the temperature was increased, showing no evidence for a change in the composition of ramsdellite.

Difference Fourier mapping of the high temperature ramsdellite structure indicated the presence of two different Li sites within the structure, these sites being

found at approximately $(-0.06, 0.45, 0.25)^3$ and $(0.5, 0.05, 0.25)^2$. The coordinates of these two sites are similar to that seen by Morosin in reference 2 for $\text{Li}_2\text{Ti}_3\text{O}_7$. It was found possible to refine the position of these two sites in the temperature range 850 to 940°C. The TiO_6 octahedra was also found to be stable over the temperature examined, with little change seen in the positions of these octahedra, indicating that they are stable as a function of temperature. Attempts were also made to refine Li on the Ti framework sites, this was found to make no improvement to the quality of the fits and hence it could be concluded that this does not occur.

Examination of the temperature factors of Li, shows an increase in Li1 temperature factor $(-0.06, 0.45, 0.25)$ as the temperature is increased, which is not surprising considering the apparent mobility of Li at room temperature (see chapters 5 and 6). A similar trend is seen for Li2 $(0.5, 0.05, 0.25)$ in the region 850-880°C, after which the temperature factors are seen to decrease. This could be an indication of the site occupancy of this site decreasing (this will be discussed at a later stage).

The isotropic temperature factors for Ti, O1 and O2 show a basically linear behaviour over the temperature range examined. On conversion to anisotropic temperature factors it was seen that they changed most noticeably in the region of transformation.

Refinement of the site occupancies for Li1 shows a gradual increase as the temperature is raised, with a corresponding decrease seen in the temperature factors for Li2. This decrease in occupancy should also manifest itself as a decrease in the isotropic temperature factors, which was seen as described previously. The total occupancy of the two Li sites was seen to be very close to the ideal total occupancy of 50 % (within errors).

Some of the inter site distances for Li1 and Li2 were seen to be short, however the site occupancies are low and hence the interaction between the two sites will be minimal.

The results presented in this section of work suggest that the transformation temperature was lower in this experiment than had been previously suggested in the ISIS experiment. The transformation temperature in this experiment was found to be in the region of 850-900°C compared to the 875 to

925°C found in the ISIS experiments. The onset temperature of the transformation agrees well with the results obtained from X-ray diffraction experiments (see chapter 3), which suggested the onset occurs in the region of 850-860°C.

5.7. Conclusions.

The results presented in this chapter suggest that the spinel to ramsdellite transformation is not straightforward. The results presented in chapter 3 (section 3.4.3) show a deviation in the unit cell dimensions (and consequently the unit cell volume) from linear behaviour in the region of 870°C. This can be interpreted¹⁶ as being due to a second order transition occurring in the sample.

The composition of the spinel was not seen to vary at temperatures approaching the transformation temperature (see chapter 3), however a deviation was noted in the unit cell dimensions, this is consistent with a second order phase transition. The unit cell dimensions of ramsdellite were not seen to deviate over the temperature range examined. Refinement of the site occupancies at high temperature for the ramsdellite gave values consistent with stoichiometric LiTi_2O_4 , and it thus could be concluded that transformation does not proceed via Li rich or deficient spinel/ramsdellite phases.

The two Li sites seen in the second neutrons experiment are very similar to the models proposed by Morosin and Abrahams¹⁷ for $\text{Li}_2\text{Ti}_3\text{O}_7$ ^b, with Li to be found at approximately (-0.057, 0.47 0.25) and (0.5, 0.05, 0.25). The total occupancy of the Li1 was seen to increase as the temperature was increased, whereas the Li2 site decreases as a function of increasing sample temperature.

This may suggest that the model presented for $\text{Li}_2\text{Ti}_3\text{O}_7$ ramsdellite by these authors may be a consequence of the sample preparation. Although no mention of the method of sample preparation is made in Morosin work, Abrahams used the methods described by Izquierdo et al⁵, which involved sample quenching from the

^b Abrahams found that one of the sites was actually 8-fold rather 4 fold, but was very similar to the model indicated in this chapter.

preparation temperature. It may be possible that quenching $\text{Li}_2\text{Ti}_3\text{O}_7$ ramsdellite from high temperature may “trap Li over two sites”.

Experiments presented in chapter 6 do not show the presence of a second Li site in $\text{Li}_2\text{Ti}_3\text{O}_7$, however these samples were furnace cooled and this may have allowed all of the Li to move back onto the Li1 site. It is conceivable that at lower temperature the Li1 site is fully occupied and Li2 may be an intermediate for Li hopping. Further experiments would need to be performed to determine whether this is the case.

Vacuums were used during the high temperature neutron studies in order that the sample did not undergo oxidation. Although the effects of vacuum on the absolute transformation temperature has not been studied it would be foolish to assume that the transformation temperature would necessarily be the same.

5.8. Acknowledgements

An acknowledgement must be made to Raymond R. Thomas of the Intense Pulsed Neutron Source for collection of the neutron powder patterns in the second neutron study.

5.9. References.

1. D.C. Johnston, H. Prakash, W.H. Zacharisen and R. Viswanthan, *Mater. Res. Bull.*, **8** (1973) 777
2. B. Morosin and J.C. Mikkelsen, *Acta. Crystallogr, sect B.*, **35** (1979) 798.
3. J. Akimoto, Y Gotoh, M. Sohma, K. Kawaguchi, Y. Oosawa and H. Takei, *J Solid State Chem.*, **110** (1994) 150.
4. A.R. West, *Solid state chemistry and its application*, John Wiley and son, Chichester, 1984.
5. G. Izquierdo and A.R. West, *Mat Res. Bull.*, **15** (1980) 1655.
6. M.J. Buerger, *Fortchr. Miner.*, **39** (1961) 9.
7. M.J. Buerger, *Soviet Physics - Crystallography.*, **16** (1972) 959

-
8. M.M. Thackeray, M.H. Rossouw, R.J. Gumnov, D.C. Liles, K. Pearce, A. De Kock, W.I.F. David and S. Hull, *Electrochim. Acta.*, **38** (1993) 1259.
 9. J.C. Mathewmann, P. Thompson and P.J. Brown, *J. Appl. Crystallogr.*, **15** (1982) 167.
 10. P.J. Brown and J.C. Mathewmann, Rutherford Appleton Laboratory Report, RAL-87-010 (1987).
 11. M Dalton, *PhD thesis*, Univ. of Cambridge, 1992.
 12. A.C. Larsen and R.B. Von Dreele, *Los Alamos Laboratory report*, NO-LA-U-86-748 (1987).
 13. J.W. Richardson Jr, *IPNS progress report.*, **1** (1991-1996) 16.
 14. J. Akimoto, Y. Gotoh, K. Kawaguchi and Y. Oosawa., *J. Solid State Chem*, **96** (1992) 446.
 15. R.B. Von Dreele, J. Jorgensen and A. Windsor., *J. Appl. Cryst.*, **15** (1982) 581.
 16. P.W. Atkins, *Physical Chemistry, 4th Edition*, Oxford University Press, (1990) 144.
 17. I. Abrahams, P.G. Bruce, W.I.F. David and A.R. West, *J Solid State Chem.*, **78** (1989) 170.

Chapter 6. Studies on LiTi_2O_4 ramsdellite.

6.1. Introduction.....	169
6.2. Powder neutron diffraction studies on LiTi_2O_4 Ramsdellite.....	169
6.2.1. Experimental.....	169
6.2.2. Results.....	170
6.2.3 Discussion.....	173
6.3. The magnetic properties of LiTi_2O_4 ramsdellite.....	173
6.3.1. Experimental.....	173
6.3.2. Results.....	174
6.3.3. Discussion.....	177
6.4. Longitudinal μ^+SR Studies.....	178
6.4.1. Experimental.....	178
6.4.2. Results.....	179
6.4.3. Discussion.....	184
6.5. Electrical property measurements.....	186
6.5.1. Introduction.....	186
6.5.2. Experimental.....	186
6.5.3. Results.....	186
6.5.4. Impedance spectroscopy measurements.....	188
6.5.5. Results.....	188
6.5.6. Discussion.....	189
6.6. Conclusions.....	190
6.7. References.....	192

6.1. Introduction.

The ramsdellite structure was first described by Bystrom et al¹ for $\gamma\text{-MnO}_2$ and consists of distorted MO_6 octahedra, which link up with adjacent octahedra, by sharing opposite edges, therefore forming columns. Adjacent pairs of columns share edges to form double columns, giving rise to an open framework type structure. In between these columns are tetrahedral channel sites into which smaller ions² such as H^+ and Li^+ can be placed. It has been suggested that LiTi_2O_4 spinel converted to LiTi_2O_4 ramsdellite at high temperatures, but it wasn't until 1994, that Akimoto³ succeeded in preparing single crystals of LiTi_2O_4 ramsdellite and confirmed that the stoichiometry of this phase was LiTi_2O_4 with a ramsdellite structure type.

The aims of this chapter are to re-examine the structure as determined by Akimoto for LiTi_2O_4 ramsdellite, and to investigate the properties of this material. Akimoto determined the crystal structure of LiTi_2O_4 ramsdellite using single crystal X-ray diffraction. However, even using single crystals, the scattering power of Li is still relatively low. Due to the superior resolving power of neutron with respect to lighter atoms such it Li, it was decided that the structure should be re-examined using powder neutron diffraction.

6.2. Powder neutron diffraction studies on LiTi_2O_4 Ramsdellite.

6.2.1. Experimental

Structural studies on LiTi_2O_4 ramsdellite were performed using Time Of Flight neutron powder diffraction on the Polaris diffractometer⁴. An in-situ^A prepared sample of ramsdellite was placed in a standard vanadium can, and a powder pattern collected at room temperature for four hours ($\sim 700\mu\text{Ah}$). Rietveld⁵ refinement was performed using the TF14LS CCSL software running on the ISIS HUB mainframe computer^{6,7} with only the data collected from the backscattering detectors being used ($135^\circ < 2\theta < 160^\circ$).

^A Prepared as a result of a previous experiment.

6.2.2. Results.

The structure of the ramsdellite form of LiTi_2O_4 was refined using the $P6mm$ space group (number 62)⁸ and based on the model proposed by Akimoto³. Initially the structure was refined holding the lithium atomic parameters constant. The background, lattice, Ti, O1 and O2 atomic co-ordinates and isotropic temperature factors were refined giving R_{wp} and R_p of 5.40 and 5.26 respectively. With the TiO_6 octahedra stable, the lithium atomic positions and isotropic temperature factors were refined with values of R_{wp} and R_p of 3.28 and 4.15 respectively being obtained. The temperature factors of the lithium were then refined anisotropically and final R_{wp} and R_p values of 2.91 and 3.74 obtained. The obtained neutron powder patterns for the ramsdellite phase are presented in figure 6.1. Presented below in table 6.1, is the obtained crystallographic data for LiTi_2O_4 ramsdellite.

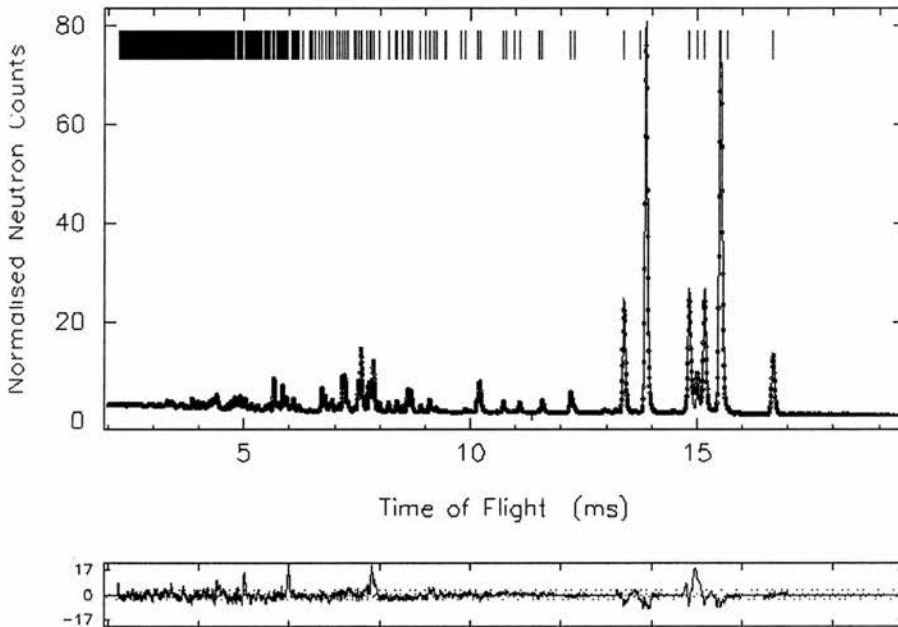


Figure 6.1. Refined Time of Flight neutron powder diffraction pattern and difference profile of LiTi_2O_4 ramsdellite. Experimental point shown as dots, with the calculate model shown as a line.

Crystal system	Orthorhombic
Space group	Pbnm
a(Å)	5.03426(3)
b(Å)	9.62019(6)
c(Å)	2.94816(2)
Rwp (%)	2.91
Rp (%)	3.74

Table 6.1. Obtained crystallographic data for LiTi_2O_4 ramsdellite.

The unit cell obtained from this experiment was slightly smaller than that reported previously by Akimoto, who reported unit cell dimensions of $a = 5.0356(6)$ Å, $b = 9.6377(8)$ Å and $c = 2.9484(7)$ Å. These differences should not be viewed as significant. The total errors obtained from the refinement indicate a good fit and that the structural model described by Akimoto is correct. Presented in table 6.2 are the obtained atomic positions and the anisotropic temperature data, which again are not significantly different to those obtained previously.

	Li	Ti	O1	O2
X	-0.058(16)	-0.0182(3)	0.700(3)	0.202(2)
Y	0.47(13)	0.1420(2)	0.280(1)	-0.0355(1)
Z	0.2500	0.2500	0.2500	0.2500
B11(±) ^B	1.3(2)	0.45(5)	0.87(3)	0.37(2)
B22(±)	8.5(6)	0.49(4)	0.89(3)	0.41(3)
B33(±)	1.79(3)	0.17(3)	0.47(3)	0.54(3)
B12(±)	-0.61(4)	0.11(4)	0.43(3)	-0.02(3)
B13	0	0	0	0
B23	0	0	0	0
S.O.F ^C	0.47(5)	1	1	1

Table 6.2 Atomic position parameters and anisotropic temperature factors obtained from Rietveld refinement of LiTi_2O_4 ramsdellite.

The occupancy of the Li channel site has a final value of 0.47(5) lying between the 0.45 reported by Akimoto from X-rays³ and the 0.5 predicted from

^B B temperature factors are related to U temperature factors using the $B_{\text{iso}} = 8\pi^2 U_{\text{iso}}$.

^C S.O.F is an abbreviation for site occupancy factor.

the chemical formula. The value of 0.47 for Li occupancy is only slightly less than the ideal value of 0.5 for LiTi_2O_4 and the discrepancy is within errors and should not be viewed as being significant

Grins⁹ has proposed other possible Li channels sites within the ramsdellite structure for $\text{Li}_{2+x}(\text{Li}_x\text{Mg}_{1-x}\text{Sn}_3)\text{O}_8$ ($0 \leq x \leq 0.5$) and $\text{Li}_2\text{Mg}_{1-x}\text{Fe}_{2x}\text{Sn}_{3-x}\text{O}_8$ ($0 \leq x \leq 1$). Therefore, difference Fourier analysis was performed to determine if there was any residual scattering after the initial stages of the refinement; however no significant scattering density was found and therefore it was concluded that only one lithium channel site was present in this particular ramsdellite. Attempts were made to refine Li substitution on the Ti framework sites, with no improvement in the R factors being seen. Presented below in table 6.3, are selected bond lengths and angles. For comparison the values obtained by Akimoto³ are presented as well. As can be seen the bond angles and lengths obtained are in very good agreement with those presented by Akimoto.

Bond lengths	Neutron s (Å)	X-ray³ (Å)	Angles	Neutrons (°)	X-rays³ (°)
Li-O(1)	2.19(2)	2.22(2)	O(2)-Li-O(2')	127.4(4)	128.5(5)
Li-O(2)	1.80(6)	1.80(2)	O(2')-Li-O(2')	94.6(3)	94.4(7)
Li-O(2') x 2	2.01(1)	2.01(1)	O(2)-Li-O(2)	114.0(9)	120.4(9)
Mean Li-O	2.00	2.01	O(2)-Li-O(1)	86.06(1)	85.5(5)
Ti-O(1)	1.943(2)	1.947(2)	O(1)-Ti-O(1')	98.4(1)	98.02(3)
Ti-O(1') x 2	1.985(2)	1.993(2)	O(1)-Ti-O(2)	90.70(7)	90.77(7)
Ti-O(2) x 2	2.019(2)	2.010(1)	O(1)-Ti-O(2')	166.1(2)	166.21(9)
Ti-O(2')	2.036(2)	2.031(2)	O(1')-Ti-O(1')	95.89(3)	95.42(1)
Mean Ti-O	1.997	1.997	O(1')-Ti-O(2')	90.80(3)	91.23(7)
			O(1')-Ti-O(2)	84.44(2)	84.44(6)
			O(2)-Ti-O(2)	93.73(9)	94.34(9)
			O(2)-Ti-O(2')	79.90(1)	79.91(7)

Table 6.3. Obtained Bond lengths and angles for LiTi_2O_4 ramsdellite, with a comparison to Akimoto's³ single crystal X-ray work.

5.2.3 Discussion.

The structural parameters obtained from neutron powder diffraction for this “*in situ*” prepared sample are in good agreement with Akimoto’s³ single crystal results. Bond angle and bond length calculations show that the Ti atoms are slightly displaced away from the shared edge, distorting the TiO_6 octahedral units. The Li-O(1) and Li-O(2) bond lengths are different, indicating a distortion of the LiO_4 tetrahedra, moving the Li away from the ideal (0, 1/2, Z) position of the channel site. This is related to the Li-Li interval, which is approximately 1.69Å. This bond length would be too short for both sites to be occupied by Li ions¹⁰. It is due to this short bond length that the maximum occupancy of the undistorted Li channel site can only be 50 %.

The temperature factors for Li are higher than for Ti, O1 and O2; this suggests that the Li atoms may be mobile, as electrical studies performed by Boyce¹¹ on $\text{Li}_2\text{Ti}_3\text{O}_7$ have suggested. The largest anisotropic temperature factor is that seen for b22, which is in the b direction and this could indicate that some intersite hopping is occurring within the channels.

6.3. The magnetic properties of LiTi_2O_4 ramsdellite.

Having determined the crystal structure of LiTi_2O_4 ramsdellite, it was decided that the magnetic and electronic properties of this material should be examined. In the first instance the magnetic properties were examined using SQUID magnetometry and then using longitudinal field $\mu^+\text{SR}$.

6.3.1. Experimental

Two samples of LiTi_2O_4 ramsdellite were examined during this particular study, with the first sample prepared under 5% H_2 /95% Argon (referred to as rkb8) with the second sample being prepared under high purity Argon (referred to as rkb9). The samples were prepared under different gas atmospheres to determine whether the atmosphere has any effects of the magnetic properties of

this material. Presented in table 6.4 is a summary of experimental conditions used during this particular study.

	Rkg8	Rkg9
Preparation atmosphere	5% H_2 /95% Ar	Zero grade Ar
Magnetic field used(gauss)	10	100
Sample weight used in measurements(mg)	56.9	101.9

Table 6.4. Summary of experimental conditions used in preparation and examination of the magnetic properties of LiTi_2O_4 ramsdellite.

Magnetic measurements on the LiTi_2O_4 ramsdellite samples were performed on a Quantum Designs MPMS2 SQUID magnetometer.

6.3.2. Results.

The magnetisation results collected for the two samples of LiTi_2O_4 ramsdellite are presented below in figure 6.2. The results presented below have been corrected for field strength, weight of sample.

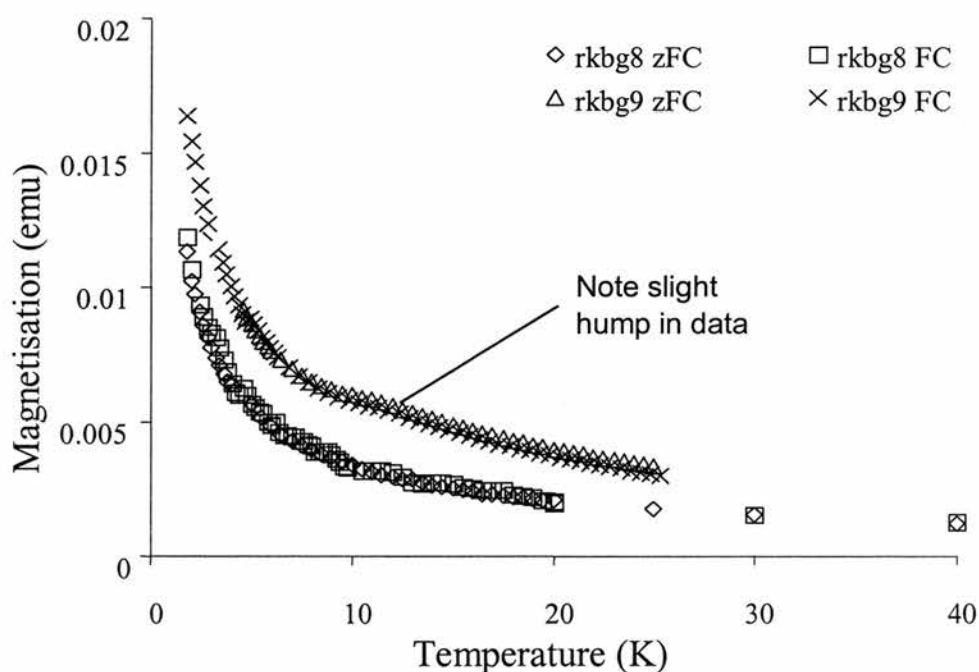


Figure 6.2. Magnetic data collected for a sample of LiTi_2O_4 ramsdellite. zFC = zero field cooled. FC = field cooled. (a) 1.8-40 K range.

As can be seen from the results presented in figure 3, there is no appreciable difference in the data collected under zero field and field cooled conditions. There is a slight bump in the data in the region of 8-12K for rkb9, this is most probably due to residual traces of LiTi_2O_4 spinel, which are difficult to remove completely from sample for magnetic measurement. The results presented above suggest that LiTi_2O_4 ramsdellite is predominantly Curie paramagnetic. A plot of reciprocal magnetisation versus temperature was used to test this observation, with the result presented in figure 6.3. If a material is paramagnetic, then a plot of the reciprocal magnetisation versus temperature should give a straight line that goes through zero.

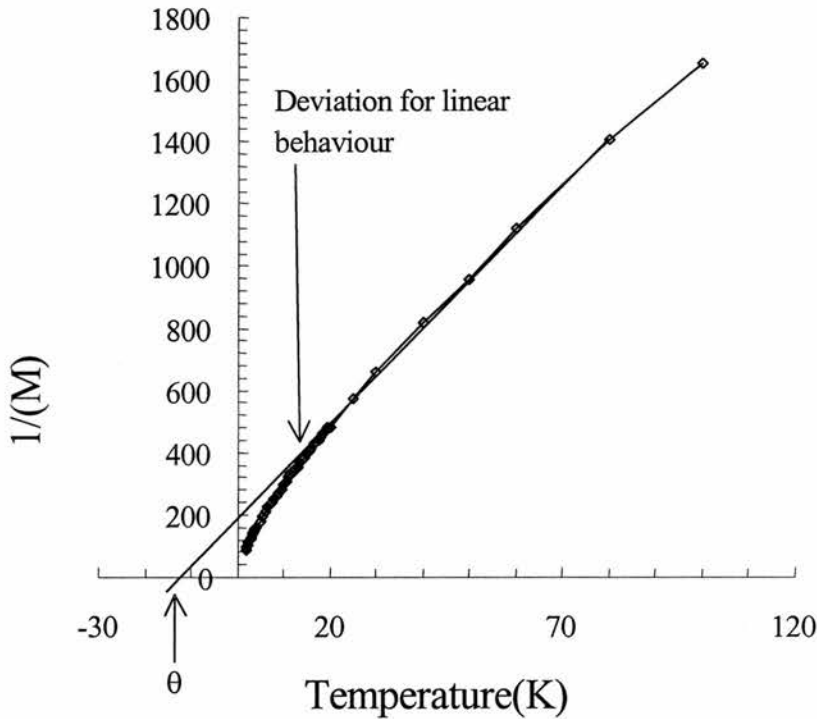


Figure 6.3. Plot of inverse magnetisation versus temperature for LiTi_2O_4 ramsdellite. θ is the asymptotic temperature. No Pauli correction made to the data.

As can be seen from the figure 6.3, LiTi_2O_4 ramsdellite does not give a straight line but shows a slight negative deviation at lower temperatures and does not go through zero. The data was then fitted for both χ and $\frac{1}{\chi}$ using the equation 6.1, which comprises of Curie-Weiss and Pauli contributions. Therefore it is felt that perhaps antiferromagnetism is not present.

$$\chi = \chi + \frac{C}{T - \theta} \quad (6.1.)$$

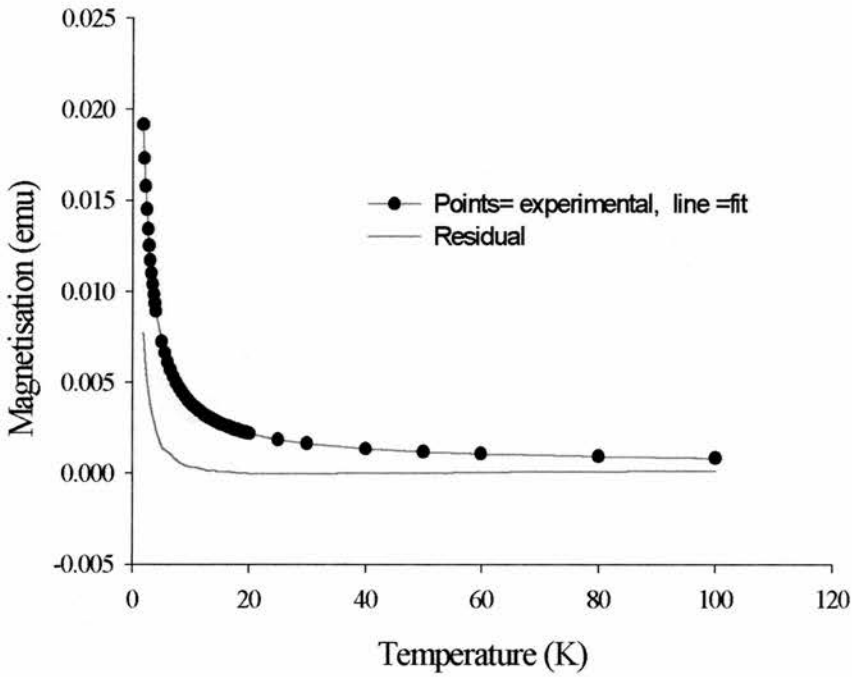


Figure 6.4(a). Susceptibility versus temperature obtained for LiTi_2O_4 ramsdellite.

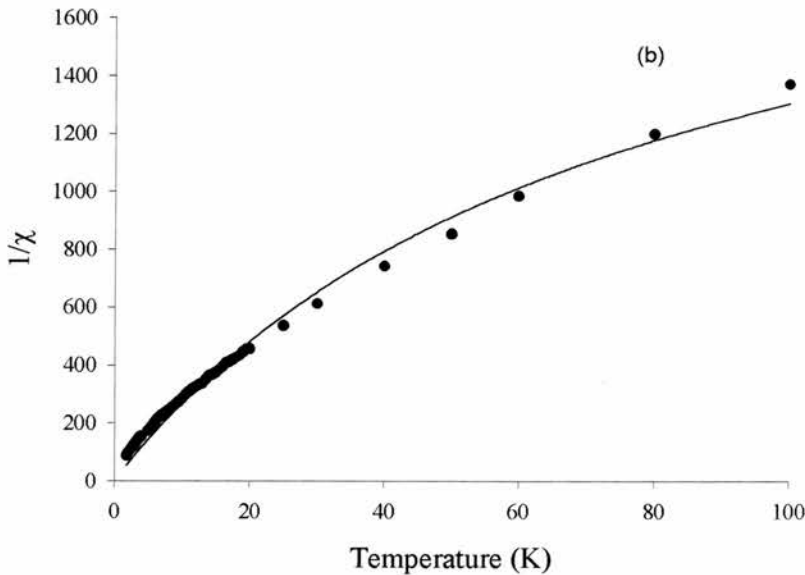


Figure 6.4(b). Inverse susceptibility versus temperature.

Shown above in figure 6.4, are the plots obtained from fitting the data to equation 6.1. The data fitted well at higher temperatures, however the green line in figure 6.4(a) shows the residual obtained after deducting the calculated Curie

and Pauli contributions from the experimental data. Such functions are widely used to model paramagnetic susceptibility in titanates¹². Both fits gave values of χ_p of 0.0005(1) emu mol^{-1} , Curie constant 0.0336(5) emu mol^{-1} and a Weiss temperature of 0.0(1). This indicates simple paramagnetic behaviour with both Curie and Pauli terms.

Calculation of the magnetic moment gave a value of 0.52 Bohr magnetons, which is equivalent to 0.3 spins per formula unit of LiTi_2O_4 ramsdellite, and is approximately 30% of the theoretical value assuming one 1 spin per formula unit. At low temperature an additional strong magnetic component is observed indicating the onset of some form of magnetic order. The value obtained for the Pauli term is similar to value reported previously for various metals¹³. The value obtained is consistent with the presence of conduction electrons.

It should be noted that magnetic measurements are very difficult to perform on this particular phase and several attempts were made to obtain "clean" ramsdellite. This is due to the relationship between the spinel and ramsdellite polymorphs. The low temperature LiTi_2O_4 spinel phase is superconducting in the region of 10-13K, as shown previously in chapters 3 and 4. Therefore, great care must be taken in preparing the ramsdellite phase, or else conversion back to spinel will occur on cooling. These problems may be avoided by preparing the sample of ramsdellite using quenching methods or applying field in excess of the spinel upper critical field H_{c2}^D . By applying a field in excess of H_{c2} , the superconducting flux lattices associated with the mixed state will have collapsed and hence superconductivity will have been suppressed.

6.3.3. Discussion.

The magnetic results presented by Akimoto in reference 3 indicated that this material was a paramagnet, although some kind of magnetic anomaly was reported in the region of 100 Kelvin. This was reported to be due to some kind of impurity present in the sample.

^D Field strength at which superconductivity is completely suppressed.

A hump was seen in both sets of data in the region of 8-12 Kelvin and is seen in both the zero field cooled and field cooled runs. The appearance of this trend in both the field and zero field cooled results suggests that it is unlikely to be a spin glass. The plot of reciprocal magnetisation versus temperature (without correction for Pauli term)(figure 6.4), show a deviation from linear behaviour in the region of 20 Kelvin. The value obtained for θ was seen to be negative, a negative value of θ indicates the presence of antiferromagnetism. Examination of figure 6.5(b) has a contribution from Pauli paramagnetism, suggesting the presence of conduction electrons.

The number of spins obtained for LiTi_2O_4 indicates that each formula unit has approximately 0.52 Bohr magnetons associated with it.

6.4. Longitudinal μ^+ SR Studies.

The results presented above suggest that the LiTi_2O_4 ramsdellite has antiferromagnetic tendencies, and therefore it was decided that the ramsdellite should be examined using muon spin relaxation. As mentioned above, it is possible that the data contains a predominantly paramagnetic response and an antiferromagnetic response. It is felt that the muons will see different responses from different magnetic internal field of the sample and hence it may be possible to separate the two different responses out from each other.

The muon is essentially a sensitive microscopic magnetometer with spin $\frac{1}{2}$ and a magnetic moment three times that of the proton. The frequency of its magnetic resonance or precession signals gives a direct measurement of local magnetic or hyperfine fields and environments. Measurement of the relaxation of the muon polarisation characterises the internal fields of the system.

6.4.1. Experimental.

The sample examined was prepared according to the methods described in chapter 2. The actual sample used during this experiment was of a known high quality, with its structure having been examined fully using X-ray and Time Of Flight powder neutron diffraction (see chapter 6).

Longitudinal field muon spin relaxation experiments was performed at the pulsed muon facility at ISIS, RAL, UK using the MuSR spectrometer in longitudinal geometry. A field of 20 gauss was applied perpendicular to the incident muon beam and a spectrum collected. This was performed in order that the forward and backward detectors could be calibrated such that they appear identical. Two programs were used to perform the iterative fitting, these being T20FIT and LNG. T20FIT is a program used to calibrate the detectors, this is performed to take account of the relative efficiencies of the different detectors in the forward and backward detector arrays. This gives a value for α which is a correction for the detectors, and T_0 , which is the deadtime correction. The dead time is the time at which so many muons are arriving at the detector array that it becomes unusable. The sample was then cooled to 2 Kelvin in zero field with spectra being collected in the range of 2 to 150 K. The value of α and T_0 were then used in the grouping of the data from all of the detectors, using the program LNG. The data collected in the temperature runs is then analysed using least squares fitting.

6.4.2. Results.

It was immediately apparent in the data collected on this sample that the spectra at low temperatures were completely different from those collected for LiTi_2O_4 spinel. Presented in figure 6.5(a) to (c) are the raw patterns collected at 3, 10 and 12.5 Kelvin respectively.

It should be noted that the data presented in figure 6.5 (a) to (c) have been binned so that every 5th data point is shown. The raw spectrum presented in figure 6.5(a) shows a fast component at short muon decay time, with a similar small component seen in the data presented in figure 6.5(b). Shown in the insert is a blown up portion of the spectra in the 0-3 microseconds region, which shows the behaviour more clearly. The spectrum shown in figure 6.5(c) shows a similar response to that seen for LiTi_2O_4 spinel, which was interpreted as being due only to the nuclear moments present

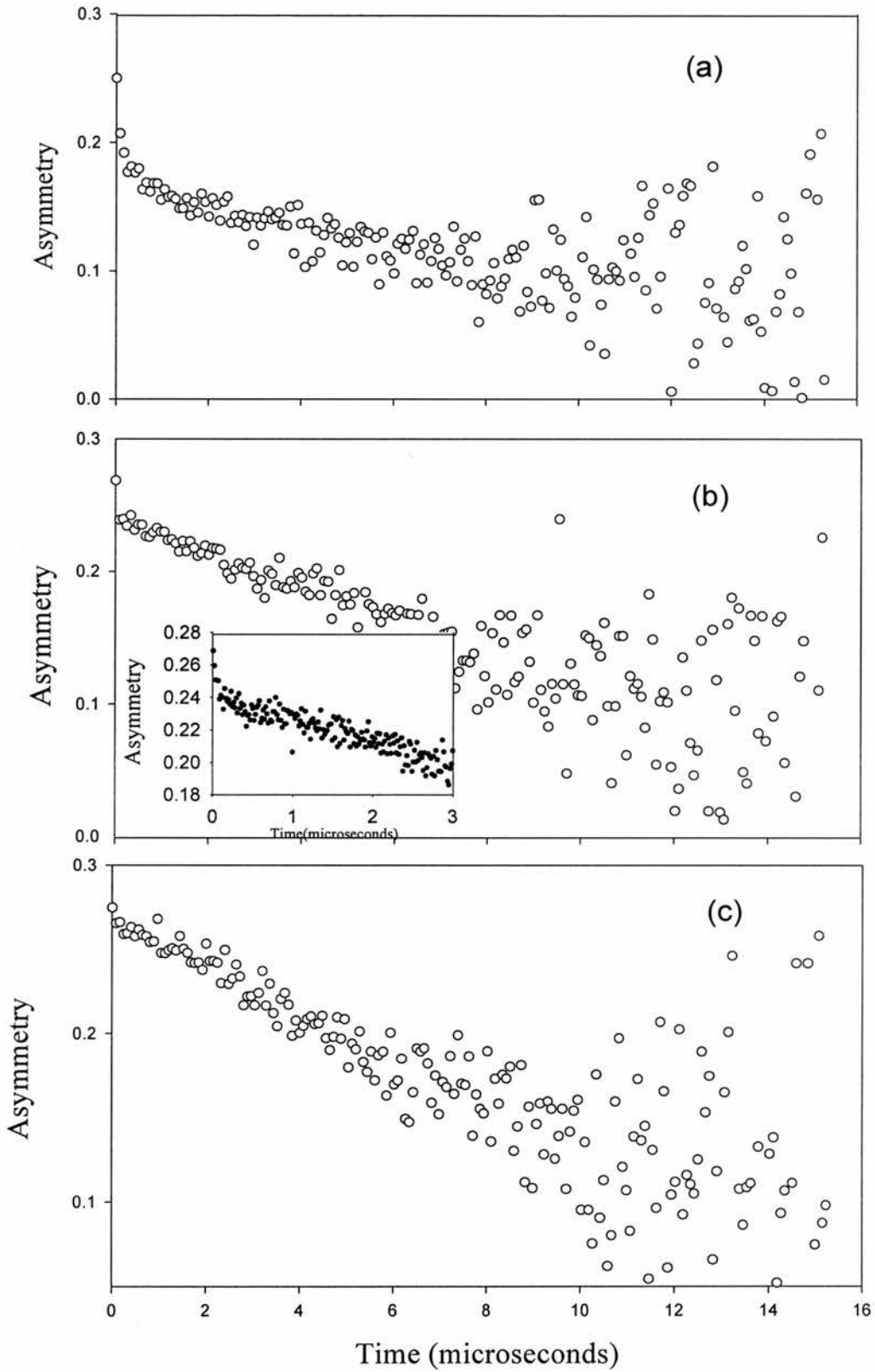


Figure 6.5. Raw patterns collected at (a) 3K, (b) 10K and (c) 12.5K.

The presence of a second component at short muon decay times for the spectrum collected at 10 K and below could indicate the presence of two muon sites within the structure.

A number of different experimental models were used to try and fit the spectra, with the most sensible and physically meaningful model used was a function that had a stretched exponential term and a dynamic Kubo-Toyabe for each of the components. Presented below is equation 6.2, which was used to fit the data.

$$G_z = a1\left(\frac{1}{3} + \frac{2}{3}\left(\exp\left(\frac{\sigma_1^2 t^2}{2}\right)\right)\exp(-\lambda_1 t)^\beta + a2\left(\frac{1}{3} + \frac{2}{3}\right)(1 - \sigma_2 t)^2\right)\exp\left(\frac{\sigma_2^2 t^2}{2}\right)\exp(-(\lambda_2 t)^\beta)$$

(6.2.)

Where $a1$ and $a2$ are the asymmetry terms associated with the muon decay, λ term described the fluctuation rate of the moments as experienced by the muon. A high value of λ is an indication that the moments are fluctuating slowly. The β term describes the magnetic frustration as experienced by the muon¹⁴. To an approximation the two β presented in equation 6.2 are the same, as the frustration is summed over the whole of the lattice and hence only an average of the two responses can be adequately modelled. The Kubo-Toyabe is the same as was modelled in the previous experiments performed on the spinel analogue and describes the dipole from the nuclear moments experienced by the muons. The term σ describes the field width of the nuclear moments.

It is believed that at higher temperatures the two components have rapidly fluctuating moments and we are only observing the nuclear components. As the temperature is lowered the similarity between the two components changes and therefore two components are seen in the collected spectra. It was found very difficult to fit the spectra in the region of 5-10K, where the initial rapid decay is difficult to model. Presented below in figures 6.6(a) and 6.6(b) are the fitted spectra for the data collected at 2 and 150 Kelvin respectively.

Assymetry

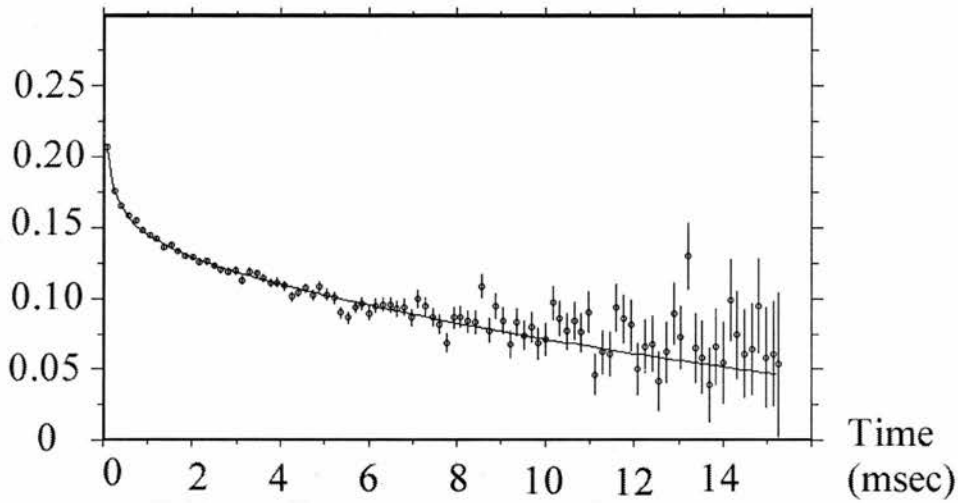


Figure 6.6(a). The fitted μ^+ SR spectra at 2K for LiTi_2O_4 ramsdellite.

Assymetry

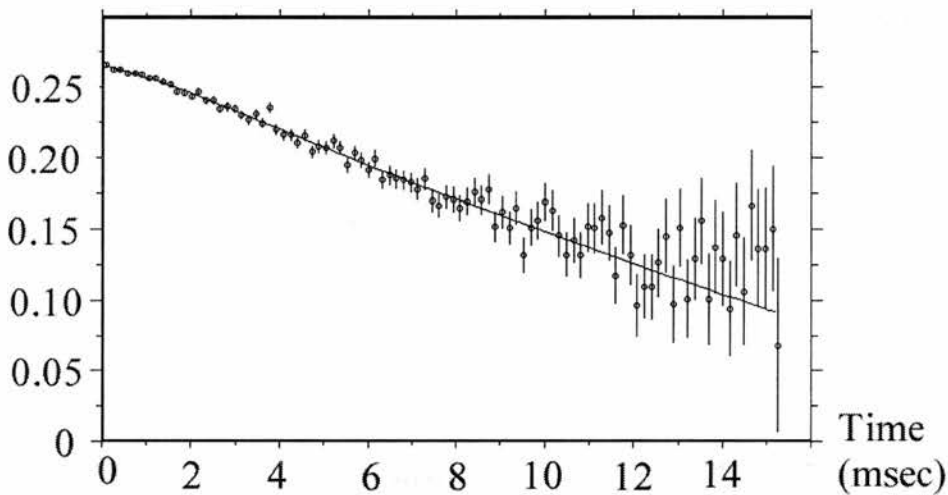


Figure 6.6(b). The fitted longitudinal μ^+ SR spectra at 150K for LiTi_2O_4 ramsdellite.

As can be seen from the fitted spectra presented above, the model proposed in equation 6.2 is a good fit to the spectra collected. Presented below in figure 6.7 are the results relating to the magnetic moment fluctuation rate, λ and field width. This term in the equation is seen to be negligibly small at higher temperatures and then becomes a dominant term in the equation at low temperatures. Due to the problems associated with fitting this data in the 5-10 Kelvin temperature range, it could not be fully determined when this behaviour started.

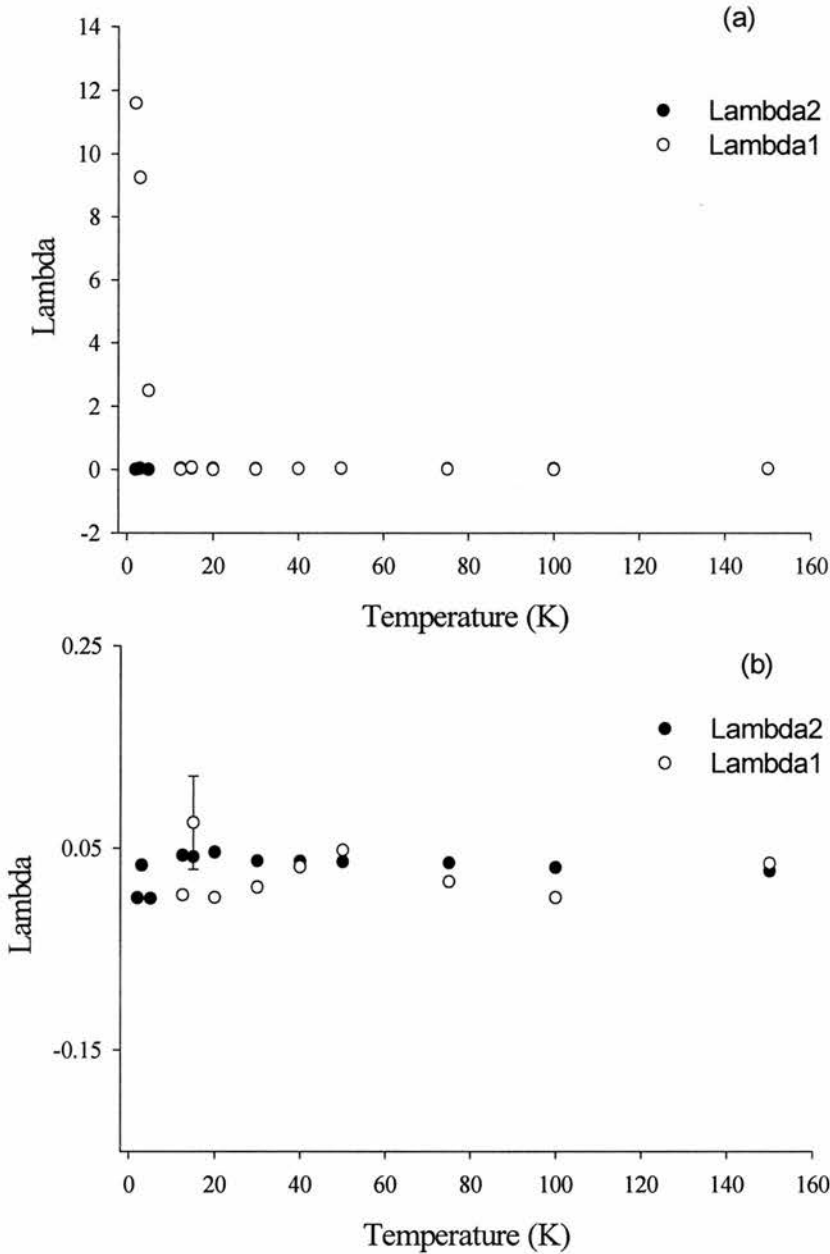


Figure 6.7(a). Plot of Λ versus temperature for LiTi_2O_4 ramsdellite, (b) limited range

Presented in figure 6.7(a) are the values obtained for λ_1 and λ_2 . λ_1 is seen to be high at low temperature after which it rapidly decreases as the temperature is increased. This indicates that the field fluctuation is slow at low temperatures after which they begin to fluctuate rapidly. For the second λ component (known as λ_2) the moments are seen to be rapidly fluctuating at all temperatures. The data are also presented in figure 6.7(b) and show how little the value of λ changes over the temperature range examined. The error bars have been included on the plot, but are very

small. The slowing of the fluctuations at low temperature indicates that the moments are beginning to order and may indicate the approach of magnetic ordering in this material.

The opposite effect is seen for the Beta term, as can be seen from the function presented in equation 6.2, this suggested that as the material is cooled then magnetic moments are becoming more frustrated.

The results presented above in figures 6.5, 6.6, 6.6 and 6.8 all indicate that the magnetic properties are changing in the region of 10-12 K, which is the approximately the same temperature as seen from the SQUID measurements.

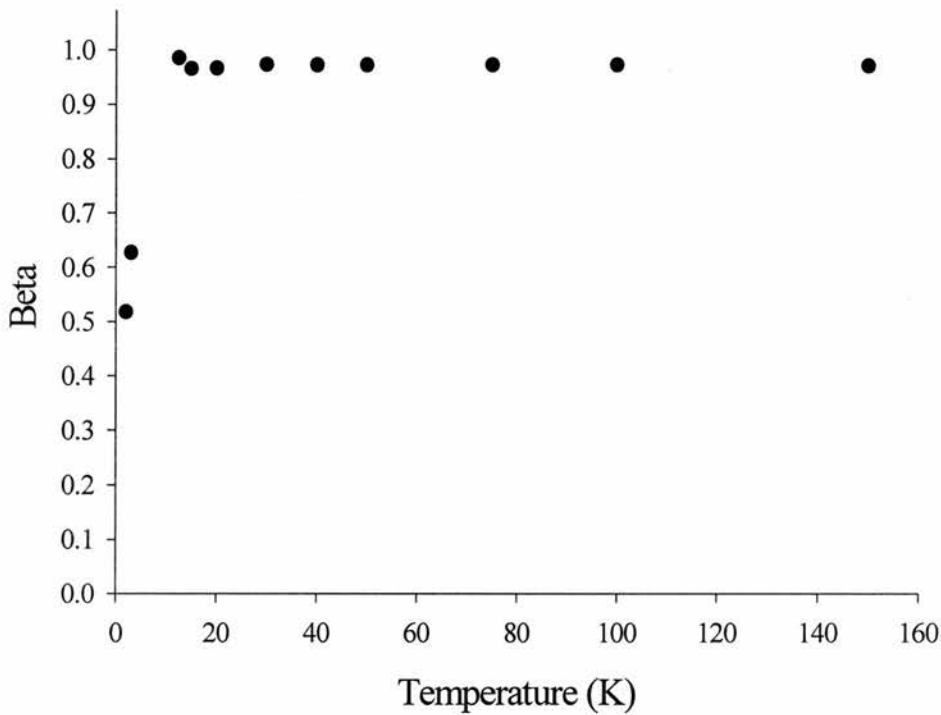


Figure 6.8. Plot of Beta versus temperature for LiTi_2O_4 ramsdellite

6.4.3. Discussion.

The LiTi_2O_4 ramsdellite system has shown results that suggest the presence of two different muon sites within the structure. This statement is made on the strength of the two stretched exponential and two Kubo-Toyabe functions needed to model the spectra.

It is proposed that at higher temperatures, the contributions from the two muon sites are approximately equal, therefore only one response is seen in the spectrum. In the region of 10-12.5 K, a second component is seen at short muon

It is proposed that at higher temperatures, the contributions from the two muon sites are approximately equal, therefore only one response is seen in the spectrum. In the region of 10-12.5 K, a second component is seen at short muon decay. Studies on the high T_c cuprates indicated that muons generally form a weak $\text{O}-\mu^+$ bond¹⁵, with an associated bond length of approximately 1.0\AA ¹⁶. Presented in figure 6.9 are the suggested locations of the two different muon sites, labelled as 1 and 2 respectively. It can be suggested that the position marked as 1 is part of the Ti-O ladders and is seeing magnetic ordering, whereas the muon at site 2 is seeing no magnetic ordering. The muon studies presented in this chapter could not determine which of the sites was responsible for the fast component. However, as muon site 1 is in closer proximity to Ti and O2, it is proposed that this is the site responsible for the fast component.

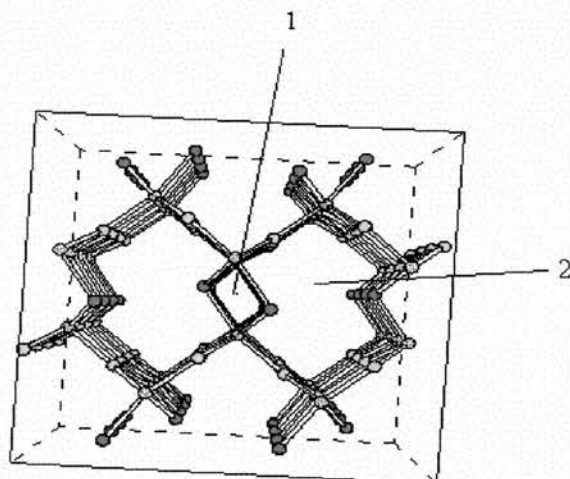


Figure 6.9. Proposed muons sites within the structure of LiTi_2O_4 ramsdellite at low temperatures. Grey atoms Ti, Yellow atoms are oxygen 1, red atoms are oxygen 2. N.B. Lithium has been removed for the sake of clarity.

Although the μ^+ SR has not actually helped to determine the nature of the low temperature magnetic transition, it gives clear evidence of a magnetic transition. This could probably be determined if longer counting times are used and would probably also be aided by using a single crystal of LiTi_2O_4 ramsdellite.

6.5. Electrical property measurements.

6.5.1. Introduction.

The electrical properties of LiTi_2O_4 ramsdellite were examined at low temperature to determine whether LiTi_2O_4 ramsdellite was metallic, semiconducting or insulating in nature.

6.5.2. Experimental.

A sample of LiTi_2O_4 ramsdellite was prepared according to the method indicated in chapter 2 and examined using 4 terminal D.C. conductivity methods and A.C Impedance spectroscopy.

After a number of attempts to connect electrodes to the sample, it was found that the best method of attaching electrodes was to paint four gold electrodes onto the sample using Engelhard gold paste. The sample was then fired at 500°C for 2 hours under an argon atmosphere. These connections were then polished using emery paper. Gold wires were then attached to the gold contacts using silver dag (and allowed to dry for approximately 30-60 minutes). The pellet was then attached to the conductivity jig using standard electrical solder with the pellet held in place using PTFE tape.

For the D.C. four probe measurements, the sample was cooled down to 120K using liquid nitrogen and allowed to heat up slowly to room temperature.

6.5.3. Results.

The results obtained from the electrical measurements are presented below in figure 6.10 and indicate that the electrical resistance is decreasing as the sample was allowed to warm.

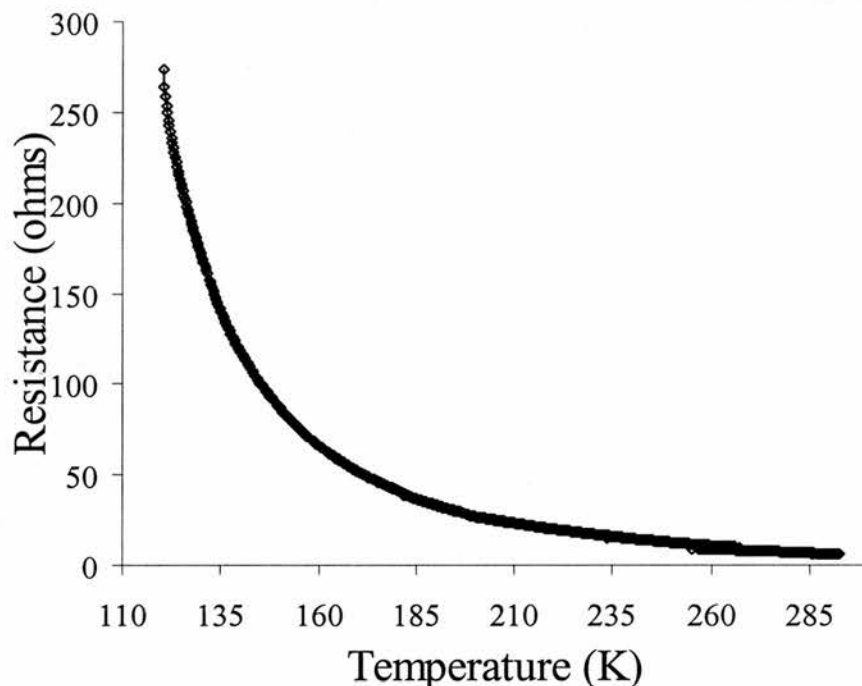


Figure 6.10. Electrical resistance of a sample of LiTi_2O_4 ramsdellite

The data presented above suggest that this material is semiconducting in nature. The activation energy for any component can be obtained by measuring the change in conductivity with temperature. The slope of an Arrhenius plot, $\log \sigma T$ versus $1000/T$ was used to obtain the activation energy. The conductance of the sample can be determined from the inverse of the resistance. The term presented below has not been corrected for geometric factor, which is calculated from resistivity = l/a , where l =length of sample and a = cross sectional area.

$$\sigma = \frac{1}{R} \quad (6.3).$$

The activation energy of LiTi_2O_4 ramsdellite was determined to be 0.08(1) eV. The sample examined using 4 probe method may have grain boundaries and the 4 probe D.C. experiments are actually probing the total rather than the bulk conductivity of the sample.

6.5.4. Impedance spectroscopy measurements.

A.C. Impedance spectroscopy can be used to determine multiple electrical components in materials, with the separation of the responses being achieved by scanning a wide range of frequencies. This enables separation of components from bulk and grain boundaries. The samples examined using impedance spectroscopy was the same sample as used above. The resistances obtained have not been corrected for geometry and it must be noted that the electrode configuration was also far from ideal. This may cause the resistance values obtained to be slightly higher than they actually are.

6.5.5. Results

Presented below in figure 6.11, is the total response obtained from the sample of LiTi_2O_4 ramsdellite at 140 K. The value obtained for capacitances are obtained using curve fitting and are determined as described in chapter 2.

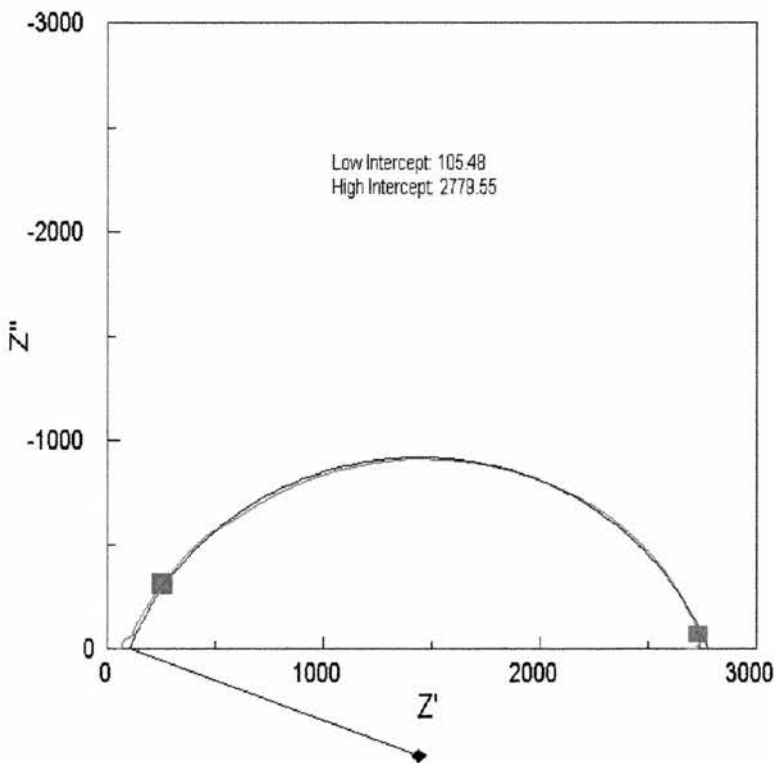


Figure 6.11. Obtained impedance plot for sample of LiTi_2O_4 ramsdellite collected at 140 K.

The capacitance of this large main component at 116K was found to be in the region of 1.6×10^{-9} F, which is consistent with a grain boundary response (see chapter 2, section 2.5.4). No semicircular component could be found relating to the bulk of this material, therefore the low frequency intercept was used to determine the resistance of the bulk component. At 116K the resistance of the bulk was found to be in the region of 324 ohms. The resistance was seen to decrease to approximately 105 ohms as the sample temperature was increased to approximately 140 K, as shown in figure 6.11. The capacitance was found to be in the region of 1.8×10^{-9} F, which is still consistent with a grain boundary response. This decrease in the resistance could indicate that the bulk is semiconducting in nature.

6.5.6. Discussion.

The 4 D.C. terminal measurements and the A.C. Impedance measurements indicate that the sample was semiconducting in nature. Closer examination of the obtained capacitance's values from the impedance plots shown that the main response seen at these temperatures is actually related to a grain boundary. The values obtained for the bulk resistance is approximately, the same for the impedance and D.C. measurements, with any differences between the two techniques likely to be any electrode contributions, which will be minimal in the D.C. results. The impedance measurements suggest that the following equivalent circuit could be used to model the system, with the right hand side of dominating the impedance response.

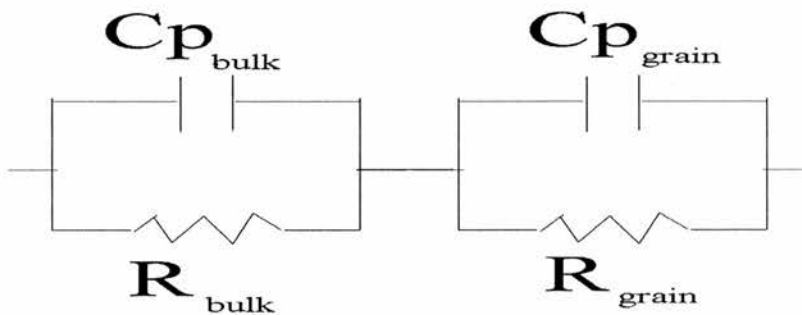


Figure 6.12. Proposed equivalent circuit for LiTi_2O_4 , assigned on the basis of the impedance results, where C_p = capacitance and R = resistance.

The activation energy obtained from the D.C. 4 probe measurements is consistent with that associated with small polarons. A polaron is a charge carrier that results from an electron and lattice deformation, known as the strain field¹⁷. Polarons can be described as being either large or small polarons. The electrons associated with a large polaron move in bands. The electron associated with a small polaron spends most of its time trapped on a single ion. At high temperatures the electron moves from site to site by thermally activated hopping; at low temperatures the electron tunnels slowly through the crystal.

6.6. Conclusions.

The experiments performed by Akimoto et al³ suggested that the LiTi_2O_4 ramsdellite was a straightforward material, with little in the way of interesting properties. The results presented in this chapter suggest this is not the case.

The neutron powder diffraction experiments performed on the structure of LiTi_2O_4 ramsdellite indicate the structure determined by Akimoto³ was correct. The anisotropic temperature factors obtained for this sample suggest that the Li is mobile within the 4C channel sites. Conversion to anisotropic temperature factors indicated that the thermal vibrations are dominant along the b axis. This is shown schematically in figure 6.13.

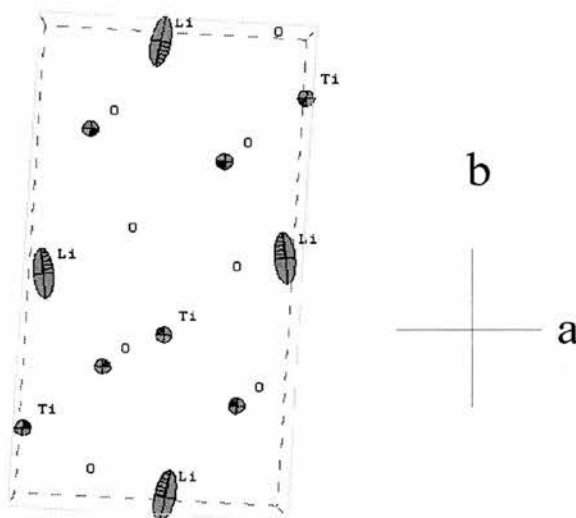


Figure 6.13. Schematic of LiTi_2O_4 ramsdellite showing dominant thermal vibrations of Li within the structure. As determined from powder neutron diffraction.

The magnetic measurements have shown that the overall response is probably a mixture of two different responses. It could suggest that the magnetic responses obtained are due to two different domains within the magnetic structure. One portion of the structure is dominantly paramagnetic, with the other domain being antiferromagnetic in nature. This observation is supported in part by the results obtained from the muon experiments which indicated that two different responses are present in the spectra, a fast component is seen at short muon decay times, with a second slower response seen at longer decay times. Attempt to separate out the two components was only partially successful and therefore this model still needs to be verified.

This form of ramsdellite exhibits a number of properties associated with spin ladder compounds¹⁸. Examination of the magnetic data collected by Azuma¹⁹ for SrCu_2O_3 showed an unusual magnetic response, which was attributed as being due to the presence of antiferromagnetism. Matsuda²⁰ found a peak at 3 Kelvin in magnetic susceptibility measurements on SrCuO_2 . The results were interpreted as being signatures of low-dimensional magnetic behaviour with competing interactions. Examination of SrCuO_2 using muon spin methods showed a similar behaviour to that seen for LiTi_2O_4 ramsdellite. Matsuda assigned this type of behaviour as being due to a zigzag spin ladder spin ladder system as described by Affleck and White²¹. Further attempts to determine the nature of this magnetic order using powder neutron diffraction proved to be problematic, with no magnetic Bragg peaks apparent in the collected powder patterns. This was interpreted as being due to suppression of the Cu^{2+} moments by quantum fluctuations.

Presented in figure 6.14, is a graphical representation of the proposed zigzag spin ladder structure in LiTi_2O_4 ramsdellite.

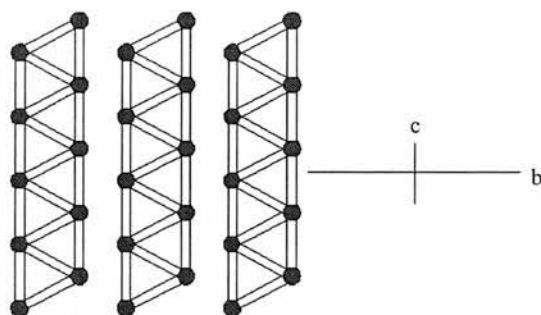


Figure 6.14. Graphical representation of the proposed zigzag spin ladder in LiTi_2O_4 ramsdellite.

Although more evidence is need before it can be stated that LiTi_2O_4 is a zigzag spin ladder, the results collected so far and the similarities in the observed magnetic data and muon spectra to that obtained for SrCuO_2 suggests that this may be the case.

The electrical measurements performed on LiTi_2O_4 ramsdellite indicate that the material is semiconducting in nature. The impedance measurements indicated the presence of a semiconducting grain boundary. These observations could probably confirmed by performing Transmission Electron Microscopy (TEM).

6.7. References.

1. A.M. Bystrom, *Acta. Chem. Scand.*, **3** (1949) 163.
2. A Le Bail and J.L. Fourquet, *Mat.. Res. Bull.* **27** (1992) 75.
3. J. Akimoto, Y Gotoh, M. Sohma, K. Kawaguchi, Y. Oosawa and H. Takei, *J Solid State Chem.*, **110** (1994) 150.
4. Powder diffraction at ISIS, User guide for the Polaris powder diffractometer at ISIS, R.I. Smith and S. Hull, Version 3, May 1997.
5. H.M. Rietveld, *J. Appl. Cryst.* **2** (1969) 65.
6. J.C. Mathewmann, P. Thompson and P.J. Brown, *J. Appl. Crystallogr.*, **15** (1982) 167.

-
7. P.J. Brown and J.C. Mathewmann, Rutherford Appleton Laboratory Report, RAL-87-010 (1987).
 8. International Table for crystallography, Vol. A, 4th edition, edited by Theo. Hahn, 288.
 9. J Grins and A.R. West, *J. Solid State Chem.*, **65** (1986) 265.
 10. R.D. Shannon and C.T. Prewitt, *Acta Crystallogr. Sect B*, **25** (1969).
 11. J.B. Boyce and J.C. Mikkelsen Jr, *Solid State Comms.*, **31** (1979) 741.
 12. K. Isawa, J. Sugiyama and H. Yamuchi, *Phys Rev B*, **49** (1994) 1462
 13. C. Kittel, “*Introduction to solid state physics*”, Wiley, New York, (1986) 417.
 14. I.A. Campbell, A. Amato, F.N Gyax, D. Herlach, A. Schenk, R. Cywinski and S.H. Kilcoyne, *Phys Rev Lett*, **72** (1994) 1291.
 15. *Proceedings from the 5th μSR International conference.*, edited by S.F.J. Cox, G.H. Eaton, D. Herlach and V.P. Koptev, *Hyperfine Interact*, **63** (1990) 169.
 16. *Proceedings from the 5th μSR International conference.*, edited by S.F.J. Cox, G.H. Eaton, D. Herlach and V.P. Koptev, *Hyperfine Interact*, **63** (1990) 279.
 17. C. Kittel, “*Introduction to solid state physics*”, Wiley, New York, (1986) 281.
 18. E. Dagotto and T.M. Rice, *Nature*, **271** (1996) 618.
 19. M. Azuma, Z. Hiroi, M. Takano, K. Ishida and Y. Kitaoka, *Phys. Rev Lett.*, **73** (1994) 3463.
 20. M. Matsuda, K. Katsumata, K.M. Kojima, M. Larkin, G.M. Luke, J. Merrin, B. Nachumi, Y.J. Uemura, H. Eisaki, N. Motoyama, S. Uchida and G. Shirane, *Phys. Rev. B.*, **55** (1997) 11953.
 21. Proceedings from Miniworkshop on strong electron correlation’s “Disorder and interaction in quantum systems and their classical analogs”, S.R. White and I. Affleck, July 1996.

Chapter 7.

7. Introduction.	195
7.1. Experimental.	197
7.2. Results.	198
7.2.1. X-ray diffraction.	198
7.2.2. Thermal analysis.	199
7.2.3. Refinement of X-ray powder patterns.	201
7.2.4. Combined Time Of Flight Neutron and X-ray powder diffraction.	202
7.3. Conclusions.	211
7.4. References.	215

7. Introduction.

In the search for fast ionic conductors a number of materials have been examined, with Li ion containing materials^{1,2} being the focus of the most attention. Lithium containing materials are particularly attractive because of the electropositive nature of Li, combined with its light weight makes it attractive for various battery applications. A number of lithium titanates have been investigated including Li_4TiO_4 ,³ Li_2TiO_3 ⁴ and $\text{Li}_2\text{Ti}_3\text{O}_7$. The phase, $\text{Li}_2\text{Ti}_3\text{O}_7$ was first reported by Jonkers⁵ and subsequently by Kim et al⁶. This phase was found to have a ramsdellite structure type as described by Bystrom et al⁷ for $\gamma\text{-MnO}_2$.

The crystal structure of $\text{Li}_2\text{Ti}_3\text{O}_7$ ^{8,9} was found to be $(\text{Li}_{0.86})_{\text{c}}(\text{Ti}_{1.715}\text{Li}_{0.285})_{\text{f}}\text{O}_4$, with **c** and **f** indicating channel and framework sites respectively. Abrahams reported that Li was distributed over two sites within the channels for $\text{Li}_2\text{Ti}_3\text{O}_7$ (can also be written as $\text{Li}_{1.145}\text{Ti}_{1.710}\text{O}_4$) with approximately 60% of the total on an 8 fold site $(-0.058, 0.445, 0.181)$ and the remaining amount 40% at $(0.054, 0.047, 0.25)$. Morosin reported that approximately 50% Li was to be found at $\sim(-0.06, 0.45, 0.25)$ and 50% at $\sim(0.5, 0.05, 0.25)$. It was also found that $\text{Li}_2\text{Ti}_3\text{O}_7$ exhibited fairly high Li ionic conductivity, (typically $1.55 \times 10^{-5} \text{ Scm}^{-1}$ at 298 Kelvin)¹⁰.

In 1994, Akimoto¹¹ prepared single crystals of LiTi_2O_4 and deduced the structure of the high temperature polymorph of LiTi_2O_4 to have a ramsdellite structure. It was reported that Li exclusively occupied a channel site within the structure at $(-0.057, 0.45, 0.25)$.

Examination of the ternary phase relationship in the $\frac{1}{2}\text{Li}_2\text{O}$, $\frac{1}{2}\text{Ti}_2\text{O}_3$ and TiO_2 system, shows that LiTi_2O_4 spinel and ramsdellite are at the 33:33:33 point in the phase diagram (see figure 7.1). It is known that LiTi_2O_4 and $\text{Li}_4\text{Ti}_5\text{O}_{12}$ are end members of a spinel solid solution and therefore, it was considered probable that LiTi_2O_4 ramsdellite and $\text{Li}_2\text{Ti}_3\text{O}_7$ could be end members of second solid solution series. LiTi_2O_4 and $\text{Li}_2\text{Ti}_3\text{O}_7$ (when written as $\text{Li}_{1.145}\text{Ti}_{1.710}\text{O}_4$) can be related to each other as end members of the same solid solution series by using the mechanism $\text{Li}_{1+x}\text{Ti}_{2-2x}\text{O}_4$.

A possible mechanism for this proposed solid solution mechanism is that for every two titanium atoms in the framework replaced with a lithium atom, one

lithium should be lost from the channel. This will create one vacancy in the channel sites, as shown below in equation 7.1.

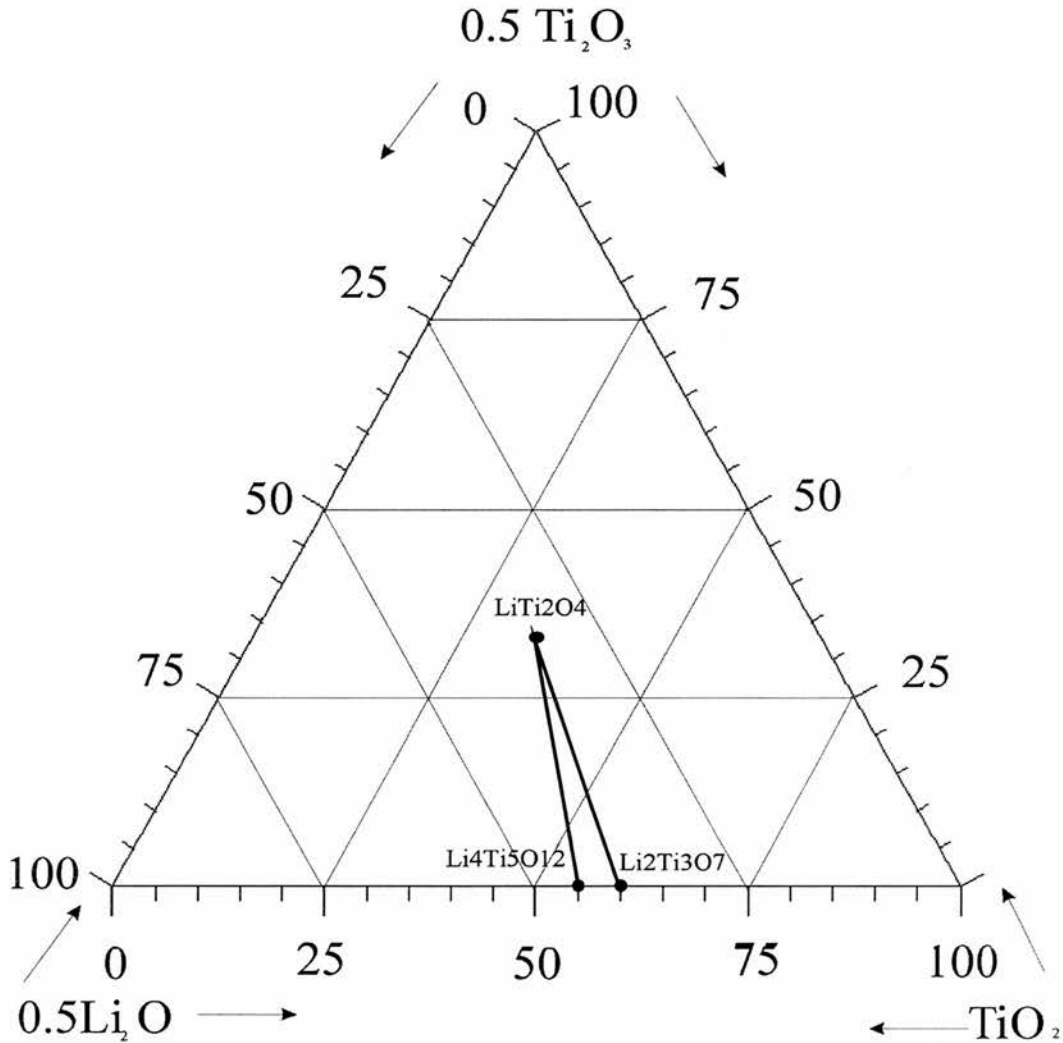
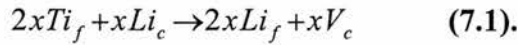


Figure 7.1. Phase relationship between $0.5Li_2O$, $0.5Ti_2O_3$ and TiO_2 .

It is well known that X-ray powder diffraction cannot be used to determine the location of Li within the majority of structures, and neutron diffraction is usually a preferred technique. Even using neutron diffraction locating Li can be difficult in lithium titanates, as the coherent scattering factors of lithium ($-2.22 \times 10^{-24} \text{ cm}^2$) and titanium ($-3.438 \times 10^{-24} \text{ cm}^2$) are both negative¹², and using the relationship presented in equation 7.2, it can be seen

that the amplitude of the scattered intensity (σ) for Ti is approximately 2.5 times greater than that of Li. Therefore, if the Li and Ti share sites, the total scattering from that site will always be dominated by Ti.

$$\sigma = 4\pi b^2 \quad (7.2)^{13}$$

In the proposed model, the occupancy of Li on framework sites can be quite low and hence the total contribution to the scattering intensity is small. In an attempt to get around this problem, data from X-ray diffraction can be used, as Ti is the dominant X-ray scatterer in these phases.

The GSAS¹⁴ Rietveld software allows the use of multiple histograms from different techniques to be used in refinements, so that the dominant scatterer from each technique can be examined in more detail, and hopefully the contributions from each atom can be separated out from each other.

7.1. Experimental.

The samples were prepared in the manner described in chapter 2, with compositions $x=0, 0.04, 0.0715, 0.1$ and 0.145 being prepared (In accordance with $\text{Li}_{1+x}\text{Ti}_{2-2x}\text{O}_4$ solid solution mechanism). X-ray phase purity was determined using a Philips PW1170 diffractometer using $\text{Cu K}\alpha$ (radiation), or a Stoe Stadi P transmission diffractometer, using $\text{Cu K}\alpha_1$ radiation. The unit cells of all members of the proposed solid solution series were initially indexed using the STOE computer program LATREF¹⁵. Thermal analysis was performed to determine phase purity using a TA Instruments 2960 connected to a personal computer. The samples were heated at $10^\circ\text{C} / \text{min}$ up to 400°C and then held isothermally for 1 hour. All of the experiments were performed in a flowing oxygen atmosphere, with a flow rate of $75\text{ml}/\text{min}$ being used during all experiments.

Rietveld analysis was performed on the powder patterns collected on a Stoe Stadi X-ray transmission diffractometer and the neutron General Purpose Powder Diffractometer (GPPD) at the IPNS facility, located at Argonne National Laboratory, Illinois, USA. Each X-ray data set was collected for at least 14

hours in the 2θ range $15-85^\circ$ and the neutron data sets were collected for 16-20 hours with refinements being performed using the 148° backscattering bank. Rietveld refinement of the structural models was performed using the GSAS software package running on a personal computer.

7.2. Results.

7.2.1. X-ray diffraction.

All samples prepared in this solid solution mechanism were seen to have very similar X-ray patterns, with the phase purity of all compositions prepared found to be high. It was found possible to index all of the samples in the proposed solid solution series as being primitive orthorhombic. Least squares fitting of the unit cells gave a gradual decrease in the unit cell dimensions a function of increasing lithium content. Presented in figure 7.2(a) and (b) are the collected powder patterns LiTi_2O_4 and $\text{Li}_{1.1}\text{Ti}_{1.8}\text{O}_4$ ramsdellite.

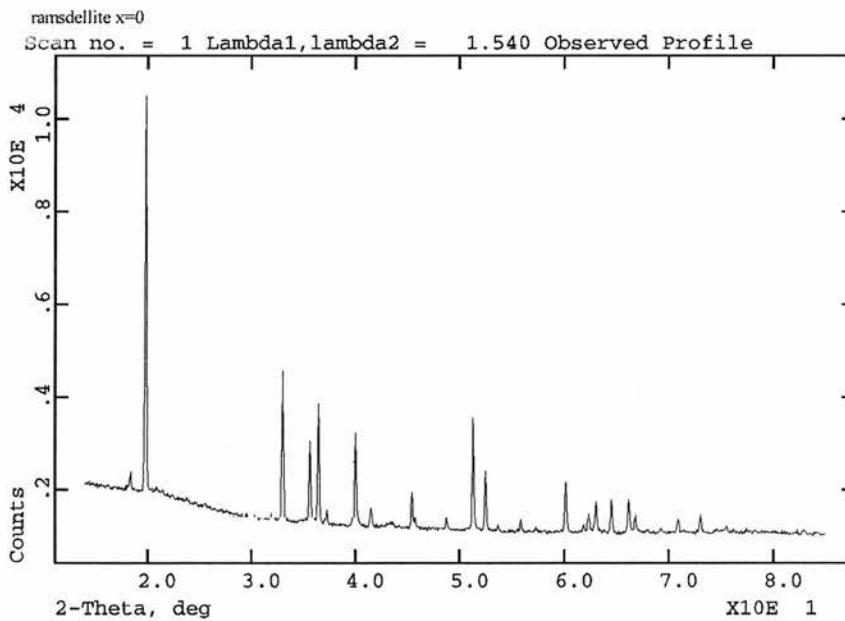


Figure 7.2(a). Raw X-ray powder pattern of LiTi_2O_4 ramsdellite.

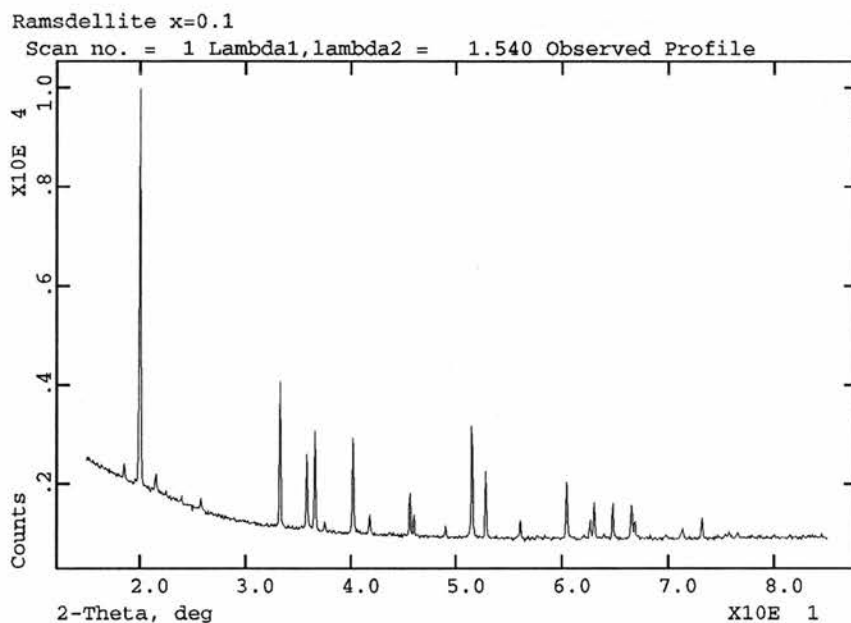


Figure 7.2(b). Raw X-ray powder pattern of $\text{Li}_{1.1}\text{Ti}_{1.8}\text{O}_4$ ramsdellite

As can be seen from the powder patterns presented above in figures 7.2 (a) and (b), the phase purities are good, with sharp peaks being obtained, indicating good crystallinity. Peaks present at 21.4 and 23.8 are due to the Vaseline used in sample mounting. The samples were also examined using thermogravimetric analysis (TGA) to help determine the phase purity and composition.

7.2.2. Thermal analysis.

The aim of this experiment was to confirm the phase purity of the samples. This was achieved by deliberately oxidising the sample as a function of temperature and determining the overall oxygen uptake. The weight increase of each sample was then compared to that expected and from this the titanium oxidation state determined in the starting material.

The results obtained from the thermal analysis indicate a number of different things. It was seen that as the total lithium content of the sample increased the total oxygen uptake decreases. It was noted that the total oxygen uptake in two of the samples was slightly lower than predicted, these being $\text{Li}_{1.04}\text{Ti}_{1.92}\text{O}_4$ and $\text{Li}_{1.0715}\text{Ti}_{1.857}\text{O}_4$. The results obtained from the thermal analysis are presented below in table 7.1.

sample	0	0.04	0.0715	0.1
Onset O ₂ uptake (°C)	115	111	76	86
Weight uptake % (expected)	4.58	3.41	2.34	1.500
Weight uptake % (observed)	4.5(1)	2.8(5)	2.0(3)	1.50(3)
Oxidation state (expected)	3.500	3.625	3.733	3.833
Oxidation state (observed)	3.50(7)	3.688(7)	3.774(8)	3.833(7)

Table 7.1. Results obtained for thermal gravimetric analysis of $Li_{1+x}Ti_{2-2x}O_4$ solid solution series.

The onset of oxidation occurred at quite low temperatures, indicating that the samples, especially powder samples are likely to be unstable to room temperature oxidation. This means that the samples may have been oxidised between grinding and performing the TGA experiment, which would increase the apparent titanium oxidation state. An additional error for the $x=0.04$ sample arises from the discontinuity in the trace which may have affected the results obtained. After allowing for these factors, the values obtained experimentally are fairly close to that expected and certainly within the error of the instrument, and should not be a major cause of concern. Presented in figure 7.3 are the collected TGA traces obtained during these experiments.

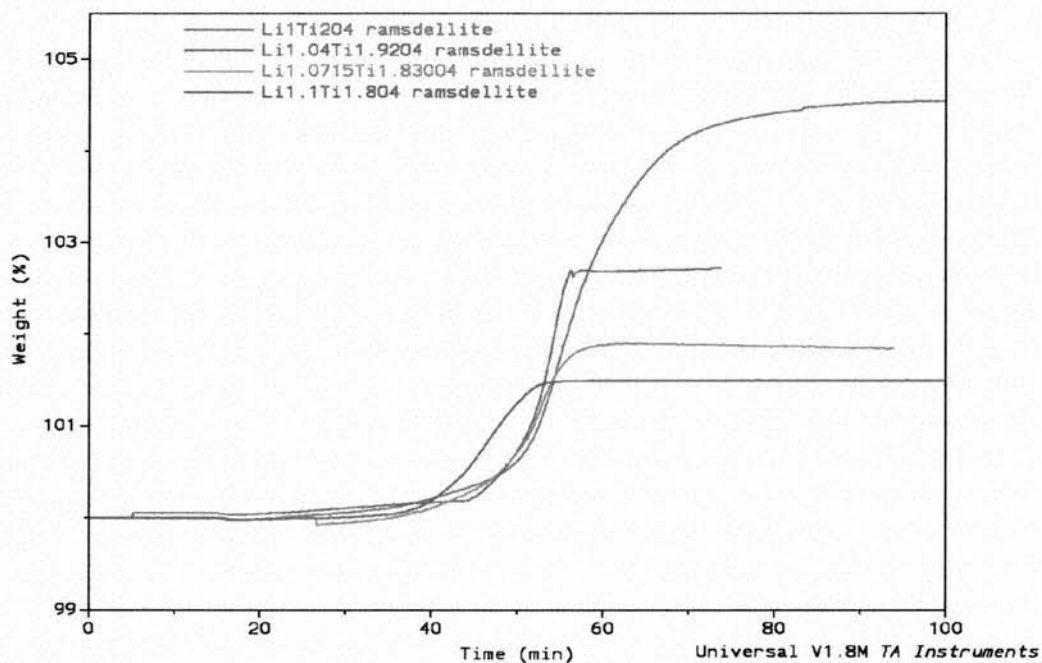


Figure 7.3. TGA results collected for the $Li_{1+x}Ti_{2-2x}O_4$ solid solution series.

7.2.3. Refinement of X-ray powder patterns.

The basic model used in the refinement of all members of the solid solution series was as described in section 5.2, with the Pbnm space group being used (number 62). The following parameters were used in refinement of the models.

1. Shifted Chebyshev background function with 8 polynomials and histogram scaling.
2. Zero point, polarisation and lattice parameters.
3. Profile coefficients for Simpson's rule integration of pseudovoigt function¹⁶, using 2 gaussian, 2 Lorentzian functions as well as a function for peak asymmetry.
4. The atomic co-ordinates for Ti, O1 and O2.
- 5.

No attempt was made to refine the Li position or temperature factors, due to the low X-ray scattering factors of this element. It was found impossible to refine the temperature factors for Ti, O1 and O2. Presented in table 7.2 are the obtained unit cell dimensions obtained for the solid solution series, with a refined X-ray powder pattern for $\text{Li}_{1.1}\text{Ti}_{1.8}\text{O}_4$ presented in figure 7.4.

X Composition	a	b	c
0	5.0356 (1)	9.6394 (2)	2.9464(5)
0.04	5.0315(6)	9.6235(1)	2.9486(4)
0.0715	5.0215(3)	9.5924(5)	2.9490(1)
0.1	5.0225(1)	9.5912(3)	2.9490(8)
0.145	5.0202(2)	9.5570(4)	2.9473(1)

Table 7.2. Unit cell edge versus composition for $\text{Li}_{1+x}\text{Ti}_{2-2x}\text{O}_4$ solid solution as determined from X-ray powder diffraction.

The unit cell and crystal structures of both $\text{Li}_2\text{Ti}_3\text{O}_7$ ^{8,9} and LiTi_2O_4 ¹¹ have been reported previously, with the result presented above found to be in good agreement with those reports previously. As can be seen from the pattern, the sample is of high phase purity and a good crystallinity. The two extra peaks found at approximately 21.4 and 23.8° 2 θ , are due to the Vaseline used during the sample mounting.

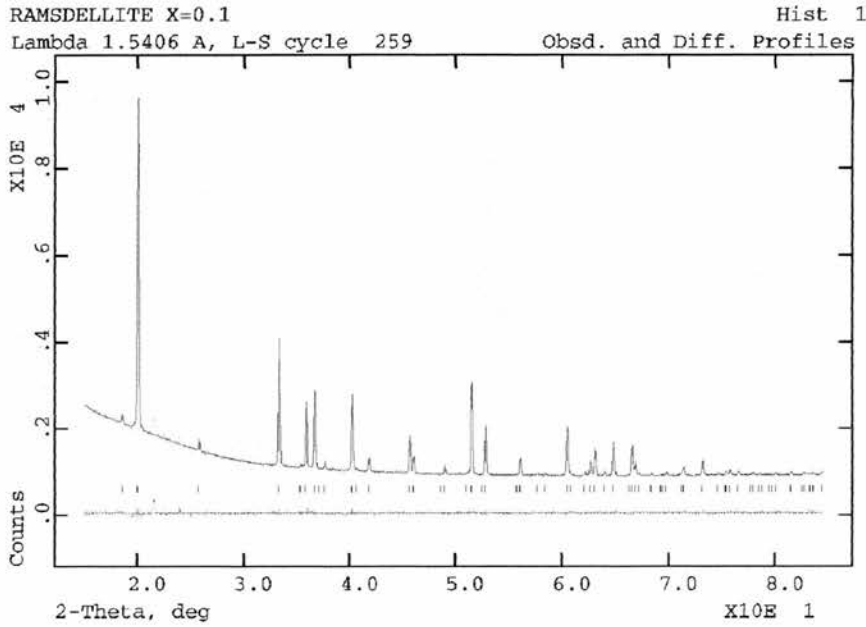


Figure 7.4. Refined X-ray powder pattern obtained for $\text{Li}_{1.1}\text{Ti}_{1.8}\text{O}_4$ ramsdellite. Experimental data presented as points, Calculated profile presented as a line. Along the bottom is the observed difference profile.

This preliminary X-ray study indicates that as the total Li content increased the unit cell volume decreased. The results presented in table 7.2 indicate that as the lithium content of the phases increases there is an associated decrease in the dimensions of the unit cell. This could be indicative of the overall oxidation state of the Ti moving from 3.5^+ (in LiTi_2O_4) towards 4^+ (in $\text{Li}_2\text{Ti}_3\text{O}_7$). These observations are in agreement with that obtained previously using thermal analysis.

7.2.4. Combined Time Of Flight Neutron and X-ray powder diffraction.

The structural parameters obtained from the X-ray results were used as the starting point for the neutron refinements, with the data collected from the X-ray study being used in conjunction with the neutron data. The reasons for this were highlighted previously in this chapter. Presented below in table 7.3 are the neutron scattering cross sections used during the refinement of the neutron powder patterns.

Element.	Coherent neutron scattering cross section
Li	-0.22220
Ti	-0.35580
O	0.58050

Table 7.3. Neutron cross sections for lithium, titanium and oxygen

The use of two histograms from two different techniques requires very careful refinement. The X-ray powder patterns were refined in accordance with the method presented in section 7.2.2, with the neutron patterns being refined using the following parameters.

1. Set minimum time of flight set to 3 microseconds.
2. Background fitting using $Q^{2n/n!}$ Function, with 5 variables and histogram scaling.
3. Zero point and lattice parameters.
4. Profile coefficients using the function described Von Dreele, Jorgensen & Windsor convolution function¹⁷.
5. The atomic co-ordinates for Ti, O1 and O2.
6. Isotropic temperature factors for Ti, O1 and O2.
7. Anisotropic temperature factors for Ti, O1 and O2.
8. Atomic positions for Li.
9. Isotropic temperature factors for Li refined.
10. When appropriate the Li isotropic temperature were converted to anisotropy.
11. Absorbance correction for ⁶Li.

As is usual with this type of refinement, it was necessary to link the atomic positions and temperature factors for the framework Li and Ti together, such that they remained identical to each other.

Presented below in table 7.4 are the unit cell edges obtained from refinement of the combined X-ray and neutron data sets.

X	a	b	c
0	5.0325(1)	9.6229(2)	2.94564(4)
0.04	5.0265(1)	9.6102(1)	2.94601(5)
0.0715	5.0192 (2)	9.5836(4)	2.94824(10)
0.1	5.0194(1)	9.5743(2)	2.94671(5)
0.145	5.0141(1)	9.5436(2)	2.94328(6)

Table 7.4. Obtained lattice parameters as a function of x Li composition using X-ray and neutron data sets.

This is also presented graphically in figures 7.5 (a) to (c) below.

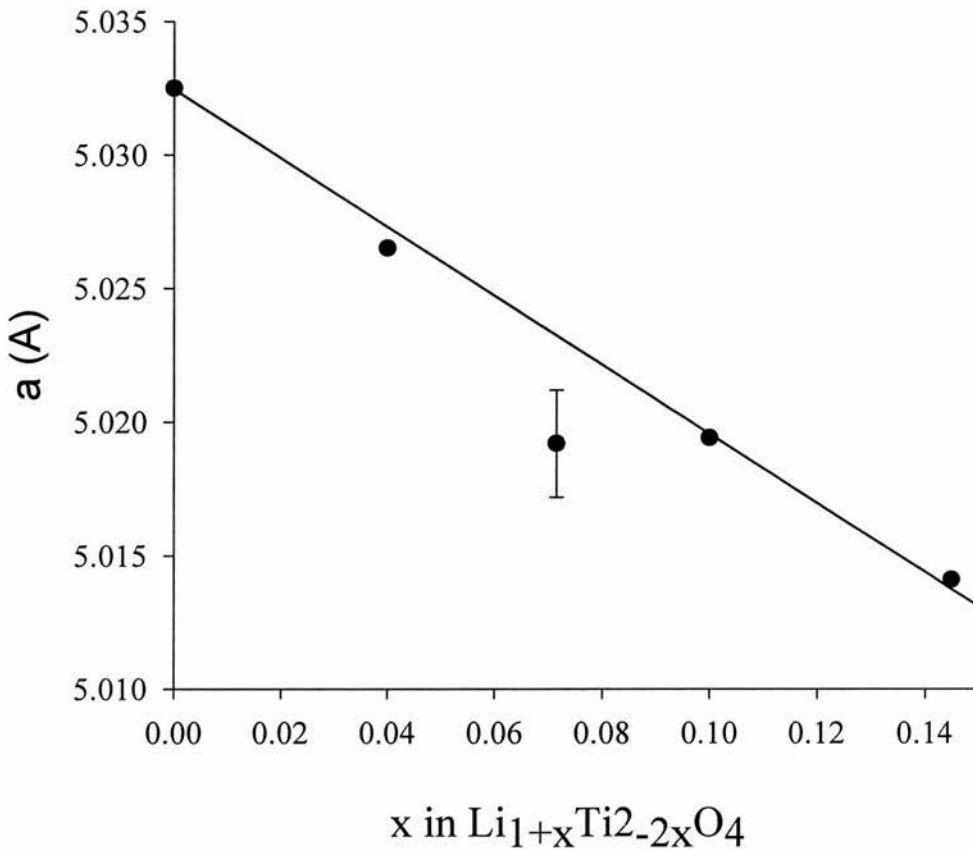


Figure 7.5(a). Unit cell edge a versus composition as determined from refinement of combined X-ray and neutron diffraction data. Line of best fit used as a guide to the eye.

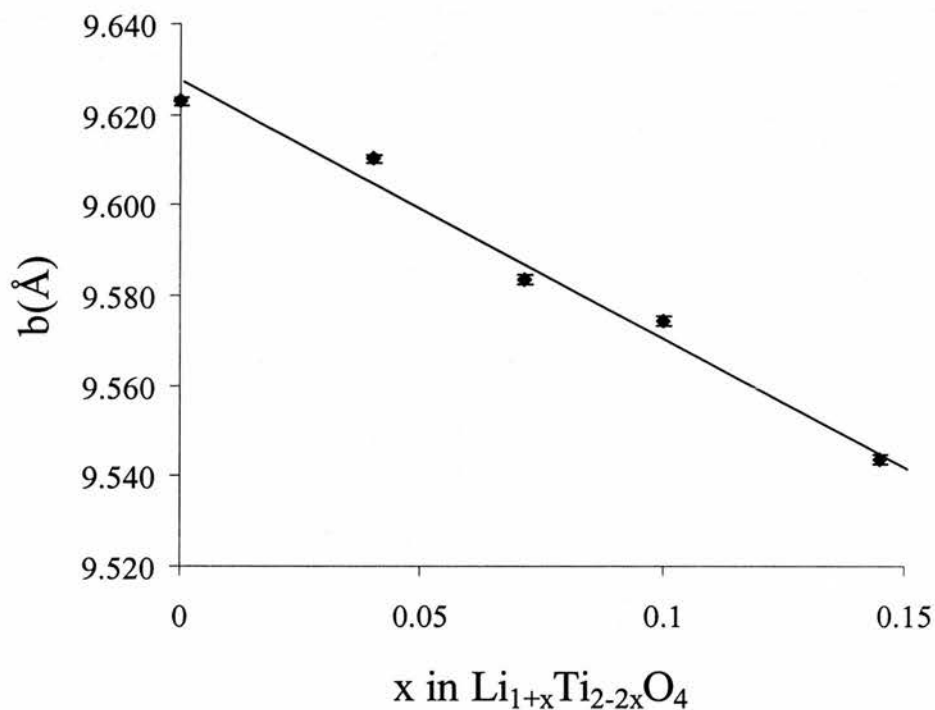


Figure 7.5(b). Unit cell edge b versus composition as determined from refinement of combined X-ray and neutron diffraction data. Line of best fit used as a guide to the eye.

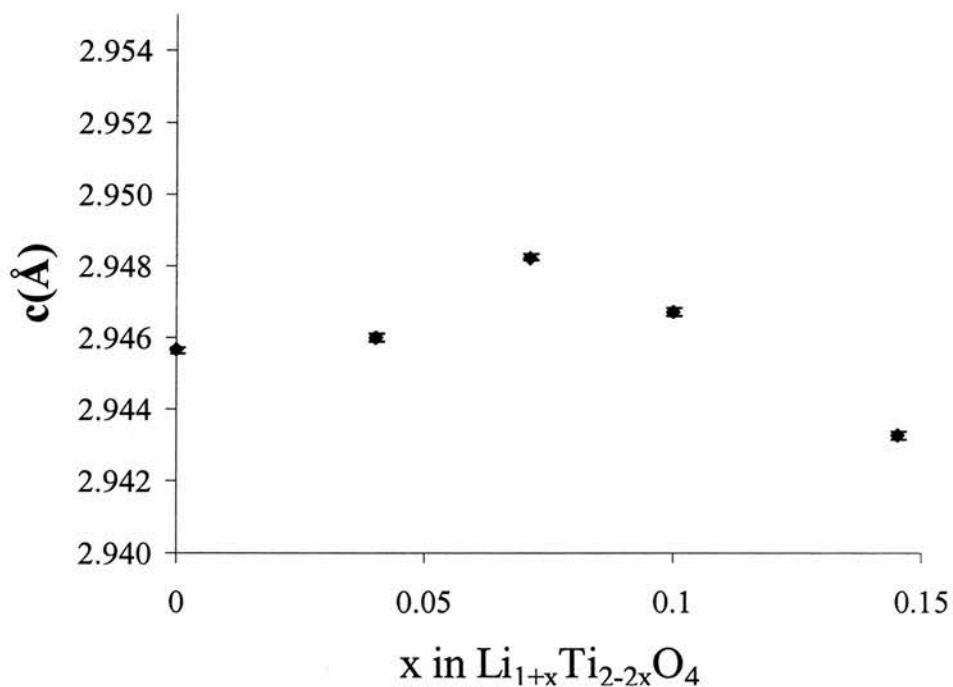


Figure 7.5(c). Unit cell edge c versus composition as determined from refinement of combined X-ray and neutron diffraction data.

As can be seen from the refined powder patterns presented in figures 7.6 and 7.7, the samples are of a high phase purity.

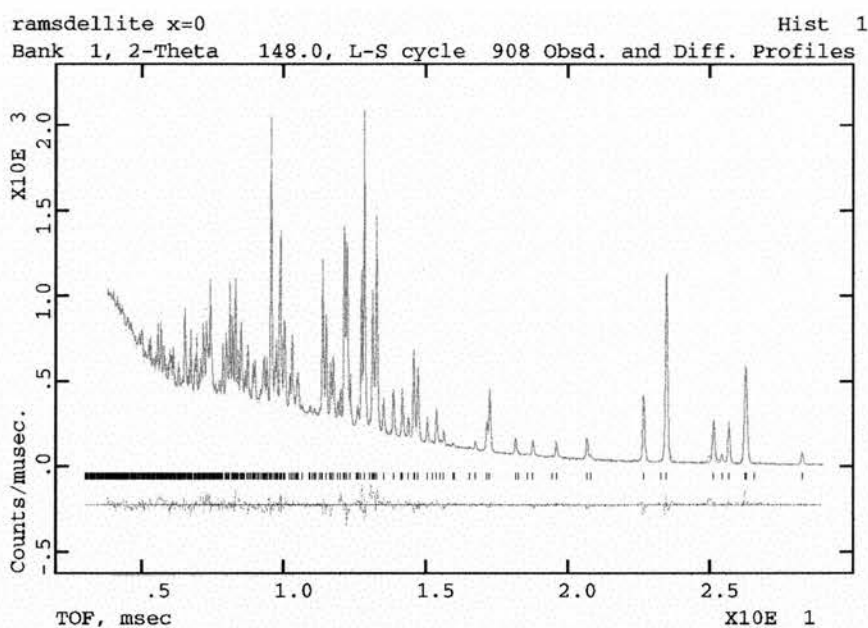


Figure 7.6. Refined neutron powder pattern obtained for LiTi_2O_4 ramsdellite. Experimental data presented as points, calculated profile presented as a line. Along the bottom is the observed difference profile.

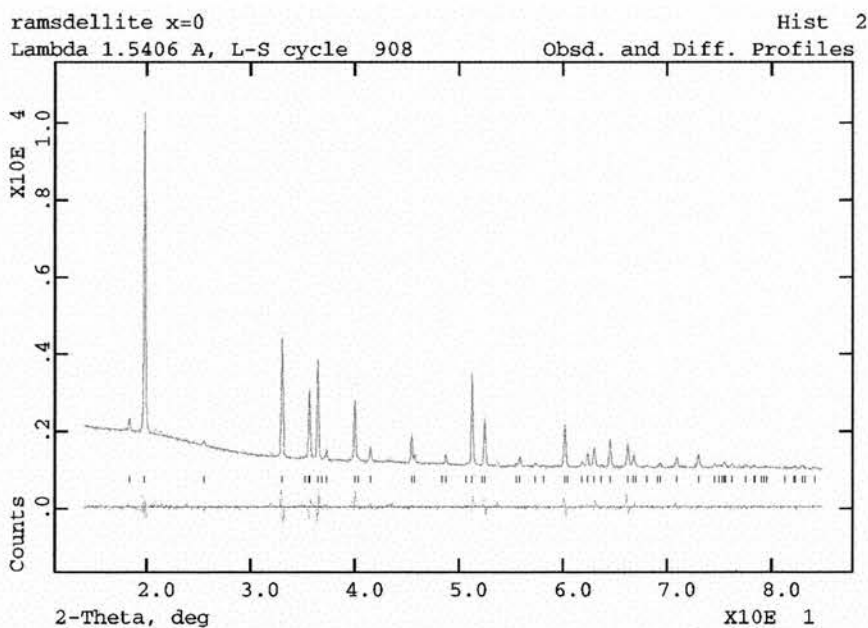


Figure 7.7. Refined X-ray powder pattern obtained for LiTi_2O_4 ramsdellite. Experimental data presented as points, calculated profile presented as a line. Along the bottom is the observed difference profile.

The proposed site occupancy model presented earlier was used during the refinements and found to be stable. The obtained R factors are presented in table 7.5. Atomic positions, site occupancies and temperature factors presented in table 7.6 and 7.7 respectively, with selected bond angles and lengths presented in table 7.8.

	R_{wp} (N)	R_{wp} (X)	R_{wp} (C)	R_p (N)	R_p (X)	R_p (C)	χ^2
0	5.24	3.31	4.44	3.34	2.18	2.87	2.636
0.04	6.13	3.27	5.08	3.27	2.34	3.39	2.263
0.0715	6.71	4.84	3.19	4.46	3.19	3.92	3.586
0.1	5.05	3.37	4.24	3.27	2.15	2.74	1.820
0.145	6.06	3.79	5.10	3.83	2.55	3.29	2.680

Table 7.5. Residual factors obtained during refinements of combined X-ray and neutron data sets. N = Neutron, X = X-ray, C = Combined.

Examination of the neutron patterns in conjunction with obtained errors indicates that the proposed model is correct, although the results for $x=0.0715$ is not quite as good as the others due to the presence of a slight second phase.

Reasonable attempts were made to refine the site occupancies of all atoms that have indicated site occupancy of one. It was found that the values came out as one or very close to one, thus indicating that no framework vacancies were present in these samples.

	0	0.04	0.0715	0.1	0.145
Li(1)					
x	-0.0559(2)	-0.0598(2)	-0.0580(4)	-0.0605(2)	-0.0629(2)
y	0.4687(2)	0.4675(2)	0.4411(3)	0.4752(3)	0.4581(3)
S.O.F	0.47(1)	0.479(1)	0.416(3)	0.432(1)	0.425(1)
Ti/Li(2)					
x	-0.0177(3)	-0.0196(3)	-0.0248(5)	-0.0247(3)	-0.0327(3)
y	0.1416(2)	0.1416(2)	0.1401(3)	0.1409(1)	0.1407(2)
S.O.F	1	0.943(4)/ 0.063(7)	0.913(6)/ 0.084(12)	0.893(3)/ 0.124(7)	0.837(4)/ 0.111(8)
O(1)					
x	0.6987(2)	0.6953(2)	0.6851(4)	0.6851(2)	0.6721(2)
y	0.2794(1)	0.2765(1)	0.2754(2)	0.2765(1)	0.2738(9)
S.O.F	1	1	1	1	1
O(2)					
x	.2022(2)	0.2031(2)	0.2031(3)	0.2027(2)	0.2042(2)
y	-.0354(1)	-.03531(9)	-0.0347(2)	-0.0342(9)	-0.0322(8)
S.O.F	1	1	1	1	1

Table 7.6. Obtained atomic positions and site occupancies for the $Li_{1+x}Ti_{2-2x}O_4$ solid solution series as a function of x . S.O.F. is an abbreviation for site occupancy factor.

Presented in table 7.7 are the obtained temperature factors for the solid solution series.

	0	0.04	0.0715	0.1	0.145
Li(1)					
u11	3.5(5)	1.67(43)	-	1.61(41)	-
u22	19.3(14)	27.93(237)	-	34.85(280)	-
u33	4.2(5)	8.22(87)	-	4.83(69)	-
u12	3.0(7)	1.35(76)	-	1.71(84)	-
uI₁	6.89(25)	7.60(30)	9.47(75)	7.76(31)	7.45(36)
uI₂	9.01	9.38	-	13.72	-
Ti(Li2)					
u11	1.44(7)	1.37(7)	1.44(1)	1.50(7)	1.60(8)
u22	0.72(6)	0.92(6)	1.70(1)	0.78(6)	1.16(7)
u33	0.60(5)	0.46(5)	0.82(9)	0.99(5)	0.83(6)
u12	0.12(6)	0.24(6)	.13(1)	0.11(5)	0.53(6)
O(1)					
u11	1.20(4)	1.32(4)	2.04(9)	1.49(4)	1.74(5)
u22	1.63(6)	1.62(6)	1.79(9)	1.31(5)	1.43(5)
u33	0.68(5)	0.60(5)	0.23(7)	0.86(5)	0.71(5)
u12	0.74(5)	0.73(5)	0.85(8)	0.60(4)	0.74(4)
O(2)					
u11	0.83(3)	0.78(4)	0.86(6)	0.75(3)	0.78(4)
u22	0.95(5)	1.13(5)	1.53(9)	0.97(4)	1.20(5)
u33	0.70(6)	0.96(5)	1.09(9)	0.90(5)	1.48(5)
u12	-.04(4)	-0.16(4)	-0.14(8)	0.00(4)	0.04(4)

Table 7.7. Temperature factors for $Li_{1+x}Ti_{2-2x}O_4$ as a function of composition.

The temperature factors for u23 and u13 are equal to zero, as determined by symmetry. The value obtained for uI₁ for refinement with isotropic temperature factors, uI₂ equivalent isotropic temperature factors calculated from anisotropic values. Note all thermal parameters are multiplied by 100.

It was found impossible to refine the anisotropic temperature factors for x=0.0715 and 0.145. In the case of $Li_{1.0715}Ti_{1.830}O_4$ it is thought that the presence

of the second phase was responsible for instability of the refinement of Li anisotropic temperature factor. Abrahams⁹ also found it impossible to refine the anisotropic temperature factors for Li on the 4C channel site in $\text{Li}_2\text{Ti}_3\text{O}_7$ ramsdellite. To make it possible to compare the temperature factors for all of the solid solution series all members of the series have the isotropic temperature factors quoted for Li (1). To ensure that the comparison is fair, these values were refined and also calculated using the BIJCALC routine contained in GSAS.

	0	0.04	0.0715	0.1	0.145
Li-O1	2.239 (11)	2.225(13)	2.053(25)	2.220(13)	2.132(13)
Li-O2	1.792(10)	1.771(12)	1.785(21)	1.767(12)	1.784(12)
Li-O2' x 2	2.010(7)	2.015(8)	2.104(2)	2.031(8)	2.072(8)
Mean	2.011	2.007	2.012	2.012	2.015
Li-Li	1.688(7)	1.709(4)	1.945(2)	1.662(1)	1.788(2)
Ti-O1	1.952(2)	1.954(2)	1.955(3)	1.957(2)	1.955(2)
Ti-O1' x 2	1.979(1)	1.971(1)	1.979(2)	1.970(1)	1.969(1)
Ti-O2 x 2	2.020(1)	2.020(1)	2.004(3)	2.004(1)	1.997(1)
Ti-O2'	2.032(1)	2.035(2)	2.025(3)	2.026(1)	2.029(1)
Mean	1.997	1.995	1.996	1.989	1.986
Angles					
O2-Li-O2'	128.3(3)	128.0(4)	136.8(3)	126.8(4)	122.0(5)
O2'-Li-O2'	94.8(4)	94.0(5)	94.1(9)	93.0(5)	90.5(5)
O2-Li-O1	120.6(6)	122.8(7)	120.9(9)	126.7(7)	136.5(1)
O2-Li-O1	85.4(4)	85.1(4)	88.4(2)	85.0(4)	86.3(1)
O1-Ti-O1'	98.16(5)	98.18(5)	97.20(9)	97.59(5)	97.23(6)
O1-Ti-O2	90.16(6)	90.10(2)	89.92(1)	90.20(6)	90.58(6)
O1-Ti-O2'	165.40(9)	165.24(9)	165.78(2)	165.53(8)	166.11(9)
O1-Ti-O1	96.19(8)	96.75(9)	96.28(1)	96.79(8)	96.80(8)
O1-Ti-O2'	91.56(6)	91.58(6)	92.27(1)	91.99(5)	91.97(6)
O1'-Ti-O2	84.46(3)	84.19 (3)	84.04(4)	83.75(3)	83.55(3)
O2-Ti-O2	93.65(7)	93.62(8)	94.73(2)	94.62(7)	92.01(8)

Table 7.8. Selected bond angles and lengths obtained from combined X-ray and neutron data sets for $\text{Li}_{1+x}\text{Ti}_{2-2x}\text{O}_4$ solid solution series.

Presented in table 7.8 are the obtained bond lengths and angles obtained from the refinements. Grins et al¹⁸ proposed other possible Li sites within the channels of the ramsdellite structure for the $\text{Li}_{2+x}(\text{Li}_x\text{Mg}_{1-x}\text{Sn}_3)\text{O}_8$ ($0 \leq x \leq 0.5$) and $\text{Li}_2\text{Mg}_{1-x}\text{Fe}_{2x}\text{Sn}_{3-x}\text{O}_8$ ($0 \leq x \leq 1$) analogues. A number of attempts were made to refine Li on these sites, but the results obtained for these refinements were found to be unstable. Difference Fourier mapping analysis was performed to try and determine if any of the residual scattering could be assigned to Li in the channels, however no stable sites could be found in the channels.

7.3. Conclusions.

The initial X-ray results obtained for this solid solution series indicated that preparation of the proposed new solid solution series had been successful and this was supported by the thermal analysis experiments performed on the samples, with the errors seen in the thermal analysis within experimental error.

The crystal structures of both $\text{Li}_2\text{Ti}_3\text{O}_7$ ^{8,9} and LiTi_2O_4 ¹¹ have been reported previous in the literature, and it was found that the unit cells obtained from our studies are in good agreement with these values. The b axis of LiTi_2O_4 was found to be slightly smaller than reported by Akimoto et al¹¹ and that obtained from refinement of the X-ray patterns, however this should not be viewed as significant.

As the Li content of the solid solution increased it was seen that the **a** and **b** directions of the unit cell decreased in magnitude which is consistent with the overall titanium oxidation state is moving away from 3.5+ towards 4+. The **c** axis was found to be relatively insensitive to the Li content. This lack of sensitivity of the c axis to the composition has been seen previously by Thackeray whilst working on MnO_2 ramsdellite¹⁹, Akimoto working on topotactic oxidation of LiTi_2O_4 ²⁰, and by Lacorre²¹ working on $\text{Li}_{1+x}(\text{Li}_{2x/3}\text{Fe}_{1-x}\text{Sn}_{1+x/3})\text{O}_4$ ramsdellites ($0 \leq x \leq 0.28$).

It is noted from examination of table 7.6 that the atomic positions of the atoms within the unit cell are not significantly different when compared to each other, with no discernible differences seen in the position of the lithium atoms within the channels. The site occupancy of Li in the channel sites was found to

be 0.47, however this should not be viewed as being significantly different to that predicted from the chemical formula, it also falls within the expected errors associated with Li occupancies²². From $x=0.04$ to 0.0145, the general trend is for the total channel occupancy to decrease with increasing total Li content. The decreasing Li content within the channel was as expected and approximately matches that expected from the proposed model. Presented below in figure 7.8 is a plot of the experimental and expected lithium sites occupancies of channel and framework sites respectively. Present in figure 7.9 are the results obtained from refinement of Ti framework sites.

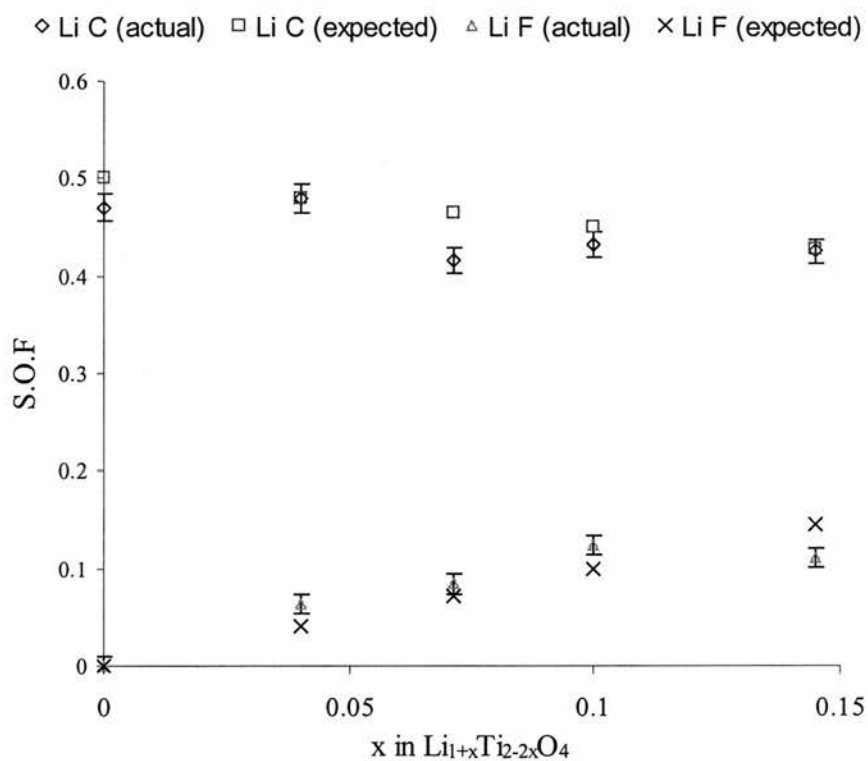


Figure 7.8. Lithium site occupancies obtained from combined X-ray and neutron powder diffraction. C = channel site, F = framework site.

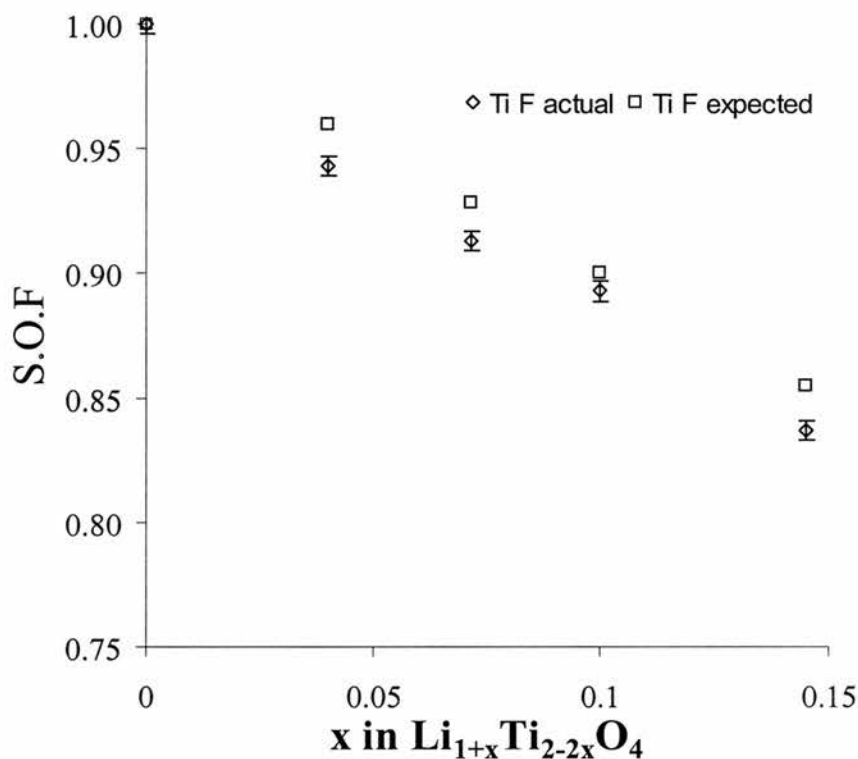


Figure 7.9. Titanium site occupancies obtained from combined X-ray and neutron powder diffraction. F = framework site.

It must be noted that it was not possible to refine either of the two channel site models proposed by Abrahams⁹ and Morosin⁸. The refinement performed by Abrahams indicated that the Li was distributed over two different sites, with 60% to be found on an 8 fold channel site and 40% on a 4 fold site. Morosin described the lithium distribution as being split 50:50 over two different 4 fold sites. Possible explanation for the differences in the results may be related to slightly different methods of preparation. The samples prepared for this study were not cooled as fast as those prepared by Abrahams⁹. The model proposed is consistent across the entire solid solution mechanism, whereas previous models have only been proposed for $\text{Li}_2\text{Ti}_3\text{O}_7$ ramsdellite ($\text{Li}_{1.145}\text{Ti}_{1.710}\text{O}_4$).

The results indicate that the overall temperature factors obtained for the Li channel sites were high, with the standard refinements of the isotropic temperature factors shown to be reasonably constant over the composition range examined. The isotropic temperature factors obtained from calculations using the anisotropic temperature factors show an increase with increasing Li content,

which is consistent with the Li being more mobile. This would be expected due to the increase in the number of Li channel site vacancies.

The anisotropic temperature factors indicated that the dominant thermal vibration in this series of material was along u_{22} , this is in agreement with previous neutron studies on this class of materials (see chapter 5). The u_{22} thermal vibration is parallel to the b axis. This could be related to the decrease in the number of channel lithiums with a subsequent increase in the total number of vacancies present in the channels, i.e., the lithium has more possible sites onto which they can move. The high value obtained in these samples for u_{22} may indicate that some interstitial hopping is occurring. It could also indicate that the Li might be split over two sites, with the neutrons unable to separate out the contributions from each.

No trends are apparent in the Ti, O1 and O2 temperature factors. This indicates that substitution of Li onto the Ti framework sites does not adversely affect the framework stability, Akimoto²⁰ found that the TiO_6 framework was stable on removal of Li from $Li_xTi_2O_4$ in compositions when $x=0$, and hence it comes as no surprise that this is the case.

The bond lengths presented in table 7.9 indicate that the mean Li bond length is basically unchanged as the total Li content increases, this indicates the decrease in overall unit cell dimension is being compensated for by the slight increase in the Li channel site vacancies. This type of stabilisation was seen previously, when Akimoto studied the removal of Li from the $Li_xTi_2O_4$ channel sites (where X is the Li content). He noted that the degree of distortion on the Li-O₄ units was basically unchanged until the Li content was less than 0.14. Therefore it is not surprising that the degree of distortion does not change, as the degree of removal from the channel sites is far less drastic in this particular study. It was also noted that the average Li-O bond lengths are in agreement with Akimoto's study into the effects of chemical lithium deintercalation on the structure of $Li_xTi_2O_4$ ramsdellite.

The average Ti-O bond length is seen to remain constant over the composition range. The average bond length would be expected to decrease as the average titanium oxidation state moves from $Ti^{3.5+}$ (in $LiTi_2O_4$) towards Ti^{4+} (in $Li_{1.145}Ti_{1.710}O_4$), however the change is not gradual as would be expected as the oxidation state changes. Examination of the individual bond lengths suggests

that the Ti-O1' ($\times 2$) is decreasing more than the other bond lengths, however this is apparently compensated for by the other bond lengths.

The results presented in the chapter indicate that the proposed model for this solid solution series is indeed correct. Electrochemical testing²³ experiments performed on these materials have shown a charge/discharge potential in the range of 1.5 to 2.5 volts. High capacities were observed, which were typically found to be in the region of 200mAh/g. The materials were also found to be stable on cycling.

7.4. References.

1. H.Y.P. Hong, *Mater. Res. Bull.*, **13** (1978) 117.
2. I. Abrahams, P.G. Bruce, W.I.F. David and A.R. West, *J Solid State Chem.*, **75** (1988) 390.
3. B.L. Dubey and A.R. West, *Nature Phys. Sci.*, **235** (1972) 155.
4. M. Castellanos and A.R. West, *J. Mater Sci.*, **14** (1979) 450.
5. G.H. Jonkers, *Trabajos reunion intern reactividad solidos*, Madrid., (1957) 413.
6. K.H. Kim and F.A. Hummel, *J Amer. Ceram Soc.*, **43** (1960) 611.
7. A.M. Bystrom, *Acta. Chem. Scand.*, **3** (1949) 163.
8. B Morosin and J.C. Mikellsen Jr, *Acta. Crysta.*, **B35** (1979) 798.
9. I Abrahams, P.G. Bruce, W.I.F. David and A.R. West, *J Solid State Chem.*, **78** (1989) 170.
10. J.B. Boyce and J.C. Mikkelsen Jr, *Solid State Comms.*, **31** (1979) 741.
11. J. Akimoto, Y Gotoh, M. Sohma, K. Kawaguchi, Y. Oosawa and H. Takei, *J Solid State Chem.*, **110** (1994) 150.
12. V.F Seers, *Neutron News.*, **3** (1992) 29.
13. G. E. Bacon, *Neutron diffraction*, Oxford University Press, (1962) 21.
14. A.C. Larsen and R.B. Von Dreele, *Los Alamos Laboratory report*, NO-LA-U-86-748 (1987).
15. STOE Stadi P user guide. Stoe Automated diffractometer systems for powder and single crystal diffractometry, Damstradt, 1987.
16. C.J. Howard, *J. Appl. Cryst.*, **15** (1982) 615.

-
17. R.B. Von Dreele, J. Jorgensen and A. Windsor., *J. Appl. Cryst.*, **15** (1982) 581.
 18. J. Grins and A.R. West, *J. Solid State Chem.*, **65** (1986) 265.
 19. M.M Thackeray, M.H Rossouw, R.J. Gummow, D.C. Liles, L Perce, A. De Kock, W.I.F. David, S. Hull, *Electrochimica Acta.*, **9** (1993) 1259.
 20. J. Akimoto, Y. Gotoh, Y. Oosawa, N. Nonose, T. Kumaghi, K. Aoki and H. Takei. *J Solid State Chem.*, **113** (1994) 27.
 21. P. H. Lacorre, M. Hervieu, J. Pannetier, J. Choisnet and B. Raveau, *J Solid State Chem.*, **50** (1983) 196.
 22. P. Raedeilli, Private communication
 - 23 R.K.B. Gover, J.R. Tolchard, J.T.S.Irvine, T. Murai and H. Tukamoto, *Submitted to Solid State Ionics.*

Chapter 8. Conclusions and future work.

8.1. LiTi_2O_4 spinel.....	218
8.2. μ+SR studies on LiTi_2O_4 spinel.	218
8.3. The spinel to ramsdellite transformation.	219
8.4. Work on LiTi_2O_4 ramsdellite.....	220
8.5. The $\text{Li}_{1+x}\text{Ti}_{2-2x}\text{O}_4$ ramsdellite solid solution series.	221
8.6. References.....	223

8.1. LiTi_2O_4 spinel.

Experiments on the effects of temperature on phase purity indicate spinel can only be made in a narrow temperature range (840-850°C). This temperature is slightly lower than studies by Dalton¹ and Mousa² have previously suggested. These experiments indicated the presence of an unknown(s) at low and high temperature, examination of the neutron patterns collected for LiTi_2O_4 spinel also show similar peaks for unknowns at room temperature and at elevated temperatures. Closer examination of the powder patterns collected for the samples fired in the region of 860 to 880°C indicated the presence of the high temperature LiTi_2O_4 ramsdellite polymorph. This suggests that the transformation occurs at similar temperature to that required to produce single phase spinel samples.

Neutron diffraction showed deviations from linear behaviour for the Li temperature factors at temperatures below the ramsdellite transformation, this was found to be linked to changes in the occupancy of the 8a tetrahedral Li site. Soubeyroux³ and Kanno⁴ have seen similar behaviour previously for other spinels at high temperatures. Refinement of spinel distribution at high temperature indicated that lithium was present on the octahedral 16c site.

The results obtained from the neutron diffraction could explain the apparent differences seen in the literature for the superconducting transition temperature of LiTi_2O_4 spinel. Annealing and quenching from various temperatures indicated that the T_c was linked to the thermal history of the samples. This was further proved by solid state ^6Li MAS NMR experiments, which showed different responses for the different annealing and cooling regimes used.

8.2. μ +SR studies on LiTi_2O_4 spinel.

An experiment performed on a fresh and aged sample of LiTi_2O_4 spinel produced a number of new results. The penetration depth of the fresh sample was found to be larger than had been previously published in the literature, with a value of 320nm being obtained. This is compared to the 270nm

obtained by Harrison using conduction methods⁵ and 210nm obtained by Wu using transverse field muon rotation methods⁶.

The large difference seen between the results obtained during these studies and those obtained by Wu may be related to a number of reasons. Wu made no indication of the method of sample preparation, and as the results above indicated, this can be important in terms of the T_c . It was also assumed in Wu's work that the distribution of field in the mixed state was gaussian in nature. Analysis of the data using the Maximum Entropy⁷ method indicated this was not the case.

Examination of the sample using longitudinal field μ^+ SR indicated no magnetic phases in the temperature range examined.

The sample examined above was then aged for three months under vacuum and found to have a significantly different penetration depth to that of a fresh sample. Examination of the sample using X-ray powder diffraction and D.C. magnetisation indicated significant changes in the character of the sample. Powder X-ray diffraction showed a significant broadening of the Bragg peaks, with the magnetisation showing a drop in the T_c and superconducting volume. Although the mechanism of the degradation could not be fully determined, it is believed that the sample may have undergone some kind of segregation or oxidation.

Future work on this system should include examination by high resolution powder neutron and/or X-ray diffraction and electron microscopy to study the ageing mechanism of spinel. Further studies should also be performed using transverse field μ^+ SR, to determine any changes in the superconducting properties of other members of the $Li_{1+x}Ti_{2-x}O_4$ spinel solid solution as the metal insulator transition is approached.

8.3. The spinel to ramsdellite transformation.

The X-ray studies performed in chapter 3, indicated that the transformation from the spinel to ramsdellite structure probably occurred in the region of 850-860°C. The two neutron experiments gave transformation temperatures of 875 to 925°C and 850 to 900°C respectively, which is in

approximate agreement with the X-ray study presented in chapter 3. The two structure types were seen to co-exist over the transformation temperature range. The difference in temperature seen for the ISIS and IPNS experiments is believed to be due to positioning of sample and thermocouples.

The second neutron study indicated that the unit cell dimensions of spinel phase deviated from linear behaviour in the region of 870°C. This may possibly indicate a second order phase change as the spinel converts to ramsdellite. No anomalous behaviour was seen in the unit cell dimensions of the ramsdellite in or above the transformation region.

It was found best to refine a two site lithium distribution for LiTi_2O_4 ramsdellite at high temperatures. It was seen that the occupancy of the expected 4c site⁸ was significantly lower than the 50 % expected. Subsequent Rietveld refinements indicated that approximately half of the Li was to be found at Li1 (-0.06, 0.47, 0.25) with the balance found at Li2 (0.50, 0.05, 0.25). It was noted that as the temperature was increased, the total occupancy of Li1 increased, with an opposite trend seen for Li2. The model proposed for LiTi_2O_4 ramsdellite at high temperature is very similar to that of $\text{Li}_2\text{Ti}_3\text{O}_7$ ramsdellite as proposed by Morosin⁹ at room temperature.

It might be possible to determine the mechanism more accurately if samples were quenched from temperatures known to be within the transformation region. This would allow Rietveld refinement using combined X-ray and neutron diffraction, which might allow more accurate determination of the structural changes.

8.4. Work on LiTi_2O_4 ramsdellite.

A sample of LiTi_2O_4 was prepared and the structure determined using powder neutron diffraction. The structure was found to be close to that described by Akimoto in reference 8. The anisotropic temperature factor was found to be dominant along the b axis and may indicate intersite hopping.

SQUID magnetometry suggested the presence of magnetic order at low temperature. In an attempt to determine the origins of the ordering, the material was examined using longitudinal muon spin relaxation. This

technique suggested the presence of two different muon sites within the structure, with one of the sites having a different local magnetic environment. It was found that the response obtained for the muon experiment was similar in nature to seen recently for SrCuO_2 ¹⁰, this system is believed to be a zigzag spin ladder¹¹.

D.C. Electrical measurements indicated that ramsdellite was semiconducting in nature, with an activation energy consistent with a small polaron hopping mechanism. Further examination using A.C. Impedance spectroscopy indicated that grain boundaries were present and were an important component of the electrical response.

This particular system has much potential for further work, with at least three new studies probably being worthwhile.

Low temperature neutron studies (either polycrystalline or single crystal) could be useful in determining if any anomalous features can be found, whether this is in the unit cell dimensions or extra reflections associated with the suspected magnetic transition.

Powder neutron diffraction to help determine whether the Li located in the Li channel sites become mobile along the c axis as the sample temperature is increased^A.

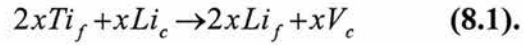
A new muon study using single crystals could be performed using longer counting times and going to lower temperatures than used in the previous study. This would help in the collection of better statistics and more careful investigation of the magnetic behaviour.

8.5. The $\text{Li}_{1+x}\text{Ti}_{2-2x}\text{O}_4$ ramsdellite solid solution series.

A new solid solution mechanism was found that linked LiTi_2O_4 and $\text{Li}_2\text{Ti}_3\text{O}_7$ ramsdellite (can also be written as $\text{Li}_{1.145}\text{Ti}_{1.710}\text{O}_4$) as end members of a new solid solution series. The unit cell dimensions were seen to decrease as the Li content was increased, which is consistent with the average Ti oxidation state going from 3.5+ towards 4+.

^A Beam time has been awarded for this experiment, but cannot be included because of time constraints.

The Li channel and framework occupancy was seen to vary as a function of Li content. However the model proposed by Morosin and later by Abrahams for $\text{Li}_2\text{Ti}_3\text{O}_7$ ¹² was found to lead to unstable Rietveld refinements. The model proposed in equation 8.1. was found to be stable across composition range examined.



The mechanism for this new solid solution is that for every two titanium atoms in the framework replaced with a lithium atom, one lithium is lost from the channel, with the formation of one channel vacancy site.

Combined X-ray/neutron powder diffraction indicated that Li was to be found on only one channel site across the solid solution series. Previous studies by Morosin⁹ and Abrahams¹² on $\text{Li}_2\text{Ti}_3\text{O}_7$ indicated the presence of two lithium channel sites. Experiments performed in chapter 5 on the spinel to ramsdellite transformation indicated that presence of two channel sites in at elevated temperatures in LiTi_2O_4 ramsdellite. This could indicate that the method of sample preparation and thermal history is important. Abrahams followed the method of preparation proposed by Izquierdo¹³, which involved quenching the samples from high temperature. The samples examined in chapter 7 were not quenched but allowed to cool naturally from the preparation temperature. The method employed by Abrahams may have “trapped” Li over the two sites, whereas normal cooling favours the Li site at approximately (-0.06, 0.45 0.25).

The lithium temperature factors were seen to increase over composition range from 0 to 0.145. This is likely to be related to an increased number of channel vacancies into which Li can hop. Future work should include electrical and magnetic characterisation of the properties of the solid solution series.

8.6. References.

1. M Dalton, *PhD thesis.*, Univ. of Cambridge., 1992.
2. A.H. Mousa and N.W. Grimes., *J. Mat. Sci. Lett.* **15** (1980) 793.
3. J.L. Soubeyroux, C. Cros, Wang. Gang, R. Kanno and M. Pouchard., *Solid State Ionics*, **15** (1985) .293.
4. R. Kanno, Y. Takeda, O. Yamamoto, C. Cros, Wang Gang, P Hagenmueller., *Solid State Ionics*, **20** (1986) .99
5. M.R. Harrison, P.P. Edwards, and J.B. Goodenough, *Philos. Mag.*, **52** (1985) 679.
6. W. D. Wu, A. Keren, L.P. Le, G.M. Luke, B.J. Sternlieb, Y.J. Uemera, D.C. Johnston, B.K. Cho, and P. Gehring. *Hyperfine Interact*, **86** (1994) 615.
7. E.H. Brandht, *Phys Rev Let.*, *66* (1991) 3213.
8. J. Akimoto, Y Gotoh, M. Sohma, K. Kawaguchi, Y. Oosawa and H. Takei, *J Solid State Chem.*, **110** (1994) 150.
9. B Morosin and J.C. Mikellsen Jr, *Acta. Cryst.*, **B35** (1979) 798
- 10 M. Matsuda, K. Katsumata, K.M. Kojima, M, Larkin, G.M. Luke, J. Merrin, B. Nachumi, Y.J. Uemura, H. Eisaki, N. Motoyama, S. Uchida and G. Shirane, *Phys. Rev. B.*, **55** (1997) 11953.
11. Proceedings from Miniworkshop on strong electron correlation's "Disorder and interaction in quantum systems and their classical analogs", S.R. White and I. Affleck, July 1996.
- 12 I Abrahams, P.G. Bruce, W.I.F. David and A.R. West, *J Solid State Chem.*, **78** (1989) 170.
13. G. Izquierdo and A.R. West, *Mat. Res. Bull.*, **15** (1980) 1655.